

Ion-Ion Interactions of Lithium Salts in Poly(siloxanes) & Ionic Liquids



A Thesis Presented for the Degree of
Doctor of Natural Sciences
(Dr. rer. nat.)

At the Natural Sciences Faculty IV
Chemistry & Pharmacy
Universität Regensburg

John De Roche MChem.

Regensburg
2004

“I do not know what I may appear to the world, but to myself I seem to have been only a boy playing on the seashore, and diverting myself now and then in finding a smoother pebble or a prettier shell than ordinary, whilst the great ocean of truth lay undiscovered before me”

Sir Isaac Newton [Letter 1676]

Official Registration	: 18 th December 2003	
Defence	: 29 th January 2004 - 2 pm.	Room 12.0.16
Ph.D. Supervisor	: Priv. Doz. Dr. H. J. Gores	
Adjudicators	: Priv. Doz. Dr. H. J. Gores	Universität Regensburg, Deutschland.
	: Prof. Dr. M. D. Ingram	University of Aberdeen, United Kingdom.
	: Prof. Dr. W. Kunz	Universität Regensburg, Deutschland.
Chair	: Prof. Dr. A. Merz	Universität Regensburg, Deutschland.

Acknowledgments:

Regensburg, 14th December 2003

“The presented work took place between November 2000 and December 2003 at the Department of Physical Chemistry for Natural Sciences at the Universität Regensburg under the stewardship of Priv. Doz. Dr. Heiner. J. Gores.

During this time, an enormous number of friends and colleagues in which a single page of thanks would not suffice gratefully assisted me both professionally and privately. I would like to thank Prof. Dr. Andreas Merz and Priv. Doz. Dr. Richard Buchner for thier professional assistance at the initial stages of this work. I would like also to thank the head of the chair of Physical & Theoretical Chemistry Prof. Dr. Werner Kunz for his moral and logistical support throughout the duration of this work. I would like without reverence to thank the technical staff within and without of the faculty for any work rendered. I would like to thank in advance Prof. Malcolm D. Ingram for his willingness to come from Aberdeen Scotland to Regensburg twice in the capacitance as advisor and adjudicator respectively.

I would personally like to thank my research-group colleagues, starting with Dr. Michael Eberwein, Dr. Steffen Jordan, Hartmut Bruglachner Dipl. Chem., Hans-Georg Schweiger Dipl. Chem., and Michael Multerer Dipl. Chem. for their ever-ready moral and technical support down the years.

Finally, but not least, I would like to particularly offer my heartfelt thanks to my “Taoiseach” (supervisor) Priv. Doz. Heiner. J. Gores for his unstinting support in countless ways both privately and professionally from the inception of this work and in its conclusion. I will be to Priv. Doz. Dr. Heiner. J. Gores forever eternally grateful for this unique opportunity that was offered to me through the experience of living and learning in Regensburg and Germany as a whole.”

Go ráibh méile maith agam!

J.D.R.

Notation: main symbols – IUPAC†T

<i>Symbol</i>	<i>Name</i>	<i>Definition</i>	<i>SI-Unit</i>
x, y, z	cartesian space coordinates		m
r	[1] position vector [2] radius		m
h	height		m
m	mass		kg
A, A_s	area		m ²
l	length		m
A	area		m ²
V	volume		m ³
T	thermodynamic temperature - kelvin		K
θ	celsius temperature	$\Theta/^{\circ}\text{C} = T/\text{K} - 273.15$	$^{\circ}\text{C}$
ρ	density	$\rho = m/V$	kg m ⁻³
c	concentration		mol ⁻³
t	time		s
$\text{atm}, (\text{Torr})$	atmosphere	(760 torr)	N m ⁻² (Pa)
m, b	molality	$m_B = n_B/m_A$	mol kg ⁻¹
$\eta, (P)$	viscosity		Pa s (Ns m ⁻²)
n	chemical amount - mole		mol
M	molar mass		kg mol ⁻¹
M_r	molecular weight		-
pH	pH		-
U	internal energy	$\Delta U = q + w$	J
H	enthalpy	$H = U + pV$	J
G	Gibbs energy	$G = H - TS$	J
S	entropy	$dS = dq_{\text{rev}}/T$	J K ⁻¹
C_p	heat capacity		J K ⁻¹
μ	chemical potential		J mol ⁻¹
$u_{\rightarrow}, u_{\leftarrow}$	ion mobility		m ² s ⁻¹ V ⁻¹
ε	permittivity	$D = \varepsilon E$	F m ⁻¹
z	charge number of ions	$z_B = Q_B/e$	-
K	association constant		-
c^+	cationic salt concentration		mol m ⁻³
c^-	anionic salt concentration		mol m ⁻³
c^{+-}	ion pair concentration		mol m ⁻³
Q	electric charge		C
D	diffusion coefficient		m ² s ⁻¹
D_0	diffusion coefficient of ion-pair		m ² s ⁻¹
D_{\cdot}	diffusion coefficient of ions		m ² s ⁻¹
D_+^0	diffusion coefficient of ions in ideal electrolyte	$dN/dt = -DA(dn/dx)$	m ² s ⁻¹
ϕ	internal potential difference across the cell		V
ψ	external potential difference across the cell	$\psi = Q/4\pi\epsilon_0 r$	V
I_+	steady state current cation		A
I_0	initial current in cell		A
I_+^k	steady state cation diffusion current in cell with ideal electrolyte		A
$[c^+]_x$	steady state cation concentration at distance x from cathode		mol m ⁻³
$[c^+]_c$	steady state cation concentration		mol m ⁻³
$[c^+]_a$	steady state anion concentration		mol m ⁻³
$U, \Delta U$	electric potential difference voltage		V
E	Nernst potential		V

† As far as possible without straying too far from the common usage, the guidelines of IUPAC have been followed in quantities, unit and symbols of physical chemistry sourced from Hausmann, M. & Homann, K. H.;
 “IUPAC, Größen, Einheiten und Symbole in der Physikalischen Chemie, (1995). Publisher - VCH.”

<i>Symbol</i>	<i>Name</i>	<i>Definition</i>	<i>SI-Unit</i>
σ_{eff}	effective conductivity of cell in steady state		$S\ m^{-1}$
η_l	over potential	$\eta_a + \eta_c$	V
c_0	total salt concentration		$mol\ m^{-3}$
t_+	transport number		-
R_e	sum of electrode resistances		Ω
k_0	standard rate constant of electrical reaction		$(m^3\ mol^{-1})^{n-1}\ s^{-1}$
E_a	activation energy		J
σ_0	initial conductivity		$S\ m^{-1}$
I	current		A
U	potential	$kg\ m^2\ s^{-3}\ A^{-1} = J\ A^{-1}\ s^{-1}$	V
R	resistance	$kg\ m^2\ s^{-3}\ A^{-1} = V\ A^{-1}$	Ω
C	capacitance	$A^2\ s^4\ kg^{-1}\ m^{-2} = A\ s\ V^{-1}$	F, CV^{-1}
ν, f	frequency	$\nu = 1/t\ (s^{-1})$	Hz
ω	angular frequency	$\omega = 2\pi\nu$	$rad\ s^{-1},\ s^{-1}$
Φ	phase shift	$2\pi f$	$rad\ s^{-1},\ s^{-1}$
R^c	uncompensated resistance		Ω
$\kappa\ (\sigma)$	electrolytic conductivity		$S\ m^{-1}$
G	electrical conductance		S
K_{cell}	cell constant	$K_{cell} = \kappa.R$	m^{-1}
ρ	resistivity		$\Omega\ m$
Λ	molar conductivity (of an electrolyte)	$\Lambda = \kappa./c_B$	$S\ m^2\ mol^{-1}$
λ	molar conductivity (of an ion)		$S\ m^2\ mol^{-1}$
Z	impedance	$Z = R + iX$	Ω
Y	admittance	$Z = 1/Z$	S
τ	relaxation time		s
E_a	Arrhenius activation energy	$E_a = RT^2 d \ln k/dT$	$J\ mol^{-1}$

<i>Physical Constants</i>			<i>Mathematical Constants</i>	
<i>Symbol</i>	<i>Name</i>	<i>Value</i>	<i>Symbol</i>	<i>Name</i>
R	gas constant	$8.31451\ J\ K^{-1}\ mol^{-1}$	π	3.14159265
F	Faraday constant	$9.648\ 456 \times 10^4\ C\ mol^{-1}$	e	2.71828182
L	Avogadro constant	$6.022\ 045 \times 10^{23}\ mol^{-1}$	$\ln 10$	2.302585
e_0	unit of electron charge	$1.608 \times 10^{-19}\ A\ s$		
ϵ_0	charge of electron			
ϵ_0	permittivity of vacuum	$8.854\ 19 \times 10^{-12}\ F\ m^{-1}$		


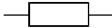
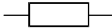
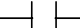


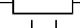
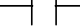


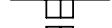
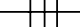
Subscripts

<i>Symbol</i>	<i>Name</i>
M	metal salt cation
X	negative salt anion
a	anode
c	cathode
∞	infinity
i	Initial state/form
n	number of entities

Acronyms & Abbreviations

<i>Abbreviation</i>	<i>Meaning</i>
PEO	Polyethylene Oxide
SPE	Solid Polymer Electrolytes
EO	Ethylene Oxide
PO	Propylene Oxide
VTF	Vogel-Tamman-Fulcher
EIS	Electrochemical Impedance Spectroscopy
AC	Alternating Current
DC	Direct Current
CPE	Constant Phase Element
CNLS	Complex Non-Least Squares
TA	Thermal Analysis
TG	Thermogravity
DTA	Differential Thermal Analysis
DSC	Differential Scanning Calorimetry
FRA	Frequency Response Analysis
FTT	Fast Fourier Transform
ADC	Analogue to Digital Converter
PID	Proportional Integral Differential- Thermal Regulator
NMR	Nuclear Magnetic Resonance
Li [F8]	lithium bis-[3,4,5,6-tetrafluoro-1,2-benzenediolato(2-)-O,O']borate
Li [H8]	lithium bis-[1,2-benzenediolato(2-)-O,O']-borate
Li [F2H6]	lithium bis-[3- fluoro-1,2-benzenediolato (2)-O,O']borate
[C ₁₆ -mim] ⁺	1-N-hexadecyl-3-methylimidazolium
DMSO	dimethylsulphur oxide
EGE-A	4,7-dioxa-1-octen (ethylenglycolallylmethylether)
DME	dimethoxy ethane
EGE-B	4,7,10-trioxa-1-undecan (di-ethylenglycolallylmethylether)
C _I /C _{II}	Crystal Phase
S _A	Smectic Phase
Iso	Isotropic Phase
POM	Polarised Optical Microscope
MS	Mass Spectroscopy
DMC	dimethylcarbonate
L	Ligand
R	Organic alkyl chain

Equivalent Circuit Symbols & Notation

<i>Element</i>	<i>Shorthand</i>	<i>Symbol</i>
Inductor	L	
Resistor No. x	R_x	
Charge Transfer Resistance	R_{CT}	
Capacitance double layer	C_{DL}	
Warburg element	Z_W	
Warburg resistive element	R_{WE}	
Warburg capacitance element	C_{WE}	
Constant Phase Element CPE	Z_{CPE}	
CPE - Bulk	$Z_{CPE-Bulk}$	
CPE - Electrode	Z_{CPE-E}	
CPE –Bulk resistance	$R_{CPE-Bulk}$	
CPE –electrode capacitance	C_{CPE-E}	

Contents

	Page
Chapter (1) <i>Literature Review</i>	
1.1. Abstract	1
1.2. Introduction	1
1.3. Aims & Objectives	10
Chapter (2) Theory	
2.1. Ion-Ion Interactions	13
2.1.1. Reasons for Understanding ion-ion Interactions	13
2.1.2. The Debye-Hückel Theory of Ion-Ion Interactions	14
2.1.3. Debye-Hückel Theory – Review and Limitations	17
2.1.4. The Conductivity Mechanism	19
2.2. Diffusion & Migration – Ionic Transport	21
2.2.1. Convection, Diffusion & Migration	21
2.2.2. DC Polarisation	24
2.2.3. Ideal & Non-Ideal Electrolytes	26
2.2.4. Transport & Transference Measurement Methods	31
2.2.4.1. Hittorf Cell Measurements	31
2.2.4.2. Radiotracer Measurements	32
2.2.4.3. The Current Fraction Method	32
2.2.5. Summation	33
2.3. The Temperature Dependence of Conductivity	34
2.3.1. Theoretical Foundation	34
2.3.2. T_g , Viscosity in Liquids & Polymers.....	36
2.3.2.1 T_g & Conductivity.....	36
2.3.2.2 Viscosity & Conductivity	37
2.3.3. Conductivity of Ionic Liquids	39

	Page
2.4. Electrochemical Impedance Spectroscopy (EIS)	40
2.4.1. AC Input Signal Response - Laplace Transform	40
2.4.2. Impedance Spectroscopy and it's Functions – Z , Y , M & ε	44
2.4.2.1. Impedance Response of Circuit Elements and their Combinations	46
2.4.3. EIS - Anomalies and Interfaces	52
2.4.3.1. Warburg Impedance	52
2.4.3.2. Concentration Polarisation	55
2.4.3.3. Bulk, Intergrain, Grain Boundary, & Constant Phase Element (CPE)	56
2.4.4. EIS - Physical Models for Equivalent Circuit Elements	61
2.4.4.1. Methodology of Equivalent Circuit Modelling	64
2.4.4.2. Practical Application of Equivalent Circuit Modelling in this Work	65
2.4.5. EIS - Advantage & Limitations	67
2.5. Thermal Analysis (TA)	69
2.5.1. Thermal Analysis - (DTA) & (DSC)	69
2.5.2. TA – Applications	72

Chapter (3) Experimental Procedure

3.1. Impedance Spectrometer & Software	75
3.1.1. Principles of Electrochemical Impedance Spectroscopy (EIS)	75
3.1.1.1. AC bridges	76
3.1.1.2. Frequency Response Analysis (FRA)	76
3.1.1.3. Fast Fourier Transform (FTT)	77
3.1.1.4. General Points of Note for Impedance Measurements	78
3.1.2. Gain-Phase Analyser 1260 & Software	79
3.1.2.1. “Parasitic” Influences	80
3.1.3. Zplot™ & Zview™ for Windows 2000	82
3.1.4. Test Module	83
3.1.5. Circuit Modelling	84
3.2. Thermostat Design & Calibration	87

	Page
3.3. Cell Design & Construction	92
3.3.1. Theoretical and Practical Considerations in Cell Design	92
3.3.2. Cell Size	97
3.3.3. Test Cell Design	98
3.3.4. Cell Testing & Calibration	98
3.3.4.1. Theoretical Background	101
3.3.5. Standard Preparation - Potassium Chloride (KCl)	103
3.3.6. Measuring Procedure	104
3.4. DSC – Differential Scanning Calorimetry	106
3.5. DTA – Differential Thermal Analysis	107
3.6. Infrared Spectroscopy – (IR)	107
3.7. Nuclear Magnetic Resonance – (NMR)	108
3.8. Mass Spectroscopy	108
3.9. Glove box Inert Gas System MB 150B-G-I	109
 Chapter (4) Synthesis	
4.1. Lithium salts with new (recently published) Anions	111
4.1.1. Synthesis of Lithium bis-[3,4,5,6-tetrafluoro-1,2- benzenediolato (2-)-O,O']borate – Li [F8] . .	113
4.1.2. Synthesis of Lithium bis-[1,2-benzenediolato(2-)-O,O']borate – Li [H8]	121
4.1.3. Synthesis of Lithium bis-[5- fluoro-2-ola benzenediolato (2-)-O,O']borate – Li [H2F6]	124
4.2. Synthesis of 1-<i>N</i>-hexadecyl-3-methylimidazolium Chloride Salt - [C₁₆-mim] [Cl]	126
4.3. General Procedure for the Substitution of Anions with Imidazolium Cations	132
4.3.1. Purification of Newly Synthesised Imidazolium Salts – Titration of LiCl	132
4.4. Procedure for the Synthesis (Oligo)ethylenglycolallylmethylethers (EGE)	138
4.4.1. Synthesis of (oligo)ethylenglycolmomoallyethers	138
4.4.2. Synthesis of (oligo)ethylenglycolallylmethylethers	140
4.4.3. Procedure for the Hydrosilylation of H-Silicone	142
4.4.4. Procedure for the Doping of Poly(siloxane) with Lithium Salts	144

	Page
4.5. Procedure for the Purification of Organic Solvents	145
4.5.1 Acetonitrile for Synthesis: CH_3CN	145
4.5.2 Acetone for Synthesis: $\text{C}_3\text{H}_6\text{O}$	146
4.5.3 Tetrahydrofuran (THF) for Synthesis: $\text{C}_4\text{H}_8\text{O}$	146
4.5.4 Ethyl Acetate for Synthesis: $\text{CH}_3\text{COOC}_2\text{H}_5$	147
4.5.5 1-ethyl-3-methylimidazol for Synthesis: $\text{CH}_3\text{C}_3\text{H}_3\text{N}_2\text{H}$	147

Chapter (5) Experimental Results

5.1. Poly(siloxane) Polymers	149
5.1.1. Preparative Work	149
5.1.1.1. Review & Strategy to Poly(siloxanes)	149
5.1.1.2. Hydrosilylation insertion of (oligo)ethylenglycolallylmethylethers side chains (EGE) & Selection	151
5.1.1.3. Solvation of the Polymer Matrix and Doping with Lithium Salts	154
5.1.1.4. (O:Li) ratio doping with lithium salts	155
5.1.2. Poly(siloxane) Polymers and Lithium Salt Mixtures at Ratios of (O:Li) – (32:1) & (24:1)	160
5.1.3. Final Commentary	168
5.2. Ionic Liquids – Imidazolium Salts	169
5.2.1. Preparative Work	169
5.2.1.1. Choice of Cation Salt	169
5.2.1.2. Choice of Anion Salt	172
5.2.2. Synthesis & Salt Substitution	174
5.2.3. Structural Analysis of $[\text{C}_{16}\text{-min}]$ in the Presence of Anion	176
5.2.4. DSC Analysis of $[\text{C}_{16}\text{-min}]$ in the presence of Different Anions	179
5.2.5. EIS investigations of $[\text{C}_{16}\text{-min}]$ in the Presence of Anion	184
5.2.5.1. Phase Transitions	184
5.2.5.2. Suspected Decomposition of $[\text{PF}_6]$ Anion due in the Presence of Unsolved LiPF_6	189
5.2.5.3. Undoped $[\text{C}_{16}\text{-mim}] [\text{X}^-]$	193
5.2.5.4. $[\text{C}_{16}\text{-mim}] [\text{X}^-]$ Doped with 0.1 – 0.5 MF Li $[\text{X}^-]$	196
5.1.6. Final Commentary	203

	Page
Chapter (6) Discussion	
6.1. Poly(siloxane) Polymers	206
6.1.1. Discussion of Structural & Conductive Behaviours of Doped Poly(siloxanes)	206
6.1.1.1. Polymer Gels	206
6.1.1.2. Effects of Lithium Salt Concentration	211
6.1.1.3. Effects of Lithium Salt Fluorination at the Anion	213
6.1.1.4. Effects of Side Chain Units	217
6.1.1.5. Arrhenius & VTF Approaches	220
6.1.2. Application of Equivalent Circuit Methodology	222
6.2. Ionic Liquid Electrolytes	223
6.2.1. Discussion of Structural & Conductive Behaviours of Ionic Liquids	233
6.2.1.1. A Multiphase System “lamellar bilayer” Systems	233
6.2.1.2. Pre-ordered Crystal Phase / [C _I] – [C ₁₆ -mim] [PF ₆]	236
6.2.1.3. Crystal Phase / [C _{II}] – [C ₁₆ -mim] [PF ₆]	238
6.2.1.4. Crystal to Liquid Crystal Phase transition / [C _{II}] – [S _A] – [C ₁₆ -mim] [PF ₆] ...	240
6.2.1.5. Liquid Crystal Phase / [S _A] – [C ₁₆ -mim] [PF ₆]	245
6.2.1.6. Isotropic Phase – [Iso] / [C ₁₆ -mim] [PF ₆]	246
6.2.1.7. Phase Transitions of [C ₁₆ -mim] [F8]	250
6.2.2. Influence of Anion Salt Size on the Structural & Conductive Behaviours of Ionic .	253
6.2.3. Influence of Doped Lithium Salt on the Structural & Conductive Behaviours of Ionic Liquids	256
6.3. Conclusion	262
Appendix	270

Chapter 1

Literature Review

1.1. Abstract:

In this work, two potential electrolyte systems were prepared, exhibiting thermally stable gel-like and “polymer-in-salt” behaviours respectively. Their ion-ion interactions were studied by means of impedance spectroscopy utilising modified Voigt equivalent circuits, which were fitted successfully to the measured data. A number of newly synthesised lithium salts {lithium bis-[3,4,5,6-tetrafluoro-1,2- benzenediolato (2-)-O,O']borate}, {lithium bis-[1,2-benzenediolato(2-)-O,O']borate}, and {lithium bis-[3- fluoro-1,2- benzenediolato (2)-O,O']borate} were mixed and doped with the presented systems. The conductive behaviours of the mixed salts exhibited original behaviours characteristic of the dissociative nature of the added lithium salts. The poly(siloxane) demonstrated comparable conductivities with those reported in the literature [$1.57 \times 10^{-5} \text{ S cm}^{-1}$ at 25 °C for (α)-poly(siloxane) lithium bis-[3,4,5,6-tetrafluoro-1,2-benzenediolato (2-)-O,O']borate (O:Li)-(32:1). The ionic liquid conductivities of the previously unreported presented lithium salts were highly temperature dependent lamella-like self-organising multiphase systems [$9.7 \times 10^{-7} \text{ S cm}^{-1}$ at 21°C & $1.02 \times 10^{-1} \text{ S cm}^{-1}$ at 111 °C for 1-*N*-hexadecyl-3-methylimidazolium lithium bis-[3,4,5,6-tetrafluoro-1,2-benzenediolato (2-)-O,O']borate.]

1.2. Introduction:

Power sources for electric vehicles and portable electronic equipment are contingent upon the discovery of electrochemical systems that store a large amount of energy, deliver high power output, utilise lightweight materials and depending on application ideally reversibly recharged. Most importantly, they should be mechanically and chemically stable in environments for realistic commercial application ^[1]. Most of the commercially known electrolytes contribute to one or two of the above-described attributes, but the ideal electrolyte that fulfils all the mentioned requirements needs has remained very elusive to those involved in electrochemistry research.

Since the mid-to late 60's and early 70's the NASA moon-landing programme had focused minds within and without the organisation in working on alternative ways of reducing the weight and optimising concept electrolytes by improving the compatibility of portable electrical energy sources ^[2]. In addition, researchers were looking for alternatives to the then ubiquitous liquid electrolyte in order to combat the problem of electrolyte leakage, and chemical degradation of the electrolyte cells. Therefore, a new direction was sought in electrolyte research ^[1]. In the mid-1970's the publication by Wright ^[3] in the *British Polymer Journal* of a new type of electrolyte medium concerning ionic conducting polyethylene oxide (PEO) Na⁺ complexes is seen by many as the product of this new focus. Wright's ^[3] solid polymer electrolyte (SPE) was one of the first documented deviations away from the classical liquid electrolyte power systems. Later a publication by Armand and co-workers ^[4] concerning a review of the status of electrolyte systems and the elucidation of the virtues of solid polymer electrolytes started a rush of research in this field. The contributions of both Wright ^[3] and Armand ^[4] were to revolutionise the whole concept of electrolyte research. In recent years, an ever-growing variety of power hungry portable electric devices has led to the development of a large number of sub-families of solid polymer electrolytes. Background concerning these systems is available in more detail elsewhere in a number of sources ^{[2] [5 - 7]}.

Within these sub-families over the last 15 to 20 years the lithium solid polymer electrolyte has come to dominate the electrolyte landscape, initially they were manufactured for military use, but gradually have over the last ten years lithium solid polymer electrolytes have become commonly available to the consumer market. In recent years, batteries have been especially required for superior electrochemical performance in response to the need for miniature power supplies most notably for consumer applications ^[8 - 13]. In a recent review of assorted electrolytes by Muranta ^[14], the author pointed out that current trends in electrolyte development are moving towards gel-like systems, which are expected to play a growing role in the future of consumer electronics. The diagram in figure (1.2.1) shows the current trend towards ever more sophisticated amorphous gel-like polymeric electrolyte systems. Gel electrolytes should preferably have a homogenous macrostructure, which physically prevents separation of the matrix and the polymer electrolyte ^[14]. One of the desired attributes of any new electrolyte, gel or otherwise, is a structure with a large matrix domain with in particular a long molecular chain length and coarse cross-linking. Therefore, it is important specifically to design an electrolyte composed of polymers, which have little affinity towards interaction with the lithium ion. Hence, the matrix should have a strong attraction towards the anions and

at the same time repels the cations. The material should have a high packing density for miniaturisation applications taking advantage of inherent safety and leak-proof battery designs. In addition to the above-mentioned factors in gel design, the direct reduction of the interfacial impedances between the active materials and the electrolyte is paramount. Most importantly, the gel-like material should be responsive to cope with thermal expansion and contraction of the active materials. Thereby a good electrical contact between active material particles plus between the active material current collectors is important for good battery performance.

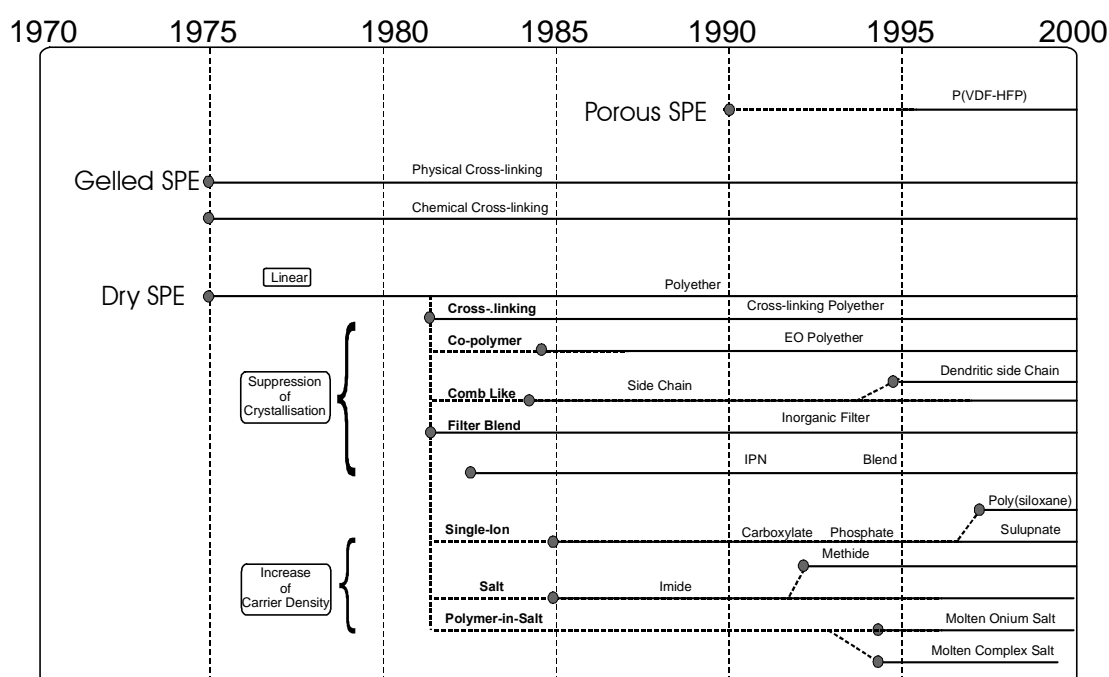


Fig. (1.2.1) History of solid polymer electrolyte development ^[14]

But before we consider the presented systems in detail a number of aspects should be considered in the design of a modern polymer based electrolyte ^[14 - 20]:

- Suppression of the crystallinity of the polymer chains to improve the polymer chain mobility.
- Increase the charge carrier concentration through discouraging the formation of large ionic aggregates that reduce the number of charge carriers. The matrix should have good solvating properties.
- Utilisation of comb-like structures by polymerisation of flexible highly solvating backbones.

- Selective design of charge carrier salts. Salts where anions readily dissociate from the alkali cations, especially Li^+ . The anionic part of the salt should be large enough to be immobilised by the side chains. The cation should be the main charge carrier.

Poly(siloxane) systems – Gel-like Systems:

Andreev and Bruce ^[16] elegantly commented on gel electrolytes as being “liquid electrolytes entrapped in a polymer matrix”. This statement is not far from the truth, since many of the problems associated with liquid electrolytes are retained in gels. However in recent years, despite innovative designs of flexible polymers and the synthesis of salts containing asymmetric anions capable of suppressing crystallinity the level of ionic conductivity cited from Andreev ^[16] is presently “stuck at a ceiling of around $1 \times 10^{-4} \text{ S cm}^{-1}$ at ambient temperatures”. Over the years, a number of routes and angles to electrolyte design have been pursued in an attempt to overcome this conductive barrier.

Killis ^[22] proved that the ionic conductivity could be improved in solid polymer systems by cross-linking block polymers of ethylene oxide (EO) and propylene oxide (PO) in conformation obtaining a conductivity of $1 \times 10^{-5} \text{ S cm}^{-1}$ at 25 °C. By the early 1990’s most possibilities had been exploited in attempts to improve conductivity of dry electrolytes in relation to the ability of the amorphous state and lowest possible glass-transition temperature T_g controlling the ion mobility. A remaining option was to use additives known in polymers as plasticisers to act as chain lubricants. This lead to the work of Hall ^[23] who produced evidence of enhanced conductivity capabilities of poly(siloxane) systems by adding polyethylene oxide (PEO) side chains. Watanabe ^[24 - 25] extended the use of poly(siloxane) back-bone polymers by synthesising dendrite polymers through attaching (PEO) chains and glycidyl ether side chains. The bedevilling issue of increasing the carrier concentration without reducing conductivity can be affected through the application of highly dissociative salts similar to that report by Barthel et al. ^[26 - 30]. Their larger radii greatly assist in the charge delocalisation effects and if fluorinated the salts produce strong dissociation effects and increased numbers of charge carriers. A recent publication by Yoshio ^[71] indicated that ionic conductivities of polymer electrolytes are far lower for liquid electrolytes. Yoshio ^[71] goes on to say, “gelled polymer electrolytes which are composed of polymer matrices and solvents or plasticisers, have been developed in place of genuine polymer electrolytes to improve ionic

lithium polymer batteries”. A recent example is the lithium ion secondary batteries developed by the Sony Corporation in (1991) based on PEO. This battery system consists of a positive electrode coated with LiCoO_2 , a negative electrode coated with graphite and polyethylene micro-porous separator. This design has proved to be indispensable for mobile phone and other hand-held consumer goods that have spurred their growth ever since ^[71].

Gel electrolytes and in particular poly(siloxanes) systems were investigated in this work with the intention of designing an amorphous polymer electrolyte with low a T_g . Polymeric systems have considerable structure and similar structural order can be suspected for gel electrolytes according to Bruce ^[18] and other authors ^{[31 - 32] [69] [70]}. It is vital to understand the structure in particular the relative conductive relationships of mobile ions in order to understand the mechanisms of ion transport leading to ionic conductivity above the current maximums in polymer gel electrolytes.

Ionic Liquids/Room Temperature Molten Salts:

The second system known as ionic liquids or “room temperature molten salts” have only recently received attention as potential electrolytes ^{[25] [33 - 38]} see Fig. (1.2.2). The figure (1.2.2) shows the results of a literature search conducted by the author using the keywords “ionic liquids” as one can observe there has been an explosion of interest in the area of ionic liquids over the last two decades and in particular for their potential electrolyte applications in the last ten years. According to some authors, room temperature molten salts or ionic liquids are acknowledged as the next generation of electrolytes and are becoming increasingly applied in “green” technologies for organic synthesis. ^{[17] [39 - 44] [70]}. Unlike electrolytes that are often based on (PEO) systems, discussed earlier, these materials equally offer mechanical benefits for potential applications as electrolytes and/or capacitors composed of non-aqueous organic liquids ^[45]. Webber and Blomberg ^[72] recently listed the advantages of such systems as over hitherto systems, such as their non-flammability, low vapour pressures, high thermal stabilities, good electrochemical stabilities, low toxicities, good morphologies, high melting points, high ion, and potential rechargeability. The author Bruce ^[46] recently proposed a structural view of electrolytes, and expressed that currently “there is need for focus on aligning or self-organising the polymer chains in order to enhance the levels of ionic conductivity”.

The definition of ionic liquids has changed considerably over the years. Until the 1960's low temperature molten salts were usually highly conductive inorganic salts that melted at rather "low" temperatures e.g. $\text{LiCl/KCl} - 355\text{ }^{\circ}\text{C}$ ^[47]. Our current understanding of such systems is that they are mainly molten room temperature organic systems. Most room temperature molten salts have an organic cation and an inorganic polyatomic anion. The first reported and considered modern molten salt was the preparation of ethyl-ammonium nitrate in 1914 by Walden ^[48 - 50]. This species was synthesised by the addition of concentrated nitric acid to ethylamine, after water was removed by means of distillation to give pure salts, which was liquid at room temperature. The protonation of suitable starting materials such as amines and phosphines still represents the simplest method in the formation of such materials.

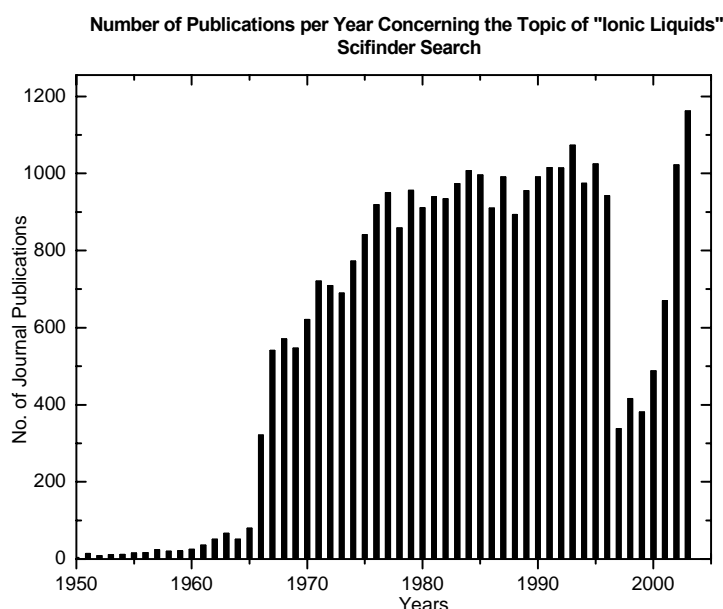


Fig. (1.2.2) Graph of the number of publications per year on entering the subject "ionic liquids" in Scifinder.

The possibility of decomposition through deprotonation has severely limited the use of such salts according to Gordon ^[17] ^[51]. Later the solvent free liquid composed of *N*-ethylpyridinium bromide-aluminium chloride was reported in 1951 ^[52]. According to the author Gordon ^[17] "the most widely used salt of this type is pyridinium hydrochloride", applications and properties of such systems may be found in a review by Pagni ^[53]. Thus, the most common liquids are formed from cations that do not contain acidic protons. A summary of the applications and properties of ionic liquids may be found in a number of review articles ^[39] ^[44] ^[53 - 54]. The most common classes of cations are those illustrated in Fig. (1.2.3).

The properties of ionic liquids can be controlled to a large degree by a variation in the nature of both the cation and the anion that will be shown later in this work. It outwardly demonstrates a polymeric gel-like membrane, which provides a relatively large transport flux in the mesogenic phase^[55]. Early work by Shinkai^[55] had demonstrated the potential of liquid crystal polymers. Shinkai and co-workers^[55] synthesised crown-mediated ion transport mediums, utilising polymer liquid crystalline composite membranes. These new materials demonstrated remarkable transport properties from fluorocarbon containing crown ethers. The work conducted by Chia^[56] on PEO's focused on different alkyl chain length of C_nH_{2n+1} ; $n = 14, 16, 18$. Chia^[56] like other authors^{[39] [57]} observed that on increasing n , many authors expect to observe an alternation in the melting point, and increase in the viscosity and hydrophobisity of the ligands.

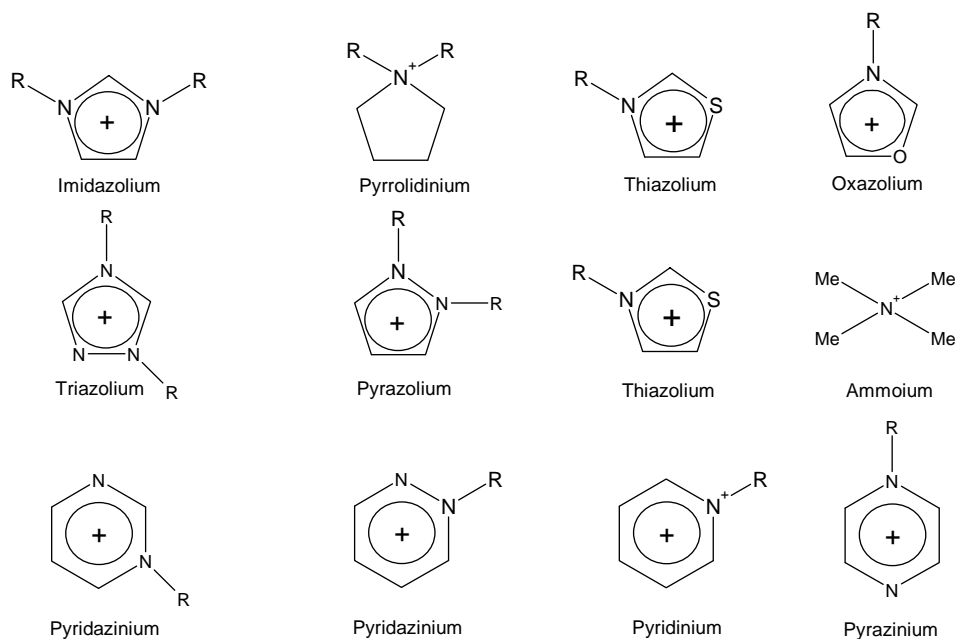


Fig. (1.2.3) Examples of cations commonly encountered as ionic liquids $R = (CH_2)_nCH_3$ ^{[47] [71]}

In recent years authors such Wright^[56] and Imrie^[58] have concentrated on the liquid crystalline state to force the solvating polymer into conformation that was dictated by the liquid crystal part. The result according to Tarascon^[59] is partial decoupling of the conductivity from the glass transition temperature, but reaches liquid-like values at elevated temperature or when kept under polarisation, and remains so upon cooling to room temperature without an appreciable activation energy. Therefore an ionic low molecular weight liquid crystal polymer membrane in which the character of a liquid crystalline material

is embedded by chemical and structural design in polymeric matrix is seen by this author to satisfy the desired requirements of a -“polymer-in-salt” electrolyte described by Angell^[60].

In working with similar systems a number of authors^{[56] [61 - 65]} have described the potential of electrolyte pathways to take form propagated by the long chained systems encompassing structures similar to those seen in bimolecular extend molecules. Such structures usually form in the presence of a strong cationic header species. These systems have exhibited the properties of bilayers correspondingly leading to lamella phases in certain incidences. The presented systems can be attributed to a steady-state approach due the investigation of the dynamic lateral charge transport in organised electrochemically active bilayer self-assemblies. The author proposes that the interactive forces between opposing supported bilayers in which two types of forces between are in operation medium range Van der Waals forces and short-range repulsive steric forces. The highly structured nature of these presented systems makes an increase in the energy density possible due to their high packing density. Therefore these systems should have more efficient conductive pathways due to their large internal volume as opposed to amorphous polymeric systems. The size and the charge number of the metal salts affect the mesogenic behaviour and ion conduction properties for the self-organising structure.

The improvement of the performance of both presented systems has a common strategy that can be summed up in two approaches:

- (i) enhancement of the mobility of the polymer chains
- (ii) increase of the charge carrier density

Currently with the combination of (i) and (ii) the ionic conductivity at room temperature is now $1 \times 10^{-4} \text{ S cm}^{-1}$ (i.e.) poly(siloxane systems) while with the polymer-in-salt system (ionic liquid) (ii) stands currently now at $1 \times 10^{-4} \text{ S cm}^{-1}$, and with single ion conductor approach, it is about $1 \times 10^{-6} \text{ S cm}^{-1}$ ^[66 - 67]. Although the polymer-in-salt systems operate at $1 \times 10^{-4} \text{ S cm}^{-1}$ at room temperature, such samples tend to crystallise at lower temperatures, which hinders their practical application. The diagram in figure (1.2.4) summarises the development of electrolytes and their conductivities to emphasise the considerable improvements of conductivities for a variety of systems over the past two decades. In the diagram Fig. (1.2.4) the so-called “polymer-in-salt” system described by Angell^[60] and the

poly(siloxane) systems have demonstrated the greatest potential for conductivity expansion. The region $10^{-2} \text{ S cm}^{-1}$ and above is the area currently being highly sought after in earnest for the appropriate electrolyte system. It can be described as the “undiscovered country” [68] in electrochemistry. Slowly researches are moving in the direction of utilising soft-polymer and gel-like materials with considerable success. The presented systems of this work such as the poly(siloxane) gel and the imidazolium ionic liquids have the potential to belong to this region.

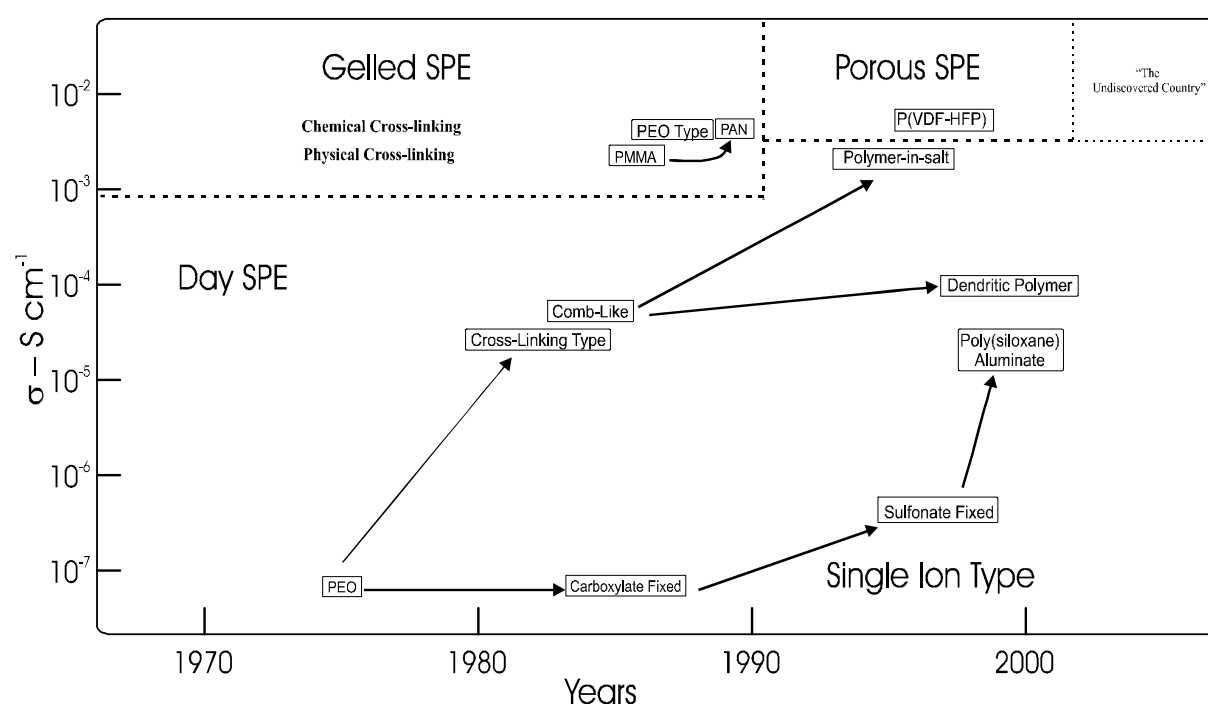


Fig (1.2.4) History of ionic conductivity improvement [14]

1.3. Aims & Objectives:

This work had two requirements; firstly the synthesis of novel electrolytes that exhibit gel-like behaviours and secondly to investigate the synthesised materials with electrochemical impedance spectroscopy (EIS) in order to understand the ion-ion interactions. The presented work is divided into two parts. The first part of the investigations concerns the polymerisation of H-siloxane⁶⁰ with different pre-synthesised (oligo)ethylenglycol side chain units to form gel-like materials. These gels are mixed with different newly synthesised lithium salts that have a minimum radii of 4.2 Å and who have large charge delocalisation and dissociation influences. In parallel to the synthesis, the investigations are intended to increase the mobility of the side chain units and to reduce the glass transition (T_g). By means of EIS, the author intends to develop the most appropriate circuit model to explain their ionic transport properties.

The second part of the investigation concerns the combination of the best aspects of the imidazolium cation header group with the newly synthesised lithium salts to form ionic liquid polymer or polymer-in-salt systems. Such salts are potentially of great interest. It appears that the geometric packing constraints of the planar imidazolium ring, plus its dangling alkyl side groups coupled with the delocalisation of the charge over the N-C-N moiety in the ring all serve to decrease ion-ion interactions and lower melting points. The aforementioned lithium salts with large anions should give an insight into the structure and some of the fundamental features of the imidazolium cation header groups. The author hopes to reduce the crystallisation point below ambient temperatures and to identify molten salts with a wide window of stability. Therefore, similar to the above a greater understanding is required concerning the nature of the ions, which promote high conductivity within most molten salts. EIS studies were performed with the intention of developing the most appropriate circuit model to explain their ionic transport properties.

References:

1. O. Dag, A. Verma, G. A. Ozin and C. T. Kresge, *J. Mater. Chem.*, **9**, 2715 (1999).
2. R. M. Dell and D. A. J. Rand, *Understanding Batteries*, No. p. 223, Springer, (2001).
3. P. V. Wright, *British Polymer Journal*, **7**, 319 (1975).
4. M. B. Armand, J. M. Chabagno and M. Duclot, *Solid Electrolytes Meeting - Extended Abstracts*, (1978).
5. G. Pristola, *Lithium Batteries - New Materials, Developments and Perspective*, **5**, No. p. 482, Elsevier, London, (1994).
6. J. P. Gabano, *Lithium Batteries*, No. p. 455, Academic Press, London, (1983).
7. P. G. Bruce, Section: Polymer Electrolytes II, *Chemistry of Solid State Materials - Solid State Electrochemistry*, **5**, 141-163, Ed. Bruce, P.G., Cambridge University Press, (1997).
8. C. Svanberg, R. Bergman, L. Borjesson and P. Jacobsson, *Electrochim. Acta*, **46**, 1447 (2001).
9. Y. Saito, H. Kataoka, T. Sakai and S. Deki, *Electrochim. Acta*, **46**, 1747 (2001).
10. H. Dai and T. A. Zawodzinski, Jr., *J. Electrochem. Soc.*, **143**, L107 (1996).
11. S. S. Zhang and C. A. Angell, *J. Electrochem. Soc.*, **143**, 4047 (1996).
12. J. B. Kerr, G. Liu, L. A. Curtiss and P. C. Redfern, *Electrochimica Acta*, **48**, 2305 (2003).
13. H. Nakagawa, S. Izuchi, K. Kuwana, T. Nukuda and Y. Aihara, *Journal of the Electrochemical Society*, **150**, A695 (2003).
14. K. Murata, S. Izuchi and Y. Yoshihisa, *Electrochim. Acta*, **45**, 1501 (2000).
15. H. R. Allcock, M. E. Napierala, D. L. Olmeyer, C. G. Cameron, S. E. Kuharcik, C. S. Reed and S. J. M. O'Connor, *Electrochim. Acta*, **43**, 1145 (1998).
16. Y. G. Andreev and P. G. Bruce, *Electrochim. Acta*, **45**, 1417 (2000).
17. C. M. Gordon, *Applied Catalysis, A: General*, **222**, 101 (2001).
18. P. G. Bruce and C. A. Vincent, *J. Chem. Soc., Faraday Trans.*, **89**, 3187 (1993).
19. C. A. Angell, *Molten Salt Forum*, **5-6**, 39 (1998).
20. J. Barthel, H. J. Gores, R. Neueder and A. Schmid, *Pure and Applied Chemistry*, **71**, 1705 (1999).
21. Y. G. Andreev and P. G. Bruce, *Electrochim. Acta*, **45**, 1417 (2000).
22. A. Killis, J. F. Le Nest, H. Cheradame and A. Gandini, *Macromolecules*, **183**, 2835 (1982).
23. P. G. Hall, J. E. Davies, J. M. McIntyre, I. M. Wards, D. J. Bannister and K. M. F. Le Brocqu, *Polymer Communications*, **27**, 98 (1986).
24. T. Michot, A. Nishimoto and M. Watanabe, *Electrochim. Acta*, **45**, 1347 (2000).
25. M. Watanabe and T. Mizumura, *Solid State Ionics*, **86-88**, 353 (1996).
26. J. Barthel, R. Buestrich, H. J. Gores, M. Schmidt and M. Wuhr, *J. Electrochem. Soc.*, **144**, 3866 (1997).
27. J. Barthel, R. Buestrich, E. Carl and H. J. Gores, *J. Electrochem. Soc.*, **143**, 3572 (1996).
28. J. Barthel, H. J. Gores, K. Gross and M. Utz, *J. Solution Chem.*, **25**, 515 (1996).
29. J. Barthel, H. J. Gores and L. Kraml, *J. Phys. Chem.*, **100**, 1283 (1996).
30. J. Barthel, M. Wuhr, R. Buestrich and H. J. Gores, *J. Electrochem. Soc.*, **142**, 2527 (1995).
31. R. A. M. Hikmet and M. P. J. Peeters, *Solid State Ionics*, **126**, 25 (1999).
32. M. Forsyth, J. Sun, F. Zhou and D. R. MacFarlane, *Electrochimica Acta*, **48**, 2129 (2003).
33. M. Morita, F. Araki, N. Yoshimoto, M. Ishikawa and H. Tsutsumi, *Solid State Ionics*, **136-137**, 1167 (2000).
34. C. T. Imrie, M. D. Ingram and G. S. McHattie, *J. Phys. Chem. B*, **103**, 4132 (1999).
35. G. S. McHattie, C. T. Imrie and M. D. Ingram, *Electrochim. Acta*, **43**, 1151 (1998).
36. N. A. Hamill, K. R. Seddon, A. Stark and M. J. Torres, *Abstr. Pap. - Am. Chem. Soc.*, **221st**, IEC (2001).
37. H. Every, A. G. Bishop, M. Forsyth and D. R. MacFarlane, *Electrochim. Acta.*, **45**, 1279 (2000).
38. K. Ito, N. Nishina and H. Ohno, *Electrochim. Acta*, **45**, 1295 (2000).
39. H. Ohno, *Electrochim. Acta*, **46**, 1407 (2001).
40. D. R. MacFarlane, J. Sun, J. Golding, P. Meakin and M. Forsyth, *Electrochim. Acta.*, **45**, 1271 (2000).
41. Y. S. Fung and R. Q. Zhou, *J. Power Sources*, **81-82**, 891 (1999).
42. M. J. Earle and K. R. Seddon, *Pure Appl. Chem.*, **72**, 1391 (2000).
43. M. J. Earle, K. R. Seddon, C. J. Adams and G. Roberts, *Chem. Commun. (Cambridge)*, 2097 (1998).

44. K. R. Seddon, *Molten Salt Forum*, **5-6**, 53 (1998).
45. M. Hirao, H. Sugimoto and H. Ohno, *J. Electrochem. Soc.*, **147**, 4168 (2000).
46. G. S. MacGlashan, Y. G. Andreev and P. Bruce, *Nature*, **398**, 792 (1999).
47. P. Wasserscheid and T. Welton, *Ionic Liquids*, Wiley-VCH, (2003)..
48. P. Walden, *Bulletins of the Academic Imperial Science*, 1800 (1914).
49. T. Welton, *Chemical Reviews*, **99**, 2071 (1999).
50. C. J. Bowlas, D. W. Bruce and K. R. Seddon, *Liquid-crystalline ionic liquids*, No. p. 6 (1996).
51. C. M. Gordon and A. McCluskey, *Chem. Commun. (Cambridge)*, 1431 (1999).
52. F. H. Hurley and J. Wier, *Journal of the Electrochemical Society*, **98**, 203 (1951).
53. R. M. Pagni, Section: Advances in Molten Salts Chemistry, **6**, 211-346 (1987).
54. J. S. Wilkes, *Abstr. Pap. - Am. Chem. Soc.*, **221st**, IEC (2001).
55. S. Shinkai and T. Kajiyama, *Pure Appl. Chem.*, **60**, 575 (1988).
56. F. Chia, Y. Zheng, J. Liu, N. Reeves, G. Ungar and P. V. Wright, *Electrochimica Acta*, **48**, 1939 (2003).
57. C. M. Gordon, J. D. Holbrey, A. R. Kennedy and K. R. Seddon, *J. Mater. Chem.*, **8**, 2627 (1998).
58. C. T. Imrie, M. D. Ingram and G. S. McHattie, *J. Phys. Chem. B*, **103**, 4132 (1999).
59. J. M. Tarascon and M. Armand, *Nature (London, United Kingdom)*, 414, 359 (2001).
60. C. A. Angell, C. Liu and E. Sanchez, *Nature (London)*, **362**, 137 (1993).
61. T. Hashimoto, K. Yamasaki, S. Koizumi and H. Hasegawa, *Macromolecules*, **26**, 2895 (1993).
62. S. Koizumi, H. Hasegawa and T. Hashimoto, *Macromolecules*, **27**, 4371 (1994).
63. T. Hashimoto, S. Koizumi and H. Hasegawa, *Macromolecules*, **27**, 1562 (1994).
64. K. M. Lee, C. K. Lee and I. J. B. Lin, *Chem. Commun.*, **9**, 899 (1997).
65. L. Soubiran, E. Staples, I. Tucker, J. Penfold and A. Creeth, *Langmuir*, **17**, 7988 (2001).
66. M. Watanabe, H. Tokuda and S. Muto, *Electrochim. Acta*, **46**, 1487 (2001).
67. S. Kohjiya, Y. Ikeda, K. Miura, S. Shoji, Y. Matoba, M. Watanabe and T. Sakashita, Polymer solid electrolyte, *Eur. Pat. Appl.*, 96-107272, 7(1996).
68. W. Shakespeare, Play - *Richard III*, (1593).
69. C. Svanberg, R. Bergman, L. Borjesson and P. Jacobsson, *Electrochim. Acta*, **46**, 1447 (2001).
70. H. Nakagawa, S. Izuchi, K. Kuwana, T. Nukuda and Y. Aihara, *Journal of the Electrochemical Society*, **150**, A695 (2003).
71. N. Yoshio, Section: Lithium-Ion Secondary Batteries with Gelled Polymer Electrolytes, Advances in Lithium-Ion Batteries, 233-249, Ed. Van Schalkwijk, W.A. & Scrosati, B., Kluwer Academic / Plenum Publishers, (2002).
72. A. Webber and G. E. Blomberg, Section: Ionic Liquids for Lithium Ion Electrolytes and Related Batteries, *Advances in Lithium-Ion Batteries*, 185-231, Ed. Van Schalkwijk, W.A. & Scrosati, B., Kluwer Academic Plenum Publishers, (2002).

Chapter 2

Theory

2.1. Ion-Ion Interactions

Foreword:

The connection between chemistry and electricity is a very old one, going back to Allesandro Volta's discovery in 1793 ^[1] ^[2], that electricity could be produced by placing two dissimilar metals on opposite sides of moistened paper. In 1800 Nicholson and Carlisle using Volta's primitive battery as a source, demonstrated that electric current could decompose water into oxygen and hydrogen ^[3]. These are still considered one of the most significant experiments in the history of chemistry [and for the future of transport], because it implied that atoms of hydrogen and oxygen were associated with positive and negative electric charges, which must be the source of the bonding forces between them. By 1812 the Swedish chemist Berzelius ^[1] who was experimenting with electrolysis speculated that when an voltage was applied across defined electrodes; this applied voltage overpowered the attraction between opposite charges, pulling the electrified atoms apart in the form of ions (named by Berzelius from the Greek for "travellers"). It would take almost a hundred years to the turn of the 20th century before the behaviours of ions in solution and in electrolytes could be with relative confidence explained. Such advances of understanding were a achieved with theories in the form of the shared electron pair theory of G. N. Lewis ^[2], Maxwell's theory of "molecular electricity" ^[1], and Debye & Hückel's theory ^[4] describing the distribution of charges around an ion in solution; and the distribution of charges about the ion.

2.1.1.

Reasons for understanding ion-ion interactions:

Why are ion-ion interactions important? The answer to this question is quite simple as will be shortly later demonstrated in this section; they affect the equilibrium properties of ionic solutions when exposed to external applied electric fields. According to Bockris ^[5] the degree to which these interactions affect the properties of solutions will depend on the mean distance apart of the ions, i.e. on how densely a solution is populated with ions because the

inter-ionic fields are distance dependent. The ionic population density will in turn depend on the nature of the electrolyte itself, i.e. on the extent to which the electrolyte gives rise to ions in solutions. The Debye-Hückel theory^[4] recognises solvents by their bulk properties, namely relative permittivity ϵ , viscosity η , and density ρ of the pure solvent. In addition, the range of validity of this theory is restricted to very low concentrations only, and is experimentally unattainable in many organic solvent systems^[6]. The importance of the bulk properties decreases as the electrolyte concentration increases. At the molecular scale, solvents may be classified according to soft/hard donor and acceptor properties of both solvent and the solute. Although Debye and Hückel^[4] is a classical image of ion-ion interactions as compared to the more modern, theoretical approaches of the Born-Oppenheimer internal charge distributions of solvent molecules. As every good historian knows in order to understand the future, one must first understand the past. The Debye-Hückel is still a valuable and viable platform for the explanation of the current view of ion-ion interaction behaviours ionic liquids and polymer-gels that are of great interest, which was alluded to in section {1}.

2.1.2.

The Debye-Hückel Theory of Ion-Ion Interactions:

In order to understand the ion-ion interactions one must develop a quantitative measure of the interactions of ions^[5]. The starting point for this discussion should of course be a short examination of the liquidus state itself. Intermolecular forces hold the particles of a liquid together, but their kinetic energies are comparable to their potential energies^[1]. As a



Fig. (2.1.1)

result, the molecules are free to escape completely from the bulk; hence, the overall structure is very mobile. The best description of the average locations of particles in a liquid

is in terms of the pair distribution function - g . In a crystal, g is a periodic array of sharp spikes, representing the certainty that defined particles lie at definite locations. This regularity continues out to large distances and therefore a material is defined as having *long-range order*. When the crystal melts to a liquid state, the long-range order is lost and is replaced by

short-range order. This means that for any reference ion within the liquid state; its nearest neighbours might still adopt approximately their original positions, even if new comers displace them and these newcomers might adopt their vacated positions.

Therefore, the basic postulates of the Debye-Hückel theory elude:

- The central ion relates to the surrounding ions in the form of a smoothed-out charge density and not as discrete charges.
- All the ions in the electrolytic solution are free to contribute to the charge density and there is, for instance, no pairing up of positive and negative ions to form any electrically neutral couple.
- Only short-range Coulombic forces such as dispersion forces play a negligible role.
- The solution is sufficiently dilute to warrant the linearisation of the *Boltzmann equation*.
- The only role of the solvent is to provide a dielectric medium for the operation of inter-ionic forces; i.e. the removal of a number of ions from the solvent that cling more or less permanently to ions other than the central ion is neglected.

Debye and Hückel proposed in their formulation a very simple but powerful model for the time-averaged distribution of ions in very dilute solutions of electrolytes. From this modelled distribution, they were able to obtain the electrostatic potential contribution from the surrounding ions as depicted schematically in Fig. (2.1.2) and hence the chemical potential change arising from the ion-ion interactions. The electrolyte solution consists of solvated ions and water molecules. The first step in the Debye-Hückel approach is to select arbitrarily any one ion out of the assembly and call it a reference ion or central ion. The water molecules are looked upon as a continuous dielectric medium. The remaining ions of the solution fall back into anonymity, their charges being under-footed into a continuous spatial distribution of the opposite sign. It is recognised that there will be a rise a net or excess charge in the particular region under consideration. The charges of the discrete ions that populate the surroundings of the central ion; are thought of as smoothed out and contribute to the continuum dielectric a net charge density. In this way, water enters the analysis in the guise of a dielectric constant ϵ and the ions except the specific one chosen as the central ion, in the form of an excess charge density ρ Fig. (2.1.3).

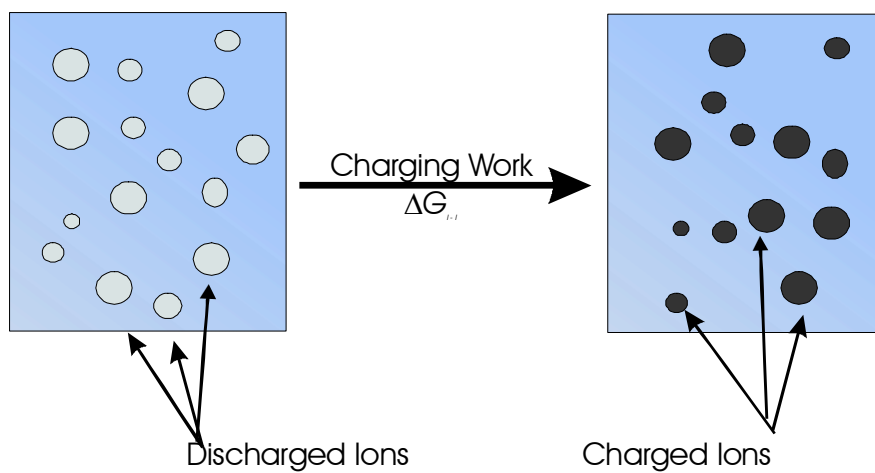


Fig. (2.1.2)

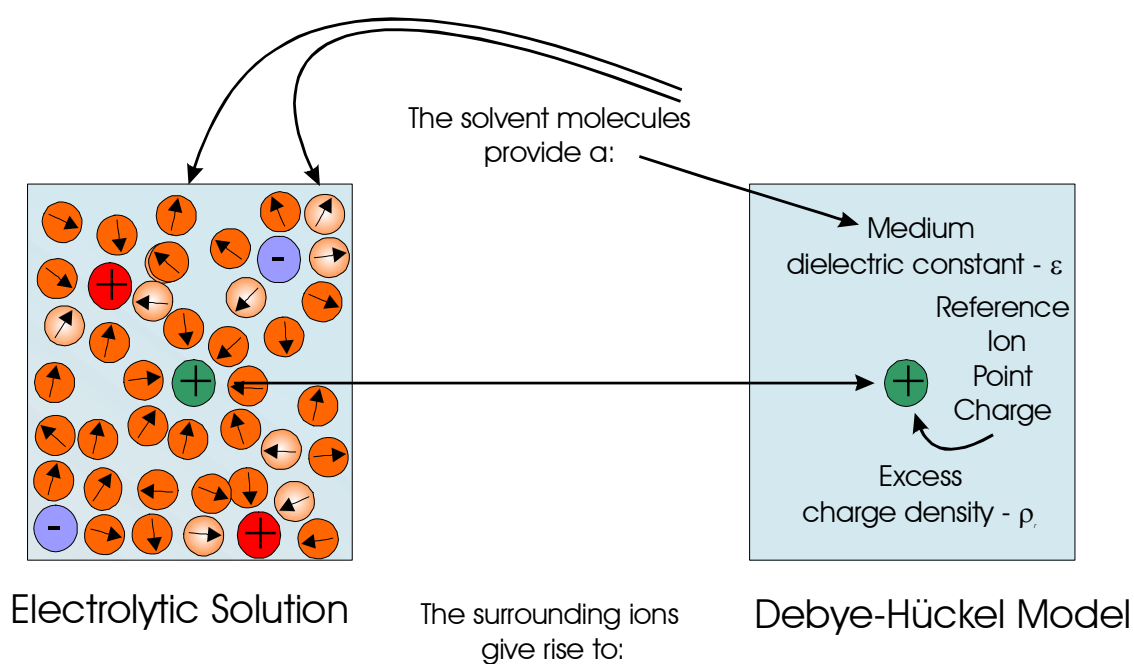


Fig. (2.1.3) The Debye-Hückel model upon selecting one ion as a point charge reference ion, replacing the solvent molecules the solvent molecules by a continuous medium of dielectric constant ϵ and the remaining ions by an excess charge density ^[5]

2.1.3.

Debye-Hückel Theory – Review and Limitations

The success of the Debye-Hückel model for ion-ion interaction of solute in solvents is so remarkable and the implications so wide that Debye-Hückel approach is regarded as one of the most significant pieces of theory in the ionics part of electrochemistry. It even rates among the leading pieces of physical chemistry of the first half of the 20th century. However one must not overstress the achievement of the Debye-Hückel limiting law as seen in Equ. [2.1.1]:

$$\log f_{\pm} = -A(z_+ z_-)I^{1/2} \quad \text{Equ. [2.1.1]}$$

This expression indicates that the activity coefficient f_{\pm} must decrease linearly with the square root of the ionic strength or, in the case of 1:1 valent electrolytes with $c^{1/2}$. Models are always simplifications of reality. They never treat all its complexities and thus can never be a perfect fit between experiments and prediction based on a model. The inadequacies of the Debye-Hückel limiting law are exposed. If one examines the experimental $\log f_{\pm}$ versus \sqrt{I} this is a curve Fig. (2.1.4) ^[5] not just in extreme regions, but also at higher concentrations, it turns out that the simple Debye-Hückel limiting law fails. The plot $\log f_{\pm}$ versus \sqrt{I} is not a straight line as promised by Equ. [2.1.1]. Furthermore, the curves depend not only on valence type (1:1 or 2:2) but also on the particular electrolyte (NaCl or KCl). The agreement of the Debye-Hückel limiting law with experiment improved with decreasing concentration and became excellent for the limiting tangent to the $\log f_{\pm}$ versus \sqrt{I} as seen in Fig. (2.1.4). With increasing concentration, however the experimental data deviated more and more from theoretical values as the concentrations continued to proceed above 1 N, there was an increase in f_{\pm} with an increase in concentration, whereas theory indicated a continued decrease.

Because the Debye-Hückel theory attempts to represent all these various aspects of real situations within solutions, the experimentally calibrated ion size parameter varies with concentration. The Debye-Hückel theory is an outstanding piece of work in itself; but at the same time, it is unfortunately inadequate in explaining and modelling some aspects of the behaviours of *ion-polymer interactions*. Such questions were tackled at the beginning of the

second half of the 20th century by Flory and Huggins ^[7 - 8] and modified aspects of Debye-Hückel theory where also intergraded by Guggenheim at around a similar time.

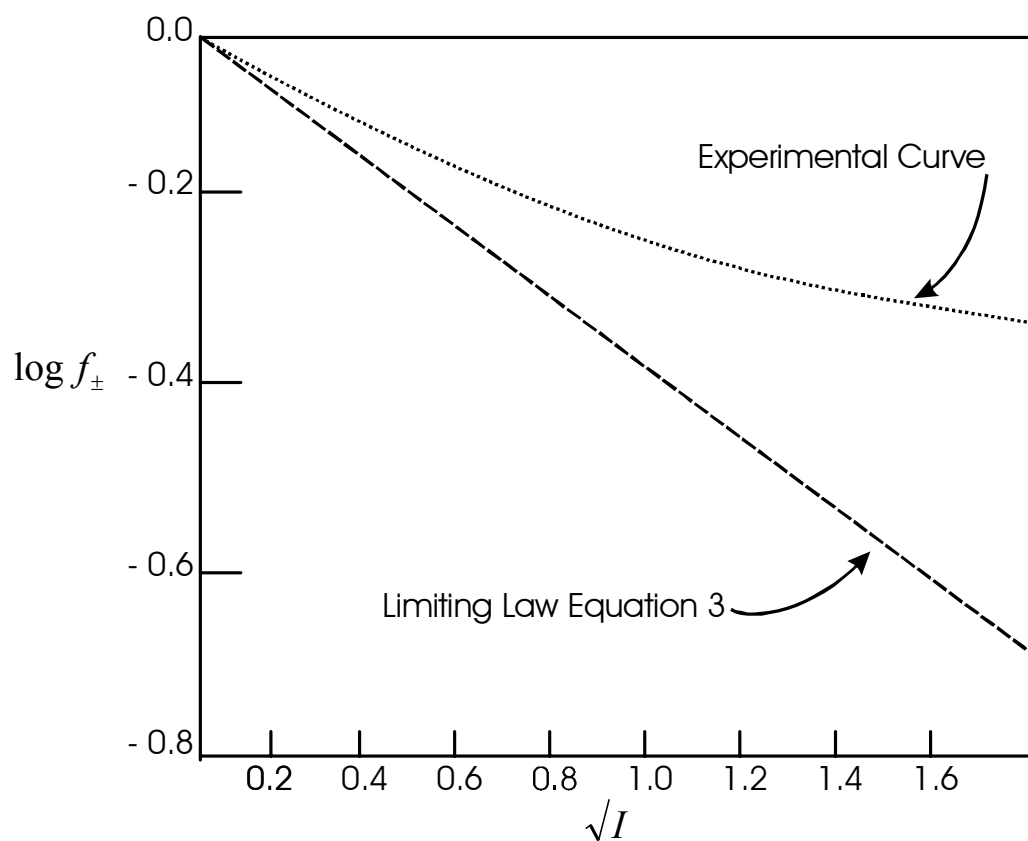


Fig. (2.1.4) The experimental $\log f_{\pm}$. vs. $I^{1/2}$ curve is a straight line only at extremely low concentrations ^[5]

2.1.4.

The Conductivity Mechanism:

To this point, we have only discussed the relationship of ions within dilute liquid systems and we have only vaguely referred to solid-polymeric electrolyte systems. The mechanism; to how charge is transported within such systems has largely remained overlooked. The model most commonly encountered for conductivity in polymer electrolytes is the free volume theory. The conductivity of such systems is often expressed by the Vogel-Tamman-Fulcher (VTF), which will be discussed later in section {2.3}. The experimental results for poly(ethylene oxide) (PEO) networks containing for example sodium tetraphenylborate exhibited in early polymeric investigations a linear plot for the conductivity versus $(T-T_0)^{-1}$ [9]. The temperature dependence of conductivity of (PEO) systems may be attributed to its excellent solvating character which implies that the X^- anion has a lesser tendency to ion-pairing with complexed M^+ cations. As was previously mentioned in Section {1} will be developed in later sections; a comprehensive theoretical approach to explaining the formation of ion-pairing and the mechanism of conductivity in polymer electrolytes has not been definitively established and is still in many scientific circles hotly debated.

In the instance of (PEO) systems at low salt concentrations, at a constant temperature a linear relationship of conductivity and salt concentration is observed. Nevertheless, this simple behaviour is not observed above the “critical” salt concentration. This phenomenon has been explained in the past through the proposal that salt molecules are associated in quantities in which dipoles (ion pairs), ion triplets; free ions, and large ionic aggregates are assumed to form at high salt concentrations. It was suggested by Torell [10], that the molecules tend to associate forming “multiplets of higher order”. The formation of larger aggregates such as the indicated triple ion species, are one of a number of aspects of these systems as one increases the salt concentration successively. In parallel to the increase in salt concentration, there is a corresponding drop in conductivity and rise in the viscosity of the polymeric test material, whereby this situation is related to the presence of “transient” or ionic cross-linking and an associated increase in T_g values [11].

The evidence of formation of such higher ionic aggregates can be determined with various spectroscopic methods and in the form of transport numbers¹. The modern tools in determining the existence of such pairs through the interpretation of transport numbers are made possible by the use of NMR and steady-state current methods (see section {2.2.4}). The contribution of the species to the overall conductivity of system is still hotly debated. For example, the author Angell^[12] maintains in (PEO) systems, that the cations are mobile charge carrying species of the system and other authors argue the contra giving the transport number of the cation in such systems as zero. The usual method for the acquisition of transference numbers² in polymer electrolytes is by means of pulsed gradient NMR and the steady-state current methods. The later method only functions well enough when the system under investigation is completely dissociated and other conditions are fulfilled. Therefore the method is very limited and system specific. It is difficult to determine the nature of the information produced by the steady-state method. Since quantitative, analysis of the non-equilibrium species is extremely complex and difficult to attain. The classical example proposed by Bruce & Vincent^[13] which will be discussed in the next section {2.2} is the method for cation transport number in a fully dissociated salt, which can be calculated from the ratio of the steady state current, where a uniform concentration gradient extends right across the cell from cathode to anode. In three compartments known by design as the Hittorf cell^[14 - 16] the transfer of anions, which would normally occur between cathode and anode compartments is prevented by diffusion down the concentration gradient. It appears that most transport numbers, which are widely quoted in the field of polymer electrolytes are not classical quantities according to Cameron & Ingram^[17]. They refer to the net migration of charged species caused by the application of an electric field. The steady-state current method is more informative for many practical purposes since it simulates accurately the conditions in a electrochemical cell where the concentration gradient is generated.

1 If potential is applied to an electrolyte and the current measured, the transport number t of any charge species is the proportion of the overall electrolyte conductivity due to the species. The sum of the transport numbers for all species present is equal to unity.

2 If potential is applied to an electrolyte and the current measured, a transference number T refers to the proportion of current carried by a constituent of the salt present.

2.2. Diffusion & Migration – Ionic Transport

2.2.1.

Convection, Diffusion & Migration:

The mechanisms of ion transport in polymer electrolytes are not completely understood (section {2.1.3}); but what is well understood is the general means by which ions move through various mediums. Ion transport in solution generally occurs by three well-known and obvious mechanisms ^[18 - 25]:

- i. Migration in an electric field
- ii. Diffusion in response to a gradient of concentration i.e. chemical potential
- iii. Convection as a result of density gradients

In solution systems, convection due to density gradients greatly complicates the study of other mass transport processes, particularly when electrolysis continues for long periods. Solid electrochemical cells have different constraints and recent developments in this field have led to some interesting changes in the way in which the operation of electrochemical cell is perceived. A factor common to all solid state systems is the absence of convection, either because of complex rigidity of the atomic lattice of a crystalline system, or as a large macroscopic viscosity i.e. glass or rubber. In most simple solid electrolytes, there is a single charge carrier, an ion with a transport number of unity, e.g. Ag^+ ions in AgRb_4I_5 . In other solid phases, the mobile species may be either cations or anions, together with electrons. Here diffusion takes place as it can in solid electrolytes where both cations and anions are mobile. Because of the absence of convection in such systems, stable concentration gradients can be established which extend over large distances. The authors Bruce ^[22] and Ingram ^[26] first considered the effect of ion association for ion transport in polymer electrolytes. They assumed *steady-state* transport under *dc* polarisation with no convection in the solid polymer electrolyte. They discussed that in the case of complete salt dissociation, only cations carried the current, and the ion concentration profiles were linear. Bruce & Vincent ^[27] extended this classic solution theory to account for finite electrode kinetics and non-ideal electrolytes possessing long-range ion-ion interactions and concentrations dependent diffusivities. Later work carried out by the above-mentioned authors accounted for ion association in ideal

electrolytes ^[22] ^[27]. Diffusion coefficients were treated by all authors as constant under the assumption of dilute solution theory, where ions were assumed to associate to form ion pairs as distinct chemical species.

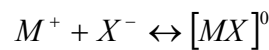
The nature of ion association in non-aqueous liquid electrolytes has traditionally been investigated by measuring the molar conductivity Λ , as a function of molar concentration c ³. For a sample uni-valent salt MX that dissolves fully into cations M^+ and anions X^- , σ is given by:

$$\sigma = ce_0(u_+ + u_-) \quad \text{Equ. [2.2.1]}$$

where c is the salt concentration, e_0 the charge on the electron and u_+ u_- represent the ion mobility. It follows that:

$$\Lambda = e_0(u_+ + u_-) \quad \text{Equ. [2.2.2]}$$

and thus provided the ion mobility is invariant ^[28] with concentration; Λ should not vary. During experiments with (PEO) materials and added salts ^[28], at low concentrations; there was a sharp decrease in molar conductivity; at higher concentrations, the expected experimental concentration decrease was not observed ^[29]. Such behaviour could not be explained by simple changes in the mobility of the ions. The sharp decrease in Λ has its origins in ion-ion interactions leading to ion association. As the concentration increases, mutual interactions between the ions are sufficiently strong to promote the formation of ion pairs that are in equilibrium with the free ions as seen below:



By the *law of mass action*, the concentration of these ion pairs will grow at the expense of the ions as the overall salt concentration increases. As the salt concentration is further increased a minimum in Λ is eventually reached at which the concentration of the ion pairs reach a maximum. Two mechanisms are postulated for the increase in ion concentrations and Λ , beyond the minimum. The first mechanism assumes that at higher salt concentrations,

³ The molar conductivity is defined as σ/c where σ is the conductivity of the electrolyte. Therefore Λ is the conductivity per unit of salt concentration.

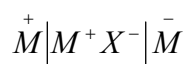
triple ions will form which will be in rapid equilibrium with the ion pairs and consequently being charged, will result in an increase in Λ . Alternately, the increasing salt concentration may be due to long range Debye-Hückel like ion interactions. As already discussed in detail in section {2.1}, which lowers the activity of the ions and in turn stabilise free ions compared with neutral ion pairs resulting in a shift of the dynamic equilibrium towards free ions. Triple ion formation is probably more important than activity effects.

Two possible mechanisms of charge transport involving triple ions may be envisaged both of which may be in fact in operation ^[29]. The first involves long-range transport of the triple ions as discrete entities through the polymers ^[29], facilitated as usual by the segmental motion of the chains as described in section {2.1.3}. This is more likely for the anion $[MX_2]^-$ than the cation $[M_2X]^+$; since the motion of the latter requires the simultaneous dissociation of two M^+ cations from a chain or chains. The second mechanism is also facilitated by chain motion but in this case, the triple ion, which moves with chain motion as it, describes its segmental motion when it encounters an ion pair, thereby transferring an ion to the pair forming a new aggregate and leaving an ion pair behind ^[26]. The liquid polymer systems are very similar to conventional non-aqueous electrolytes that show a minimum in Λ at low concentrations ^{[11][52]}. The measurements of Λ vs. concentration provide no evidence as to the nature of the ion pairs that form i.e. whether they are solvated species ^[31]. The mobility of the ion pairs does not influence the results. Contact ion pairs are likely to be more mobile separated by solvent since the latter include a section of at least one polymer chain.

2.2.2.

DC Polarisation:

Molar conductivity measurements are equally applicable to both solid and liquid electrolytes. The measurement of current flowing through an electrochemical cell on a time scale of minutes or hours while the cell is perturbed by a constant *dc* potential is only of value for solid solvents when convection is absent ^[26]. Let us begin by considering a cell of the form:



consisting of metal electrode *M* between which is placed an electrolyte *MX*, that fully dissociates into M^+ cations, and X^- anions. On application of a *dc* potential; M^+ cations are transported by the field towards the negative cathode while at the same time X^- anions are transported by the field towards the positive anode; this is termed migration as demonstrated in Fig. (2.2.1a). This initial current due to the ion migration when divided by the applied potential yields the bulk conductivity of the electrolyte. At longer times, anions arriving at the cathode, and those left behind by cations migrating away from the cathode; are consumed while an equivalent number of cations are produced at the anode. At this point electrolysis is occurring and concentration gradients are formed near each electrode. The transport near the electrodes is now influenced by diffusion down the concentration gradients as well as by migration as seen in Fig. (2.2.1b). The current flowing through the cell will change with time due to continuous extension of the diffusion layers out into the bulk electrolyte. Such semi-finite diffusion results in the current decaying with a square root dependence on time. In the case of liquid electrolytes, the extent of diffusion layers is limited by the onset of convection so that diffusion is confined to a region near the electrode. The onset of such convection limits the normal time-scale of the experiments in liquids usually to some tens of seconds unless the convection is controlled by for example the left the rotating disk electrode ^[32].

In contrast, in a solid the diffusion layers continue to grow towards each other until they merge and a *steady state* is reached as seen in Fig. (2.2.1c). In this condition the net anion flux is zero since anion migration due to the field from right to left is exactly balanced by diffusion from left to right down the concentration gradient. The current in the “steady

state” is due only to the migration and diffusion of cations ^[28]. Such steady state measurements can reveal the nature of ion association. This is more fully developed by Bruce and Vincent ^[27] where they assumed that the electrolyte to be completely dissociated and that a linear relationship existed between the steady state current and the applied potential difference. In the mentioned paper ^[27], no account was taken of the effects of ion association. A number of studies have concluded, “mobile ions-associated species play an important and possibly dominant role in charge transport” ^{[30] [33 – 35]}. Therefore, the author with the assistance of a later paper published by Bruce & Vincent ^[28] intends to expand the analysis of the $\bar{M}^+ | M^+ X^- | \bar{M}^-$ system to include the situation where ion association is important and consider cases where the associated species are mobile and immobile and three methods that are currently utilised to measure such factors.

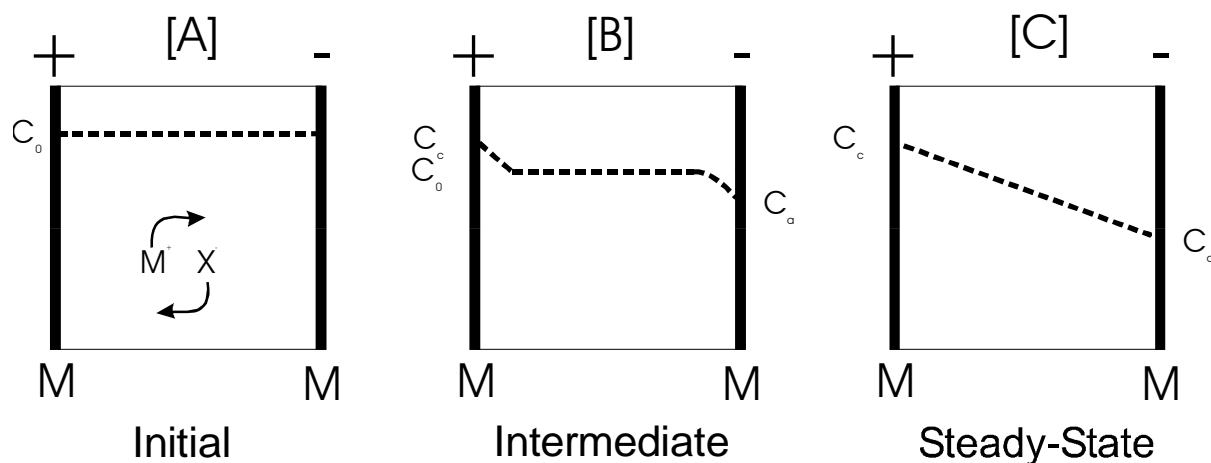


Fig. (2.2.1) Polymer electrolyte cell under de-polarisation

2.2.3.

Ideal & Non-ideal Electrolytes ^[28]:

Examining an ideal electrolyte is helpful in developing our understanding of *dc* polarisation polymer electrolytes that are non-ideal systems; since interactions between the ions of the salt are always likely to be significant in a medium of such low permittivity. It is therefore necessary to consider two effects:

- long range interactions between the ions
- long lived associated species, i.e. ion pairs, triple or higher aggregates

In brief, here is a summation of what is already established; transport in the context of electrolytes refers to the movement of species that form when a salt is dissolved in a solvent. If a uni-valent salt MX dissolves in a polymer forming the species M^+ , X^- , $[MX]^0$, $[M_2X]^+$ and $[MX_2]^-$ then the transport measurements are directed towards an understanding of the movement of each of the five species, which may vary in both their mobility and relative concentration. A distinction should be made between charged and neutral species: the former can be transported by both an electric field and a concentration gradient, and the latter can be transported only by a gradient in concentration.

In an ideal electrolyte for ion pairing, one must assume that the diffusion coefficients of the cations M^+ , anions X^- , and ion pairs MX are independent of concentration and that the association constant and electrode potentials are a function of concentration rather than activity. It is presumed that the equilibrium between free ions and ion pairs are fast and that the electrodes are reversible towards M^+ cations. A qualitative description of the establishment of a steady state following the polarisation $\overset{+}{M} | M^+ X^- | \bar{M}$ in which ion pairing is significant may be given as follows. Following the application of a constant voltage, the current is initially carried by migration of cations and anions in the electric field. The cations are continuously supplied by oxidation of M at the anode and consumed at the cathode by reduction. This is not the case for anions, which do not react at either electrode. Because of electro-neutrality, a concentration gradient of M^+ and X^- ions develops across the electrolyte. A computer simulation as seen in Fig. (2.2.2) ^[28] can generate a typical steady state profile.

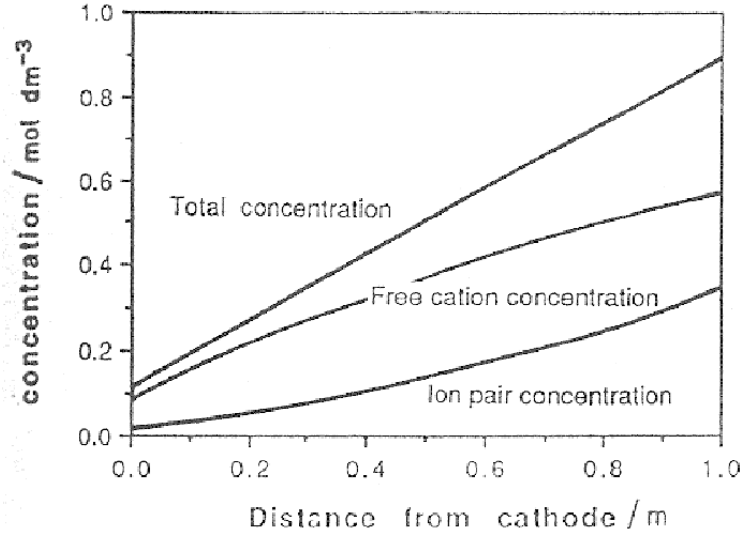


Fig. (2.2.2) Concentration profiles of ions pairs in a unit cell at steady state $c_0 = 0.5 \text{ mol dm}^{-3}$, D_+ , D_- , $D_0 = 8.10 \text{ cm}^2 \text{ s}^{-1}$, $I^+ = 150 \text{ mA m}^{-2}$ for $x = 1 \text{ m}^{[28]}$.

Let us assume a standard cell of unit length and cross-sectional area, and use the symbol K for the association constant, which is as approximated by (neglecting activity coefficients):

$$K = \frac{c^{+-}}{[c^+][c^-]} \quad \text{which since } [c^+] = [c^-] \text{ gives} \quad \text{Equ. [2.2.3]}$$

$$c^{+-} = K[c^+]^2 \quad \text{Equ. [2.2.4]}$$

where c^+ and c^- are the cationic and anionic salt concentrations respectively and c^{+-} is the concentration of the ion pair. Hence:

$$\frac{d[c^{+-}]}{dx} = 2K \left\{ c^+ \left(\frac{dc^+}{dx} \right) \right\} \quad \text{Equ. [2.2.5]}$$

In the steady state, one has for the anions:

$$\underbrace{\frac{F^2 D_- [c^-]}{RT} \frac{d\phi}{dx}}_{\text{anion migration}} = \underbrace{FD_- \frac{d[c^-]}{dx}}_{\text{anion diffusion}} + \underbrace{FD_0 \frac{d[c^{+-}]}{dx}}_{\text{ion pair diffusion}} \quad \text{Equ. [2.2.6]}$$

where D_0 and D_- is the diffusion coefficient of the ion pair and diffusion coefficient of ions respectively. The parameter ϕ is the potential difference across the cell. Hence:

$$\frac{d\phi}{dx} = \frac{RT}{F[c^-]} \left(\frac{d[c^-]}{dx} + \frac{D_0}{D_-} \cdot \frac{d[c^{+-}]}{dx} \right) \quad \text{Equ. [2.2.7]}$$

Considering now the cations, one can write form the steady state current I_+ of the cation:

$$I_+ = -FD_+ \frac{d[c^+]}{dx} - FD_0 \frac{d[c^{+-}]}{dx} - \frac{F^2 D_+ d[c^+]}{RT} \frac{d\phi}{dx} \quad \text{Equ. [2.2.8]}$$

cation diffusion
ion pair diffusion
cation migration

Thus for Equ. [2.2.5], Equ. [2.2.7] and Equ. [2.2.8], one has:

$$I_+ = -2FD_+ \frac{d[c^+]}{dx} - 2KFD_0 [c^+] \left(1 + \frac{D_+}{D_-} \right) \frac{d[c^+]}{dx} \quad \text{Equ. [2.2.9]}$$

where F is Faradays constant and D_- is the diffusion coefficient of ions. On integrating with respect to cell thickness, x :

$$\frac{-I_+ x}{2F} = D_+ ([c^+]_x - [c^+]_c) + \frac{KD_0(D_+ + D_-)}{2D_-} ([c^+]_x^2 - [c^+]_c^2) \quad \text{Equ. [2.2.10]}$$

where $[c^+]_x$ and $[c^+]_c$ is the steady state cation concentration at a distance x from cathode and the steady state cation concentration at cathode respectively:

i.e.

$$I_+ = -2FD_+ ([c^+]_a - [c^+]_c) + \frac{FKD_0(D_+ + D_-)}{D_-} ([c^+]_a^2 - [c^+]_c^2) \quad \text{Equ. [2.2.11]}$$

where $[c^+]_a$ is the steady state cation concentration at anode.

for $x = 1$, also from Equ. [2.2.5] and Equ. [2.2.7]:

$$\frac{d\phi}{dx} = \frac{RT}{F[c^+]} \cdot \frac{d[c^+]}{dx} + \frac{RT}{F} \cdot \frac{2KD_0}{D_-} \cdot \frac{d[c^+]}{dx} \quad \text{Equ. [2.2.12]}$$

on integration gives:

$$\Delta\phi = \frac{RT}{F} \left\{ \ln \left(\frac{[c^+]_a}{[c^+]_c} \right) + \frac{2KD_0}{D_-} ([c^+]_a - [c^+]_c) \right\} \quad \text{Equ. [2.2.13]}$$

For reversible electrodes, the electrode potential difference is given by:

$$\Delta E = \frac{RT}{F} \ln \left(\frac{[c^+]_a}{[c^+]_c} \right) \quad \text{Equ. [2.2.14]}$$

where ΔE is the Nernst potential difference:

so that as before:

$$\Delta U = \Delta\phi + \Delta E \quad \text{Equ. [2.2.15]}$$

where ΔU is the applied *dc* voltage.

$$\Delta U = \frac{2RT}{F} \left\{ \ln \left(\frac{[c^+]_a}{[c^+]_c} \right) + \frac{KD_0 ([c^+]_a - [c^+]_c)}{D_-} \right\} \quad \text{Equ. [2.2.16]}$$

According to Bruce ^[15], the equations for the steady state current in Equ. [2.2.11] and for the applied voltage Equ. [2.2.16], both of which are functions of the free cation concentration at the cathode and anode may be combined to derive an expression for $I_+/\Delta U$. Under certain conditions, the value of this ratio is independent of the applied voltage and it may therefore be regarded as the effective conductivity σ_{eff} of the cell in the steady state. Then two conditions may be considered:

- 1) When the difference between the cation and the concentration at the cathode and the anode is small:

$$\ln \left(\frac{[c^+]_a}{[c^+]_c} \right) \cong 2 \left(\frac{[c^+]_a - [c^+]_c}{[c^+]_a + [c^+]_c} \right) \quad \text{Equ. [2.2.17]}$$

and in this situation:

$$\begin{aligned}
\sigma_{eff} &= \frac{-I_+}{\Delta V} \\
&= \frac{F^2}{2RT} \left([c^+]_a + [c^+]_c \right) \left\{ (D_+ + D_-) - \frac{2D^2}{2D_- + KD_0([c^+]_a + [c^+]_c)} \right\} \\
&= \frac{F^2 D ([c^+]_a + [c^+]_c)}{2RT} \left\{ 1 + \frac{KD_0([c^+]_a + [c^+]_c)}{2D_+ (1 + KD_0([c^+]_a + [c^+]_c)/2D_-)} \right\}
\end{aligned}$$

Equ. [2.2.18]

This expression can be further simplified, in establishing the steady state. Clearly, the concentration of the cations rises at the anode and falls at the cathode. For conditions under which the average ionic concentration at the electrodes $([c^+]_a + [c^+]_c)/2$ is equal to $[c^+]_0$ the initial concentration of free ions throughout the electrolyte, then:

$$\sigma_{eff} = \frac{F^2 D_+ [c^+]_0}{RT} \left\{ 1 + \frac{KD_0 [c^+]_0}{D_+ (1 + KD_0 [c^+]_0 / D_-)} \right\}$$

Equ. [2.2.19]

- 2) In cases where the second (linear) term in the equation for the potential (Equ. [2.2.16]) is large in comparison with the first term:

$$[c^+]_a - [c^+]_c = \frac{FD_- \Delta V}{2RTKD_0}$$

Equ. [2.2.20]

Substituting Equ. [2.2.20] in to Equ. [2.2.11] then gives:

$$\sigma_{eff} = \frac{F^2}{RT} \left\{ \frac{D_+ D_-}{KD_0} + (D_+ + D_-) \frac{([c^+]_a + [c^+]_c)}{2} \right\}$$

Equ. [2.2.21]

and

$$\sigma_{eff} = \frac{F^2}{RT} \left\{ \frac{D_+ D_-}{KD_0} + (D_+ + D_-) [c^+]_0 \right\}$$

Equ. [2.2.22]

where $[c^+]_0$ may be substituted.

2.2.4.

Transport & Transference Measurement Methods:

Conductivity measurements are often first to be carried out on an electrolyte, however they provide information only on the total transport⁴ of the charge. Even in fully dissociated electrolytes such measurements do not differentiate between the current by the cations and anions. Transport⁵ and transference⁶ measurements attempt to probe more deeply into the movement of species in electrolytes. The different techniques that can be applied to determine transport in polymer–gel electrolytes can be seen in Table (2.2.1). This author does not intend to discuss each technique in detail as this work is not directly concerned with measuring transport or transference numbers but the author will briefly describe their main experimental attributes.

Technique [I]	Technique [II]	Technique [III]
Hittorf Concentration cell	Radiotracer PFG NMR	<i>dc</i> Polarisation

Table (2.2.1)

2.2.4.1.

Hittorf Cell Measurements

This method involves the passage of a measured quantity of charge through a cell and subsequent determination of changes in composition of the electrolyte near an anode and a cathode. More information can be read on this technique from a number of sources^{[28] [36]}. To date there have been few reliable measurement by this technique in solid electrolytes because of the experimental difficulties in applying the technique^[26].

⁴ The terms transport number and transference number, both of which are used often in such circumstance are often by many authors confused in their definition. This author defers to the definition of Bruce^[29] Firstly they both refer to excessively to the transport of charged species.

⁵ If potential is applied to an electrolyte and the current measured, the transport number t of any charge species is the proportion of the overall electrolyte conductivity due to the species. The sum of the transport numbers for all species present is equal to unity.

⁶ If potential is applied to an electrolyte and the current measured, a transference number T refers to the proportion of current carried by a constituent of the salt present.

2.2.4.2. Radiotracer Measurements

These measurements are based on following the progress of radioactively labelled nuclei of salt constituents as they diffuse through the polymer electrolyte. The labelled salt having been first deposited as a thin layer on the polymer surface ^[37].

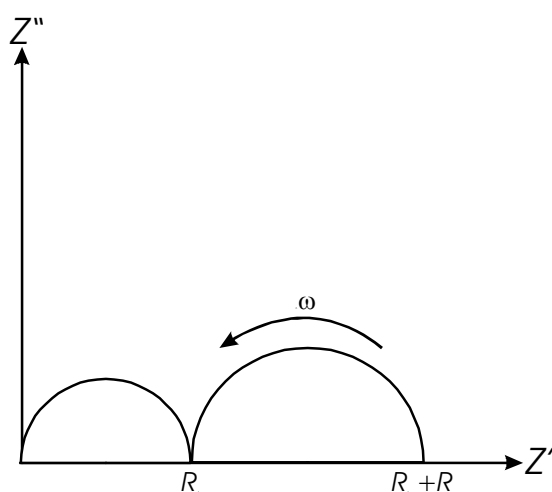


Fig. (2.2.4) Complex impedance plot for cell with finite kinetics. The high frequency semi-circle corresponds to the response of the bulk electrolyte; the low frequency semi-circle is associated with the two electrodes Bruce ^(2.8).

2.2.4.3. The Current Fraction Method

The *dc* polarisation technique has already been discussed in detail in section {2.2.2}. The authors Bruce & Vincent ^[37] used a potentiostat to determine the small signal *ac* response of a two-electrode cell in the steady state. A complex impedance plot such as that seen in Fig. (2.2.4). The

high frequency semicircle corresponds to the bulk electrolyte response whereas that at lower frequencies is associated with the electrode. Provided the *ac* signal is sufficiently small, the electrode response will be linear. R_e corresponds to the sum of the individual electrode resistances $RT/k_0 F^2 c_s^\beta$. Having obtained linear. R_e from the complex impedance plot η_t ⁷ over potential may be obtained from the expression:

$$\eta_t = R_e I_+^k \quad \text{Equ. [2.2.23]}$$

Hence:

⁷ $\eta_t = (\eta_a + \eta_c)$ total over potential at of anode and cathode. Defined and explained in detail by Bruce and Vincent – Steady State Current Flow in Solid Binary Electrolyte Cells – Bruce; P. G., Vincent; C. A., *J. Electroanal. Chem.* Vol. **225** pp 1 – 17 (1987).

$$I_+^k = \left(\frac{F^2 D_+^0 c_0}{RT} \right) (\Delta U - \eta_t) \quad \text{Equ. [2.2.24]}$$

where c_0 is the total salt concentration and:

$$t_+ = \frac{I_+^k}{I_0} \left[\frac{\Delta U}{\Delta U} - \eta_t \right] = \frac{I_t^k}{[\Delta U - \eta_t] \sigma} \quad \text{Equ. [2.2.25]}$$

where t_+ is the transport number of ion.

2.2.5.

Summary:

A combination of electrochemical and spectroscopic measurements indicate that ion association is prevalent in solid polymer electrolytes as it is for over century and a half already known for liquid electrolytes in solvents of low dielectric permittivity. As the author has already discussed in this section a variety of spectroscopic methods are at our disposal to identify ion pairs and high order clusters in various electrolyte mediums. Although the population distribution of ions and clusters are not known precisely, the experimental evidence to date strongly suggests the view that ion association occurs in most polymer electrolytes. For simple uni-valent salts in poly(ethers) measurements of molar conductivity vs. salt concentrations ($\ll 10^{-3}$ mole dm^{-3}) free ions dominate. Ion pairs on raising the salt concentration to 10^{-2} mole dm^{-3} [29] in turn increasingly replace these free ions. At high concentrations, triple ions may move as discrete entities as mentioned earlier in section {2.2.1}; or transfer a single cation or anion to the neighbouring ion pair. The *dc* measurements above one mole dm^{-3} suggest that neutral associates i.e. ion pairs or larger clusters may be present. However, in such high concentration ranges, these systems are best regarded as solvated molten salts to ionic liquids and more shall be said later on this topic in section {5}.

2.3. The Temperature Dependence of Conductivity

Foreword:

Above the experimental glass transition temperature T_g , polymers of low molecular weight can be considered as viscous liquids. Increasing the molecular weight brings a corresponding increase in viscosity and eventually at sufficiently high molecular weights; rubbery rather than liquid behaviours take form. This gradual change in the bulk character results from possible chain entanglements but does not reflect a significant change in the internal structure of the sample or in the segmental dynamics, which according to Ingram^[17]^[38] remains essentially liquid like. In attempting to understand such behaviours, a theoretical interpretation is necessary.

2.3.1.

Theoretical Foundation:

On passing into the glassy state very substantial decreases in solution, heat capacities C_p are observed. The heat capacities decreases, which are utilised in the experimental determination of T_g result from the loss of the configurational degrees of freedom. This implies that at lower temperatures the potential energy of the system is determined by the relative positions of the particles, which remain essentially constant. The changes in C_p occur at T_g because the structural relaxation times become too long for the internal structure equilibrium to be maintained on the timescale of the cooling process^[39]. Hence as observed in the laboratory the transition is a relaxational phenomenon. However from a thermodynamic standpoint utilising additional data from crystalline phases, it can be seen that the decrease in the heat capacity must occur in an equilibrium phenomenon at slightly lower temperatures in order that the liquid total entropy is not less than the crystal better known as the Kauzmann paradox^[40]. Kauzmann^[40] discovered what could be described as a thermodynamic contradiction for super-cooling liquids. Kauzmann^[40] proved that due to the large heat capacity of the liquid relative to the crystal the extra entropy i.e. ΔS_{fus} introduced on fusion would be completely lost from the super-cooling liquids not far below the observed glass transition temperature. This implied that at a temperature now called by a number of authors^[41] as the Kauzmann temperature T_K , the liquid and crystal would have cooled slowly enough

without crystallisation to avoid the “ergodicity-breaking”^[41] which occurs at T_g on normal cooling.

An example provided by Angell^{[39] [42]}, the calorimetric data for $\text{Ca}(\text{NO}_3)_2 \cdot 4\text{H}_2\text{O}$ liquid (i.e. the 20 mol % solution) and crystal phases place a lower limit for the maintenance of the observed liquid heat capacity at $\sim 203^\circ\text{K}$. This is obviously very close to the value of T_o extracted from the presented transport data ($T_o = 205^\circ\text{K}$ and $T_{oA} = 200$) seen in Fig. (2.3.1), and since similar results are found for many other liquids it seems patent that the relaxation ratios are closely related to the extent of excitation of the systems configurational degrees of freedom previously mentioned. For chain polymeric liquids and systems with some cross-linking, T_o can be related to chain stiffness and the hole energy parameters. This is not only very important conceptually but also provides the means for a connection between equilibrium and relaxation properties developed by Adam and Gibbs^[43 - 44]. Adam and Gibbs^[43] suggested that for densely packed liquids the conventional transition state theory for liquids, which is based on the notion of single molecules passing over energy barriers established by their neighbours, was inadequate. Instead, they proposed viscous flow occurs by increasingly cooperative rearrangements of groups of particles. Each alterable group was conceived as acting independently of the other groups in the system but it was supposed that the minimum would depend on the temperature.

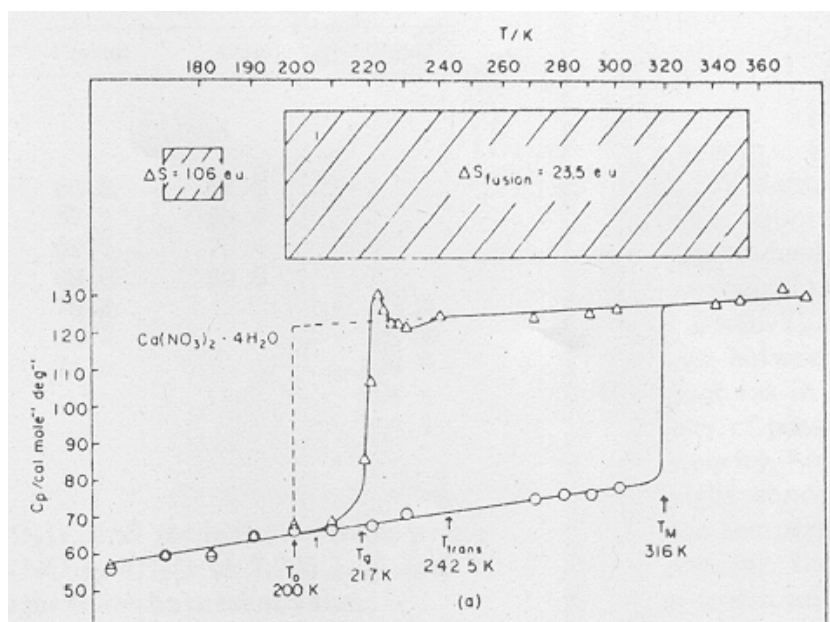


Fig. (2.3.1) Heat capacities of crystal, glass, and liquid state of $\text{Ca}(\text{NO}_3)_2 \cdot 4\text{H}_2\text{O}$ liquid (i.e. the 20 mol % solution). Also shown in the figures are the areas equivalent to the entropies of fusion and solid-state transition and the temperature $T_{o(\text{cal})}$ ^[42].

2.3.2.

T_g , Viscosity, Conductivity in Liquids & Polymers:

2.3.2.1.

T_g & Conductivity

The relationship between T_g and conductivity are closely intertwined. The effect of a dissolved salt on the T_g parameter of a polymer has implications in the search for polymer electrolytes of high conductivity^[17]. According to Angell^[41], it is commonly found; that the mass transport properties especially near and below the melting point usually do not follow the familiar Arrhenius equation:

$$\sigma = \sigma_0 \exp\left(\frac{-E_a}{RT}\right) \quad \text{Equ. [2.3.1]}$$

where σ_0 is the limiting conductivity, E_a is the activity energy and R is the gas constant. Instead, the transport properties are better described by the empirical Vogel-Tamman-Fulcher (VTF) equation^[45–47]]:

$$\sigma = \sigma_0 \exp\left(\frac{-B}{T - T_0}\right) \quad \text{Equ. [2.3.2]}$$

where σ_0 , B , and T_0 are empirical constants and σ is the property of interest. The factor T_0 , which has dimensions of temperature replaces 0 °K in the Arrhenius equation as the temperature of vanishing ionic mobility and has been called by Angell^[48] and Cameron^[17] the “ideal” glass transition temperature. The Equ. [2.3.2] attributes thermodynamic significance to T_0 suggesting that if the liquid could be cooled to this temperature while in a state of internal equilibrium, the magnitude of a thermodynamic quantity, which determines the state of the liquid, would fall to zero. The most plausible of such theories according to Choi and Bae^[49] in a recent publication, tends to Adam and Gibbs^[43], the thermodynamic quantity that vanishes as T_0 is the configurational part of the total entropy.

The VTF equation does not always accurately describe the conductivity data taken at low temperatures. The best-fit values fall systematically below the measured data of T_0 , i.e. the transport processes at low temperatures (and high viscosities) do not agree. These

discrepancies become more pronounced, the lower the temperature range of the data considered ^{[42] [48] [50]}. Such occurrences are probably due to a gradual change in character of the dominant transport mechanism. One mechanism is the fluctuations in configurational entropy (which according to Angell ^[42] determine the configurational heat capacity) determine the relaxation time. Another mechanism, the relaxation process is more solid-like in character and involves to an increasing extent successive individual ionic displacements within a temporarily rigid environment.

When a dopant salt is introduced into the polymer, matrix the conductivity σ increases rapidly owing to an increased number of charge carriers, despite the fact that the viscosity increases by means of a growing number of transient cross-links. When the concentration is large enough, the viscosity has increased to such an extent that the ion mobilities have decreased, i.e. that a maximum in conductivity versus salt concentration occurs. It has been suggested by Schantz ^[51] that the conductivity drop at high salt concentrations is not only due to reduced ion mobility but also to the formation of ion pairs. Neutral ion pairs imply a decrease in the number of charge carriers and therefore a reduced conductivity. To achieve maximum ionic conductivity in any material, one must optimise the number of charge carriers as well as their mobilities ^[51]. Therefore, it is desirable to choose a polymeric host matrix, which is flexible as a possible, and to utilise its liquid state.

2.3.2.2.

Viscosity & Conductivity

Earlier in this discussion, the author mentioned that viscosity is a further variable in the conductive behaviours of liquidus and polymeric systems. According to Cameron & Ingram ^[17] depending on whether one adopts the free volume or the configurational entropy model, the parameter T_0 is defined as the “ideal” glass transition. The alluded to parameter T_0 is defined as the equilibrium T_g , at which free volume disappears at the temperature whereby the configurational entropy becomes zero. The parameter T_0 usually lies 35 to 40 °K below T_g . Therefore, the ideal polymer for electrolyte applications will have in addition to high permittivity, which promotes dissociation of the added salt, must also have a low T_g and probably most importantly have a weak concentration dependence of T_g . Cameron & Ingram ^{[17] [38]} indicated that an increase in the degree of dissociation of the dissolved salt tends to increase the ion-polymer interactions therefore producing an increase in the T_g value

accordingly. The rise in T_g of liquid polymer electrolytes as the concentration of dissolved salt increase is paralleled by the rise in viscosity. Both T_g and viscosity are dependent on polymer weight. The glass transition is less sensitive to the molecular weight changes than viscosity. The T_g eventually reaches a limiting value but continues to rise with increasing molecular weight. As with conductivity, the temperature dependence of viscosity η of liquid polymer electrolytes can be fitted to a modified VTF equation for relevance to viscosity:

$$\eta = \eta_0 \exp\left(\frac{-B'}{T - T_0'}\right) \quad \text{Equ. [2.3.3]}$$

where η_0 , B' , and T_0' are again empirical constants and T_0' is related to T_g suggesting that similar molecular processes control both viscosity and conductivity. However, caution is required, as this does not hold in all circumstances^[17].

In the case of the association equilibrium, the number of charge carriers is also temperature dependent. In an example provided by Gerber^[52] concerning the temperature dependence of LiBF_4 in dimethoxyethane, a solvent of low dielectric permittivity (DME), the conductivity of lithium salts can in situations exhibit negative temperature dependence. Such solutions of salts in solvents of low permittivity show particular properties, which can be attributed to the formation of triple-ions in solution. The equilibrium between the various aggregate species in solution depends often on the solvents permittivity, which increases with decreasing temperatures. The higher the permittivity at low temperatures entails higher concentrations of the free ions. The negative temperature coefficient previously mentioned is the consequence of a large negative temperature coefficient of the ion-pair formation constants and a small temperature dependence of viscosity. Hence, the effect of reduced mobility (due to viscosity increasing) is overcompensated by the increase of the concentration of charge carriers due to decreasing association constants with decreasing temperature. At certain concentrations of lithium salts, there is often little temperature dependence of conductivity observed. In this case the effects of viscosity, which has the usual effect at increasing conductivity with temperature is compensated by an increase in the dissociation constant, thereby cancelling the effects of one another out. In such circumstances, the VTF approach becomes essentially pointless in its application.

2.3.3.

Conductivity in Ionic Liquids:

Ionic liquid systems often exhibit classical Arrhenius behaviours far above ambient temperatures. However, at low temperatures especially near to their T_g the conductivity in most circumstances displays a significant negative deviation from linear behaviour. The observed temperature dependence of conductivity behaviour is consistent with glass forming liquids and is better described by the VTF equation. The temperature dependence of conductivity of an ionic liquid involves a complex interplay of short range and long-range forces that is strongly impacted by the type and character of the cations and anions present within the system. No less important is the morphology of the materials. The materials utilised for this work can be described as hybrids of liquid or polymer in salt systems. According to Trulove & Mantz ^[53], who described such systems “at our current understanding, it is not possible to predict accurately how conductivity of a given ionic liquid will vary with temperature”. It is hoped that this work will perhaps throw more light to the concerning subject.

2.4. Electrochemical Impedance Spectroscopy (EIS)

Foreword:

Electrochemical Impedance spectroscopy (EIS) is a relatively new and powerful method for characterising electrical properties of materials and their interfaces with electronically conducting electrodes. This measuring technique is used to investigate the dynamics of bound and mobile charges of the bulk, and the interfacial regions of any form of solid, liquid, ionic, semi-conducting, mixed, electric-ionic conductors, and insulating material (dielectrics) ^[54 - 56].

2.4.1.

AC Input Signal Response - Laplace Transform:

The author will first initiate the discussion by developing an idea already proposed by Lasia ^[57]. Firstly we will describe a potential $U(t)$ flowing in one direction applied to the series connection of resistance R and capacitance C , the total potential difference is the sum of the potential drops on each element which is depicted in the schematic Fig. (2.4.1).

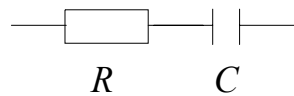


Fig. (2.4.1) Series connection R -resistance and C -capacitance

The resistance R is described by the equation ^[57]:

$$I(t) = \frac{U(t)}{R} \quad \text{Equ. [2.4.1]}$$

and the capacitance C is correspondingly described by the equation:

$$U(t) = \frac{Q(t)}{C} \quad \text{Equ. [2.4.2]}$$

where Q is the charge stored in a capacitor. The total sum of the potential across the system seen in Fig. (2.4.1) is described by the equation:

$$U(t) = I(t)R + \frac{Q(t)}{C} \quad \text{Equ. [2.4.3]}$$

$$U(t) = I(t)R + \frac{1}{C} \int_0^t I(t) dt \quad \text{Equ [2.4.4]}$$

The equation Equ. [2.4.4] is solved by utilising the Laplace transform ^[58]. The Laplace is a transform in which $U(t)$ is transformed into a new function s called frequency or $s = \nu + j\omega$, where $j = \sqrt{-1}$ ^[59].

$$\angle\{F(t)\} = \int_0^\infty F(t)e^{-st} dt \quad \text{Equ. [2.4.5]}$$

where $F(t)$ is the frequency parameter and s = some complex. Than follows:

$$\angle\left\{\int_0^t I(t) dt = \frac{i(s)}{s}\right\} \quad \text{Equ. [2.4.6]}$$

In the case of a back transform or a change in current direction than continuing from Equ. [2.4.4] we get:

$$U(s) = I(s)R + \frac{I(s)}{Cs} \quad \text{Equ. [2.4.7]}$$

$$U(s) = I(s) \left[R + \frac{1}{Cs} \right] \quad \text{Equ. [2.4.8]}$$

Therefore these relationships imply:

$$Z(s) \text{ impedance} = \frac{U(s)}{I(s)} = R + \frac{1}{Cs} \quad \text{Equ. [2.4.9]}$$

$$Y(s)_{\text{admittance}} = \frac{1}{Z(s)} = \frac{1}{R} \quad \text{Equ. [2.4.10]}$$

$$I(s) = \frac{U(s)}{R + 1/Cs} \quad \text{Equ. [2.4.11]}$$

For a current operating in the other direction. In case of a back transform \angle^{-1} then $U(t) = U_0$ and $t \geq 0$. We get:

$$\angle(\text{cont.}) = \frac{\text{const}}{s} \quad \text{Equ. [2.4.12]}$$

$$I(s) = \frac{U_0}{s(R + 1/Cs)} \quad \text{Equ. [2.4.13]}$$

$$I(s) = \frac{U_0}{sR + 1/C} \quad \text{Equ. [2.4.14]}$$

then:

$$I(s) = \frac{U_0}{R \left(s + \frac{1}{RC} \right)} \quad \text{Equ. [2.4.15]}$$

By back transformation, we find:

$$I(t) = \frac{U_0}{R} \exp\left(\frac{-t}{RC}\right) \quad \text{Equ. [2.4.16]}$$

Up to this point, we have only discussed *dc* current, and have explained what occurs within the impedance machine as the current travels in one direction. The next step is to discuss the Laplace transform for *ac* current:

$$U(t) = U_0 \sin(\omega t) \quad \omega = 2\pi\nu \quad \text{Equ. [2.4.17]}$$

$$\angle\{\sin(\omega t)\} = \int_0^\infty e^{-st} \sin(at) dt = \frac{\omega^2}{s^2 + \omega^2} \quad \text{Equ. [2.4.18]}$$

$$\angle\{e^{at}\} = \int_0^\infty e^{-st} e^{at} dt = \frac{1}{s-a} \quad \text{Equ. [2.4.19]}$$

$$\angle\{e^{jat}\} = \frac{1}{s-ja} \cdot \frac{s+ja}{s-ja} \quad \text{Equ. [2.4.20]}$$

$$\frac{s+ja}{s^2+a^2} \Rightarrow \frac{s}{s^2+a^2} + \frac{ja}{s^2+a^2} \quad \text{Equ. [2.4.21]}$$

real imaginary

Euler's expression ^[60]:

$$e^{jat} = \cos(at) + j \sin(at) \quad \text{Equ. [2.4.22]}$$

$$= \angle\{\cos(at)\} + \angle\{j \sin(at)\} \quad \text{Equ. [2.4.23]}$$

$$= \int_0^\infty e^{-st} \cos(at) dt + \int_0^\infty e^{-st} j \sin(at) dt \quad \text{Equ. [2.4.24]}$$

$$= \frac{s}{s^2+a^2} + i \frac{a}{s^2+a^2} \quad \text{Equ. [2.4.25]}$$

yielding:

$$i(s) = \frac{U_0}{R(\omega^2 + 1/RC)^2} \left(\omega^2 \frac{\omega}{s^2 + \omega^2} + \frac{\omega}{RC} \frac{s}{s^2 + \omega^2} + \frac{\omega}{RC} \frac{1}{s + 1/RC} \right) \quad \text{Equ. [2.4.25]}$$

and finally:

$$\Im(t) = \frac{U_0}{R^2 + (1/\omega C)^2} \sin(\omega t + \rho) \quad \text{Equ. [2.4.26]}$$

2.4.2.

Impedance Spectroscopy and its Functions – Z , Y , M & ε :

Impedance spectroscopy is in most circumstances characterised by the measurement and analysis of some or all of the four functions Z , Y , M and ε ; and the plotting of these functions in the complex plane. Historically, “the use of Z and Y in analysing the response of electrical circuits made up of ideal elements (R , L and C) goes back to the beginning of the discipline of electrical engineering”^[61]. An important milestone according to Macdonald^[54]^[61] for the analysis of real systems, is distributed systems in a complex plane form Cole and Cole^[62] of ε' and ε'' for dielectric systems in the complex plane or better known as Cole-Cole plots. This was later adapted to the dielectric constant level from the circle diagram of electrical engineering emplied by a Smith-Chart^[63] impedance diagram. Complex plots are sometimes called *Nyquist diagrams*. The author at this stage only intends to deal with the theoretical implications of the impedance; the fundamentals, usage, and applications of impedance instrumentation will be dealt with in detail in section {3.1}.

A system is perturbed by an *ac* voltage in sinusoidal form of $U = U_0 \sin(\omega t)$ as seen in section {2.4.1}, the relationship between the radial frequency and the frequency f (in Hz) is $\omega = 2\pi f$. The current response $I(t)$ will be sinusoid as the same frequency but shifted in phase^[64].

$$I(t) = I_0 \sin(\omega t + \Phi) \quad \text{Equ. [2.4.27]}$$

where $I(t)$ is the current time t , I_0 is the current amplitude, and Φ is the phase shift by which the voltage lags the current as seen in Fig. (2.4.1). Analogous to Ohm’s law for a *dc* circuit, the impedance is defined as the ratio of voltage and current:

$$Z = \frac{U(t)}{I(t)} \quad \text{Equ. [2.4.28]}$$

The impedance has a magnitude ($Z_0 = U_0/I_0$) and a phase (Φ) and is thus a vector quantity. It is therefore convenient to present impedance I complex notation as seen in Fig (2.4.1) and mathematical in the form:

$$Z = Z_0 (\cos \Phi + j \sin \Phi) = Z' + jZ'' \quad \text{Equ. [2.4.29]}$$

where $j = \sqrt{-1}$, Z' is the real part and Z'' is the imaginary part of the impedance. Using Euler's relationship ^[60], one can also write:

$$Z = Z_0 e^{j\Phi} \quad \text{Equ. [2.4.30]}$$

The complex plane diagram presented by the author in Fig. (2.4.2) shows the relationship between the two different forms of presentation.

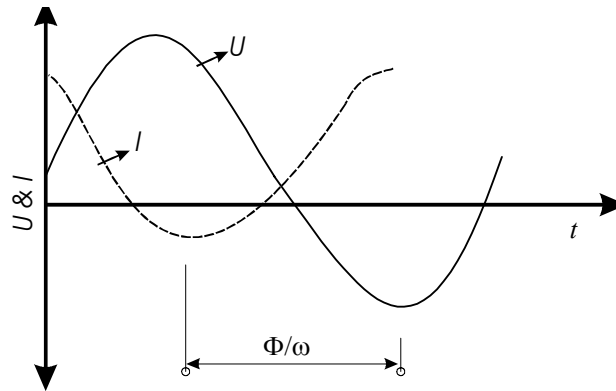


Fig. (2.4.1) Sinusoidal voltage perturbation and current response ^[64]

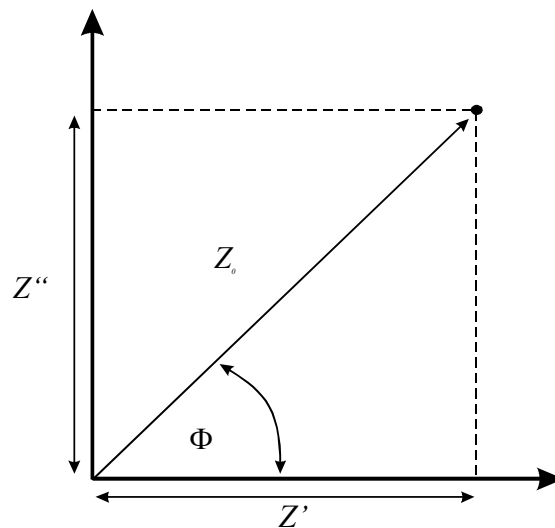


Fig. (2.4.2) Impedance plot in the complex plane Z' vs. Z'' are the imaginary and real parts of the impedance, Z_0 is the magnitude of the impedance and Φ is the phase angle.

2.4.2.1.**Impedance Response of Circuit Elements and their Combinations:****[A] Resistance**

If a sinusoidal voltage is applied to a pure resistor of value R , then $Z_0 = R$ and $\Phi = 0$ for all frequencies. This is shown in Fig. (2.4.3a), which is also called the complex plane or Nyquist plot.

[B] Capacitance

If a sinusoidal voltage is applied across a pure capacitor, the impedance can be calculated according to the relationship:

$$Z = \frac{1}{j\omega C} = -\frac{j}{\omega C} \quad \text{Equ. [2.4.31]}$$

where C is the capacitance . The magnitude of the impedance for a pure capacitor is:

$$Z_0 = \frac{1}{\omega C} \quad \text{Equ. [2.4.32]}$$

and the phase angle is $\Phi = -\pi/2$, that is the impedance depends on frequency and is entirely imaginary as seen in Fig. (2.4.3b).

[C] Resistance & Capacitor in Series

For the serial combination of a resistor and capacitor, the result is shown in Fig. (2.4.3c). According to Kirchhoff's law ^[56], the current flowing through both elements are the same. The total potential equals the sum of the potentials across the capacitor and the resistor:

$$U(t) = I(t)R + \frac{1}{C} \int_0^t I(t) dt \quad \text{Equ. [2.4.33]}$$

and the total impedance can be calculated according to:

$$Z = R - \frac{j}{\omega C} \quad \text{Equ. [2.4.34]}$$

The magnitude of the impedance is:

$$Z_o = \sqrt{R^2 + \frac{1}{\omega^2 C^2}} \quad \text{Equ. [2.4.35]}$$

and the phase angle is:

$$\Phi = \arctan\left(-\frac{1}{R\omega C}\right) \quad \text{Equ. [2.4.36]}$$

[D] Resistance & Capacitor in Parallel

The impedance for a resistor and a capacitor in parallel shows the shape of a semi-circle in complex plane plots as seen in Fig. (2.4.3d). According to Kirchoff's law ^[56] for a parallel circuit elements the potentials across both elements are equal, while the total current can be calculated from the sum of currents flowing through resistor and capacitor:

$$I(t) = \frac{U(t)}{R} - \frac{j\omega U(t)}{j} \quad \text{Equ. [2.4.37]}$$

For the impedance, one writes:

$$\frac{1}{Z} = \frac{1}{R} - \frac{j\omega C}{j} \quad Z = \left(\frac{1}{R} - \frac{j\omega C}{j}\right)^{-1} \quad \text{Equ. [2.4.38]}$$

The magnitude of the impedance is:

$$Z_o = \left(\frac{1}{R^2} + \omega^2 C^2\right)^{-1/2} \quad \text{Equ. [2.4.39]}$$

and the phase angle is:

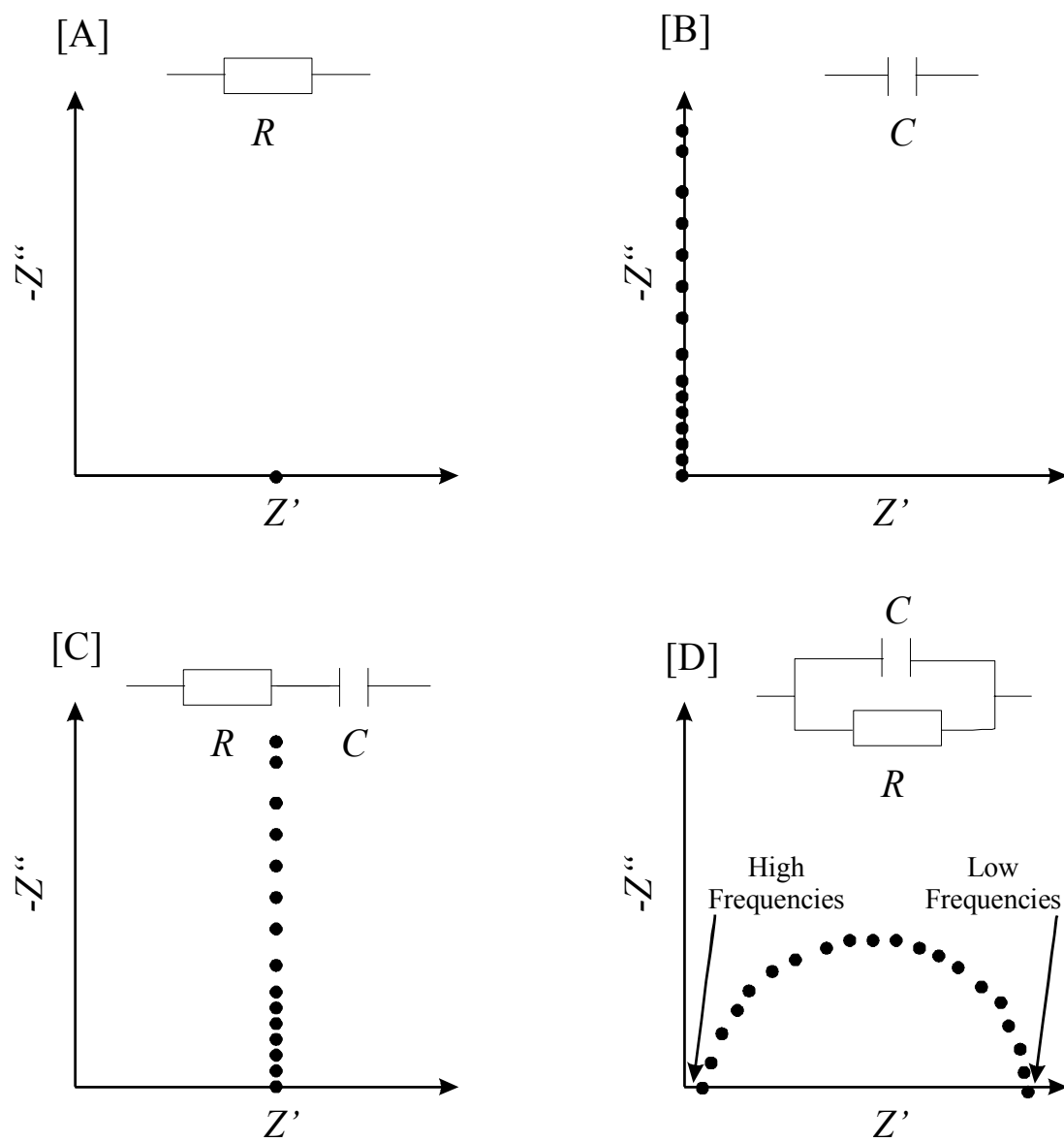


Fig. (2.4.3) Nyquist plots for different equivalent circuits

$$\Phi = \arctan(-R\omega C) \quad \text{Equ. [2.4.40]}$$

Besides the complex plane plots there are several other measured or derived quantities related to the impedance that this work will utilise to explain the behaviours of the materials under examination; where they play an import roles if not complementary roles. All of them are generally called immittances. First on the list is admittance (*Bode plots*) is:

$$Y \equiv Z^{-1} \equiv Y' + jY'' \quad \text{Equ. [2.4.41]}$$

In the complex domain where v , i and Z are all taken to be complex, one writes $v = Zi$ or alternatively $I = Yv$. It is common in EIS to express Z and Y in terms of resistance and capacitance components as $Z = R_s(\omega) - jX_s(\omega)$ and $Y = G_p(\omega) + jB_p(\omega)$, where the reactance $X_s \equiv [\omega C_s(\omega)]^{-1}$ and the susceptance $B_p \equiv \omega C_p(\omega)$. Here the subscripts s and p represent series and parallel respectively. The other quantities are usually defined as the *modulus function* - M :

$$M = j\omega C_c Z = M' + jM'' \quad \text{Equ. [2.4.42]}$$

and the complex *dielectric constant* or *dielectric permittivity* - ε :

$$\varepsilon = M^{-1} \equiv \frac{Y}{j\omega C_c} \equiv \varepsilon' - j\varepsilon'' \quad \text{Equ. [2.4.43]}$$

In these expressions $C_c \equiv \varepsilon_0 A_c / l$ is the capacitance of an empty measuring cell of electrode A_c and the electrode separation length l . The quantity ε_0 is the *dielectric permittivity of free space*. The dielectric constant ε is often written elsewhere as ε^* or $\hat{\varepsilon}$ to denote its complex nature. Nevertheless, this author will reserve the superscript asterisk to denote complex conjugation; thus:

$$Z^* = Z' - jZ'' \quad \text{Equ. [2.4.44]}$$

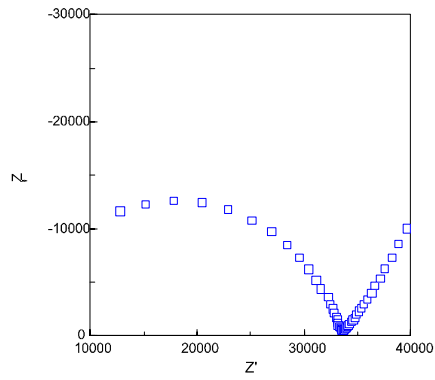
The interrelations between the four-immittance functions have been summarised by Macdonald in Table. (2.4.1).

Complex plane (Nyquist) plots are the most often used in the electrochemical literature because they allow an easy prediction of the circuits elements ^[57]. However they do not show all details; for example exactly the same why as Nyquist plots as seen in Fig. (2.4.4a-h) from experimental data, which may be obtained for different values of capacitance C . The only difference between them will be the fact that the points on the semi-circle should correspond to different frequencies. Nevertheless, Nyquist plots allow an easy relation to the electrical model. On the other hand, Bode plots contain all the necessary information. That is why Bode plots are mainly used in circuit analysis.

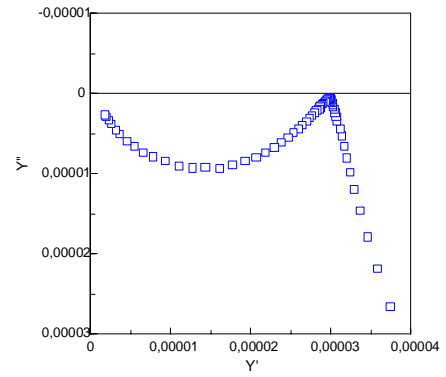
	M	Z	Y	ε
M	M	μZ	μY^I	ε^I
Z	$\mu^{-I} M$	Z	Y^I	$\mu^{-I} \varepsilon^I$
Y	μM^I	Z^I	Y	$\mu \varepsilon$
ε	M^I	$\mu^{-I} Z^I$	$\mu^{-I} Y$	ε

Table (2.4.1) Relations between the four basic immittances functions⁸ [54] [61]

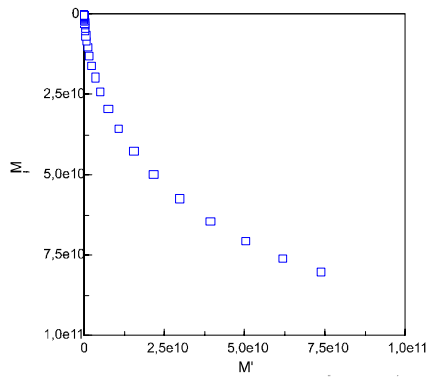
⁸ $\mu \equiv j\omega C_c$, where C_c is the capacitance of the empty cell.



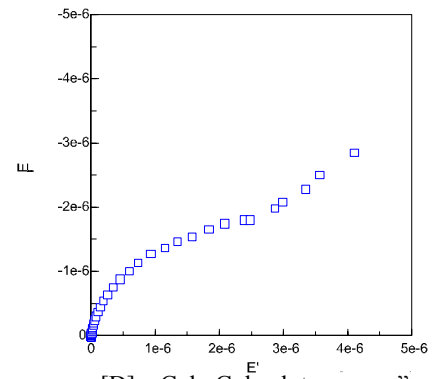
[A] Nyquist plot - $Z''(\Omega)$ vs. $Z'(\Omega)$
C₁₄ImidCl - 70 °C



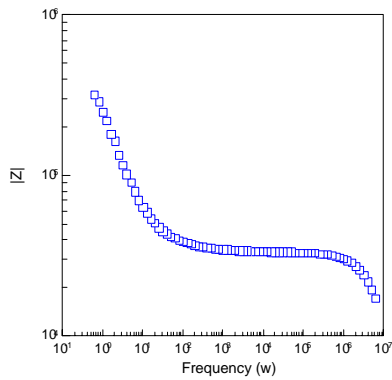
[B] Nyquist plot - $Y''(\Omega^{-1})$ vs. $Y'(\Omega^{-1})$
C₁₄ImidCl - 70 °C



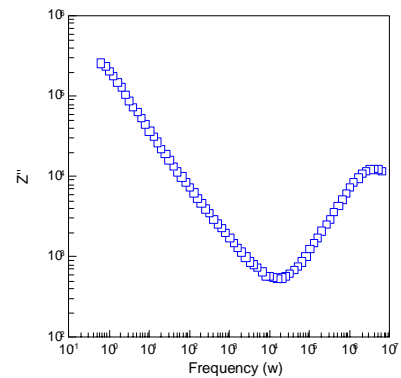
[C] Modulus plot - M'' vs. M'
C₁₄ImidCl - 70 °C



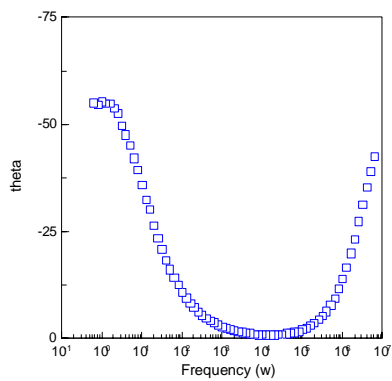
[D] Cole-Cole plot - ϵ'' vs. ϵ'
C₁₄ImidCl - 70 °C



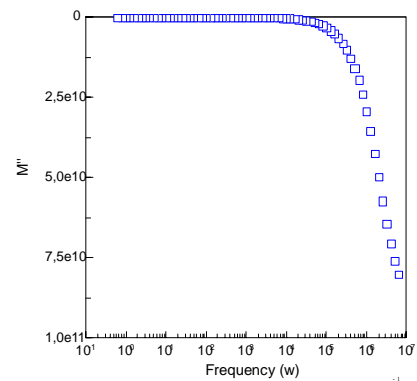
[E] Bode plot log $Z(\Omega)$ vs. ω (rad s⁻¹)
C₁₄ImidCl - 70 °C



[F] Bode plot $Z''(\Omega)$ vs. ω (rad s⁻¹)
C₁₄ImidCl - 70 °C



[G] Bode plot theta vs. ω (rad s⁻¹)
C₁₄ImidCl - 70 °C



[H] Bode plot M'' vs. ω (rad s⁻¹)
C₁₄ImidCl - 70 °C

Fig. (2.4.4) Examples of experimental data with various function forms

2.4.3.

EIS - Anomalies and Interfaces:

2.4.3.1.

[A] Warburg Impedance

The author previously indicated that, the flux equations (e.g. Nernst-Planck) contain in addition to the diffusion terms, a contribution from migration that is the movement of charged particles under the influence of an electric field. Under these circumstances, it is possible to carry out experiments in which the field is negligibly small compared to the concentration of activity driving force ^[54]. In aqueous solutions electrochemistry, this situation is usually accomplished with a supporting electrolyte. Usually this salt is added to the solution in high concentrations to increase conductivity enough for the migration terms. In solid-state electrochemistry, this is not the case because it is difficult to achieve the same effect electronic or ionic, in a good solid electrolyte for an analogous situation. The equivalent circuit analogue of this situation is a *finite-length transmission* line terminated with an open circuit. A constant activity or concentration is also a common condition for the interface removed from $x = 0$. In this case, the finite-length transmission line would be terminated in resistance, and the impedance is given by the expression:

$$Z(j\omega) = \frac{dE}{dc} \cdot \frac{1}{zF} \cdot \frac{\tanh l \sqrt{(j\omega/D)}}{\sqrt{(j\omega D)}} \quad \text{Equ. [2.4.45]}$$

where D is the diffusion coefficient of the particles. From equation [2.4.45] the *Warburg impedance* can be identified. It was shown earlier that an electrochemical cell could be described with a simple equivalent circuit containing the electrolytic resistance, the double layer capacitance and the impedance of the faradic process, which was described by simple terms of charge transfer resistance neglecting the diffusion of the electroactive species. For the interpretation of the faradic impedances in the presence of diffusion related phenomena, it is convenient to subdivide it into two circuit elements. This can be done in two possible ways. Z_f can be presented by resistance R_s in series with a pseudo-capacitance C_s according to Fig. (2.4.5a) or it can be subdivided into charge transfer resistance R_{ct} and the mass-transfer impedance Z_w as seen in Fig. (2.4.5b) also known as the Warburg impedance.

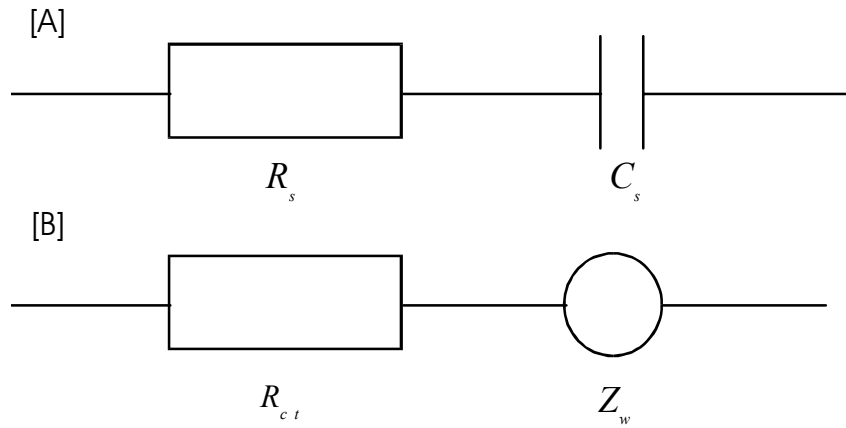


Fig. (2.4.5) Here are two possible presentations of the Faradaic impedance Z_f as an equivalent circuit.

The above terms in Fig. (2.4.5) can be defined by:

$$R_s = R_{ct} + \frac{\sigma}{\omega^{1/2}} \quad \text{Equ. [2.4.46]}$$

and

$$\frac{1}{C_s} = \sigma \omega^{1/2} \quad \text{Equ. [2.4.47]}$$

From the Equ. [2.4.45] and Equ. [2.4.46], the Warburg impedance can be identified. According to Krause ^[64], a comparison with the two forms of presentation of the faradic impedance in Fig [2.4.5] and the second term in Equ. [2.2.45] is identical to the real part of the Warburg impedance:

$$Z'_w = -\frac{1}{\omega C_s} = -\frac{\sigma}{\omega^{1/2}} \quad \text{Equ. [2.4.48]}$$

that is:

$$Z_w = \frac{\sigma}{\omega^{1/2}} - j \frac{\sigma}{\omega^{1/2}} \quad \text{Equ. [2.4.49]}$$

Since real and imaginary parts of the Warburg impedance Z_W have the same value, a plot of Z_W'' vs. Z_W' would show a straight line with phase angle of 45° as seen in Fig. (2.4.6a). In resulting equivalent circuits or also known as *Randles circuits* the semicircle is caused by a charge transfer controlled reaction. The straight line with a slope of (1) is due to Warburg impedance and indicates a purely diffusion-controlled reaction at the low frequency limit. It predicts that the impedance diverges from real axis at low frequencies that is, according to the above analysis the dc impedance of the electrochemical cell would be infinitely large.

The first considered case is that of an enforced or natural convection in an electrolyte solution, which would cause the concentration of solution species to be constant at certain distance from the electrode surface. In this case, the impedance is given by the expression ^[54]:

$$Z_W^{\text{finite}} = R_0 \frac{\tanh(\delta\sqrt{j\omega/D})}{\delta\sqrt{j\omega/D}} \quad \text{Equ. [2.4.50]}$$

where δ is the diffusion layer thickness. The term R_0 is the diffusion resistance for $\omega \rightarrow 0$ and D is the diffusion coefficient of diffusing particles. This behaviour is analogous to finite length transmission line terminated with a resistance. In contrast to the Warburg impedance for semi-finite diffusion, the finite Warburg impedance as was described in Equ. [2.4.49] will bend over to real axis at low frequencies giving rise to a distorted semi-circle as seen in Fig. (2.4.6b). This concurs with the fact that electrochemical cells usually have a finite dc resistance. A finite length diffusion layer thickness can not only be caused by a constant concentrations of species in the bulk of the solution but also by reflective boundary ^[64], that is, a boundary that can not be penetrated by electroactive species. This can happen when blocking occurs at the far end of the diffusion region and no dc current can flow through the system as seen in Fig. (2.4.6c).

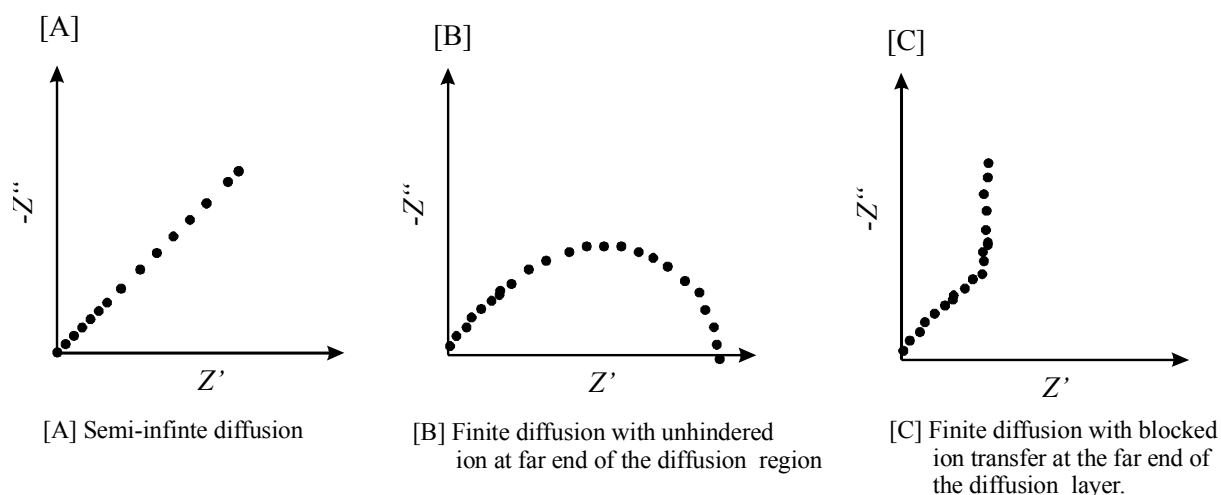


Fig. (2.4.6) Impedance spectra of diffusion behaviour^[64]

2.4.3.2.

[B] Concentration Polarisation

Such a phenomenon is often encountered where, upon the passage of current through an electrochemical cell, only one mobile species is discharged at the electrodes. Examples are the use of liquid or polymeric electrolytes, where both ions are mobile, and yet where only one is able to participate in the electrode reaction and the other example is a mixed conducting solid in which current is passed by electrons, but in which cations also have a significant transport number. Under certain circumstance, the presence of concentration polarisation^{[25] [56] [65]} might be confused with interference impedance. At different ratios of mobilities of anions and cations. Either diffusion-like response (finite-length transmission line behaviour) or parallel capacitive resistance behaviour may appear, in the case where *ac* impedance methods have been used to determine ionic transference numbers in polymeric electrolytes using this principle^[18].

2.4.3.3.

[C] Bulk, Intergrain, Grain Boundary & Constant Phase Element (CPE)

Earlier in this section, it was suggested that the electrical analogue of an isotropic, homogenous ionically conducting solid is a pure resistance in parallel with a high frequency ideal capacitor Fig. (2.4.3d). The model assumes the absence of electrode polarisation and relaxation processes within the crystal that would lead to additional parallel branches in the equivalent circuit ^[64]. West and co-workers ^[55] discusses the intricacies of impedance spectroscopy and its practical applications for the interpretation of the behaviours of materials at a macroscopic scale. They take for example an electro-ceramic of an oxide ion conductor $\text{Ca}_{12}\text{Al}_{14}\text{O}_{33}$ to demonstrate the distinct features attributable to similar structured materials. Impedance data is presented in the classical form of imaginary, Z'' capacitance against real Z' resistance impedances. Having obtained values for the R and C components the next stage is to assign them to regions of the sample. The assignment is based on the magnitude of the capacitances as seen in Table (2.4.2). For a parallel plate capacitor with area A , separation l between the plates and a medium of permittivity ε' between the plates, the capacitance is given by:

$$C = \varepsilon' e_0 \frac{A}{l} \quad \text{Equ. [2.4.51]}$$

where e_0 is the permittivity of free space⁹. For a material with unit cell constant l/A ¹⁰ and a typical permittivity of ≈ 10 , a capacitance value of 1×10^{-12} F is expected. Thus, this is a typical value for the bulk capacitance of a sample. The high frequency semi-circle in Fig. (2.4.7) has a capacitance of this order and therefore, this semi-circle and its associated resistances are attributed to the bulk properties of the sample. Such a formation would be explained as ion diffusion and accumulation at the electrode. However, for the purposes of explaining the usefulness of this technique the example proposed by West ^[55] is considered by this author to be most appropriate. In order to assign the second semi-circle to a feature of the ceramic, it is essential to have a picture of an idealised ceramic with grains and grain boundaries and to consider the factors, which control the magnitude of the grain boundary impedance.

⁹ Permittivity of free space = 8.854×10^{-14} F cm⁻¹

¹⁰ $l/A = 1$ cm⁻¹

Capacitance - F	Phenomenon Responsible
10^{-12}	Bulk
10^{-11}	Minor, second phase
$10^{-11} - 10^{-8}$	Grain boundary
$10^{-10} - 10^{-9}$	Bulk ferroelectric
$10^{-9} - 10^{-7}$	Surface layer
$10^{-7} - 10^{-5}$	Sample-electrode interface
10^{-4}	Electrochemical reactions

Table (2.4.2) Capacitance values and their possible interpretation for the oxide ion conductor $\text{Ca}_{12}\text{Al}_{14}\text{O}_{33}$ [55], although these interpretations are specific to this material a number of them could be carried over in the interpretation of the macroscopic behaviours of other materials under investigation.

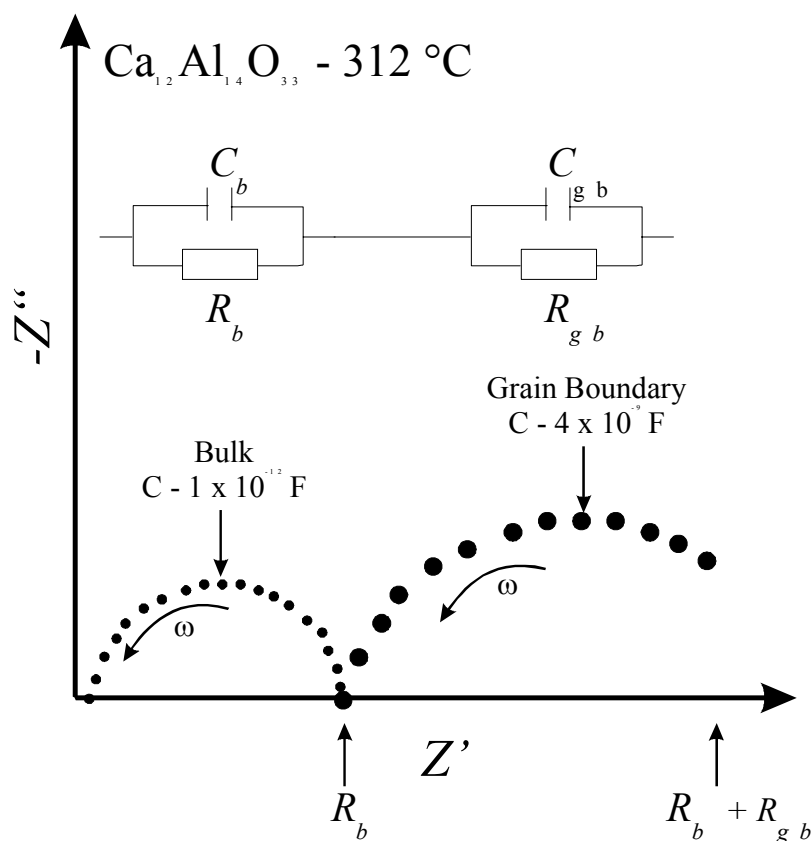


Fig. (2.4.7) Impedance data for $\text{Ca}_{12}\text{Al}_{14}\text{O}_{33}$ presented in complex plane format [55]

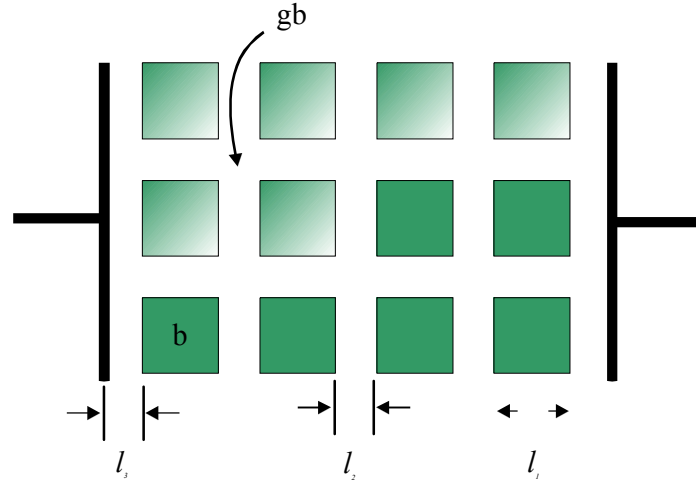


Fig. (2.4.8) “Brickwork” model of grain (bulk) [b] and grain boundary [gb] regions in a ceramic placed between two metal electrodes ^[55]

The “brickwork” model shown in Fig. (2.4.8) represents a ceramic compound of cube-shaped grains of dimensions l_1 , separated from each other by a boundary of thickness l_2 , for this idealised case the equation below holds true:

$$\frac{C_b}{C_{gb}} = \frac{l_2}{l_1} \quad \text{Equ. [2.4.52]}$$

This arises from the inverse relation between thickness and capacitance given in Equ. [2.4.50]. However except for the very densest of materials, polycrystalline samples always showed anomalous frequency dispersion. The circuit element now often known as the *constant phase element* (CPE) is introduced to fit the data:

$$Y_{CPE}^* = A(j\omega)^\alpha \quad \text{Equ. [2.4.53]}$$

The result of such effects is usually a curved complex plane plot, approaching the straight vertical line at higher frequencies. A less trivial deviation may be caused by diffusion-controlled adsorption of species present at a low concentrations. At solid electrodes interfering effects especially contamination and surface roughness are likely to be present ^[66], but apart from these mentioned unhelpful aspects a more marked behaviour has frequently been observed and reported ^{[56] [66 - 68]}: instead of a vertical line the complex impedance diagram exhibits a straight line intersecting the Z' – axis at $R = 0$ at an angle smaller than 90° as seen in Fig. (2.4.9).

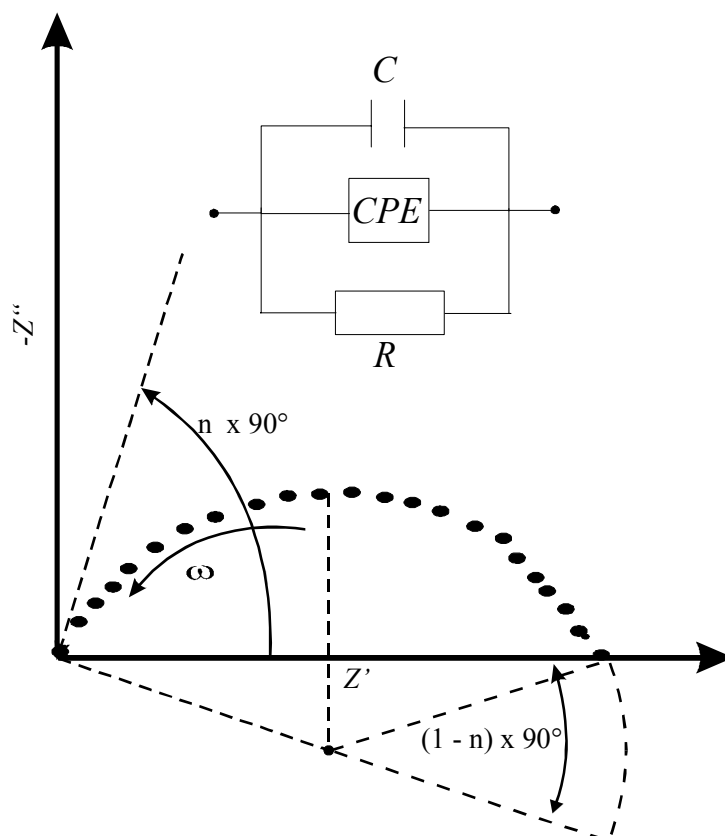


Fig. (2.4.9) Schematic diagram of rotated impedance spectrum and equivalent circuit which describes the electrical response of polycrystalline solid electrolyte.

In other words, the electrode impedance consists of a resistance R in series with complex impedance Z_{CPE} with the special property that its phase angle is independent of frequency. This phenomenon of the constant phase angle gives reason to designate Z_{CPE} constant phase element CPE in Fig. (2.4.9). The CPE is a non-intuitive circuit element that was “invented” while examining the response of real systems in the real world. In some systems, where the complex plane plot was expected to be a semi-circle with the centre on the x – axis, the observed plot was an elongated arc of a circle, but with the centre some distance below the x - axis i.e. complex resistance x - axis. These depressed semi-circles have been explained by a number of phenomena depending on the nature of the system investigated. The common thread among these explanations is that some property of the system is not homogenous or that there is some dispersion of the value of some physical property of the system under investigation. It is also often proposed that the CPE originates from the distribution in current density along the electrode surface because of surface inhomogeneity. This can be inferred from analogy with the behaviour of porous electrodes ^[67]. Mathematically, a CPE’s impedance is given by ^[69]:

$$\frac{1}{Z} = Y_{CPE}^* = A(j\omega)^{-n} \quad \text{Equ. [2.4.54]}$$

$$0 \leq n \leq 1$$

where A is the admittance $(1/|Z|)$ at $\omega = 1 \text{ rad s}^{-1}$. A consequence of this simple equation is that the phase angle of the CPE impedance is independent of the frequency and has a value of $-(90^\circ n)$ degrees. When $n = 1$, it is the same as that for the impedance of a capacitor:

$$\frac{1}{Z} = Y = j\omega A = j\omega C \quad \text{Equ. [2.4.55]}$$

When n is close to 1, then the CPE resembles a capacitor, in reality the phase angle rarely 90° but somewhat less than 90° as one sees in Fig. (2.4.9) at all frequencies. The factor n reflects the degree inhomogeneity within the system under investigation.

2.4.4.

EIS - Physical Models for Equivalent Circuit Elements:

A detailed physicochemical model of all processes that might occur for investigations of potential electrolyte materials is required. In attempting to model the behaviours of an electrochemical system, the model, which may be helpful to a materials scientist in fabrication of new solid electrolytes, but may provide little assistance to an engineer attempting to design a portable power source, which meets rigid cost and performance specifications ^[54]. The development of a proper model requires knowledge of the chemistry and physics of the system under investigation through complementary prior information about the system by means of a good understanding of the characteristics of the measured values with respect to the application of other analytical methods. These issues will be further developed in section {3.1.4}.

At the most fundamental levels of description are atomistic or microscopic models, which attempt to provide an accurate description of the motions of individual charge carrying particles in the system. According to Macdonald ^[54], at the least detailed level are the equivalent circuit models, in which hypothetical electrical circuits, consisting of elements with well-defined electrical properties are utilised to describe the response of the system to a range of possible signals. Such models are of special interest in impedance spectroscopy, since the frequency response behaviour of linear electrical circuits is now extremely well understood ^{[54] [56] [70]}. The modelling of various systems under investigation; may be classified into two forms according to Lasia ^[57]:

- (1) Physicochemical processes or structural modelling
- (2) Measuring, formal or mathematical modelling.

Process modelling links measured impedances with physicochemical parameters of the process (kinetics parameters, concentrations, diffusion coefficients, sample geometry, etc.) Measurement modelling explains the experimental impedances in terms of mathematical functions in order to obtain a good fit between the calculated and experimental impedances. In the later, the parameters obtained do not necessarily have a clear physicochemical significance.

The physical interpretation of the distributed elements in an equivalent circuit is somewhat more elusive. However, they are essential in understanding and interpreting most impedance spectra. There are two types of distributions to consider. The first is associated directly with non-local processes, such as diffusion, which can occur even in completely homogeneous material, one whose physical properties such as charge mobilities, are the same everywhere. The other type which has already been fully discussed in the previous section {2.4.3.3.} is the CPE because of microscopic material properties are themselves often distributed. In order to interpret such behaviours an equivalent circuit is chosen and a fitted to the experimental data, which is performed using complex non-linear least squares technique. When utilising such a technique it is often the case that the data may be presented in a number of different equivalent circuit forms. In taking an example by Lasia ^[57]; a system containing one capacitive loop as seen in Fig. (2.4.10) may be described by either of two equivalent circuit forms as seen in Fig. (2.4.10a-b) respectively. The admittance may be written in the general form:

$$Y = \frac{a_1 j\omega + a_0}{j\omega + b_0} = a_1 + \frac{a_0 - a_1 b_0}{j\omega + b_0} \quad \text{Equ. [2.4.56]}$$

where:

$$a_1 = R_1^{-1}, \quad a_0 = \frac{1}{C_2 R_1 R_2} \quad \text{and} \quad b_0 = \frac{(R_1^{-1} + R_2^{-1})}{C_2} \quad \text{which represents circuit [a]:}$$

$$\text{or :} \quad \text{Equ. [2.4.57]}$$

$$a_1 = R_1^{-1} + R_2^{-1}, \quad a_0 = \frac{1}{C_2 R_1 R_2} \quad \text{and} \quad b_0 = \frac{1}{R_1 C_2} \quad \text{which represents circuit [b]:}$$

where these two formats are indistinguishable. Similarly, the three circuits in Fig. (2.4.11a-c) may adequately describe a system displaying two capacitance loops and their admittance can be written as:

$$Y = \frac{a_2 (j\omega)^2 + a_1 j\omega + a_0}{(j\omega)^2 + b_1 j\omega + b_0} \quad \text{Equ. [2.4.58]}$$

As in the one capacitance loop, these three circuits are also indistinguishable; that is for a proper choice of parameters, they display the same impedance spectrum at all frequencies. The circuit forms most often used in measurement modelling are the, Ladder, Voigt, and Maxwell circuits as seen in Fig. (2.3.11).

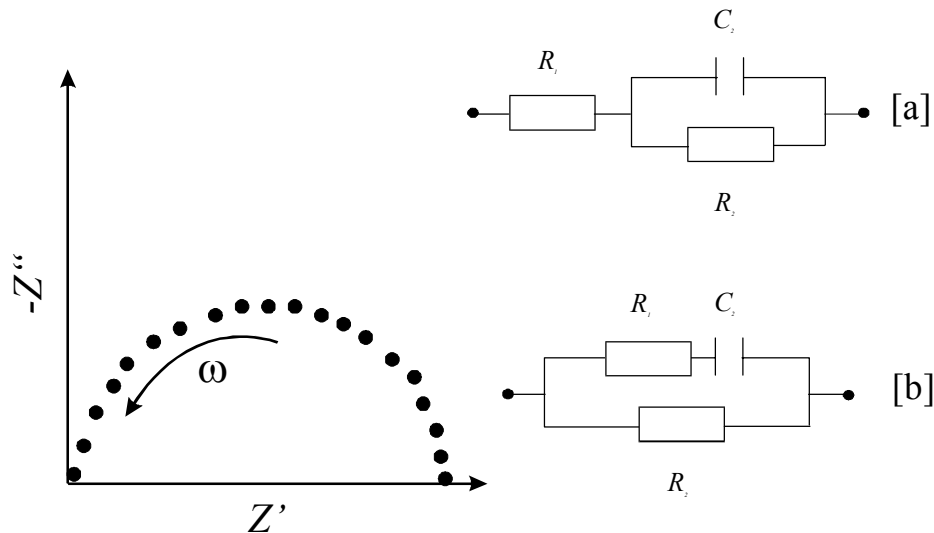


Fig. (2.4.10) System containing one capacitance loop; with alternative circuits for the impedance behavior.

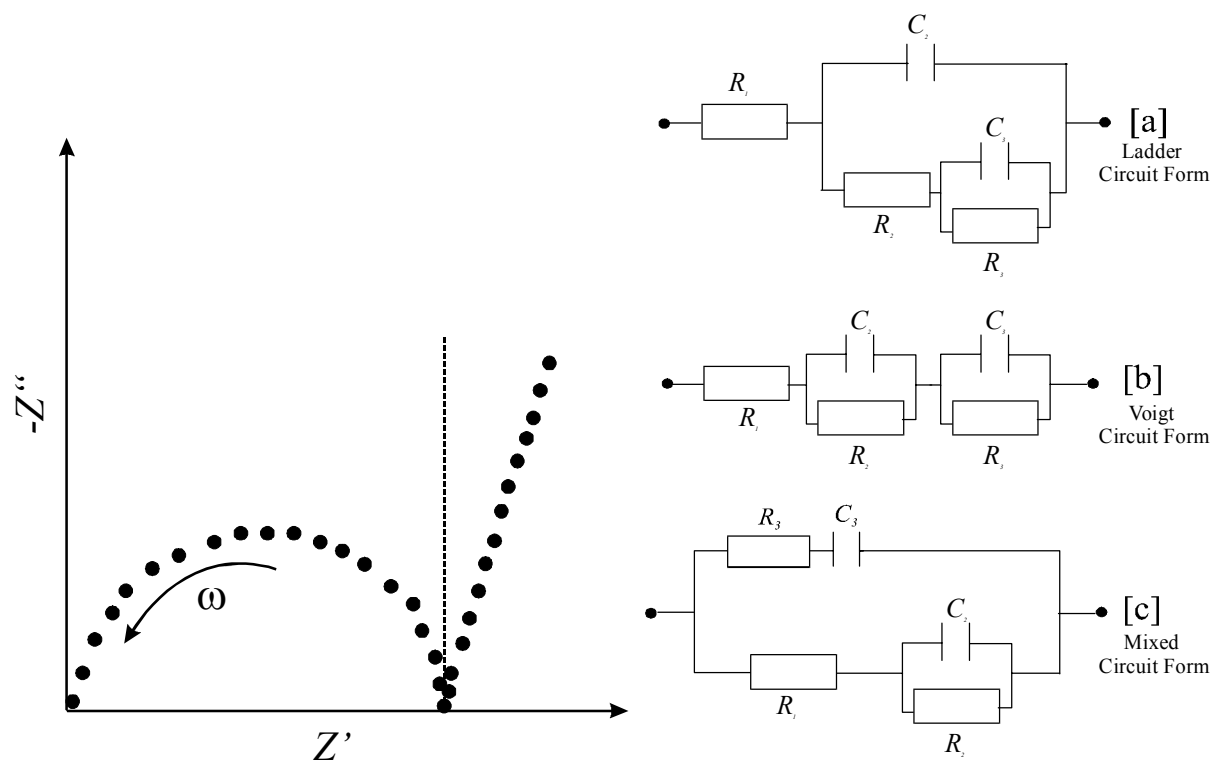


Fig. (2.4.11) System containing two capacitance loop; with alternative circuits for the impedance behavior

2.4.4.1.

Methodology of Equivalent Circuit Modelling:

After validated data is obtained, one can proceed with modelling. In order to achieve this aim, a *complex non-linear least squares* (CNLS) programme is utilised as mentioned in the previous section. This is usually a non-linear fit least square fit of the real and imaginary parts, or the magnitude and phase angle of the experimental impedance and admittance to a given model ^[57]:

$$S = \sum_{i=1}^N \left\{ w_i' [Z_i' - Z_{i,calc.}']^2 + w_i'' [Z_i'' - Z_{i,calc.}'']^2 \right\} \quad \text{Equ. [2.4.59]}$$

must be minimised, where Z_i' and Z_i'' are the real and imaginary parts of the experimental impedances at the given frequencies ω_i , $Z_{i,calc.}'$ and $Z_{i,calc.}''$ are the values calculated from a given model; w_i' and w_i'' are the statistical weights of the data; and the summation runs over all N experimentally used frequencies. The minimisation is often carried out using the Marquadt-Levenberg algorithm ^[57]. In addition to comparing the sum of the squares, the experimental and simulated data should be compared by using complex Bode plots. The phase angle Bode plot is particularly sensitive in detecting time constants.

Macdonald ^[54] ^[61] and the software supplied by Scribner Associates studied precision of parameters determined by EIS. Macdonald added noise to the simulated impedance data and used the CNLS technique to determine the parameters and their standard deviations. By using this technique, it was possible to determine how the impedance errors are transferred to the determined parameters, depending on their relative values. This method allows sensitivity of the parameters to the random errors to be determined. During the progress of this work, the author utilised the Scribner Associates Inc. software Zplot™ supplied with the Solartron impedance instrument for the data acquisition and analysis. It is based on Macdonald's algorithm ^[54] ^[61] and the data analysis has been simplified. It uses a number of predefined and flexible circuits. Further discussions and details to the application of this software can be read in section {3.1.3}.

2.4.4.2.

Practical Application of Equivalent Circuit Modelling in this Work:

Up to this point, the author has discussed the theoretical background to circuit modelling and has justified the application of equivalent circuits. The objective of this work is to extend the use of the measurement circuit models to poly(siloxane) systems and ionic liquid systems. Of course, the practical difficulties of this technique lie in the choice of an appropriate equivalent circuit and the fitting procedure. The development of such models for the impedance response of the aforementioned systems. EIS investigations and applied equivalent circuits of polymer systems are well documented due to their relative simplicity by nature. In the discussions, we noted earlier that Macdonald based much of his impedance proposals on the distribution of activation energies^{[54] [61] [72]}. The author Lukcas^[73] presented interpretations in terms of surface inhomogeneities and the author Nahir^[74], who addressed a similar issue by utilising distributed rate constants or CPE.

In reference to ionic liquids, which are relatively new with respect to detailed EIS investigations, literature is scarce concerning focused EIS investigations utilising equivalent circuits modelling. Recent literature investigations by the author turned up very little information concerning the application of equivalent circuit's methodology to map the ionic transport mechanisms of ionic liquid systems and in particular multiphase systems that form the basis of this work. Chia^[75] studied short-chained ionic liquids embedded in a polymeric matrix that exhibited lamella structures. Chia^[75] briefly discussed the application of equivalent circuit within the presented system and suggested a number of possibilities concerning the appreciation of self-organising materials. Beyond a few feeble attempts to discuss ionic transport within ionic liquids by means of impedance output data alone further investigations are wanted. There has been to date no comprehensive analysis of ionic transport properties in ionic liquids by means of the proposed equivalent circuit's method.

The author will employ in the work the equivalent circuits used to model the impedance of ionically conducting polymers systems and the procedure for the impedance analysis of these systems will account for the deviation from the ideal behaviour model. Ferloni^[76] proposed that the impedance data of ionically conducting polymers could be analysed based on the equivalent circuit seen in Fig. (2.4.12). The presented circuit is a Randles modified circuit, where R_T is the sum of the electrolytic resistance of the polymer electronical resistance, C_T is the double layer capacitance of the polymer electrolyte

interphase, R_{CT} is the charge transfers resistance and finally Z_W is the Warburg element. The Warburg element as previously discussed in section {2.4.3.1} was developed by Warburg to describe an infinite diffusion process in a homogenous system with a reflective boundary. According to Ferloni ^[76] the presented equivalent circuit in Fig. (2.4.12) is for “a homogenous film of intercalation materials in which lithium injection and diffusion occur”. This method was successfully utilised to analyse the impedance response of redox polymers.

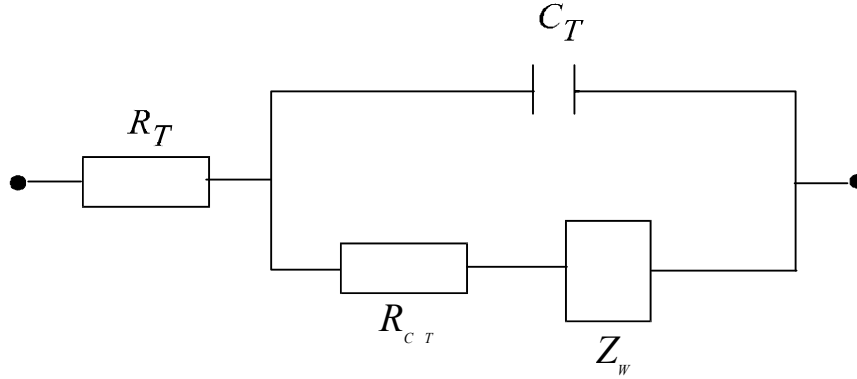


Fig. (2.4.12) Randles modified equivalent circuit model ^[76]

During the initial stages of EIS investigations of the presented materials, preliminary tests with equivalent circuit models using Warburg elements proved inadequate when applied to ionic liquid systems. The Warburg element did not generally depict real systems accurately. This circumstance is mainly attributable to ionic liquid systems, as the scale of the ion diffusion differs from that of the charge transfer. In addition, the energy dissipation processes is less than 45° of the angled Warburg from the straight line and the pseudocapacitance straight line towards the real axis (section {2.4.3.}). Therefore, in the real systems, as those under investigation and in particular ionic liquid systems, the components of the real systems are analysed by breaking down the Warburg element Z_W element into sub-circuits containing only resistance, capacitance, and Warburg elements i.e. Ladder and Voigt equivalent circuit models (section {2.4.4}). It is possible to take into account the deviation from the ideal behaviour utilising the Constant Phase Element (CPE) seen in section {2.4.4} and defined by the equation [2.4.54] previously:

$$\frac{1}{Z} = Y_{CPE}^* = A(j\omega)^{-n} \quad \text{Equ. [2.4.54]}$$

$$0 \leq n \leq 1$$

These investigation demanded separate analysis of the high and low frequency impedance data plots, which were later combined and fitted. The above-described procedure provides a commendable fitting method to the experimental data, which will be discussed in more detail in section {6}. Because ionic liquids systems are of a complex nature, compared to most other systems, their multiphase transitions will require special attention. Therefore, variations of Randles and Voigt circuits are employed to better fit the appropriate phase present.

2.4.5.

EIS - Advantage & Limitations:

EIS has become over the last two decades an indispensable tool in materials research and development because it involves a relatively simple electrical measurement that can be automated. The results from this measurement technique may often be correlated with many complex variables as already discussed in detail by the author i.e. mass transport, rates of chemical reactions, corrosion, dielectric properties, defects, microstructure, and compositional influences. It is an extremely useful technique in the area of quality control where it can contribute to the interpretation of fundamental electrochemical and electronic processes. The figure (2.4.12) summaries the methodology of the typical characterisation procedure using EIS.

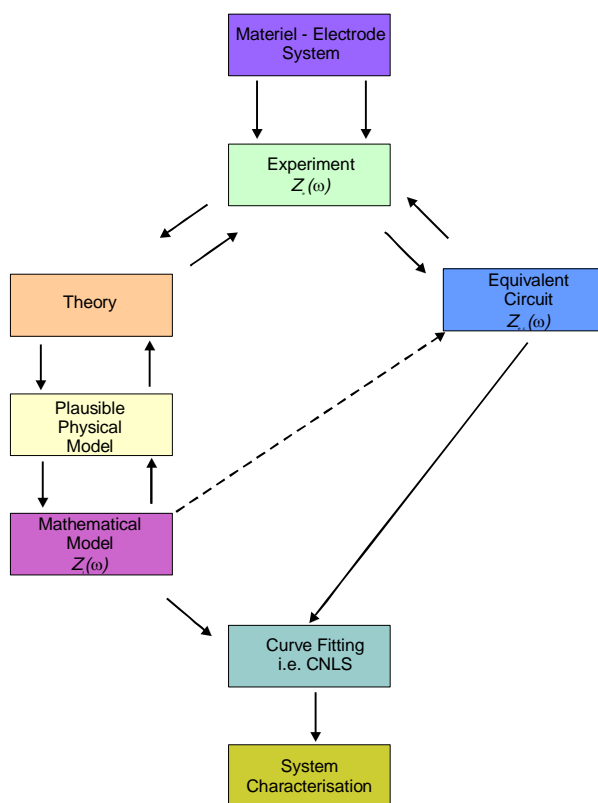


Fig. (2.4.12) Flow diagram of the methodology and characterisation of a typical material-electrode system.

As one sees, experimentally obtained impedance data for a given electrode materials system may be analysed by using an exact mathematical model based on a plausible physical theory that predicts theoretical impedance $Z_t(\omega)$ or by a relatively empirical equivalent circuit whose impedance predictions may be denoted by $Z_{ec}(\omega)$. In either the cases of the relatively empirical equivalent circuit or of the exact mathematical model, the parameters can be estimated and the experimental $Z_e(\omega)$ data compared to either the predicted equivalent circuit impedance $Z_{ec}(\omega)$ or the theoretical impedance $Z_t(\omega)$. Such fitting is accurately accomplished by the CNLS method as already discussed in detail in section {2.4.4.1}.

The disadvantages of EIS are primarily associated with possible ambiguities in interpretation. An important complication of analyses based on equivalent circuits is that ordinary ideal circuit elements represent ideal combined constant properties i.e. Warburg, CPE. Inevitably, all electrolytic cells are distributed in space and their microscopic properties may be inadequately distributed. Under these conditions, ideal circuit elements may be inadequate to describe the electrical response. There is a further problem with equivalent circuit's analysis, not shared by direct comparison with $Z_t(\omega)$ of theoretical model: Often specific equivalent circuits involving three or more circuit elements can often be rearranged in

various ways and still yield the same $Z_{ec}(\omega)$ for all ω . For the different interconnections the values of the elements will have to be different to yield the same $Z_{ec}(\omega)$ for all ω but an essential ambiguity is present. An approach to its solution can only be made by employing physical intuition and carrying out several $Z_e(\omega)$ sets of measurements under different conditions.

2.5. Thermal Analysis (TA):

Foreword:

Thermal analysis, involves the measurement of certain physical and chemical properties as a function of temperature ^[77]. Applications of thermal analysis in electrochemistry are many and varied and include the study of reactions, phase transitions and the determination of phase diagrams. Most solids are “thermally active” ^[77] ^[78] in one way or another and may be profitably studied by means of thermal analysis. The main techniques are thermogravimetry (TG), which records the mass of a sample as a function of temperature or time, and differential thermal analysis (DTA), which measures the difference of temperature, ΔT between a sample and an inert reference material as a function of temperature i.e. DTA therefore detects changes in heat content. A closely related technique is differential scanning calorimetry (DSC). In DSC, the equipment is designed to allow a quantitative measure of the enthalpy changes that occur. During the progress of this work, the author utilised two main techniques to study the thermal and physical behaviours of the materials under investigation.

2.5.1.

Thermal Analysis - (DTA) & (DSC):

In DTA, the temperature of a sample is compared with that of an inert reference material during a programmed change of temperature. The temperatures should be the same until some thermal event, such as melting, decomposition or change in the “crystal” structure, occurs, in which case the sample temperature either lags behind (if the change is endothermic) or leads (if the change is exothermic) the reference temperature. The reason for having both sample and reference is shown in Fig. (2.5.1). In figure (2.5.1a) a sample is shown heating at a constant rate; its T_s monitored with a thermocouple, varies linearly with time as seen in Fig. (2.5.1.b) until the endothermic event occurs, e.g. melting at temperature T_c . The sample temperature remains constant at T_c until the event is completed; the T_c increases rapidly to catch up with the temperature required by the user. The thermal event in the sample at T_c therefore appears as a rather broad deviation from the sloping baseline as seen in Fig. (2.5.1b). Such a plot is insensitive to small heat effects. Furthermore, any spurious variations in the baseline, caused for example by fluctuations in the heating rate, would appear as apparent thermal events. Because of the insensitivity of this technique; it has limited applications, its main use historically has been in method of cooling curves which was used to

determine phase diagrams the sample temperature was recorded on cooling rather than on heating and since heat effects associated with solidification and crystallisation are usually large, they could be detected by this method.

The figure (2.5.1c) shows the arrangement used in DTA. Sample and reference are placed side by side on a heating block, which is heated or cooled at a constant rate; identical thermocouples are placed at each and are connected back to back. When the sample and reference are at the same temperature, the net output of this pair of the thermocouples is zero. When a thermal event occurs in the sample, a temperature difference, ΔT exists between sample and reference, which is detected by the net voltage of thermocouples. A third thermocouple is used to monitor the temperature of the heating block and the results are presented as ΔT against temperature as seen in Fig. (2.5.1d). A horizontal baseline corresponding to $\Delta T = 0$, occurs and superimposed on this is a sharp peak due to the thermal event in the sample. The temperature of the peak is taken wheather as the temperature at which deviation form the baseline begins, T_1 or as the peak temperature T_2 . While it is probably more correct to use T_1 , it is often not clear where the peak begins and therefore, it is more common to use T_2 . The size of the peak g to ΔT peak may be amplified so that the events with very small enthalpy changes may be detected.

The technique DSC is very similar to DTA. A sample and an inert reference sample are also used but the cell design is different. In some DSC, cells the sample and reference sample are maintained at the same temperature during heating and the extra heat input to the sample (or reference if the sample undergoes an exothermic change) required in order to maintain this balance is measured. Enthalpy changes are therefore measured directly. In other DSC cells, the difference in temperature between the reference is measured, similar in DTA.

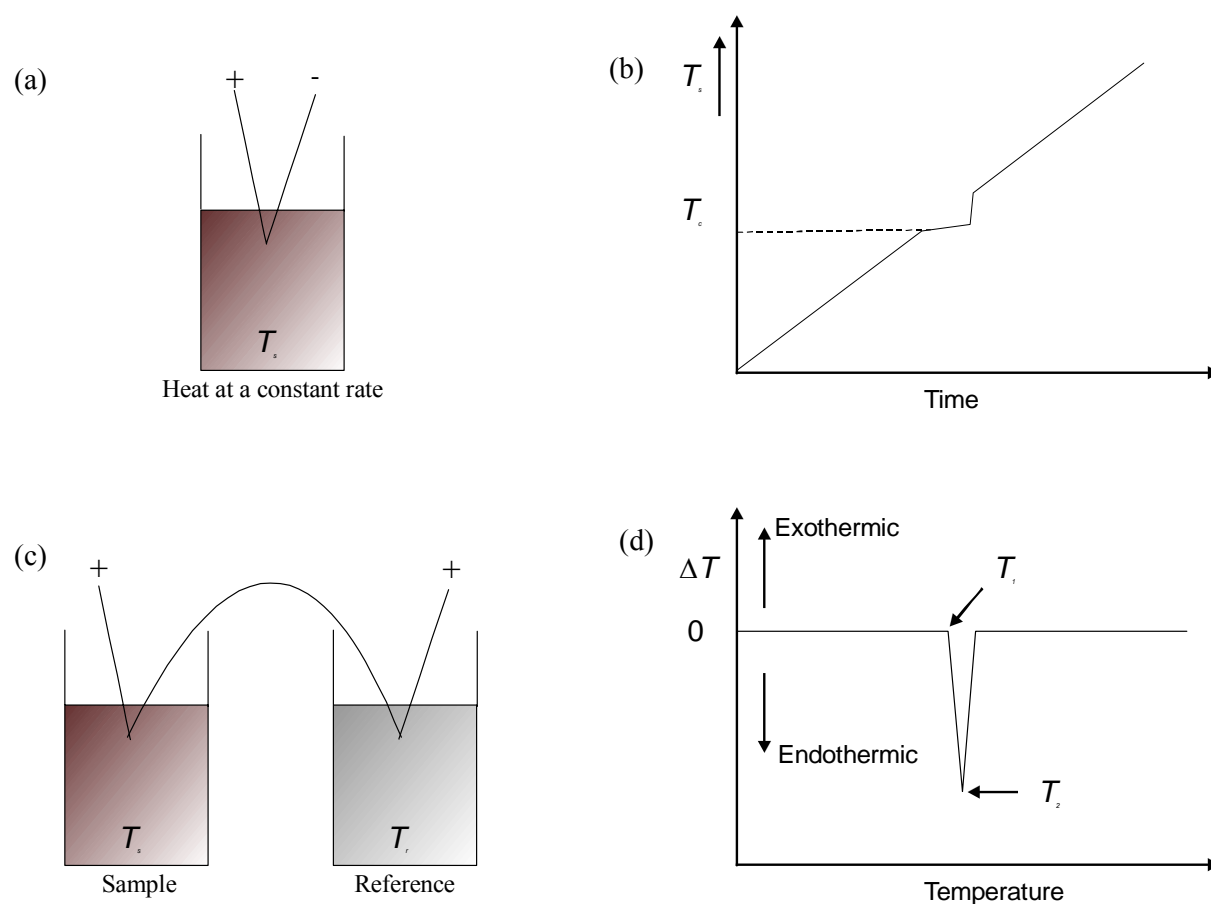
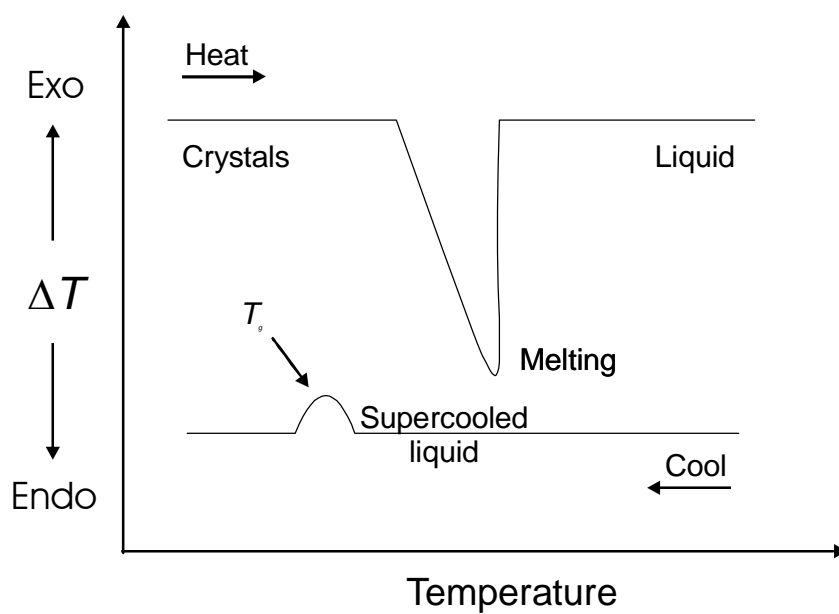


Fig. (2.5.1) DTA & DSC techniques

Fig. (2.5.2) Schematic of DTA curves showing melting of crystal on heating and a large hysteresis on cooling which gives T_g

2.5.2.

TA – Applications:

An important use of DTA and DSC in glass, polymer, and liquid crystal science is the measure of the glass transition temperature T_g .^{[11] [79 – 82]} This appears as a broad anomaly in the baseline of the DTA curve, as seen in Fig. (2.5.2); the T_g value represents the temperature at which the glass of polymer transforms from a rigid solid super-cooled, to a very viscous liquid. The T_g represents the upper temperature limit at which the material under investigation can be used and also provides a readily measurable parameter for studying such aforementioned materials. For glasses and other materials, which are kinetically very stable, such as silica glasses, the glass transition is only a small thermal event observed in DTA since crystallisation it usually very slow in occurring^[77]. For glasses, however crystallisation or devitrification may occur at some temperature above T_g and below the melting point T_m . Devitrification appears as an exotherm and is followed by an endotherm at higher temperature that corresponds to melting of these same crystals. DTA and DSC are both powerful techniques for the determination of phase diagrams, especially in conjunction with other techniques such as impedance spectroscopy. Both techniques are particularly useful during studies of ion mixtures and substitution reactions; in order to study new behaviours of the substituted materials.

References:

1. P. W. Atkins, The Elements of Physical Chemistry, No. p. 495, Oxford University Press, Oxford, (1996).
2. F. M. Gray, Solid Polymer Electrolytes – Fundamentals and Technological Applications, VCH Publishers Inc, (1991).
3. S. Hawking, *Das Universum in der Nußschale*, dtv, (2001).
4. P. Deybe, *Physicalische Zeitschrift*, **13**, 97 (1912).
5. J. O'M Bockris, K. Amulya and N. Reddy, Section: Ion-Ion Interactions, in *Modern Electrochemistry*, **1**, 225-293 (1998).
6. W. Kunz, J. M. G. Barthel and H. Krienke, Section: Ion Association and Solvation in Electrolyte Solutions, in *Modern Aspects Physical Chemistry of Electrolyte Solutions*, **5**, 3-57 (1998).
7. H. Yamakawa, Modern Theory of Polymer Solutions, No. p. 419, Harper & Row, San Francisco, (1971).
8. K. H. Lee, K. H. Kim and H. S. Lim, *J. Electrochem. Soc.*, **148**, A1148 (2001).
9. A. Killis, J. F. Le Nest, H. Cheradame and A. Gandini, *Macromolecules*, **183**, 2835 (1982).
10. L. M. Torell and C. A. Angell, *Br. Polym. J.*, **20**, 173 (1988).
11. C. T. Imrie, M. D. Ingram and G. S. McHattie, *J. Phys. Chem. B*, **103**, 4132 (1999).
12. C. A. Angell, *Solid State Ionics*, **9-10**, 3 (1983).
13. J. Evans, C. A. Vincent and P. G. Bruce, *Polymer*, **28**, 2324 (1987).
14. K. Jinqing, X. u. Qin and C. Ke, *J. Chem. Educ.*, **78**, 937 (2001).
15. P. G. Bruce and C. A. Vincent, *Faraday Discuss. Chem. Soc.*, **88**, 43 (1989).
16. H. Dai and T. A. Zawodzinski, Jr., *J. Electrochem. Soc.*, **143**, L107 (1996).
17. G. G. Cameron and M. D. Ingram, Section: Liquid Polymer Electrolytes, *Polymer Electrolyte Reviews* (2), 168-190 (1989).
18. E. Strauss, D. Golodnitsky, G. Ardel and E. Peled, *Electrochim. Acta.*, **43**, 1315 (1998).
19. M. M. Doeff, P. Georen, J. Qiao, J. Kerr and L. C. De Jonghe, *J. Electrochem. Soc.*, **146**, 2024 (1999).
20. R. A. M. Hikmet and M. P. J. Peeters, *Solid State Ionics*, **126**, 25 (1999).
21. H. Every, A. G. Bishop, M. Forsyth and D. R. MacFarlane, *Electrochim. Acta.*, **45**, 1279 (2000).
22. G. G. Cameron, J. L. Harvie and M. D. Ingram, *Solid State Ionics*, **34**, 65 (1989).
23. J. J. Xu and G. C. Farrington, *J. Electrochem. Soc.*, **145**, 744 (1998).
24. M. G. McLin and C. A. Angell, *J. Phys. Chem.*, **100**, 1181 (1996).
25. J. A. Manzanares and K. Kontturi, Section: Diffusion and Migration, in *Encyclopaedia of Electrochemistry - Interfacial Kinetics and Mass Transport*, 2, 81-122, Ed. Calvo, E.J., Bard-Stratmann, (2003).
26. J. Evans, C. A. Vincent and P. G. Bruce, *Polymer*, **28**, 2324 (1987).
27. P. G. Bruce and C. A. Vincent, *J. Electroanal. Chem. Interfacial Electrochem.*, **225**, 1 (1987).
28. P. G. Bruce, M. T. Hardgrave and C. A. Vincent, *J. Electroanal. Chem. Interfacial Electrochem.*, **271**, 27 (1989).
29. P. G. Bruce, Section: Polymer Electrolytes II, *Chemistry of Solid State Materials - Solid State Electrochemistry*, 5, 141-163, Ed. Bruce, P.G., Cambridge University Press, (1997).
30. C. A. Angell, C. T. Imrie and M. D. Ingram, *Polym. Int.*, **47**, 9 (1998).
31. C. T. Imrie and M. D. Ingram, *Electrochim. Acta*, **46**, 1413 (2001).
32. J. Newman, *Journal of the Electrochemical Society*, **113**, 501 (1966).
33. Y. Zheng, F. Chia, G. Ungar, T. H. Richardson and P. V. Wright, *Electrochim. Acta*, **46**, 1397 (2001).
34. C. A. Vincent, *Polym. Prepr. (Am. Chem. Soc., Div. Polym. Chem.)*, **30**, 422 (1989).
35. K. A. Striebel, S. J. Wen, D. I. Ghantous and E. J. Cairns, *J. Electrochem. Soc.*, **144**, 1680 (1997).
36. P. G. Bruce, M. T. Hardgrave and C. A. Vincent, *Solid State Ionics*, **53-56**, 1087 (1992).
37. P. G. Bruce and C. A. Vincent, *J. Chem. Soc., Faraday Trans.*, **89**, 3187 (1993).
38. G. G. Cameron, J. L. Harvie, M. D. Ingram and G. A. Sorrie, *Br. Polym. J.*, **20**, 199 (1988).
39. C. A. Angell and R. D. Bressel, *J. Phys. Chem.*, **76**, 3244 (1972).
40. W. Kauzmann, *Chemical Reviews*, **43**, 219 (1948).
41. C. A. Angell, *J. Non-Cryst. Solids*, **131-133**, 13 (1991).
42. C. A. Angell and J. C. Tucker, *The Journal of Physical Chemistry*, **78**, 278 (1974).

43. G. Adam and J. H. Gibbs, *J. Chem. Phys.*, **43**, 139 (1965).
44. C. A. Angell, *J. Chem. Phys.*, **46**, 4673 (1967).
45. H. Vogel, *Phys. Z.*, **22**, 645 (1921).
46. G. S. Fulcher, *Journal of the American Ceramic Society*, **8**, 339 (1925).
47. G. Tamann and W. Hesse, *Z. Anorg. All. Chem.*, **156**, 245 (1926).
48. C. A. Angell and J. C. Tucker, *J. Phys. Chem.*, **84**, 268 (1980).
49. S. Y. Choi and Y. C. Bae, *Polymer*, **44**, 3753 (2003).
50. C. A. Angell, *Tech. Rep. - Purdue Univ. Water Resour. Res. Cent.*, **75**, 15 (1976).
51. S. Schantz and L. M. Torell, Section: Light Scattering in Polymer Electrolytes, *Polymer Electrolyte Reviews* (2), 1-42 (1989).
52. J. Barthel, R. Gerber and H. J. Gores, *Ber. Bunsen-Ges. Phys. Chem.*, **88**, 616 (1984).
53. P. C. Trulove and R. A. Mantz, Section: Electrochemical Properties of Ionic Liquids, *Ionic Liquids in Synthesis*, 109-123 (2003).
54. J. R. Macdonald, *Impedance Spectroscopy*, No. p. 344 (1987).
55. J. T. Irvine, D. C. Sinclair and A. R. West, *Materials Chemistry*, **2**, 132 (1990).
56. A. J. Bard and L. R. Faulkner, Section: Techniques Based on Concepts of Impedance, in *Electrochemical Methods: Fundamentals and Applications*, 368-389, Ed. anonymous, Wiley, (2003).
57. A. Lasia, Section: Electrochemical Impedance Spectroscopy and its Applications, *Modern Aspects of Electrochemistry*, 32, 143-242, Ed. Conway, B.E. et al., Plenum Press, New York, (1979).
58. C. Doetsch, *Laplace Transformation*, Dover, (1953).
59. J. Ye and K. Doblhofer, *Journal of Electroanalytical Chemistry*, **272**, 29 (1989).
60. I. H. Gascha, *Taschenbuch: Mathematik Formeln, Regeln & Merksätze*, No. p. 447, Tratwein, (2003).
61. J. R. Macdonald, *The Journal of Chemical Physics*, **61**, 3977 (1974).
62. S. Cole and R. H. Cole, *Journal of Chemical Physics*, **9**, 341 (1941).
63. P. H. Smith, *Electronics*, **17**, 318 (1944).
64. S. Krause, Section: Impedance Spectroscopy, *Encyclopaedia of Electrochemistry - Instrumentation and Electroanalytical Chemistry*, **3**, 1996-229 (2003).
65. Y. Y. Tong, E. Oldfield and A. Wieckowski, Section: NMR Spectroscopy in Electrochemistry, *Encyclopaedia of Electrochemistry - Interfacial Kinetics and Mass Transport*, **2**, 147-169, Ed. Calvo, E.J., Bard-Stratmann, (2003).
66. X. Qian, N. Gu, Z. Cheng, X. Yang, E. Wang and S. Dong, *Journal of Solid State Electrochemistry*, **6**, 8 (2001).
67. G. J. Brug, A. L. G. Van Den Feden, M. Sluyters-Rehbach and J. H. Sluyters, *Journal of Electroanalytical Chemistry*, **176**, 275 (1984).
68. B. M. Quinn, Z. Ding, R. Moulton and A. J. Bard, *Novel Electrochemical Studies of Ionic Liquids*, (2002).
69. anonymous, www.comulsr.com/resources/eis/cpe1.htm, (2002).
70. X. Wu, H. Ma, S. Chen, Z. Xu and A. Sui, *Journal of the Electrochemical Society*, **146**, 1847 (1999).
71. K. Hoffmann, *Imidazole and Its Derivatives Part 1*, **1**, No. p. 445, Interscience, (1953).
72. D. D. Macdonald and M. C. McKubre, Section: Impedance Measurements in Electrochemical Systems, in *Modern Aspects of Electrochemistry*, **14**, 61-146, Ed. Conway, B.E. et al., Klumer, (1982).
73. Z. Lukacs, *Journal of Electroanalytical Chemistry*, **464**, 68 (1999).
74. T. Nahir and E. Bowden, *Journal of Electroanalytical Chemistry*, **410**, 9 (1996).
75. F. Chia, Y. Zheng, J. Liu, N. Reeves, G. Ungar and P. V. Wright, *Electrochimica Acta*, **48**, 1939 (2003).
76. P. Ferloni, M. Mastragostino and L. Meneghello, *Electrochimica Acta*, **41**, 27 (1996).
77. A. R. West, *Basic Solid State Chemistry*, No. p. 480, Wiley, (1996).
78. Navrotsky, A., Section: Thermodynamic aspects of inorganic solid-state chemistry, *Solid State Chemistry Techniques*, 362-393, Ed. Cheetham, A.K. & Day, P., Clarendon Press, Oxford, (1987).
79. Y. G. Andreev and P. G. Bruce, *Electrochim. Acta*, **45**, 1417 (2000).
80. T. Ohtake, Y. Takamitsu, K. Ito-Akita, K. Kanie, M. Yoshizawa, T. Mukai, H. Ohno and Kato, Takashi, *Macromolecules.*, **33**, 8109 (2000).
81. C. Liu, E. Sanchez and C. A. Angell, *Chim. Chron.*, **23**, 211 (1994).
82. C. A. Angell and E. J. Sare, *J. Chem. Phys.*, **52**, 1058 (1970).

Chapter 3

Experimental Procedure

3.1. Impedance Spectrometer & Software

3.1.1. Principles of Electrochemical Impedance Spectroscopy (EIS):

Electrochemical Impedance Spectroscopy (EIS) or otherwise known as the *ac* impedance method, studies the systems response to the application of a periodic small-amplitude *ac* signal ^[1]. As was elaborated in the previous section {2.4.}, impedance spectroscopy represents a powerful tool for the investigation of the electrochemical properties of materials and their interfaces to conducting electrodes. The relevant fields of application of this particular method are diverse ^[2 - 7]:

- Kinetics of charges in bulk and/or interfacial regions.
- Charge transfer of ionic or mixed ionic-ionic conductors.
- Semi-conducting electrodes.
- Corrosion inhibition of electrodes processes.
- Investigation of coatings on metal surfaces.
- Characterisation of material; solid electrolyte and solid-state devices.

The *dc* transient response of electrochemical systems is usually measured using a potentiostat. Therefore, the author wishes to entertain the question; what is the ideal potentiostat? The ideal potentiostat should be fast, low noise, and of high input impedance ^[8]. These three requirements rarely go together. Often one must compromise between “high speed” and “high stability”. The measuring techniques for impedance are well known ^[8 - 12] and are very adaptable for the investigation of the electrode kinetics of more complex electrochemical systems. The system impedance may be measured in one of a number of techniques ^[1].

- i. Lissajous curves
- ii. Phase-sensitive detection (PSD)
- iii. *ac* bridges
- iv. Frequency response analysis (FRA)
- v. Fast Fourier transform (FTT)

For the sake of brevity and relevance this author will only discuss the later three techniques listed above.

3.1.1.1. *ac* bridges:

This technique was first utilised to measure double layer parameters and later to measure electrode impedance in the presence of faradic reactions to determine the kinetics of the electrode processes. Although the technique is the foundation of all other electrochemical impedance spectroscopy methods, the technique is very reliable and practical. The main disadvantage of this measuring technique is its slowness, because bridge compensation must be performed for each frequency manually and this is not practical or necessary since the advent of modern digital analysers with multi-task function capabilities.

3.1.1.2. Frequency Response Analysis (FRA):

The frequency response analysers (FRA) are instruments that determine the frequency response of a measured system. In this method the measured signal, U_I , this is proportional to the *ac* current from the potentiostat defined by Equ [3.1.1] ^[1]:

$$U_I = U_{I,a} \sin(\omega t + \varphi_1) \quad \text{Equ. [3.1.1]}$$

where $U_{I,a}$ signal amplitude, φ is the phase shift and is multiplied by the same angular frequency ω . The measured signal defined by Equ. [3.1.1] is multiplied by the sine and cosine of the reference signal of the same frequency and then integrated during one or more wave periods:

$$\text{Re}(U_1) = \frac{1}{T} \int_0^T U_{1,a} \sin(\omega t + \varphi_1) \sin(\omega) dt = \frac{U_{1,a}}{2} \cos(\varphi_1) \quad \text{Equ. [3.1.2]}$$

and

$$\text{Im}(U_1) = \frac{1}{T} \int_0^T U_{1,a} \sin(\omega t + \varphi_1) \cos(\omega) dt = \frac{U_{1,a}}{2} \sin(\varphi_1) \quad \text{Equ. [3.1.3]}$$

Such integration recovers the real and imaginary parts of the measured signal. Modern FRA's perform all computational calculations digitally. They have a wide frequency range and are of high precision.

3.1.1.3.

Fast Fourier Transform (FTT):

The author has already discussed in Section {2.4.} that the system's impedances are defined as the ratio of Laplace transforms from Equ. [2.4.3] of potential and current. In general the transformation parameters is complex, $s = \nu + j\omega$. The imaginary Laplace transform:

$$F(j\omega) = \int_0^{\infty} f(t) e^{-j\omega t} dt \quad \text{Equ. [3.1.4]}$$

is called the singular-sided Fourier transform. Taking the Fourier transform of the perturbation signal and the resulting signal allows determination of the transfer function, for sample system ac impedance to be obtained from:

$$Z(j\omega) = \frac{F[U(t)]}{F[i(t)]} = \frac{U(j\omega)}{i(j\omega)} \quad \text{Equ. [3.1.5]}$$

Where F denotes the Fourier transform. The FFT provides a fast and efficient algorithm for the computation of the Fourier transform. The number of points acquired must be equal to 2^k , where k is an integer. The perturbation of the electrochemical system leads to a shift of the

steady state. The rate to which a new steady state forms is dependent upon the number of investigations performed and in their characteristic parameters such as reaction rate constants; diffusion coefficients; charge transfer resistance; and double layer capacitance ^[13]. A popular perturbation signal and which is utilised by the Solartron instrument in this work is the sum of the sine wave technique. D. E. Smith ^[1] introduced this technique. This signal form, (i.e. perturbation signal) is composed of a sum of selected sinusoids. The applied signal consists of a fundamental harmonic frequency f_0 and a number of odd harmonics $(2n+1)f_0$. This arrangement is superior to other perturbation waveforms such as pulse and noise perturbations. All these frequencies are applied at the same time and the response to each frequency is found by FFT.

The small perturbation of the electrode state has the advantage that the solutions of relevant mathematical equations used are according to Retter ^[13] transferred in limiting forms, which are normally linear. When an electrochemical system is in equilibrium and then experiences a perturbation in the form of a time dependant potential or current; the response of the system is measured. The mathematical and theoretical implications of this perturbation have already been discussed at length in Section {2.4.} ^[11]. The main advantage of the FFT technique is that the information is obtained quickly (instantaneous); therefore, it may be used to study impedance evolving with time. The limitations of FFT techniques are that the response to individual multiple frequencies is usually weaker than that when only one frequency is used.

3.1.1.4.

General points of note for Impedance Measurements

Impedance measurements should be carried out over a wide frequency range in order to identify all time-constants in the circuit. The highest frequency depends on the potentiostat used because it may introduce a phase shift at high frequencies either by means of stray capacitances or inductances from the experimental set-up i.e. cables. A typical range for a modern instrument is 1 mHz – 1 MHz. With an increase in sensitivity, the potential tends to slow down and the response on 10 mA current scale is much faster than that on 10 μ A scale. Much higher frequencies up to 10 MHz are also possible. The lowest frequency typically used is 10^{-3} Hz. This limit is connected with the possible changes in state of the electrode during

long period measurements. However lower and higher impedances, distortions may be observed.

3.1.2.

Gain-Phase Analyser 1260 & Software:

Commercially measuring systems such the Impedance Gain-Phase Analyser 1260¹¹ utilised for this work; uses a microprocessor-controlled digital and analogue technique as seen in Pic. (3.1.1). The author recommends fast Fourier Transformation (FFT) in the low frequency region ($10^{-3} - 10^2$ Hz) because the cycle duration of the highest signal frequency is large in comparison to the conversion time of the precision analogue-to-digital converters (ADC) ^[13]. Digital signal filtering is the sequence that is accommodated to the Solartron Analyser 1260 and is superior to the commonly used analogue filters. The measuring methods for the system response are physically equivalent, but different methods can be suited more or less to the relevant system under investigation. Data processing and analysis is also greatly assisted with the utilisation of software such as (Zview/Zplot^{TM12}) that accompanies the Solartron instrument. Frequency analysis can be carried out over a very wide frequency range ($10^{-3} - 10^7$ Hz) as in the case of the Solartron Analyser 1260:

- Signal sine drive and analysis of the system or component under test over a frequency range of 10 μ Hz to 32 MHz.

Normally, a single frequency signal is used and the amplitude and phase shift of real and imaginary parts of a response signal are measured. The depiction in Fig. (3.1.1.) shows a block diagram of a potentiostatic frequency response analyser. The system generating the signal must be linear over the entire frequency and amplitude scale and the noise amplitude must remain low. The sum of signals at the output of the operations amplifier [A1] seen in Fig. (3.1.1.) is known as the polarisation signal of the electrochemical cell. The amplifier [A2] and together with the cell [A3] form part of the potentiostat. The potential of the reference electrode [RE] seen in Fig. (3.1.1.), is equal to the sum from the best signal measurement signal and the *DC* polarisation.

11 Solartron AnalyticalTM UK : Unit B1 Armstrong Mall Southwood Business Park, Farnborough, Hampshire, GU14 0NR, United Kingdom. – www.solartronanalytical.com

12 Scribner Associates Inc : 150 East Connecticut Avenue, Southern Pines, NC 28387, USA
www.scribner.com

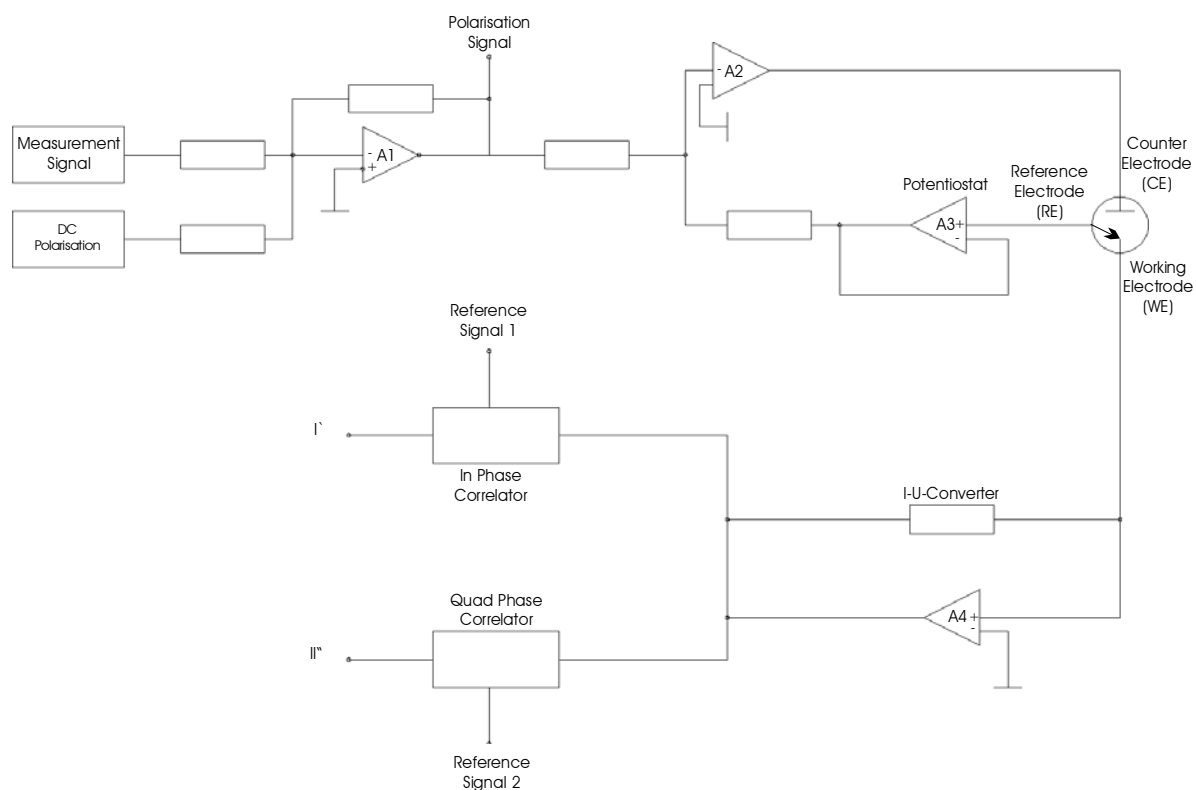


Fig. (3.1.1) Block diagram of potentiostatic frequency response analyser ^[13]

3.1.2.1.

“Parasitic” influences

An important consideration for measuring the impedance behaviours of a material at high frequencies is the influence of “parasitic” ^[13] elements and the phase shift connected with the potentiostatic control of the system. Such parasitic distortions can be often attributed to induction in series with the electrode impedance. This is particularly observed at higher frequencies and leads to large positive imaginary impedances as can be seen in Fig. (3.1.2). Induction usually arises from the connecting cables. Often such effects are minimised by shortening the cables as was carried out by the author and shielding of the reference electrode. In the worst case, the system can oscillate. However, before such an event occurs, more often than not the phase shifts and the variations of the amplitude of the response signals deliver incorrect impedance values. A solution to such a scenario is the employment of a precise dummy cell of known parameters; which will be briefly discussed in the next section {3.1.3}.

Another factor when applying an electrical current to electrodes in solution is an accumulation of ionic species near the electrode and chemical reactions at the interface

surfaces. This may imply the presence of a polarisation resistance at the electrode surface, which may lead to erroneous results, hence may be defined as a parasitic occurrence to the electrolyte resistance. The best method to limit polarisation is of course to apply an alternating current (*ac*) or to adjust the measuring frequency but such a correction is rarely required in modern *ac* impedance. Contamination of the electrode surfaces plays also a major role concerning the clarity of the results and therefore sample preparation and electrode preparation is crucial and will be discussed in section {3.3}. By simply highly polishing the test cells electrodes, before measurements commence such endeavours can lead to major improvement in the quality of the cell response output.

Impedance is only properly defined as a transfer function when the system fulfils the conditions of linearity and stability during measurement. To assess if meaningful data fulfil the above conditions, a range of diagnostic tools and techniques are available to validate impedance data. The problem of non-linearity can generally be overcome by making the amplitude of the perturbation signal small enough to approach quasi-linear conditions. This can be achieved by measuring impedance spectra at different perturbation amplitudes. Depending on the technique used for data acquisition, different methods for data validation can be applied. If sinusoidal signals were applied to non-linear systems, the response function should contain multiples (harmonics) of the excitation signal. Erroneous impedance data cannot only be caused by lack of stability of the system under investigation. The easiest way to establish whether a system has changed during the course of an impedance measurement is to repeat the experiment and compare both sets of data. For most applications, instabilities could and should be eliminated by adjusting the measuring conditions accordingly. A method that does not require extrapolating data frequency ranges not accessible by experiment, is to fit of the data with an equivalent circuit as was discussed in sections {2.4.4.} and will be discussed in section {3.1.5.}.

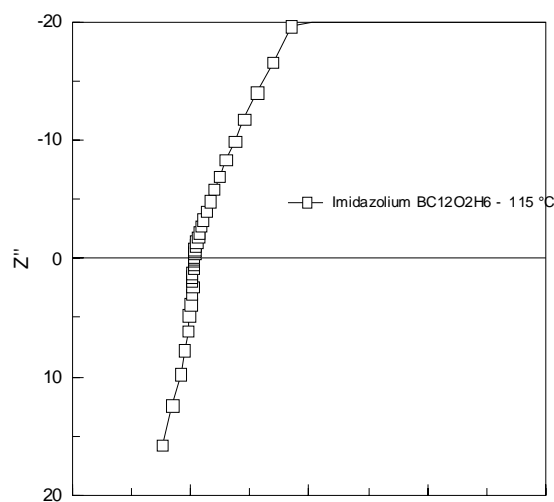


Fig. (3.1.2) Positive imaginary impedances
i.e. lead inductance



Pic. (3.1.1) Impedance Gain – Phase
Analyser 1260 with external
CPU controller.

3.1.3. **Zplot™ & Zview™ for Windows 2000:**

The programmes Zplot™ & Zview™ are two sub-programmes delivered by Solartron that perform the acquisition and analysis respectively of the data generated by the Solartron impedance instrument. Zplot™ & Zview™ is a user-friendly utility that maximises the performance of the Solartron frequency response analysers. The dexterity of this programme can be briefly summarised in the following points; Zplot™ & Zview™ is capable of:

- Performing experiments using any one of eight basic formats including frequency bias and amplitude sweeps while controlling either voltage or current.
- Examination of data through real time display measurements.
- Plot data utilising a wide variety of axi formats.
- Analyse impedance data using curve fitting¹³, linear regression¹⁴ and polarisation resistance functions.
- Simulate and fit data using equivalent circuit models¹⁵.

¹³ See section {2.4.2} Theory

¹⁴ See section {2.4.2} Theory

The aforementioned software permits the representation of the data in many formats. The impedance data is represented in the form of complex plane plots as Z'' vs. Z' which are commonly referred to as Nyquist diagrams, Y'' vs. Y' diagrams and derived quantities such as the modulus function $M = j\omega C_c$, $Z = M'' + jM'$ and the complex dielectric constant $\varepsilon = 1/M = \varepsilon' + j\varepsilon''$ depictions. Frequently used terms by many authors are the complex plane plot of the frequency normalised admittance $1/\omega R_p$ vs. C_p especially for an investigation of non-faradic processes and the Bode plot for the representation of R_s and $1/\omega C_s$ vs. $\log \nu$. It should be noted that the representation form and any mathematical transformation could never improve the quality of the data. The theoretical background to the mentioned data forms have already been discussed in detail in section {2.4.} and the author will not venture further in their discussion.

3.1.4.

Test Module:

The dummy test cell was used to verify the integrity of the impedance instrument and was regularly utilised to calibrate the instrument after extensive use. A schematic of a typical dummy cell can be seen in Fig. (3.1.4a); plus a picture of the dummy cell supplied by Solartron¹⁶ and the in-house constructed dummy cell can be seen in Fig. (3.1.4a) respectively. The figures (3.1.4b) and (3.1.4c) demonstrate the impedance output of such a dummy cell. These presented modules have a set of pre-defined number of capacitances and resistances; which test the reliability and measuring integrity of the instrument over a number of high and low frequency ranges. Over the page in Fig. (3.1.4 b –c) the output of the dummy cell seen in Fig. (3.1.4a) at a frequency of 0.1 to 1 x 10⁶ Hz for an *ac* amplitude of 10mV of step decades 10 for the working and counter electrode seen in the picture and schematic Fig. (3.1.4a)

¹⁵ See section {2.4.5} Circuit Modelling

¹⁶ Solartron instruments 12861 ECI Test Module

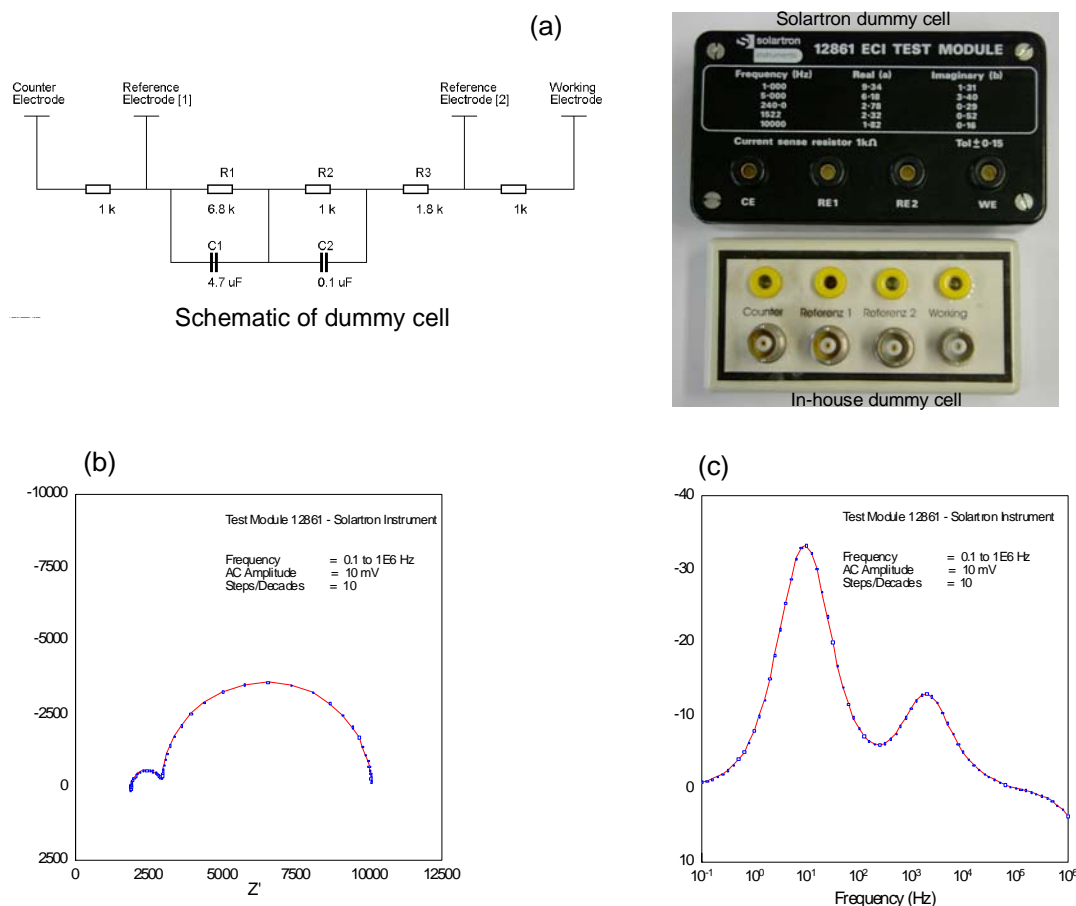


Fig. (3.1.4) Schematic of dummy cell and Solartron and in-house constructed dummy cell.

3.1.5. Circuit Modelling:

During the analysis of electrochemical impedance data generated by the Solartron instrument, one must bear in mind that the aim of analysing such data is to interpret the electrode processes and to determine the characteristic parameters of the material under study ^[1]. It should be noted in addition to the standard acquisition of impedance data; that there are limitations to the technique as to what information an operator can extract from the data. The data does not produce a final answer to the characteristics and behaviours of the material under investigation. Other electrochemical methods are required to assist in interpreting the behaviours of a material such as *dc* transients, together with a good physical knowledge of the system i.e. solution and surface composition, thickness, porosity, the presence of various

layers, and hydrodynamic conditions. Generally, the interpretation of impedance data requires the use of an appropriate model.

Any electrochemical cell can be represented in terms of an “*equivalent*” electrical circuit that comprises of a combination of resistances, capacitances, and inductances. The equivalent circuit has the character of a model, which more or less precisely reflects the reality of the material under investigation. The equivalent circuit should not involve too many elements because, in such instances this would facilitate and increase of the standard error, as generally the parameters are interdependent. Sometimes, the corresponding parameters become too large, and the model considered has to be reassessed. In the case of this work, the equivalent circuit modelling provided by Zview™ is an advanced feature integrated into the data analysis software of the Zplot™ programme. It can be used to simulate the impedance spectrum of the electrical circuit. It can also be used to fit generated experimental impedance data to pre-defined electrical circuit models.

There are two distinct methods of circuit modelling permitted by the programme. *Instant-fit* uses small-predefined models, while “Randles” uses equivalent circuits. Instant-fit is often used to create initial estimates, which are later used in manual equivalent circuit’s models. The “modelling” may be classified as physiochemical process or structural modelling and “measurement” mathematical modelling. Process modelling links measured impedances with physicochemical parameters i.e. diffusion coefficients and kinetics. Measurement modelling explains the experimental impedances in terms of mathematical functions in order to obtain a good fit between the calculated and measured values. Usually an equivalent circuit is chosen or designed from predefined principles and assumptions. The fitting of experimental data is performed using the complex non-linear least-squares technique, which is the case with the instant-fit programme in Zview. However, the model deduced from the reaction mechanism may have too many adjustable parameters, while according to Lasia ^[1] the experimental impedance spectrum is simple. The circuits most often used in measurements modelling are of the type Ladder, Voigt, and Maxwell circuits as seen in Fig. (3.1.5).

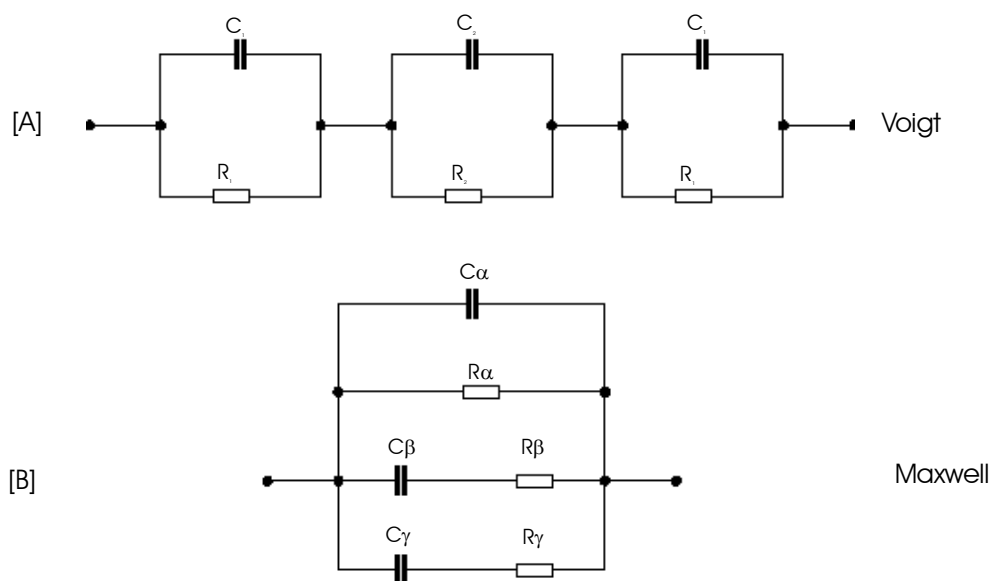


Fig.(3.1.5) [A] Voigt ladder & [B] Maxwell circuits

Measurement should be first performed. The number and nature of the circuit elements should be identified. Then sequentially the process of computational modelling is initiated. Such a procedure with the presented software programme is relatively elementary for circuits containing simple elements. It may be also carried out for circuits containing distributed elements that can be described by constant phase elements (CPE)¹⁷. However many different conditions arise from the numerical calculations. This can be in most circumstances rather difficult; therefore, each material under examination must be treated as a unique system in itself. In such circumstances, generalisations for different materials are not possible. Where circumstance permits, and requires, the results should also be verified, e.g. by application of Ohm's law. When resistances of materials are determined, it's considered wise to vary the distance of the electrodes from one another and hence the validity of the model applied i.e. altering the cell constant and therefore the application of Ohm's law.

¹⁷ See section {2.4.4.3.}

3.2. Thermostat Design & Calibration:

Foreword:

In fundamental research and especially in the area of electrolyte investigations the precision and accuracy of ones instrumentation is essential. It is notable today and with the presented work that transport properties (conductivity; ion transport; and diffusion) within systems require that the electrolyte systems under investigation be tested within an adequate temperature range. Such considerations are crucial when future commercial applications are being considered for an electrolyte. With this consideration in mind, thermal stability and reliability are essential if the behaviours of the electrolyte materials under investigation are to be understood. Therefore, the appropriate thermally regulated instrument, a thermostat must be considered to achieve the aforementioned objectives.

3.2. Thermostat Design & Calibration:

The operating temperatures of this work were in the region of $[-30\text{ °C to }+130\text{ °C}]$ and to achieve such conditions two in-house prior constructed thermostats are utilised operating between the temperatures of $[-60\text{ °C to }+25\text{ °C}]$ and $[+20\text{ °C to }+180\text{ °C}]$ respectively as seen in Fig. (3.2.1). Both thermostats operate on a similar principle and only vary in the consistency of the heating or cooling silicon oil continued within, with the appropriate silicon oil added for the applied viscometric conditions. For the purposes of simplicity the high temperature thermostat [L – 642] will now be described in detail.

The main heating chamber of the thermostat as seen in Fig. (3.2.1) is filled with Baysilon^{®*}, silicone oil. This chamber is in turn intersected with a cryostat bath also containing silicon which is essentially a heat exchanger constructed from copper piping that acts as a constant cold source. This pre-thermostat is usually regulated to remain 10 °C below the desired experimental temperature. Through this temperature difference is it possible to achieve reliable electronic regulation with the help of PID [Proportional Integral Differential] equipment. The desired temperature of the cryostat bath is controlled and regulated so that the heating coil of the regulator with thermostat remains in the appropriate region of $50 - 200\text{ W}$. At temperatures above $+120\text{ °C}$ the cold water source of the cryostat is no longer necessary

*For operating temperatures of lower than 25 °C
For operating temperatures of greater than 25 °C

Baysilon M 5 Bayer AG
Baysilon M 40 Bayer AG

[Thermostat L – 802]
[Thermostat L – 642]

for temperature regulation. The water is removed from the cryostat system and an air cooler takes over the temperature regulation. The silicon oil is circulated through the air cooler. The control of the thermostat temperature is achieved using a PID-regulator in combination with an alternating voltage bridge of “Wheatstone” design. This is coupled with a platinum thermometer {470 Ω at 0 °C}. A general schematic of the thermostat can be seen in Fig. (3.2.2a-b). In the case of the low temperature thermostat [L – 802] the cooling fluid is ethanol.

During experiments, the electrolyte cell can either be directly submerged in the main heating chamber as indicated in Fig. (3.2.1) or an insulated pump can be inserted into the same position and the silicon oil is circulated in a external cell as seen in Pic. (3.2.1). The temperature measurements of both internal and external cells can be verified through the utilisation of an variable voltage “*Wheatstone*” bridge connected to a highly sensitive platinum resistance thermometer seen in Pic. (3.2.2). The advantage of this method as described by Wachter ^[15] ^[17], is the enhanced long time stability of the sensor with linear dependence. Therefore it is possible to take reliable external measurements by performing calibrations¹⁸ beforehand where measurements with linear extrapolation being possible. Both thermostats¹⁹ were controlled during the initial stages of experiment and were controlled again two years later for their thermal and programmable stability between desired and actual temperature and there were no discernible change in readings²⁰. After 20 to 25 minutes of constant pumping thermal equilibrium in most instances is achieved and an appropriate reading can be taken.

The precision of the thermostat is reported by Wachter ^[15] to be 0.01 K and repeatability of 0.001 K with a limit of sensitivity of the temperature sensor of 2 Ω K⁻¹. Through the utilisation of a step switch with a zero resistance of 4 x 10⁻⁴ Ω permits a reproducibility of 5 x 10⁻⁵ Ω with a precision of \pm 0.05 % and a temperature coefficient of \pm 5 ppm K⁻¹ in the region of 55 °C to 125 °C. These values are well within experimental requirements.

¹⁸ See appendix

¹⁹ L - 642 & L - 802

²⁰ See appendix

Designer: H. Hilbinger
Date: 01.02.1983

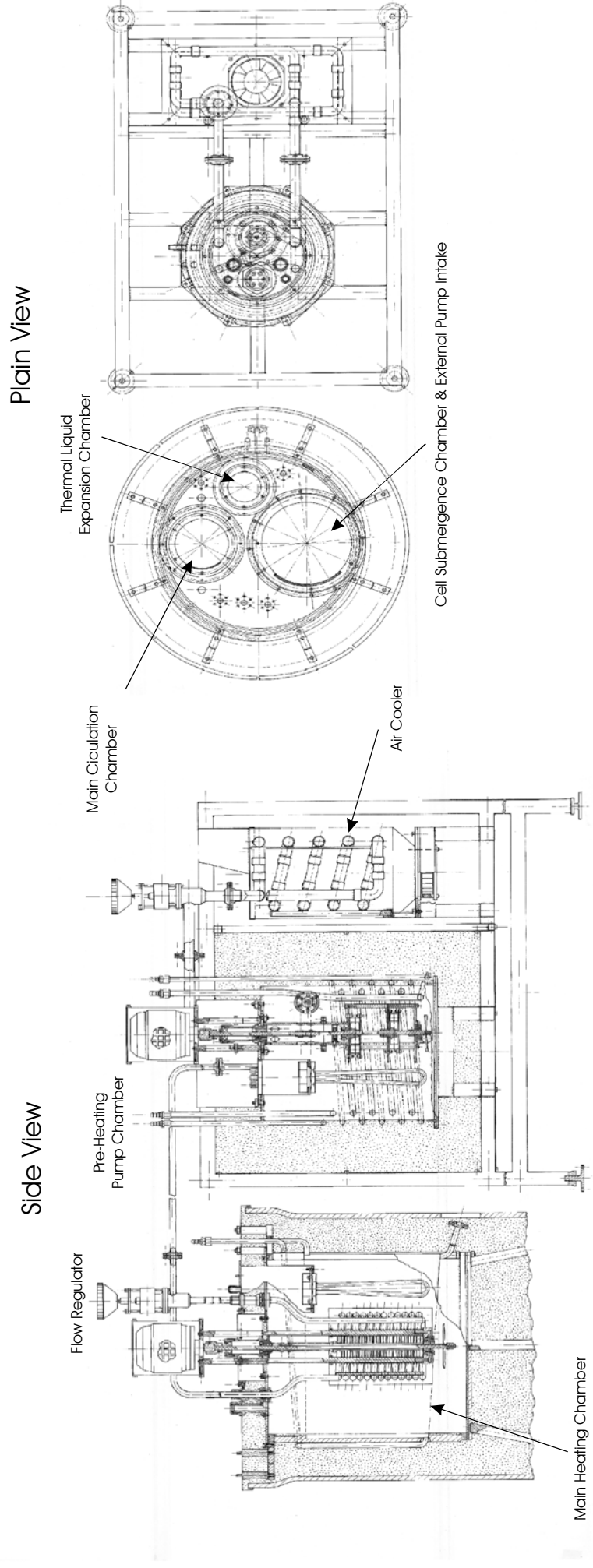
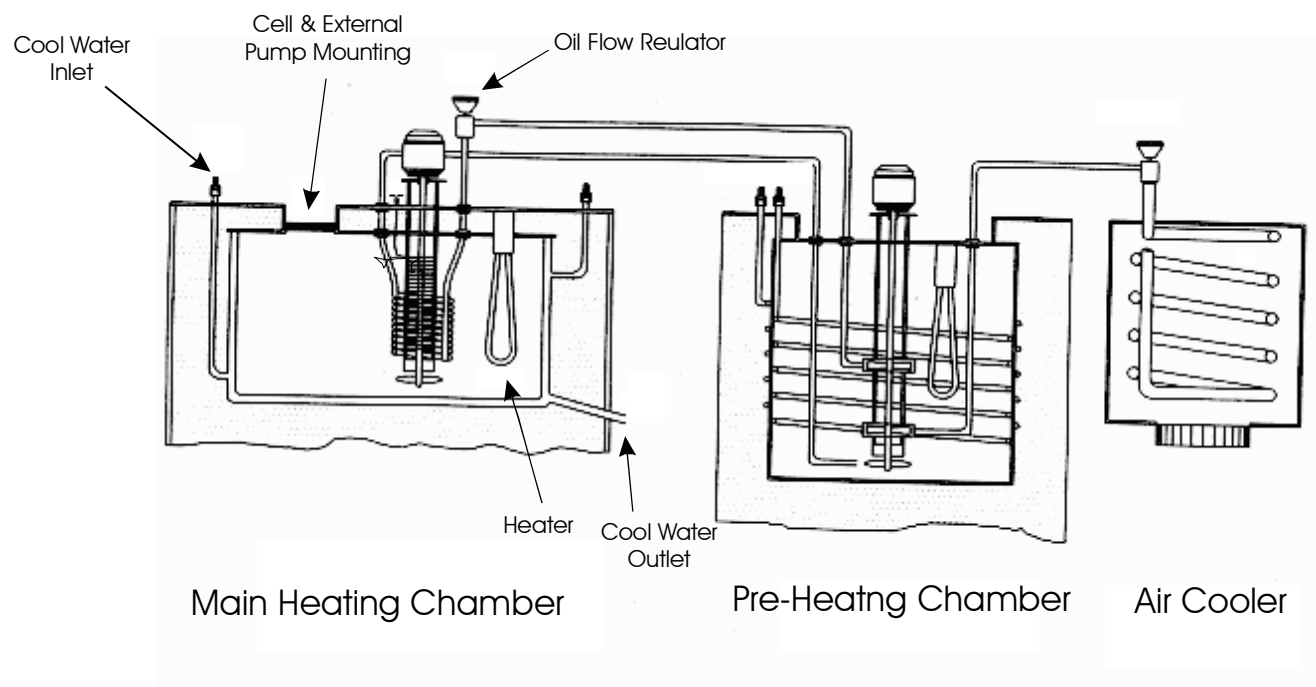
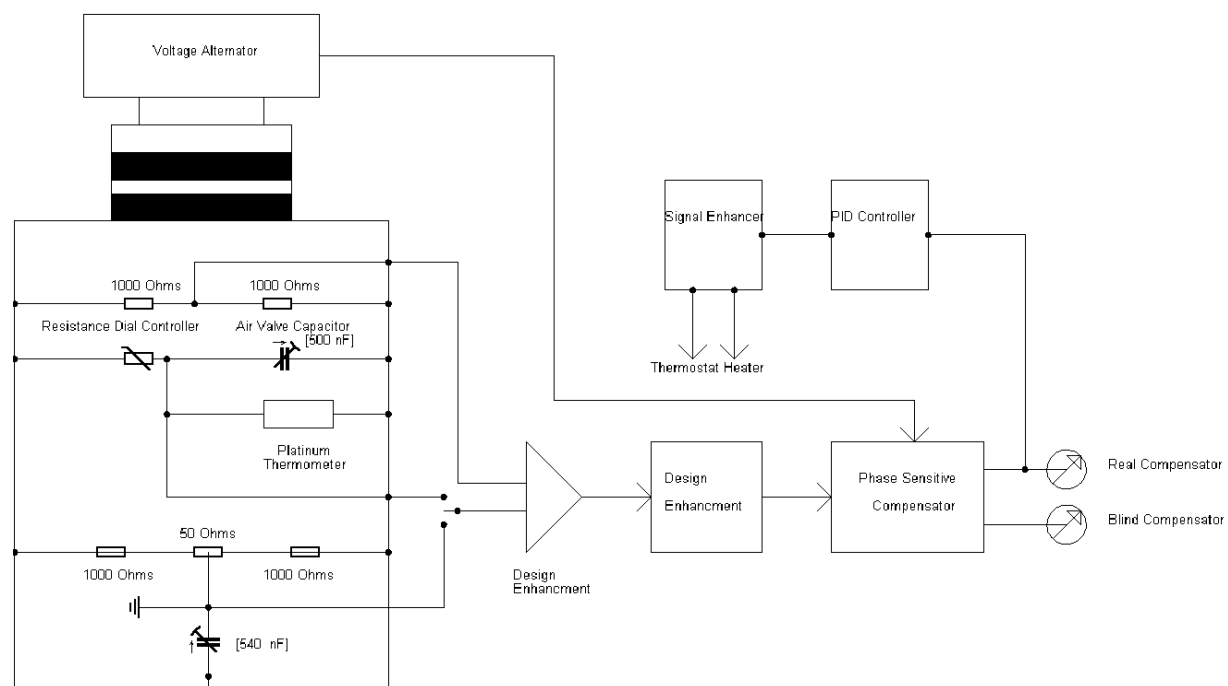
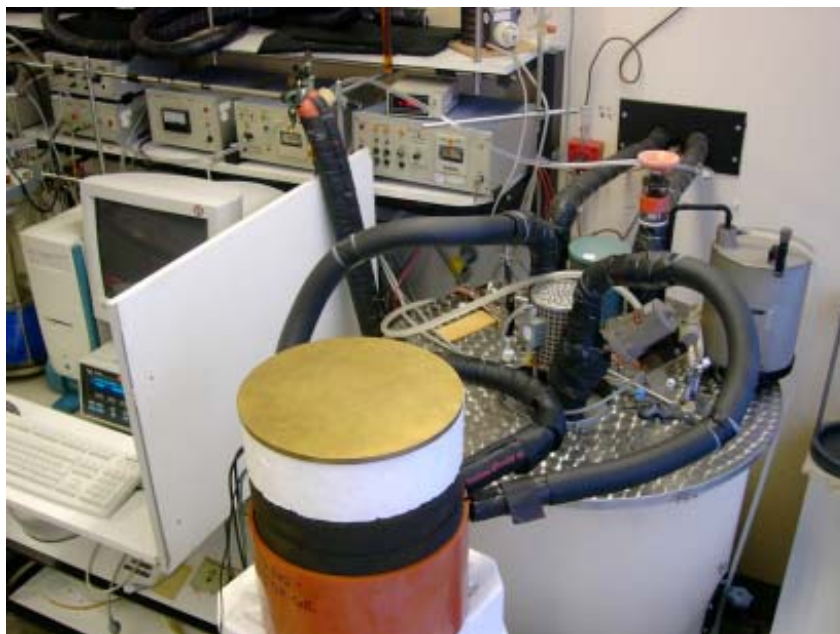


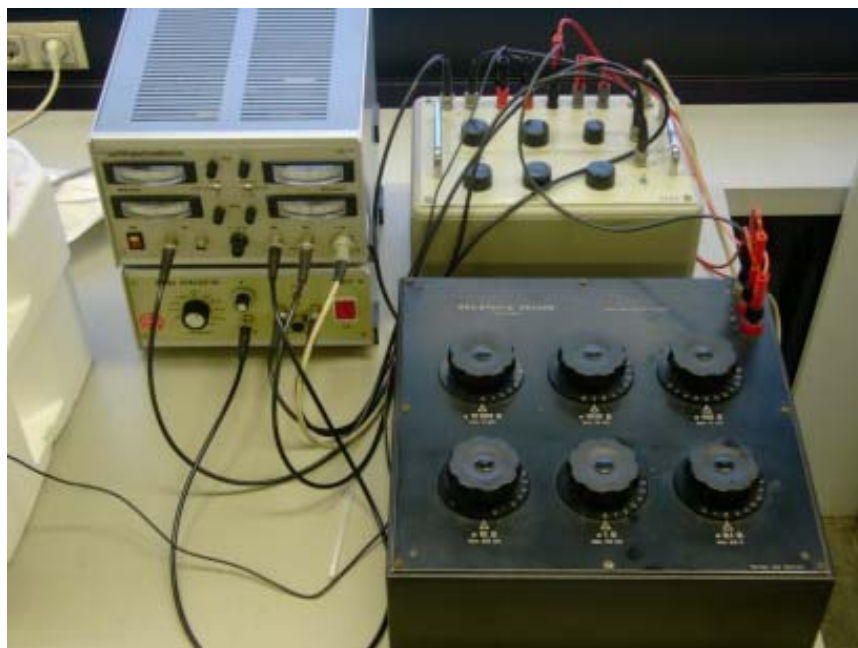
Fig. (3.2.1) High Temperature Thermostat: L – 642 25 °C to 180°C[▽]

[▽] Institute of Physical & Theoretical Chemistry, University of Regensburg, Regensburg, D-93040.
Herbert.Hilbinger@chemie.uni-regensburg.de

Fig. (3.2.2.a) Thermostat structural schematic ^[15]Fig. (3.2.2.b) Thermostat electrical schematic ^[15]



Pic. (3.2.1) Thermostat with submerged external pump connected to thermally insulated electrolyte cell.



Pic. (3.2.2) Variable voltage “Wheatstone” bridge with Platinum Thermometer

3.3. Cell Design & Construction

Foreword:

In the literature there are plenty reviews ^[18–28] relating to various designs of electrochemical test cells with specific focus on liquid electrolytes. Nevertheless, with recent trends in electrochemistry towards studies in solid (polymeric) to semi-solid (gel and ionic liquid) materials; new design considerations must be taken into consideration in the construction of test cells that can fully explore the potential of these materials. The author has come to conclude that there is a great deficit in the literature in concerning the design and construction of test cells for solid and semi-solid electrolytes. Therefore, the author intends to evaluate the theoretical and practical considerations in the design of a new electrolyte test cell encompassing the fact that the test materials are semi-solid to solid in nature.

3.3.1.

Theoretical and Practical Considerations in Cell Design:

As aforementioned, there are not many literature articles that address the electrode and cell geometry factors, which determine the magnitude and effects of interference that, occur in electrochemical cells. There are even fewer articles and references that one can draw upon in assisting in the design considerations of a cell. The difficulties in the interpretation of electrochemical data caused by a non-uniform current distribution at the electrode are a well known problem of electrochemistry ^[29]. The non-uniform reaction rate may result from a particular cell geometry, including the placement of the reference electrode, from reaction kinetics, mass-transfer limiting, or combination. Measured quantities such as ohmic and polarisation resistance, and other kinetic parameters can deviate considerably from their true values based on material and interfacial properties of the cell components. In the field of non-linear solid-state electrochemistry, a non-linear dependence of the ohmic resistance on the electrolyte thickness is often observed in experiments ^[29]. Such discrepancies can often be attributed to the constriction of the current as a result of discrete constant points at the electrolyte/electrode interface.

The most common form of cell electrode designs that one encounters in the literature are: inlaid disk; sphere; cylinder; short net; spiral wire; sponge; and inlaid ring designs ^[11]. In most situations of electrochemistry, research the working electrode most frequently appears in

one of two form: the disk design in its simplest form and usually is of solid metal or carbon construction. Its cross-section usually takes the form of a cylinder in a sealed insulating material, exposing only the cylinder surface to the electrolyte under investigation. The inlaid disk design is also the most convenient form for cleaning and polishing.

In most electrochemical measurements, it is necessary to keep one of the electrodes in an electrochemical cell at a constant potential. This so-called reference electrode permits the control of the potential of the working electrode. In most cases for test cells the majority of cells suffer from the disadvantage of having some form of internal resistance and it is difficult to distinguish the resistance generated by the electrolyte material under investigation and the cells internal resistance and especially if the test material is of very high conductivity. A form of resistance known as uncompensated resistance²¹ can arise from an inherent resistivity in the material of which the working electrode is constructed or of the electrochemical lead connecting it to the potentiostat. Therefore, the placement and general design must be carefully considered.

The presence of uncompensated resistance R^c corrupts voltametric experiments in three ways. Firstly, it deters in the determination of the electrode potential U , because an ohmic polarisation term $R^c I$ must be subtracted from the measured potential U_{app} .

$$U = U_{app} - R^c I \quad \text{Equ. [3.3.1]}$$

Though this correction is easily made, precision suffers unless both the current I and the uncompensated resistance R^c are accurately known. The second difficulty is more subtle. Most voltametric experiments apply a programmed potential to the cell and record the resulting current $I(t)$. Chemical conclusions are drawn from the analysis at the interaction between the three measurable variables I , $(U_{app} - R^c I)$, and t . The analysis relies on mathematical models of the experiment. However, what is a simple $U(t)$ programme in the absence of uncompensated resistance if it becomes distorted when R^c can not be ignored. The third and final point is the way in which uncompensated resistance impedes voltammetry and other electrochemical methods and is through its interaction with the double layer capacitance.

²¹ Uncompensated resistance is often defined as the resistance between working electrode surface and the tip of the reference electrode.

The geometry of the cell and the reference electrode itself affects uncompensated resistance. The Fig. (3.3.1) and Fig. (3.3.2) show two identical cell designs. In these, and all subsequent cell diagrams the solid black represents the electrode and the yellow hue denotes the insulating wall. The upper $[W_E]$ in Fig. (3.3.1) and Fig. (3.3.2) denotes the position of the working electrode while each lower electrode $[C_E]$ will hence be denoted as the counter electrode. The counter electrode will be assumed to be perfectly depolarisable and fills the twin roles as the reference and counter electrode. The author shall refer to the use of cylindrical coordination system with the origin at the centre of the working electrode. The z – axis, $r = 0$ is orientated towards the centre of the counter electrode, increasing in this direction. The radical r – axis is normal to the z – axis, r taking increasingly positive values as one proceeds away from the z – axis. In all the situations considered by the author there is a rotational symmetry about the major $r = 0$ axis. The subscripts W_E , C_E and R_E will be denoted in subsequent formalisms as working, counter, and reference electrodes respectively. The subscript Z_c denotes the distance separating the W_E and C_E , while z_R while r_R locates the position of the tip of the reference electrode.

The Fig. (3.3.1) depicts a cell of volume $\pi r_{w_E}^2 z_{C_E}$ which holds a solution of uniform composition and conductivity κ . The resistance of an element of the solution, which has a cross-sectional area $\pi r_{w_E}^2$ and thickness dz is $dR = dz / \pi r_{w_E}^2 \kappa$ and the total resistance is ^[30]:

$$R = \int_{z=0}^{z=Z_{C_E}} dR = \frac{1}{\pi r_{w_E}^2 \kappa} \int_0^{z_{C_E}} dz = \frac{z_{C_E}}{\pi r_{w_E}^2 \kappa} \quad \text{Equ. [3.3.2]}$$

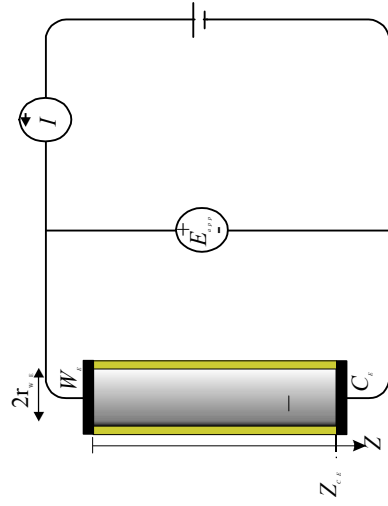


Fig. (3.3.1)
Two-electrode cell with planer symmetry,
with simple associated circuitry.

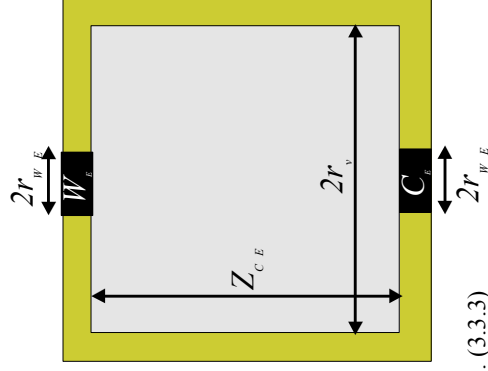


Fig. (3.3.3)
Cylindrical vessel with disk shaped working and
counter electrode in opposite faces. The effect of
varying the $r_{c,e}$ dimension was studied by Myland
& co-workers

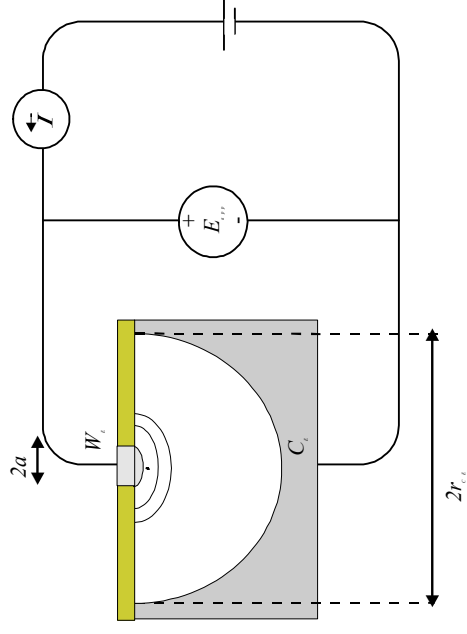


Fig. (3.3.2)
As in Fig. (3.3.1), in this case the cell
has the form of hemispherical symmetry

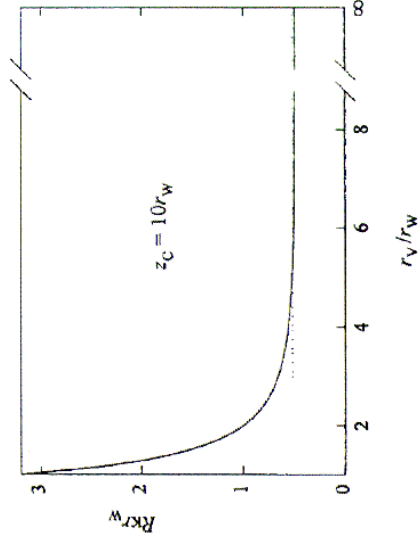


Fig. (3.3.4)
Normalised resistance of the cell as seen in
Fig. (3.3.3) plotted as a function of the radius
ratio $r_v/r_{w,E}$.

In Fig. (3.1.2), the cell has a hemispherical symmetry and volume of $2\pi(r_{CE}^3 - a^3)/3$ the total resistance of each hemispherical shell of radius dr is $dR = dr/(2\pi r^2 \kappa)$ the total resistance therefore being ^[30]:

$$R = \int_{r=a}^{r=r_{CE}} dR = \frac{1}{2\pi r \kappa} \int_a^{r_{CE}} dr = \frac{r_{CE} - a}{2\pi r_{CE} a \kappa} \quad \text{Equ. [3.3.3]}$$

The flow of current through the resistance solution causes the development of electrostatic potential ϕ at all points in the solution. Its magnitude at any point in the solution or material can be found by appropriate integration of Ohms Law. In the case of the cell in Fig. (3.3.1), one finds the potential at a distance z from the working electrode surface to be given by ^[30]:

$$\phi(z) = \int_{z=0}^{z=z} d\phi = -I \int_{z=0}^{z=z} dR = \frac{-I}{\pi r_{WE}^2 \kappa} \int_0^z dz = \frac{-Iz}{\pi r_{WE}^2 \kappa} \quad \text{Equ. [3.3.4]}$$

while for the hemispherical geometry of Fig. (3.1.2):

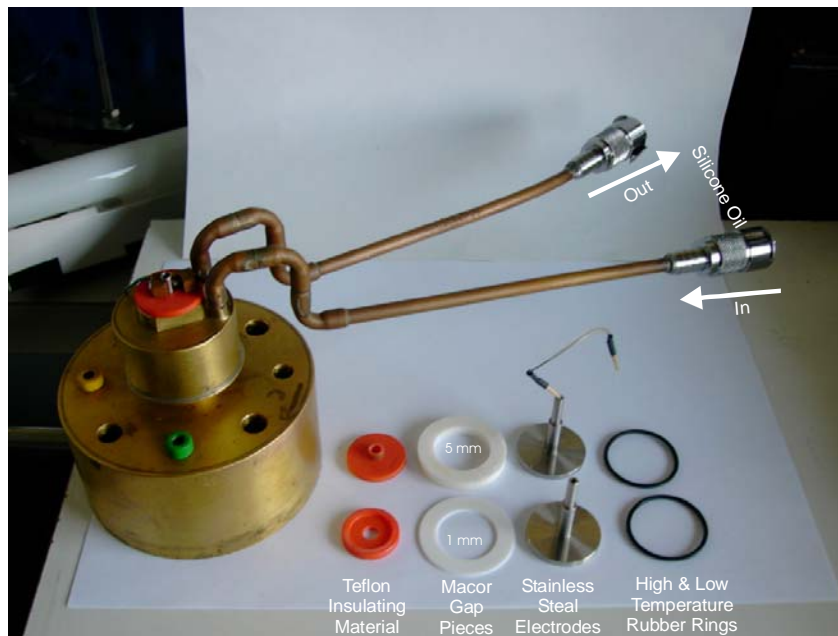
$$\phi(\rho) = \int_{\rho=a}^{\rho=\rho} d\phi = -I \int_{\rho=a}^{\rho=\rho} dR = \frac{-I}{2\pi r \kappa} \int_a^{\rho} \rho^{-2} d\rho = \frac{-(\rho - a)I}{2\pi a \rho \kappa} \quad \text{Equ. [3.3.5]}$$

where $\rho = (r^2 + z^2)^{1/2}$

Since most conductance measurements are conducted using two electrodes of the same geometry surface area these electrodes are of the same geometric surface area. The electrodes positioned parallel to and facing one another, separated by a gap of fixed dimensions. For this configuration to be visualised and in the context of impedance spectroscopy the author proposes the equivalent circuit model methodology to interpret the behaviour of the experimental cell seen in Fig. (3.3.1) & Fig. (3.3.2). The capacitance and resistance of the cell connectors and the contacts they make are shown as C_c and R_c respectively. The double layer capacitance are assumed to be equal for the two electrodes C_{WE} and C_{CE} of the working and counter electrodes respectively. Since the electrodes can be assumed that the surface areas of the electrodes have been constructed identically. The resistance of the test material under investigation between the two respective electrodes is denoted by R_{Test} . An inter-electrode capacitance term, C_i is included to account for double layer capacity. Lastly, frequency dependent Faradaic impedance, Z_f that includes both charge transfer resistance and Warburg

impedance is shown for each electrode. In later experimental discussions, the described cell will be simplified to consider the implications and behaviours of the test material alone.

3.3.2. Cell Size:



Pic. (3.3.1) Cell and accompanying parts

It was taken for granted in Fig. (3.3.1) that the cell walls were so far from the $r = 0$ symmetry axis that they could be regarded as being at infinity. Nevertheless, how far in practice, must they to be “effectively at infinity”. This has a bearing on the minimum cell volume needed to match a model based on

an infinite cell volume. It will suffice to determine how wide the vessel needs to be before the total cell resistance R is effectively that of an infinite vessel. If R is independent of cell size, so will R^c . For our purposes, one will consider the cell size shown in Fig. (3.3.3), previously in which a cylinder vessel of radius r_v houses a disk-shaped working and counter electrodes both of much smaller radius r_{W_E} . As usual z_{C_E} denotes the distance separating the two electrodes and in accordance with conclusions of the section we set $z_{C_E} = 10r_{W_E}$. The figure (3.3.4) is the result in applying the procedure from results obtained by Oldham^[31], it shows that the resistance is within 5 % of value from infinity large vessel for radii that exceed then electrode radius 5 fold. In the figures (3.3.3) and (3.3.5) was drawn with $r_v = 5r_{W_E}$ and $z_{C_E} = 10r_{W_E}$ thus represents the minimum dimensions of an acceptable vessel.

3.3.3.

Test Cell Design:

For the duration of this work, two conductance test cells were constructed as seen in Pic. (3.3.1). Both cells are of identical design but differ in their geometric volume. The general schematic drawings of the constructed cells are seen in Fig. (3.3.5) and (3.3.6). The construction of the conductance test cell took into consideration all the specifications mentioned in section {3.3.1}. It demonstrates a cylindrical design with both stainless steel “disk” working and counter electrodes positioned parallel to and facing one another. There is the added possibility for the addition of a third gold/lithium reference electrode that is in the plane of the counter electrode. The cell constant can be altered according the thickness the of macor gap pieces desired. A platinum thermometer is inserted in to the working electrode to measure the true internal temperature. Heating and cooling fluid is circulated through the cell housing and exits through the external copper coil for complete thermal control as indicated in Fig. (3.3.5).

3.3.4.

Cell Testing & Calibration:

The term calibration and adjustment are often used synonymously. Strictly speaking, calibration describes a comparison with set points or results previously determined in near ideal conditions. The determined values for any new experimental test cell must lie within specified parameters and tolerances. An adjustment means an active change in settings. Calibration should also be understood in the sense as checking and not in the sense of adjustment as any changes in the cell constant during standard calibration measurements are usually caused by contamination of the standards. Therefore, the author wishes to stress the importance of using the test cell correctly.

The cell construction presented by the author as seen in Fig. (3.3.5), is constructed of brass with two steel working and counter electrodes plus the added option in circumstance of an reference electrode within a thin gold/lithium electrode design, that protrudes from the central axis of the surface of the electrode. Most test cells that are delivered from commercial sources are already toughly tested with a predefined cell constant that often lie in the range of 1.5 to 2

% depending of the range and type of sample under investigation. When a cell is constructed on-site then an extensive procedure of testing is required to determine the true nature and conductive integrity of the new design. If such precise methods are required, the cell constant must be determined with standard materials. The cell constant can be determined by a number of standard materials which are easily available and of good quality i.e. aqueous KCl solutions ^{[10] [22] [32 - 33]}.

Designer: A. Engelhardt*
Date: 10.01.2001

■ PVC
■ MACOR
■ Teflon
■ Brass Metal

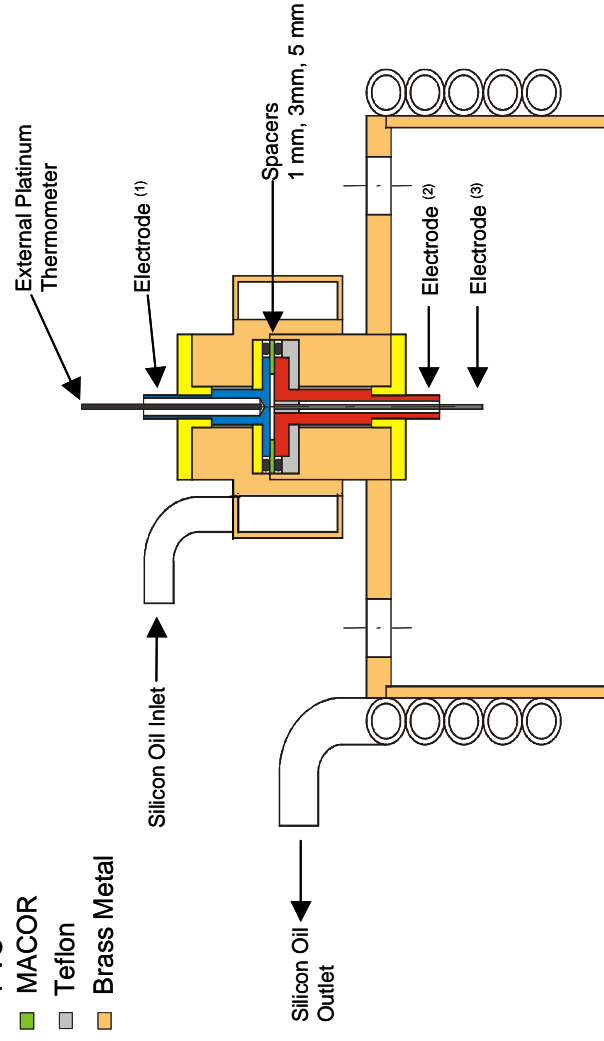


Fig. (3.3.5) Side view schematic of test cell with thermal heating and cooling system.

Electrode⁽¹⁾ counter electrode
 Electrode⁽²⁾ working electrode
 Electrode⁽³⁾ optional reference electrode

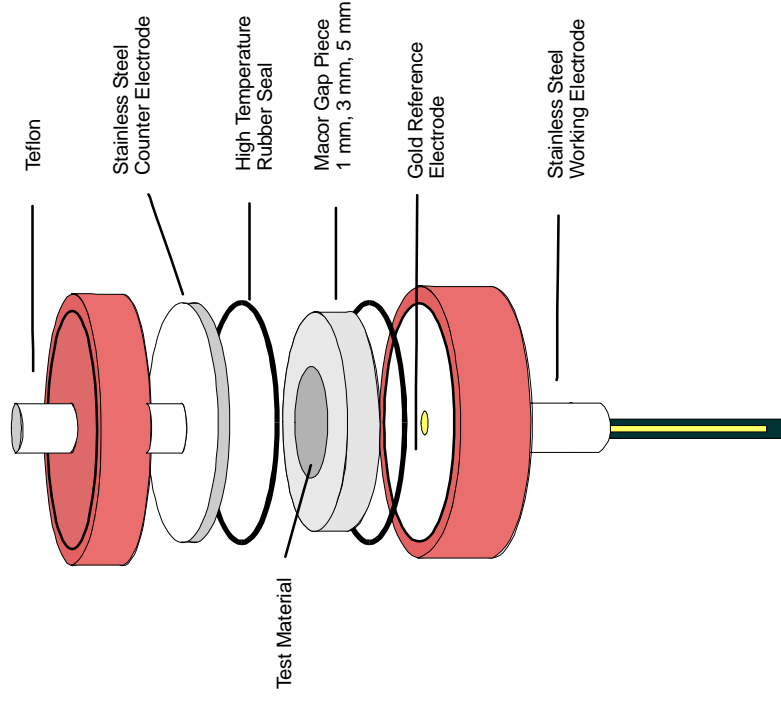


Fig. (3.3.6) Internal schematic of test cell

* Alfred Engelhardt, Institute of Physical and Theoretical Chemistry, University of Regensburg, 93040 Regensburg, Germany
Alfred.Engelhardt@chemie.uni-regensburg.de

3.3.4.1.

Theoretical Background:

The specific conductivity is a measure of the ability of a solution, metal, or gas in short, all materials to conduct an electrical current. In solutions, the current is carried by cations and anions whereas in metals and solid materials electrons transport current. A conductance G^{22} is the reciprocal of the resistance:

$$G = \frac{1}{R} \quad \text{Equ. [3.3.6]}$$

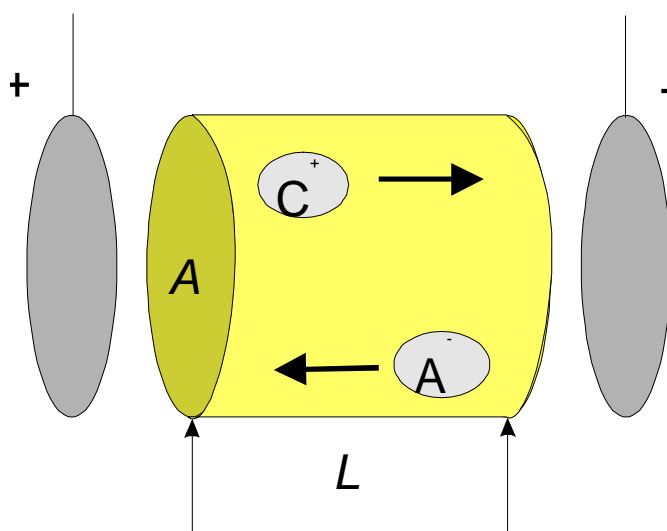


Fig. (3.3.7) Electrical conductance G

The unit of R is Ohm, Ω , and the unit of G is Siemens, S . To measure the electrical conductance, a voltage is applied to the electrode pairs and the current that flows is measured. During the process depending on the electrolyte in question i.e. the solution, the cations migrate to the negative electrode and the anions consequently to the positive electrode while the solution acts as an ionic conductor. A conductor is defined by its length l and cross-sectional area A . The smaller the gap l and the larger the A , the larger the measurable current at

the same electrolyte and same voltage as seen in Fig. (3.3.7). Therefore, the relationship is defined as:

$$G = \kappa \frac{A}{l} = \frac{1}{\rho} \cdot \frac{A}{l} \quad \text{Equ. [3.3.7]}$$

²² The symbol G is often used for cell constant in older papers; but IUPAC recommends the use of the symbol G for conductance and K_{cell} for cell constant^[34].

where κ is the electrolytic conductivity and ρ the specific resistance. The quotient of the length and the area is the cell constant K_{cell} (cm^{-1})²³ see table (3.3.1):

$$K_{cell} = \frac{l}{A} \quad \text{Equ. [3.3.8]}$$

If the cell constant is known, the specific conductivity can be correspondingly determined from the measured conductance. The electrolytic conductivity κ (S cm^{-1})²⁴ of an electrolyte solution is determined by simplifying Equ. [3.3.10]:

$$\kappa = \frac{K_{cell}}{R} \quad \text{Equ. [3.3.9]}$$

There is another important quantity for conductivity in the literature, the equivalent conductivity Λ ($\text{S cm}^2 \text{equiv}^{-1}$)²⁵, which is related to κ the following relationship:

$$\Lambda = \frac{\kappa}{c} \quad \text{Equ. [3.3.10]}$$

where c is the equivalent concentration²⁶. IUPAC recommends the equivalent conductivity be discontinued [34 - 36].

The conductivity is a parameter that is heavily dependent on temperature. A 0.01 molal aqueous KCl solution is presented as an example. The conductivity of this solution at 20 °C is 1278 $\mu\text{S cm}^{-1}$, whereas at 25 °C it is 1413 $\mu\text{S cm}^{-1}$. The temperature dependence of conductivity increases strongly with the viscosity of the liquid. Therefore to achieve a precise conductivity a highly precise thermostat is required e.g. for the example given above, a precision of about 5 mK is sufficient for obtaining a precision in conductance of about 0.01%. Such a device has already been discussed in section {3.2}. Conductivity measurements are normally conducted as follows. The measuring instrument records the actual conductivity and temperature, and the author converts it to the reference temperature

²³ IUPAC recommends the use of K_{cell} for cell constant [34]

²⁴ Electrolytic conductivity (also formally known as specific conductance) is commonly expressed in ($\mu\text{S cm}^{-1}$).

The SI of conductance is (S) and the equivalent to the inverse ohm (Ω^{-1}) [34]

²⁵ Equivalent conductivity is equal to Λ/ν_+z_+ where ν_+ is the number of cations of charge number z_+ produced in dissociation of a salt "molecule" of a given type, of which $\nu_+z_+ = \nu_-z_-$ and Λ_m is the molar conductivity [34]

²⁶ Equivalent concentration is equal to $\nu_+z_+c_m$ where c_m is the concentration.

using a temperature compensation-calibrating graph previously measured with standard materials. The geometries of both experimental test cells with their various cell constants are summarised in table (3.3.1).

<i>“Large Cylindrical Cell”</i>				<i>“Small Cylindrical Cell”</i>			
Radius <i>r</i>	Area <i>A</i>	Length <i>l</i>	Constant <i>K_{cell}</i>	Radius <i>r</i>	Area <i>A</i>	Length <i>l</i>	Constant <i>K_{cell}</i>
cm	cm ²	cm	cm ⁻¹	cm	cm ²	cm	cm ⁻¹
1.25	4.908	0.5	0.1097	0.57	1.021	0.5	0.5113
1.25	4.908	0.3	0.0610	0.57	1.021	0.3	0.2931
1.25	4.908	0.1	0.0200	0.57	1.021	0.1	0.0984

Table. (3.3.1) The geometries of both experimental test cells with their various cell constants.

3.3.5.

Standard Preparation:

Potassium Chloride (KCl)

Potassium chloride, KCl (Merck) was recrystallised from highly purified Millipore water²⁷, and dried at 60 – 80 °C in vacuum ($p < 10^{-2}$ Torr.). The sample was ground in a agate motor and dried once more for two days at 300 °C in the presence of P₂O₅. The product was stored in an atmosphere of pure argon as directed by Neueder and co-workers^[15]. In order to prevent other interferences from carbon dioxide all standard samples were prepared under protective gas of nitrogen. The test standards samples prepared are summarised in table (3.3.2). If one intends to check the test cells conductivity range smaller than 200 $\mu\text{S cm}^{-1}$, then a differentiation must be made according to the electrode material:

- 200 $\mu\text{S cm}^{-1}$ - Polished platinum or steel electrodes polarise at high conductivities so that a molality of 0.001 (m)²⁸ KCl solution must be utilised.
- 2 mS cm^{-1} – 0.01 (m) KCl solution can be utilised.
- 300 mS cm^{-1} – 3 (m) KCl solution can be utilised.

²⁷ Millipore Water – Mill-Q® water Purification System
Millipore GmbH, Hauptstraße 71-79, 6236, Eshborn

²⁸ Molality (m) is defined as the number of moles of solute per kilogram of solvent
Molality = moles of solute / kg solvent

<i>Potassium Chloride (KCl) - Solution</i>	
KCl	74.551 g mol ⁻¹
Molality (m)	g (KCl) per kg water
0.001	0.7455
0.002	0.1480
0.003	0.2236
0.004	0.2236
0.01	0.7455
0.1	7.4555
1.0	74.551

Table. (3.3.2)

3.3.6.**Measuring Procedure:**

Measurements were carried out with two different cell sizes as seen in Fig. (3.3.5). Both cells are identical in all manners other than their internal volume. The test cell is connected to a thermal fluid circulation pump, where the pump is submerged in a heating bath [L-642] as seen in Pic. (3.2.1) and Fig. (3.2.2a) with an attached highly precise external *Wheatstone bridge* as seen in Pic. (3.2.2). The temperature of the chosen temperature programme 25 °C was attained in 30 minutes with an accuracy of less than 10⁻³ °K. Both short and long-term fluctuations were below 10⁻³ °K, and no temperature drift beyond this limit was observed. Using the precise temperature bridge, the electrolyte conductance at 25 °C was obtained to an accuracy of less than 0.01 %. Further information on the measuring equipment, temperature control and measuring method can be read in the proceedings of Wachter ^[15].

Each cell was tested with two different MACOR® gap piece of thickness of 5 mm and 3 mm and various concentrations. The figure (3.3.9) and (3.3.10) shows the specific conductivity vs. molality for the mentioned cells and their respective IUPAC specific conductivities. The correlation between both data results are quite good with an average deviation between the experimental cell and IUPAC data of 7 % and 9 % in their cell constants for the “Large” and “Small” experimental cells respectively. This result is averaged from all cell constants taken in to consideration over the whole concentration range. In figure (3.3.9) there is a slight

deviation of the 5 mm gap piece from optimal (IUPAC) values. This may be attributed to the presence of gas bubbles within the standard solution on insertion. More of such data can be seen in the appendix section.

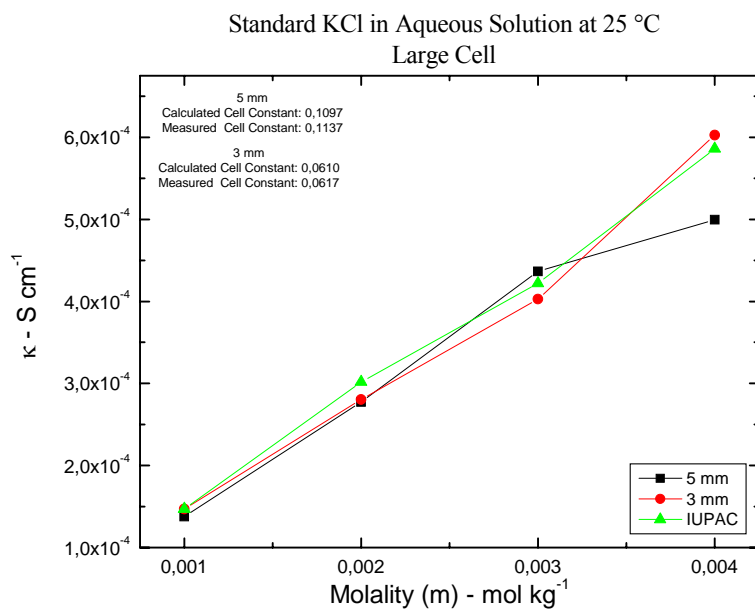


Fig. (3.3.9)

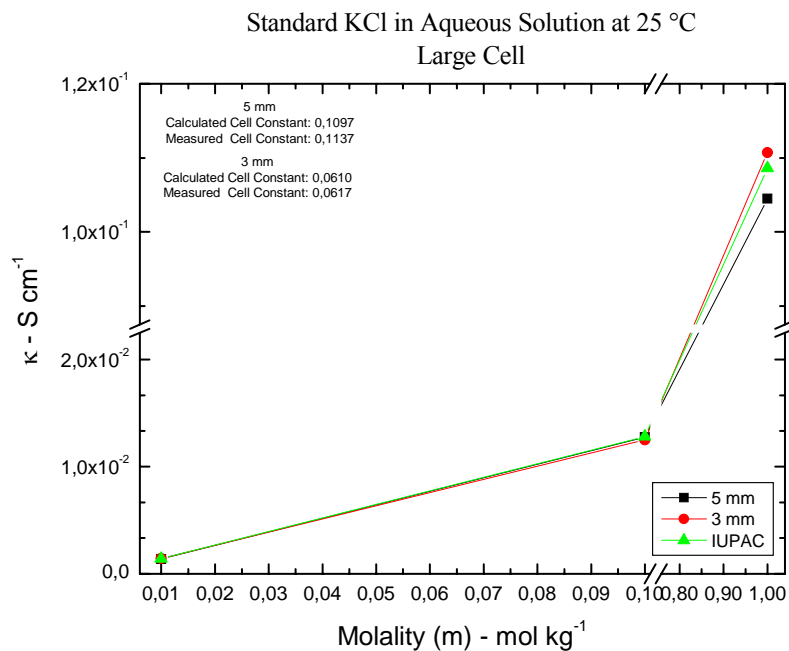
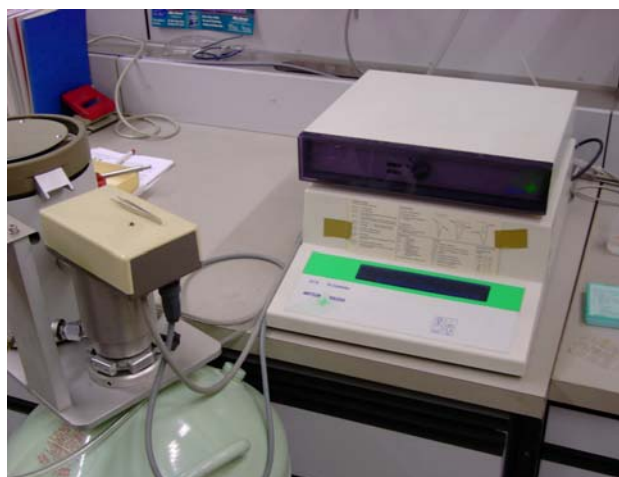


Fig. (3.3.10)

3.4. DSC – Differential Scanning Calorimetry

The technique Differential Scanning Calorimetry (DSC) is concerned with the measurement of energy changes. This technique is a well-established measuring method, which is used on large scale in varying scientific areas such as in research-development, quality control, and testing. Over a wide temperature range, [$-50\text{ }^{\circ}\text{C}$ to $+1500\text{ }^{\circ}\text{C}$] thermal effects can be quickly identified and the relevant temperature and characteristic caloric values determined using substance quantities in the *mg* range. The measurement values obtained by DSC allow heat capacity; heat transition; kinetic data; purity; and glass transitions to be determined. More details can be read on both thermal methods in section {2.5.}.

Mettler Toledo DSC – 30 – Interface TC15 TA Controller:



Pic. (3.4.1) Mettler Toledo DSC – 30

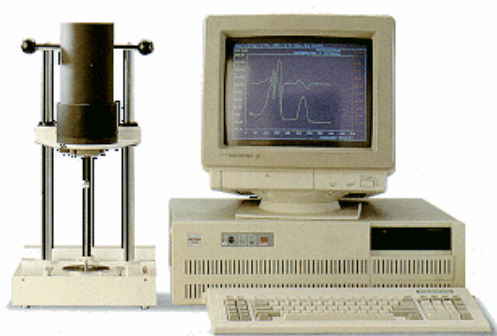
The Mettler Toledo DSC – 30²⁹ is capable of operating from $-170\text{ }^{\circ}\text{C}$ to $+600\text{ }^{\circ}\text{C}$. The nitrogen cooling facility means that rapid cooling can be obtained, thus allowing a high intake of samples. The sensor contained within the instrument is a 14-fold Au/Au-Pd ceramic based type and allows the detection of low intensity transitions not visible on other manufacturers DSC instruments. This is

particularly useful in the detection of 2nd order transitions. DSC measurements were performed for the accurate determination of phase transitions. All samples were subjected to a standard heating and cooling from $[-30\text{ }^{\circ}\text{C}$ to $+135\text{ }^{\circ}\text{C}$] at $10\text{ }^{\circ}\text{C min}^{-1}$ cycles. See Pic. (3.4.1).

²⁹ Prof. Dr. A. Pfitzner, Institut für Anorganische Chemie, Universität Regensburg, Universitätsstr. 31, Regensburg, D-93040.
arno.pfitzner@chemie.uni-regensburg.de

3.5. DTA – Differential Thermal Analysis

Differential thermal analysis (DTA) involves heating a material at a controlled rate to a pre-determined temperature and comparing any chemical emissions of heat (exothermic) or absorption's of heat (endothermic) from the material in comparison with a passive material such as alumina or quartz sand. This instrument utilised mostly for determining the precise temperature at which a reaction takes place or identifying phase change and/or reaction products.



Pic. (3.5.1) DTA Linseis L- 62

Temperature range from +20 °C up to +1550 °C

High sensitivity due to small measuring systems with very low heat capacity of sintered aluminium (Al₂O₃) or Pt-crucibles.

DTA from 0 °C – 135 °C at 10 °C min⁻¹ in air.

3.6. Infrared Spectroscopy – (IR)

These measurements were performed using the standard KBr method.

Instrument: ATIMATTON Genesis FTIR^{TM30}

Software: WinFIRST v2.10

3.7. Nuclear Magnetic Resonance – (NMR)

The Bruker Instruments AVANCE300 – wide bore (1 Hz frequency 300 MHz) system has a 7.05 T Bruker Spectrospin/Oxford 89mm vertical bore magnet, and is controlled by a Silicon Graphics computer running Xwin-NMR software. The spectrometer is also equipped with a complete Bruker micro-imaging accessory.

(300.13 MHz Proton) with 5 mm Dual sample head (^1H , ^{13}C):



Pic. (3.7.1) Bruker Instruments AVANCE300

The AVANCE300³¹ has numerous rf and gradient coils. The principal use for this instrument is high-resolution spectroscopy, micro-imaging, Rheo-NMR and PGSE studies. All probes can be connected to the AVANCE computer-controlled variable temperature apparatus, which with the use of a liquid nitrogen reservoir; can cover temperatures ranges from -10 °C to +150 °C.

3.8. Mass Spectroscopy³²

Instrumentation:

Finnigan MAT 95

ThermoQuest Finnigan TSQ 7000

Finnigan MAT SSQ 710 A

Standard Experiments:

EI-MS, High & Low-Resolution

ES-MS MI-MS

FI/FD-MS

Liquid SIMS (Cs^+) CI-MS/DCI-MS GC- LC

³¹ www-nw.uni-regensburg.de/~nmz13342.analytik.chemie.uni-regensburg.de/

³² Dr. K.K. Mayer; NWF IV - Chemie-Pharmazie ; Zentrale Analytik Massenspektrometrie; Universität Regensburg D-93040 Regensburg

3.9. Glove box Inert Gas System MB 150B-G-I

During the instigation of this work, a moisture free and refined environment was required in order to obtain precise and consistent data. In order, achieve the aim all moisture and air sensitive materials were prepared and stored in a Glove box Inert Gas System MB 150B-G-I as seen in Fig. (3.9.1). Argon functions as the inert gas within the glove box itself. The gas within the confines of the steel structure is continually purified and refined with the removal of potential water and oxygen contaminants. The regeneration of the gas within the glove box has an average cycle time of twelve hours.

Achievable environment purity: $\leq 1 \text{ ppm H}_2\text{O}$
 $\leq 1 \text{ ppm O}_2$

Working Gas: Argon – H₂-mixture 93 % - 7 %
50 L 200 bar

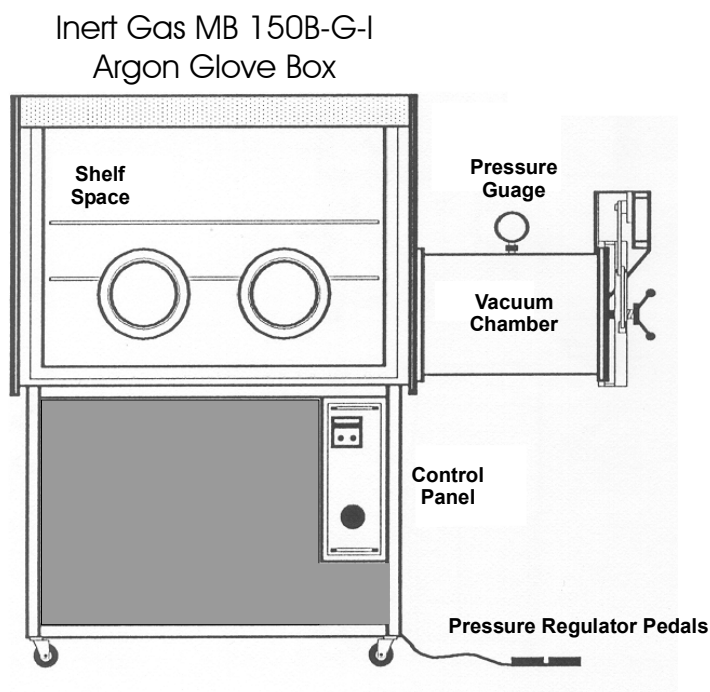


Fig. (3.9.1)

References:

1. A. Lasia, Section: Electrochemical Impedance Spectroscopy and its Applications, Modern Aspects of Electrochemistry, 32, 143-242, Ed. Conway, B.E. et al., Plenum Press, New York, (1979).
2. P. G. Bruce and C. A. Vincent, *J. Electroanal. Chem. Interfacial Electrochem.*, **225**, 1 (1987).
3. J. Fuller, A. C. Breda and R. T. Carlin, *J. Electroanal. Chem.*, **459**, 29 (1998).
4. A. Reiche, T. Cramer, G. Fleischer, R. Sandner, B. Sandner, F. Kremer and J. Kaerger, *J. Phys. Chem. B.*, **102**, 1861 (1998).
5. D. R. MacFarlane, P. J. Newman, K. M. Nairn and M. .. Forsyth, *Electrochim. Acta*, **43**, 1333 (1998).
6. X. Ren and P. G. Pickup, *J. Electroanal. Chem.*, **420**, 251 (1997).
7. M. A. Vorotyntsev, J. P. Badiali and G. Inzelt, *J. Electroanal. Chem.*, **472**, 7 (1999).
8. Zbigniew and Stojek, Section: Experimental, Electrochemical Methods – in Guide to Experiments and Applications, 300-305, Ed. Scholz, S., Springer, London, (2002).
9. R. N. Adams, *Electrochemistry at Solid Electrodes*, No. p. 402 (1969).
10. D. Dobo, *Electrochemical Data - A Handbook for Electrochemists in Industry and Universities*, 1, No. p. 340, Elsevier, (1975).
11. S. Komorsky Lovric, Section: Working Electrodes, Electrochemical Methods - Guide to Experiments and Applications, 245-260, Ed. Scholz, S., Springer, London, (2002).
12. F. M. Gray, *Solid Polymer Electrolytes – Fundamentals and Technological Applications*, VCH Publishers Inc, (1991).
13. U. Retter and H. Lohse, Section: Electrochemical Impedance Spectroscopy, Electrochemical Methods - Guide to Experiments and Applications, 149-166, Ed. Scholz, F., (2003).
14. K. Hoffmann, *Imidazole and Its Derivatives Part 1*, 1, No. p. 445, Interscience, (1953).
15. R. Wachter and J. Barthel, *Berichte der Bunsen-Gesellschaft*, **83**, 634 (1979).
16. K. S. Groß, Title: Transporteigenschaften des Systems 1-ethyl-3-methylimidazoliumchlorid/ AlCl_3 in Lösungsmitteln verschiedener Klassen im Bereich hoher Verdünnung bis zur reinen Salzschnmelze, *Theoretical & Physical Chemistry*, 1-261 (1993).
17. J. Barthel, R. Wachter and H. J. Gores, *Mod. Aspects Electrochem.*, **13**, 1 (1979).
18. X. Wu, H. Ma, S. Chen, Z. Xu and A. Sui, *Journal of the Electrochemical Society*, **146**, 1847 (1999).
19. A. Watts, R. D. Hopwood, T. J. VanderNoot and Y. Zhao, *J. Electroanal. Chem.*, **433**, 207 (1997).
20. A. M. Bredland, J. W. Paulson, T. G. Messing and B. C. Bergum, *Power Sources*, **6**, 383 (1977).
21. K. Murata, S. Izuchi and Y. Yoshihisa, *Electrochim. Acta*, **45**, 1501 (2000).
22. J. Barthel, F. Feuerlein, R. Neueder and R. Wachter, *Journal of Solution Chemistry*, **9**, 209 (1980).
23. S. S. Zhang and C. A. Angell, *J. Electrochem. Soc.*, **143**, 4047 (1996).
24. P. G. Bruce and C. A. Vincent, *Faraday Discuss. Chem. Soc.*, **88**, 43 (1989).
25. P. G. Bruce, J. Evans and C. A. Vincent, *Solid State Ionics*, **28-30**, 918 (1988).
26. K. Toda, S. Oguni, Y. Takamatsu and I. Sanemasa, *J. Electroanal. Chem.*, **479**, 57 (1999).
27. P. J. Kulesza, G. Chelmecki and B. Galadyk, *J. Electroanal. Chem.*, **347**, 417 (1993).
28. K. Jinjing, X. u. Qin and C. Ke, *J. Chem. Educ.*, **78**, 937 (2001).
29. A. M. Svensson and K. Nisancioglu, *Journal of the Electrochemical Society*, **146**, 1840 (1999).
30. J. C. Myland and K. B. Oldham, *Anal. Chem.*, **72**, 3972 (2000).
31. L. C. R. Alfred and K. B. Oldham, *Journal of Electroanalytical Chemistry*, **396**, 257 (1995).
32. K. W. Pratt, W. F. Koch, Y. C. Wu and P. A. Eerezansky, *Pure and Applied Chemistry*, **73**, 1783 (2001).
33. Y. C. Wu and P. A. Berezansky, *Journal of Research of the National Institute of Standards and Technology*, **100**, 521 (1995).
34. I. Mills, T. Cvitas, K. Homann, N. Kalley and Editors., *Quantities, Units and Symbols in Physical Chemistry*, Second Edition, (1994).
35. R. Parsons, *Manual of symbols and terminology for physicochemical quantities and units. Appendix III. Electrochemical nomenclature*, 37, No. p. 516, (1974).
36. I. Mills, T. Cvitas, K. Homann, N. Kallay and K. Kuchitu, 172 (1991).

Chapter 4

Synthesis

Foreword:

During the progress of this work all experimental materials were synthesised by the author unless otherwise stated. Some samples were synthesised from previously established procedures and others were synthesised using newly refined procedures. The earlier synthesis of these materials conducted by Gordon^[1], used a cumbersome and demanding method through the utilisation of an apparatus known as a Carius Tube³³, which required the synthesis to be performed in a low temperature environment through the use of liquid nitrogen over a period of several days. The author wishes to present a much more refined and shortened procedure that eliminates the use of nitrogen cooling and permits higher product yields compared to Gordon^[1] and Bowlas^[2]. The table (4.1.1) summarises the materials synthesised during this work. The purification of the solvents was performed according to proven literature procedures. All samples were quality controlled by a number of methods in order to keep impurities to a minimum i.e. NMR, mass spectroscopy, Karl Fischer, flame test analysis, titration, and elemental analysis. All purified solvents and salts were stored under purified argon. The preparation of the cells was performed in the glove box.

4.1. Lithium Salts with New (Recently Published)^[4-11] Anions

In electrochemical systems, one is concerned with the processes and factors that affect the transport of charges in ionic conductors across the interfaces. This section is concerned with the ionic conductor i.e. the electrolyte. The transition in electric potential in crossing from one conducting phase to another usually occurs almost entirely at the interface, and one can expect such interfaces to exert effects on the behaviour of charge carriers (electrons or ions) at the interfacial region. Typical electrolytes used in early studies included lithium salts of coordinated saturated anions such as ClO_4^- , BF_4^- , PF_6^- , and AsF_6^- ^[3] which are not easily oxidised or reduced at the electrodes and hence are used as anions of well known lithium supporting electrolytes for lithium ion batteries. Lithium hexafluorophosphate itself is thermally unstable in the solid state and decomposes above 65 °C yielding LiF and Lewis acid PF_5 . The Lewis acid based anion tetrafluoroborate is thermally stable, but the salt LiBF_4 has the disadvantage of poor conducting in solutions and poor cycling efficiencies.

³³ An example of such device can be seen in the following web link
www.dur.ac.uk/chemistry/Staff/gs/Web%20Page%20equipment%20etc.htm

The search for alternatives to the above-mentioned anions has been in progress for a number of years and has already been briefly explored by the author in section {1} earlier. More recently, anions in the form of large molecular anions with delocalised anionic charges; which have low lattice energies, and relatively small ion-ion interactions have demonstrated promising potential ^[4 - 11]. In such anions delocalisation of the charge is achieved by electron-withdrawing substituents such as -F, -CF₃, -COOR, and -SO₂ or by substituting carbon for nitrogen, which has a higher electro-negativity value. These molecular anions generally demonstrate in contrast to Lewis acid based salts better chemical stability in various solvents and are often thermally far more stable. The author has synthesised a new class of stable lithium electrolytes salts that generally compose of chelate complexes of boron with aliphatic diols see table. (4.1.1).

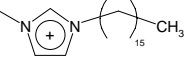
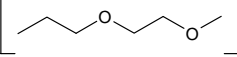
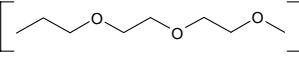
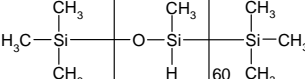
Shorthand	IUPAC - Nomenclature <i>Lithium Salt (Anions)</i> Section {4.1}	Structure
Li [PF ₆]	LiPF ₆ lithium hexafluorophosphate <i>[Merck – VWR International]</i>	$\text{Li}^+ \left[\text{PF}_6 \right]^-$
Li [BF ₄]	LiBF ₄ lithium tetrafluoroborate <i>[Merck – VWR International]</i>	$\text{Li}^+ \left[\text{BF}_4 \right]^-$
Li [F8]	LiB[C ₆ F ₄ O ₂] ₂ lithium bis-[3,4,5,6-tetrafluoro-1,2-benzenediolato(2-)-O,O']borate <i>[Synthesis]</i>	$\text{Li}^+ \left[\begin{array}{c} \text{F} & & \text{F} \\ & & \\ \text{C}_6\text{F}_4\text{O}_2 & \text{--- B ---} & \text{C}_6\text{F}_4\text{O}_2 \\ & & \\ \text{F} & & \text{F} \end{array} \right]^-$
Li [H8]	LiB[C ₆ H ₄ O ₂] ₂ lithium bis-[1,2-benzenediolato(2-)-O,O']borate <i>[Synthesis]</i>	$\text{Li}^+ \left[\begin{array}{c} \text{H} & & \text{H} \\ & & \\ \text{C}_6\text{H}_4\text{O}_2 & \text{--- B ---} & \text{C}_6\text{H}_4\text{O}_2 \\ & & \\ \text{H} & & \text{H} \end{array} \right]^-$
Li [F2H6]	LiB[C ₆ F ₁ H ₅ O ₂] ₂ lithium bis-[3-fluoro-1,2-benzenediolato (2-)-O,O']borate <i>[Synthesis]</i>	$\text{Li}^+ \left[\begin{array}{c} \text{F} & & \text{F} \\ & & \\ \text{C}_6\text{FH}_5\text{O}_2 & \text{--- B ---} & \text{C}_6\text{FH}_5\text{O}_2 \\ & & \\ \text{H} & & \text{H} \end{array} \right]^-$
Low Temperature Ionic Liquids Section {4.2}		
[C ₁₆ -mim] [Cl]	C ₂₀ H ₃₉ N ₂ Cl 1-N-hexadecyl-3-methylimidazolium chloride <i>[Synthesis]</i>	
(Oligo)ethyleneglycolallylmethylethers Section {4.4.2}		
(EGE-A)	A = C ₆ H ₁₂ O ₂ 4,7-dioxa-1-octen (ethyleneglycolallylmethylether) <i>[Synthesis]</i>	
(EGE-B)	B = C ₈ H ₁₆ O ₃ 4,7,10-trioxa-1-undecan (di-ethyleneglycolallylmethylether) <i>[Synthesis]</i>	
H-Silicone Section {4.4.3}		
H-Silicone 60	C ₆₆ H ₂₅₈ O ₆₁ Si ₆₂ Polymethylhydrosiloxanes 60 <i>[Wacker Chemie]</i>	

Table. (4.1.1)

4.1.1.

Synthesis of Lithium bis-[3,4,5,6-tetrafluoro-1,2- benzenediolato (2-)-O,O']borate Salt – Li [F8]

The following lithium salts were synthesised according to the procedures outlined by Schmid ^[10 - 11] with a few refinements as indicated. The synthesis of lithium bis-[3,4,5,6-tetrafluoro-1,2-benzenediolato(2-)-O,O']borate is relatively complex and labour intensive and is summarised in Fig. (4.1.2).

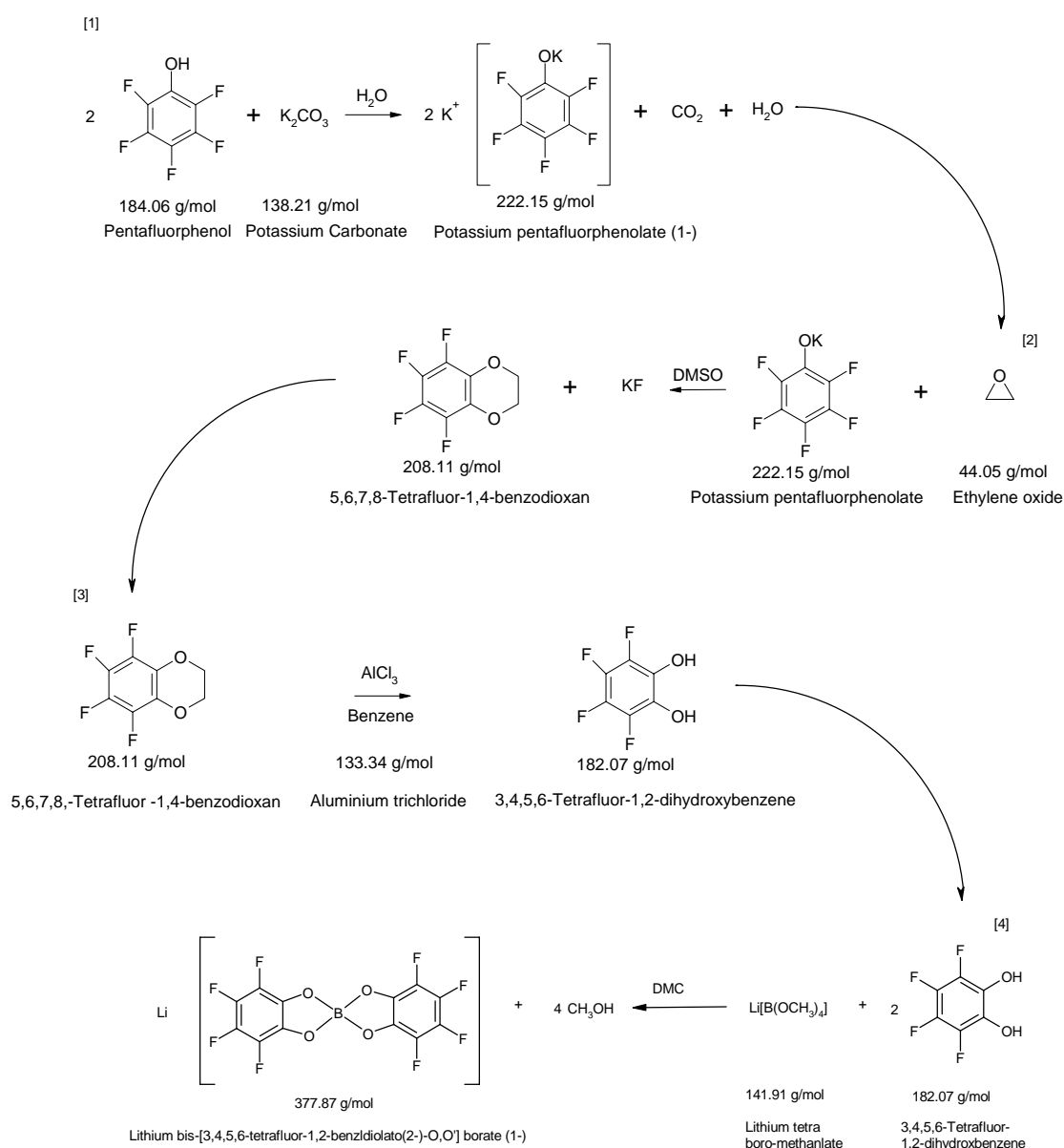
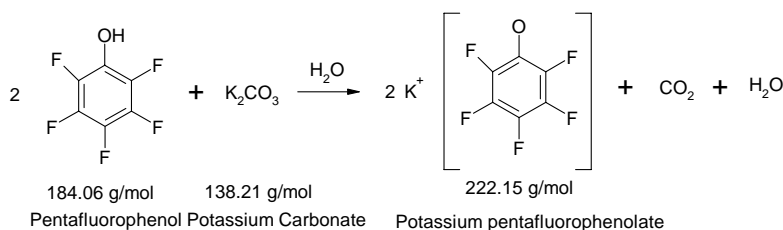


Fig. (4.1.2)

4.1.1.

[1] Potassium Pentafluorophenolate



General product information:

Material	Yield (%)	M (g mol ⁻¹)	Melting Point (°C)	Properties
potassium pentafluorophenolate (1-)	80	222.15	240	white crystals

Reagents:

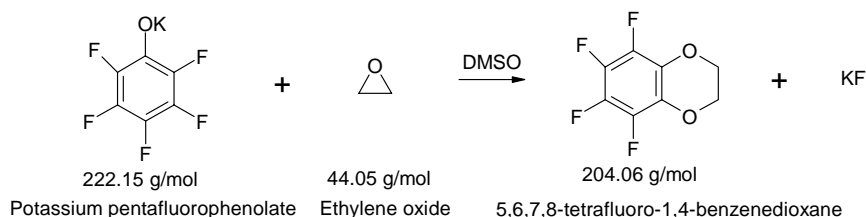
pentafluorophenol:	[Apollo]	99 %	C ₆ F ₅ HO	184.06 g mol ⁻¹
potassium carbonate:	[Merck]	99 %	K ₂ CO ₃	138.21 g mol ⁻¹

Procedure:

In a 2000 ml round bottomed flask, 96 g of pentafluorophenol is added and dissolved in 100 ml of distilled water. After vigorous stirring under nitrogen, 48.38 g of K₂CO₃ are added, where a vigorous reaction of gas ensues. On the clearing of the reaction solution, the temperature of the flask is elevated to 90 °C and a further 240 ml of distilled water is added to the solution. The reaction mixture is allowed to cool down slowly to room temperature. At approximately 50 °C, large colourless needle-like crystals begin to form. To achieve complete recrystallisation the flask is placed in a fridge for 30 hrs. at 4 °C. The solid recrystallised material is filtered in a G4 glass filter and washed with 50 ml distilled water four times. Finally, the material is dried for 24 hours at 135 °C until there is no further weight loss of the product measured.

4.1.1.

[2] 5,6,7,8-tetrafluoro-1,4-benzenedioxan



General product information:

Material	Yield (%)	M (g mol ⁻¹)	Melting Point (°C)	Properties
5,6,7,8-tetrafluoro-1,4-benzenedioxane	97	204.06	72 - 74	light brown strong smell

Regents:

ethylene oxide:	[Merck] 98.8 %	C ₂ H ₄ O	44.05 g mol ⁻¹
potassium pentafluorophenolate:	synthesised	C ₆ F ₅ KO	222.15 g mol ⁻¹
dimethylsulphur oxide (DMSO)	[Merck] 99.8 % Dried (35ppm H ₂ O)	(CH ₃) ₂ SO	78.13 g mol ⁻¹
di-phosphorus pentoxide:	[Sigma] 98 %	P ₂ O ₅	141.94 g mol ⁻¹
argon :	[Linde AG] 93% - 7 % H ₂ -mix.	Gas	

Procedure:

The chemical ethylene oxide exists at STP³⁴ in a gaseous state, therefore when in experimental use; it should be handled with extreme care due to its high reactivity and toxicity. During reaction with other materials, a special constructed flask of 1000 ml is utilised. This round bottomed glass flask has two in-built glass frits for the bubbling of ethylene oxide and argon gases respectively. The first part of this procedure takes approximately 8 hrs.

In the initial stages of the experiment 150 ml DMSO is poured into the glass flask which is flooded with argon gas for 5 mins. The flask is sealed from the atmosphere. This is followed by the dissolving of 62.52 g of the previously synthesised potassium pentafluorophenolate {4.1.1.[1]} in 250 ml DMSO in a 500 ml dropping funnel. This dropping funnel plus contents is then firmly fixed atop of the glass flask, where a flow of argon gas is initiated to maintain an inert atmosphere within the flask. The contents of the

³⁴ STP = Standard Temperature and Pressure

flask are heated slowly to 176 °C (± 1 °C). When the appointed temperature is reached and remains, stable the prepared potassium pentafluorophenolate/DMSO solution in the dropping funnel is added to the 150 ml DMSO in the mixing flask. The dissolved pentafluorophenolate/DMSO is released into the flask drop-wise at a rate of approximately 50 ml for 45 mins. At the same time in the one of the free frits the ethylene oxide gas is released and bubbled into the flask at a rate of 0.3 g in 5 mins. (Total at end 24.76 g). This reduction in mass is verified by continually weighting of the gas bottle at regular intervals. During the mixing of both gas and solution, the contents should be stirred with a magnetic stirrer at a rate of about 350 rpm. Near the completion of the reaction one should calculate that the potassium pentafluorophenolate in DMSO solution is completely used up before the proscribed amount of ethylene oxide is achieved. In an ideal situation, there should be still 2.8 – 3.0 g of ethylene oxide to be consumed by the reaction. The remaining excess gas is added for a further 1.5 hours until the target amount of ethylene oxide is achieved (24.76 g).

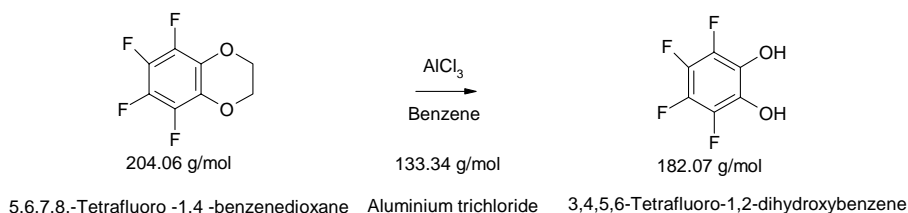
Once the above procedure is completed, the flask is allowed to cool down to 60 °C and left for 36 hrs. to further react. In the flask, one will observe the formation of a dark brown material with a very strong smell. This material is poured on top of approximately 800 g of ice and left until 60 – 70 % of the ice is melted. Then with the utilisation of a G3 glass filter under weak vacuum the rough product is extracted where it is further washed five to six times in 75 ml distilled water. The vacuum dried product is held in a recrystallisation glass and placed over di-phosphorus pentoxide powder for four days at STP in a vacuum desiccator.

Analysis:

NMR				
Type	δ (ppm)	Splitting Peaks	Group	Literature
^1H [CDCl_3] 250 MHz	4.35	singlet	$-\text{O}-\text{CH}_2^+-\text{CH}_2-\text{O}-$	Carl ^[7]
^{13}C [CDCl_3] 62.9 MHz	64.52 130.1 – 130.5 135.73 137.52	singlet multiplet doublet doublet triplet	C_2/C_3 C_9/C_{10} C_6/C_7 C_5/C_8	All peaks are comparable to the literature – Carl ^[7]

Table. (4.1.1.1.)

4.1.1.

[3] 3,4,5,6-tetrafluoro-1,2-dihydroxybenzene**General product information:**

Material	Yield (%)	M (g mol ⁻¹)	Melting Point (°C)	Properties
3,4,5,6-tetrafluoro-1,2-dihydroxybenzene	85	182.07	72 - 74	light brown strong smell

Reagents:

aluminium tri-chloride:	[Merck] 98 %	AlCl ₃	133.34 g mol ⁻¹
5,6,7,8-tetrafluoro-1,4-benzenedioxane:	synthesised 99.8 %	C ₈ F ₄ O ₂	208.11 g mol ⁻¹
benzene:	[Merck] 99.5 % "synthesis"	C ₆ H ₆	78.12 g mol ⁻¹
hydrochloric acid:	[Merck] 36 %	HCl	36.43 g mol ⁻¹
diethylether:	[Merck] 99.5 % analysis (45 ppm H ₂ O)	C ₄ H ₁₀ O	74.12 g mol ⁻¹
sodium sulphate:	[Merck] 99 %	Na ₂ SO ₄	142.04 g mol ⁻¹
argon :	[Linde AG] 93% - 7 % H ₂ -mix.	Gas	

Procedure:

Due to the chemical nature of aluminium tri-chloride when it comes in contact with moisture, the powder reagents are all mixed and weighted in a nitrogen glove box.

In the initial stages of the experiment excess 82.20g of AlCl₃ is weighted into a 2000 ml round bottomed flask. This is followed by the careful addition of 21.40 g of previously synthesised dried 5,6,7,8-tetrafluoro-1,4-benzodioxan {4.1.1.[2]}. The flask and contents are removed from the nitrogen glove box under a protective gas of nitrogen and are attached to a reflux column and the whole apparatus is then flushed for 5 mins. with argon gas. Approximately 800 ml of benzene is added. Under strong stirring, the flask is refluxed at 85 °C for 12 hrs. During this time, the product will take on a dark brown colour with the release of hydrochloric acid.

After the conclusion of the reaction the product solution is allowed to cool to 60 °C for one hour afterwards is poured on 1000 g of ice. By this action a vigorous reaction takes place (caution!), due to the remaining excess AlCl_3 reacting with water. The solution water mixture is vacuum distilled with a water vacuum pump until all benzene is removed. Concentrated HCl is added until the solution has achieved a pH of about one. This concentrated acidic solution is allowed to be stirred for 12 hours until a sticky dark brown material is formed. This solution product is filtered through normal high vacuum filter paper and the captured dark brown “sludge” is placed in a glass beaker, where it is boiled and filtered. This procedure of filtering and boiling of the dark brown “sludge” is performed three times and all filtrates are combined yielding a dark orange solution.

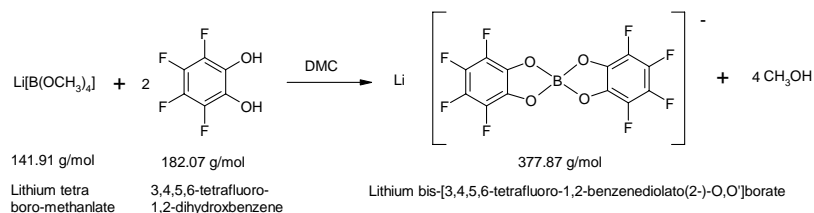
This solution is further mixed with diethylether and phaseally separated from the more dense water phase. The procedure is repeated three times and the diethylether phase solution is retained. The diethylether solution is then placed in a large round bottomed flask, where Na_2SO_4 is added for drying. This powder and solution mixture is stirred for 12 hours and is vacuum filtered. The dried diethylether solution filtrate is carefully evaporated at 45 °C. The remaining residual oil-like substance is placed in a drying oven at 25 °C for two days with the eventual formation of crystal product. This is further purified by sublimation at 60 °C under vacuum.

Analysis:

NMR				
Type	δ (ppm)	Splitting Peaks	Group	Literature
^1H [CDCl_3] 250 MHz	5.84	singlet	HO-C- C-OH*	Carl [8]
^{13}C [CDCl_3] 62.9 MHz	129.57 – 129.95 135.58 137.71	multiplet doublet of multiplet doublet of multiplet	C_1/C_2 C_4/C_5 C_3/C_6	Carl [8]

Table. (4.1.1.2)

4.1.1.

[4] **Lithium bis - [3,4,5,6 – tetrafluoro - 1,2 – benzenediolato (2-) - O,O']borate– Li [F8]****General product information:**

Material	Yield (%)	M (g mol ⁻¹)	Melting Point (°C)	Properties
lithium bis-[3,4,5,6-tetrafluoro-1,2-benzenediolato(2-)-O,O']borate	68	377.84	180	white powder

Reagents:

lithium tetramethanolatoborate:	[Lancaster] 99.8%	$\text{Li}[\text{B}(\text{OCH}_3)_4]$	141.91 g mol ⁻¹
di-methyl carbonate (DMC) - dried	[Merck] 99 % Dried	$\text{C}_3\text{H}_6\text{O}_3$	90.08 g mol ⁻¹
3,4,5,6-tetrafluoro-1,2-dihydroxybenzene:	(synthesised)	$\text{C}_6\text{H}_2\text{O}_2\text{F}_4$	182.07 g mol ⁻¹
benzene	[Merck] 99.5 % synthesis	C_6H_6	78.12 g mol ⁻¹
cyclohexane:	[Merck] 99.5 % Dried (48 ppm H ₂ O)	C_6H_{12}	82.15 g mol ⁻¹
argon :	[Linde AG] 93% - 7 % H ₂ -mix.	Gas	

Procedure:

In a 200 ml nitrogen flask, 17.74 g of lithium tetramethanolatoborate is added to 20 ml DMC under a protective gas of argon. In a second flask 45.54 g of purified and dried previously synthesised 3,4,5,6-tetrafluoro-1,2-dihydroxybenzene {4.1.1.[3]} is dissolved in 50 ml DMC. Both solutions are mixed and stirred together. On completion of the transfer to a new flask, the solution mixture is rinsed with DMC. This action caused the immediate formation of a colourless to pink solution which is stirred for one hour at room temperature. In the final step of preparation the formed methanol and solution is dried for 24 hrs. with an oil pump at a stable temperature 50 °C.

For the purification of the sample, the brown product is mixed with 20 ml of benzene. The mixture is heated to 90 °C, followed by the drop-wise addition of DMC until the raw product is dissolved. Cyclohexane is added to assist in the crystallisation of the salt. The

solution is allowed to cool down to 40 °C, where large colourless crystals are seen to form. After 24 hrs. at 6 °C the excess solvent is decanted away and the remaining crystals are washed three times with 20 ml benzene. The salt should be recrystallised a minimum of three times. The product is dried for 24 hours at 40 – 60 °C, 24 at 60 – 80 °C and finally 120 hours at 95 °C with an oil pump. This procedure leaves yields a colourless pure crystalline power.

Analysis:

Elemental Analysis

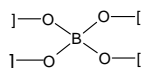
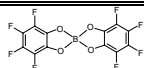
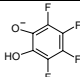
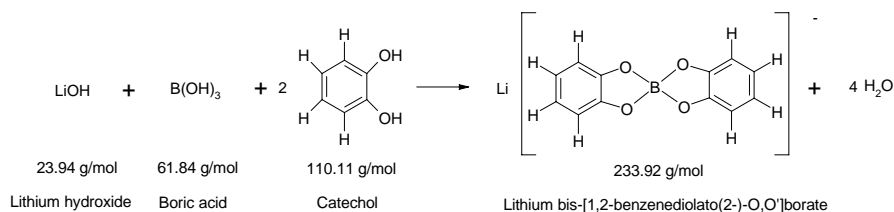
E.A.	Carbon (%)	Boron (%)	Fluorine (%)	Oxygen (%)	Lithium (%)
Calculated	38.15	2.86	40.22	16.94	1.84
Experimental	38.05	-	-	16.89	-
NMR					
Type	δ (ppm)	Splitting	Group	Literature	
¹³ C [CDCl ₃] 62.9 MHz	134.14 132.55 133.92	multiplet of doublet multiplet of doublet	C ₁ /C ₂ C ₄ /C ₅ C ₃ /C ₆	Carl ^[8]	
¹¹ B [CD ₃ CN] 128.4 MHz	-0.8	triplet		Carl ^[8]	
Mass Spectrometry					
Material	m/z	Relative Abundance	Fragment	Literature	
Li [F8]	370.10	100		371 Barthel ^[7]	
	180.70	0.2		182 Barthel ^[7]	

Table. (4.1.1.3)

4.1.2

Synthesis of Lithium bis-[1,2-benzenediolato(2-)-O,O']borate Salt – Li [H8]



General product information:

Material	Yield (%)	M (g mol ⁻¹)	Melting Point (°C)	Properties
lithium bis-[1,2-benzenediolato(2-)-O,O']borate	80	233.92	246	white powder

Reagents:

catechol:	[Merck]	99 %	C ₆ H ₆ O ₂	110.11 g mol ⁻¹
lithium hydroxide	[Merck]	99 %	LiOH	23.94 g mol ⁻¹
boric acid	[Merck]	99.8 %	H ₃ BO ₃	61.84 g mol ⁻¹
acetonitrile - dried	[Merck]	99.5 % Dried (35 ppm H ₂ O)	CH ₃ CN	44.05 g mol ⁻¹
argon :	[Linde AG]	93% - 7 % H ₂ -mix.	Gas	

Procedure:

Before initiating the experiment the reaction apparatus is filled with nitrogen and evacuated three times, parallel the flask is heated to 110 °C to eliminate the presence of water. In a 1000 ml round bottomed flask with an attached reflux cooler is added 249.80 g of brenzcatechol, 47.60 g of LiOH, 70.13 g of boric acid and 130 ml of distilled water. These reagents are placed under a protective gas of argon and heated to 95 °C until a homogenous brown solution is formed. On the formation of this brown solution, the heater is switched off and the solution is allowed to cool down to room temperature for several hours, where the formation of large colourless crystals are observed. In order to increase the yield the flask is placed over night in a fridge at 4 °C. The formed crystalline material is filtered with a water pump in a argon environment. The filtered material is then dried with an oil pump at STP for two days with the later formation of colourless crystals. The mass of the crystalline product at this point should be about 170 g. The raw crystalline product is further vacuum dried at 105 °C for 30 hours until there is no further volume weight change of the material. After this procedure, approximately 144 g (80 %) of a colourless powder is observed to form.

Purification:

Approximately 143 g of the raw product is mixed with a 300 ml of acetonitrile solution. This mixture is heated to just below the boiling point of acetonitrile and kept at all times under an argon environment. Further acetonitrile is added until the remaining dissolved raw product has dissolved to form an homogenous solution. This solution mixture is left over night to recrystallisation, which leads to the observed formation of colourless needle-like crystals. This crystal solution is placed in an ice bath for an hour and a half (1.5hrs) afterwards is transferred to an salt-ice bath (NaCl) for a further hour and a half (1.5hrs). The remaining solution is decanted away under a flow of argon gas. This procedure is repeated three times until the crystalline material changes from a yellowish-green to colourless between the first and third recrystallisation respectively. The colourless crystalline material is then is dried for a further four hours at room temperature permitting the final formation of $\text{Li}[\text{B}(\text{C}_6\text{H}_4\text{O}_2)_2] \times -2\text{AN}$ as a colourless needle-like crystalline material. Finally, the crystalline material is placed in a recrystallisation tube and stepwise heated slowly under vacuum to 150 °C. This drying procedure is continued until there is a stable mass of powder product is achieved. The purity is further verified by the use of NMR data in order to establish the elimination of acetonitrile in the product. The amount of final product should be approximately 65.46 g under the stated conditions.

Analysis:

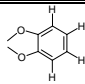
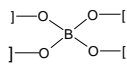
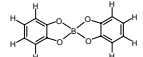
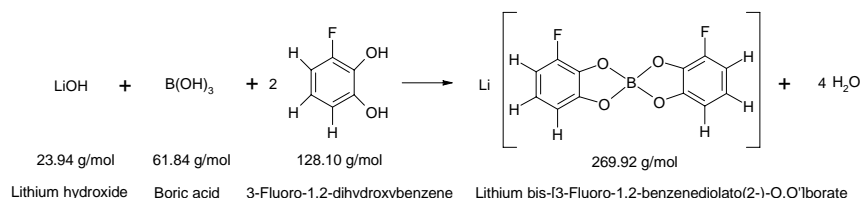
Elemental Analysis					
E.A.	Carbon (%)	Hydrogen (%)	Boron (%)	Oxygen (%)	Lithium (%)
Calculated	61.62	3.45	4.62	27.35	2.97
Experimental	61.44	4.44	-	-	-
NMR					
Type	δ (ppm)	Splitting	Group	Literature	
¹ H [CDCl ₃] 250 MHz	6.60	Quadruple		6.48 Barthel ^[6]	
¹³ C [CDCl ₃] 62.9 MHz	151.48 117.23 106.46	doublet of doublet doublet of multiplet doublet of multiplet	C ₁ /C ₂ C ₄ /C ₅ C ₃ /C ₆	151.6 117.3 107.6 Barthel ^[6]	
¹¹ B [CD ₃ CN] 128.4 MHz	6.59 - 6.66	multiplet			
Mass Spectrometry					
Material	m/z	Relative Abundance	Fragment	Literature	
Li [H8]	226.70	99.80		Barthel ^[6]	
	460.10	31.30	2(A ⁻) + Li ⁺		
	695.30	3.65	3(A ⁻) + 2(Li ⁺)		
	929.5	1.25	4(A ⁻) + 3(Li ⁺)	Barthel ^[11]	

Table. (4.1.2.1)

4.1.3.

Synthesis of Synthesis of Lithium bis-[3 - fluoro-1,2- benzenediolato (2)-O,O']borate Salt – Li [F2H6]



General product information:

Material	Yield (%)	M (g mol ⁻¹)	Melting Point (°C)	Properties
lithium bis-[3-fluoro-1,2-benzenediolato(2)-O,O']borate	67	269.92	270	white powder

Reagents:

3-fluoro-1,2-dihydroxybenzene	[Maybridge] 99.6 %	C ₆ H ₅ FO ₂	8.10 g mol ⁻¹
lithium hydroxide	[Merck] 99 %	LiOH	23.94 g mol ⁻¹
boric acid	[Merck] 99.8 %	H ₃ BO ₃	61.84 g mol ⁻¹
acetonitrile - dried	[ACROS] 99.5 % Dried (35 ppm H ₂ O)	CH ₃ CN	44.05g mol ⁻¹
argon :	[Linde AG] 93% - 7 % H ₂ -mix.	Gas	

Procedure:

In a 25 ml three neck round bottomed flask, 5.82g of 3–fluoro-1,2–dihydroxybenzene, 0.95 g of lithium hydroxide and 1.41 g of boric acid are mixed together. The contents of the flask are evacuated and gassed a minimum of five times with argon gas. This procedure is followed by the injection of 3 ml of bi-distilled water and heated to 110 °C, where a light brown solution is formed. This solution is then allowed to slowly cool down to room temperature, where miniature crystals are observed to form. The contents of the flask are allowed to crystallise for 24 hours at – 5 °C. The remaining solution is decanted away and the crystalline material is slowly heated to 130 °C under vacuum.

Purification:

The whole mass of the raw product is washed three times with decreasing amounts of acetonitrile (i.e. 36, 25, and 20 ml) and after recrystallisation is followed by vacuum drying for approximately 30 hrs. at 150 °C.

Analysis:**Elemental Analysis**

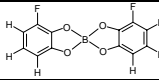
E.A.	Carbon (%)	Hydrogen (%)	Fluorine (%)	Oxygen (%)	Boron (%)
Calculated	53.40	2.24	14.07	23.71	4.01
Experimental	53.29	2.23	-	-	-
NMR					
Type	δ (ppm)	Splitting	Group	Literature	
¹ H [CDCl ₃] 250 MHz	6.28			6.58 Barthel ^[8]	
¹³ C [CDCl ₃] 62.9 MHz	154.10 146.45 136.12 104.02 105.78	doublet doublet doublet doublet doublet	C ₁ C ₃ C ₂ C ₅ C ₄	154.05 146.47 137.30 104.52 105.81 Barthel ^[8]	
¹¹ B [CDCl ₃]	15.68			15.03 Barthel ^[8]	
Mass Spectrometry					
Material	m/z	Relative Abundance	Fragment	Literature	
Li [F2H6]	262.80	99.89			
	533.20	8.34	2(A ⁻) + Li ⁺		
	803.30	0.80	23A ⁻) + 2Li ⁺		

Table. (4.1.3.1)

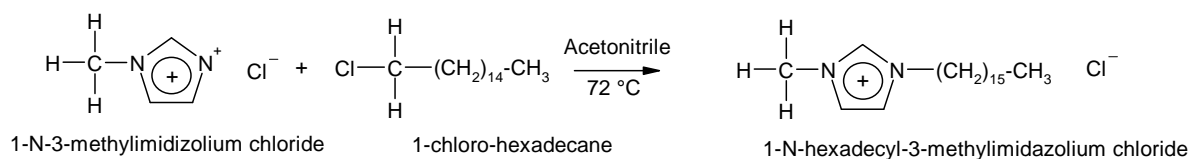
4.2. Synthesis of 1-*N*-hexadecyl-3-methylimidazolium Chloride Salt - [C₁₆-mim] [Cl]

Foreword:

Recent work conducted by Gordon and other authors ^[12 - 15] have investigated long chained 1-*N*-alkyl-3-methylimidazolium and *N*-alkyl-pyridinium ionic salts, where they demonstrated that these materials possessed relatively low melting points, combined with large mesophase ranges. Ionic liquids are now the commonly accepted term for low melting molten salts see section {1}. The alkylation possesses the advantage that there is a wide range of cheap haloalkanes available and that the substitution reactions generally occur smoothly at reasonable temperatures. The reaction temperatures and the time are very dependent on the haloalkane utilised, chloroalkanes being less reactive. The reactivity of the haloalkanes generally decreases with increasing alkyl chain length. Welton ^[16] recommends as a general guide that one should heat 1-methylimidazole with chloroalkanes to about 80 °C for 2 to 3 days to ensure complete reaction. In general, the most important requirement is that the reaction mixture remains free from contact with moisture and other impurities. The reaction may be carried out with the use of an organic solvent, as the reagents are generally liquids and mutually miscible, while halide salt products usually demonstrate a smaller solubility in the starting materials and organic solvent.

The halide salts are generally solids at room temperature, although some examples such as 1-*N*-methyl-3-octylimidazolium exist as a viscous oils at room temperature as reported by Fuller ^[17]. Crystallisation can take some time to occur, however many salts remain as oils even when purified to a high degree. Purification by this author has been best achieved by recrystallisation, through the utilisation of dried acetonitrile, acetone and ethyl acetate. The properties of ionic liquids can be controlled largely by the variation in the nature of both the cation and anion, see section {5.2}. Through increasing of the alkyl side-chain length attached to the cation leads to an alteration in the melting point, with an increase in the viscosity and hydrophobicity of the liquids. A further effect, once a chain of sufficient length is present; the material exhibits the characteristics through the formation of liquid crystalline or *mesogenic* phases on melting. More will be said on this issue latter in section {5.2}.

Synthesis:



General product information:

Material	Yield (%)	M (g mol ⁻¹)	Isotropic (°C)	Properties
[C ₁₆ -mim] [Cl]	88	342.47	66.20	white powder

Reagents:

1-methyl-imidazole – dried	[Merck]	99 % (20 ppm H ₂ O)	C ₄ H ₈ N ₂	82.11 g mol ⁻¹
1-chlorohexadecane	[Merck]	96 % (44 ppm H ₂ O)	C ₁₆ H ₃₃ Cl	260.89 g mol ⁻¹
ethyl acetate	[Merck]	99.5 % selectipur (35 ppm H ₂ O)	C ₄ H ₈ O ₂	88.10 g mol ⁻¹
acetonitrile – dried	[Merck]	99.9 % Dried (37 ppm H ₂ O)	CH ₃ CN	41.04 g mol ⁻¹
acetone – dried	[Merck]	99.5 % analysis Dried (15 ppm H ₂ O)	C ₃ H ₆ O	58.02 g mol ⁻¹
potassium carbonate:	[Merck]	99 %	K ₂ CO ₃	138.21 g mol ⁻¹

Procedure:

The product 1-*N*-hexadecyl-3-methylimidazolium chloride is derived from the reaction of 1-methylimidazole chloride with 1-chloro-hexadecyl dissolved in acetonitrile at 72 °C. The initial preparation consisted of pre-heating a 4000 ml round-bottom flask to 110 °C followed by evacuating and re-gassing with nitrogen three times successively for 15 mins. in each case. The initial experimental procedure required the insertion 100 ml of 1-methylimidazolium and followed by the slow addition of 40 ml acetonitrile at 75 °C under a low flow of nitrogen. Once a temperature equilibrium is established the nitrogen flow is switched off and is followed with the addition of a calculated mass of 328.53 g of 1-chlorohexadecane. The signs of product formation can be observed after 24 hrs. At least twice a day the flask should be rinsed with nitrogen to relieve any backpressure build-up from the reaction within the flask. After four days, the reaction should be completed with the formation of a paste-like material. This newly formed material is stored under a nitrogen environment at all times. Purification is conducted with the further addition of approximately 100 ml of ethyl acetate to assist in recrystallisation. The paste solution mixture is then placed in a cool box at – 15 °C, which greatly assists the recrystallisation process. The organic phase is decanted from the remaining crystal product. This product is a further recrystallised three times from ethyl acetate. This mixture is in turn vacuum dried at elevated temperature for three days yielding small white crystalline solids.

Analysis:

Material	Elemental Analysis			DSC			Mass Spectrometry		¹ H NMR – [C ₁₆ -mim][Cl] Solvent - DMSO			
Shorthand	Element Tested	Calculated (%)	Experimental (%)	C ₁₁ °C	S _A °C	Iso °C	m/z	Fragment	δ - ppm	Splitting	Group Literature Gordon [1]	Fig.
1-N-hexadecyl-3-imidazolium chloride	Carbon	70.14	69.50	-	55.1	66.2	307.1 649.7 673.8	C ₁₆ Imid ⁺ 2(C ₁₆ -mim) + Cl ⁻ 2(C ₁₆ -mim+CH ₃ COO ⁻) ⁺	1.22	Singlet	-C ₁₄ H ₂₈ -	[1]
	Hydrogen	11.48	11.06						3.86	Singlet	-N-CH-N-	[2]
	Nitrogen	10.35	10.10						9.34	Singlet	-N-CH-N-CH-CH-	[3]
	Chlorine	8.17	-						7.75	Doublet	-N-CH-CH-N-	[4]
[C ₁₆ -mim][Cl]									0.85	Triplet	-CH ₃	[5]
									1.77	Triplet	-N-CH ₂ -C _x -	[6]
									4.16	Triplet	H ₃ C-N-	[7]

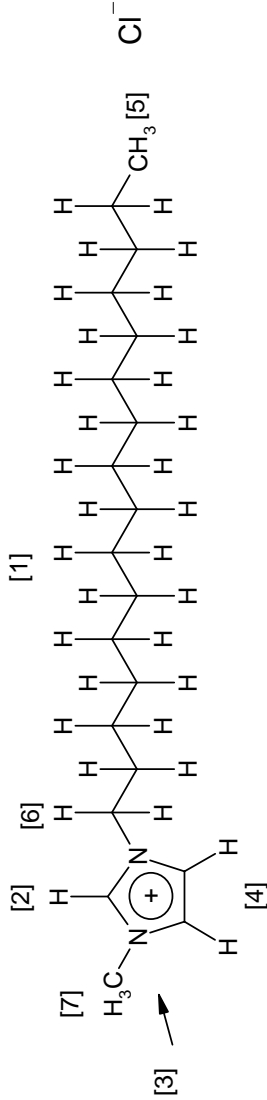
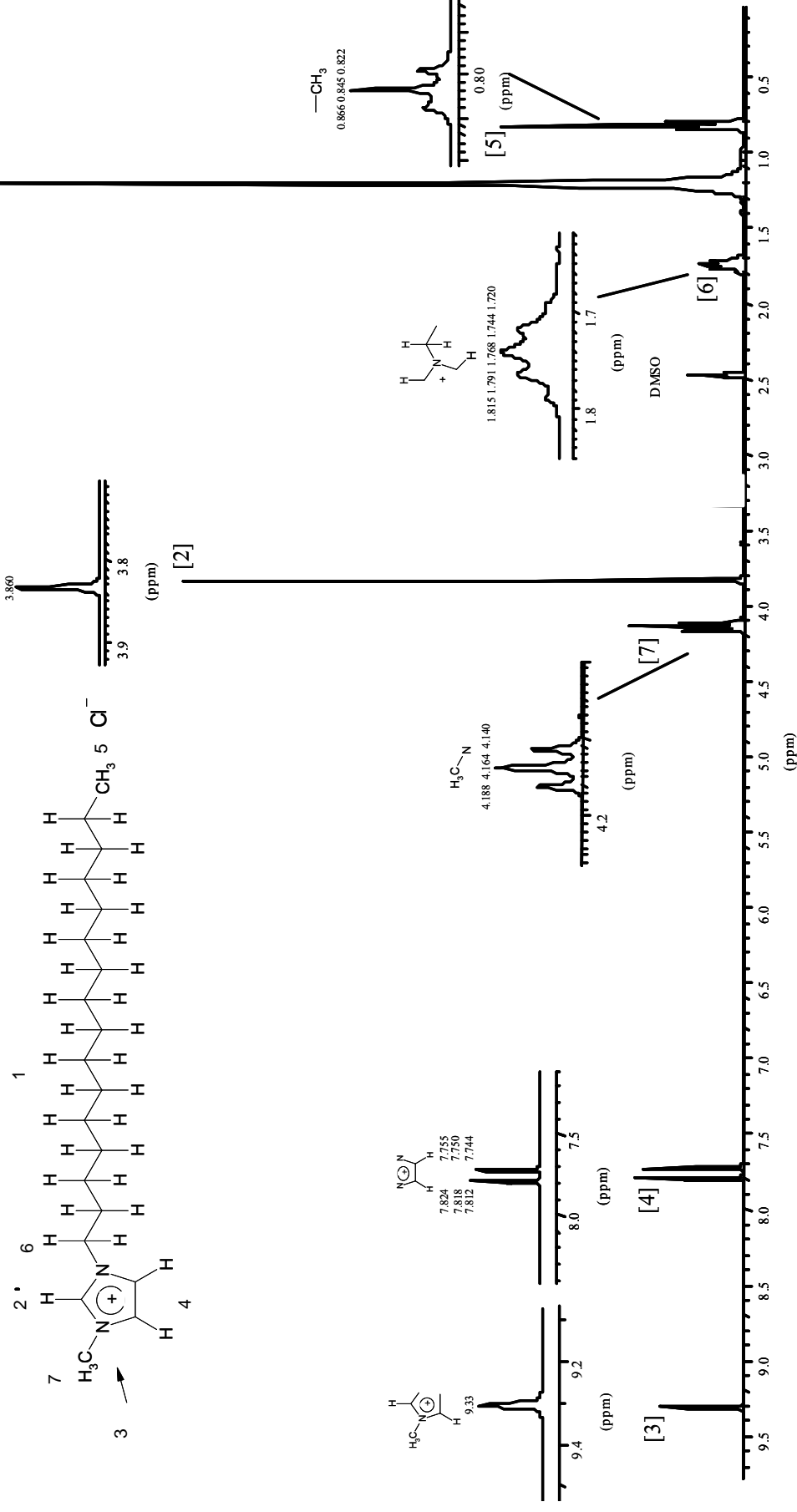


Table. (4.2.1)

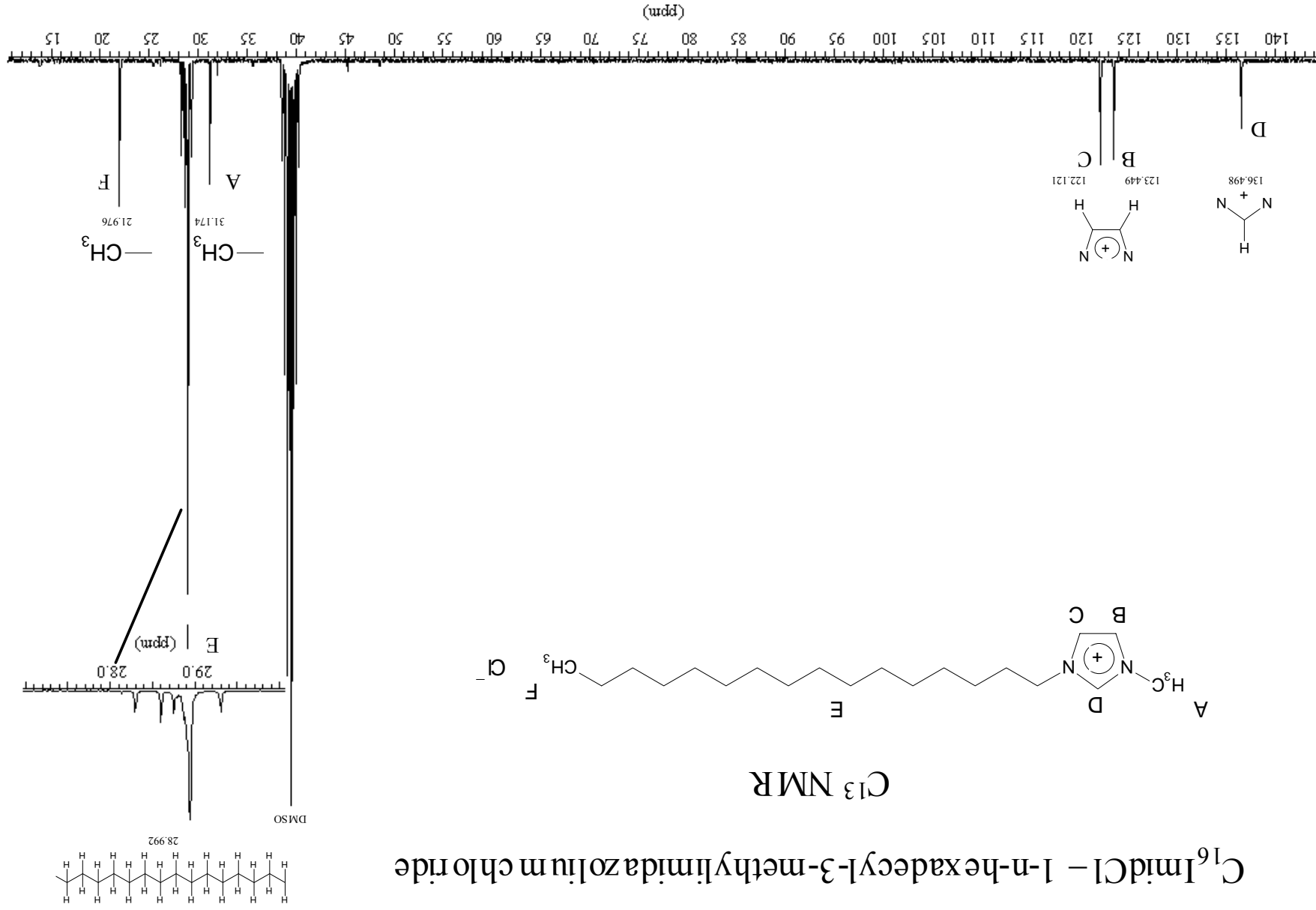
C_{16} ImidCl - 1-n-hexadecyl-3-methylimidazolium chloride

H^1 – Proton NMR



C_{16} ImidCl – 1-n-hexadecyl-3-methylimidazolium chloride

^{13}C NMR



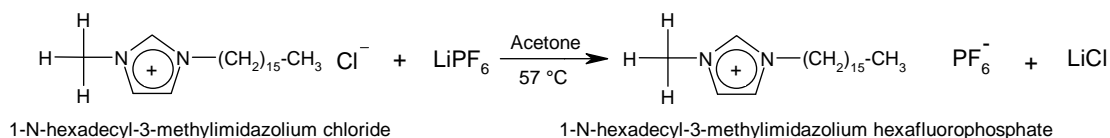
4.3. General Procedure for the Substitution of Anions with Imidazolium Cations

Foreword:

The anion exchange reactions of low temperature ionic liquids can be divided into two distinct categories as laid down by Welton^[15]: (I) direct treatment of halide salts with Lewis acids and (II) the formation of ionic liquids by anions metathesis. For the purposes of this work, the later approach was followed. There are wide ranges of methods that have been applied over the years and many authors have suggested refinements of the methods employed^[18 - 19]. The preparative methods employed by many authors generally follow similar lines^[20]. The main objective of all anion exchange reactions is the formation of the desired ionic liquid uncontaminated with unwanted cations of anions. Cammarata^[21] and Fuller^[22] demonstrated metathesis reactions can be carried out entirely in organic solvents.

Purification of ionic liquids formed by anion metathesis can expose a number of problems as this author experienced. The most common impurities are halide anions such as chlorine ion, which during anion exchange synthesis, the chloride ion is ineffectively separated from the final product. The presence of such impurities is not only extremely detrimental for further electrochemistry investigations, but the presence of such undesired impurities can also alter the nature and behaviours the materials. Many authors^[22 - 27] have reported that the physical properties such as densities and viscosities of affected materials can be radically altered by the presence of unwanted ions. In practical terms, it is suggested by this author and others that in any application where the presence of halide ions many cause problems, the concentrations of these undesired impurities should be monitored. Clearly, the impurity likely to be present in large concentrations in most ionic liquids is water. The removal of reaction solvents is generally easily achieved by heating the ionic liquid under vacuum. Water is generally one of the most problematic impurities to remove, and as described in this section during synthesis, the presence of water was kept to a minimum (35ppm) during all preparations. The ionic liquids should be heated to at least 70 °C for several hours with stirring to achieve an acceptable level of reduced water. According to Welton^[16] 1-*N*-heptyl-3-methylimidazolium chloride can absorb 2 wt % water, when exposed to air for an extended period. Therefore all ionic liquids must be stored in inert environments i.e. a glove box. If an exact knowledge of the amount of water content water present in a sample is required, then the water content of the material in question can be determined by utilising the Karl-Fischer³⁵, titration method, and the less precise method of IR spectroscopy.

35 Karl Fischer (Model CA-02, AbimED Analysen- Technik)

Synthesis:**Procedure:**

The following description is the general procedure applied to all anion exchanges that were performed with the 1-*N*-hexadecyl-3-methylimidazolium chloride ionic liquids and the named lithium salts already outlined in table (4.1.1).

In argon filled glove box an exact amount of purified 1-*n*-hexadecyl-3-methylimidazolium chloride powder is weighted into a nitrogen flask. This is followed by the corresponding calculated mole mass of the respective lithium salt. Approximately five times the mass of the combined reactants of dried ethyl acetate (99.98 % - dried 35 ppm H₂O) is added and the reactants are stirred for 24 hrs. The solution is permitted to cool down and recrystallise where fine white crystals are observed to form. The crystal suspension is filtered to remove the precipitated lithium chloride salt. The organic phase is removed by drying under vacuum. The crystalline product is redissolved in diethyl ether and washed three times with dried acetone (98.5 % analysis). The water content (≈125 ppm) within the acetone assists in the further precipitation of lithium chloride. The organic phase is cooled with ice to 4 °C encouraging recrystallisation. After low vacuum drying of the product for 6 hrs; the recrystallised product was observed to form as a fine crystalline powder. The recrystallisation process was repeated three times to ensure that all LiCl was removed from the product and that the product was as pure as possible. The pure recrystallised product was further vacuum dried in a desiccator for 24 h. The purity of all salts was checked by titration, ¹H NMR, ¹³C NMR, DSC and MS.

4.3.1.

Purification of Newly Synthesised Imidazolium Salts – Titration of LiCl:

At the beginning of this chapter, the author emphasised the current difficulties researchers are encountering in acquiring reliable published data of various statistical values of many ionic liquids. It is often the case that the data values are influenced by impurities left-over from their syntheses. From the perspective of characterisation of newly synthesised ionic liquids in many circumstances, certain quantities of impurities can be tolerated. But in the circumstances of electrochemical experiments very sample amounts of impurities can lead to serious erroneous if not invalid data results. Therefore, every possible precaution must be taken to ensure that the samples are as pure as possible.

In the previous section {4.3}, the author presented a method for an anion exchange between imidazolium and the lithium salts. The chief by-product of this procedure is LiCl. The purification of the salts and the removal of the LiCl proved extremely difficult. In normal circumstances, LiCl is extracted by washing the salt with purified water, in which the LiCl salt in most circumstances falls out of the solution. In the case of our newly synthesised lithium salts that were presented earlier in sections {4.1.1}, {4.1.2}, and {4.1.3}, the application of water as a means of removal of LiCl was out of the question due to their extreme sensitivity to moisture. The above procedure of anion exchange and purification required both patience and a good sense of feel and common sense. During literature searches, the author found presently no reliable non-aqueous method of extraction for LiCl. The aforementioned method in section {4.3} of purification was extremely effective in this work. In most salts after numerous washings with acetone and ethyl acetate, extremely low concentrations of LiCl were detected by means titration.

Titration Method:

The most common method for the measurement of the remaining amount of LiCl in the substituted imidazolium salts is accomplished by the titration of LiCl with silver nitrate solution.

Titration American Chemical Society Method^[32]:

Weigh accurately between 0.15 to 0.20 g of salt sample and dissolve in 50 ml of Millipore water (all samples are water-soluble) in a 250 ml glass-stoppered flask. Add 1 ml of dichlorofluorescein. While stirring, mix and titrate with 0.1 N silver nitrate solutions. The silver nitrate flocculates and the mixture changes to a faint pink colour.

$$\%LiCl = \frac{\text{ml} \times N \text{ AgNO}_3 \times 4.239}{\text{Sample wt (g)}} \quad \text{Equ. [4.1.]}$$

In most salts, the percentage of LiCl was found to have less than 0.001 % which is well within tolerances. Other techniques were also utilised for the detection of the remaining LiCl. The method of mass spectroscopy is also an extremely useful technique in determining the extent of the removal of the newly formed LiCl by-product after purification. Another simpler and quicker test that can be carried out in the laboratory to check for the presence of LiCl in any sample is to use a flame test. By passing a small amount of purified sample over a Bunsen flame one can determine if the substitution reaction was a success from the ensuing flame colour. The compound lithium chloride exhibits a distinctive red colour on being passed over a flame.

Note:

The presence of water within the acetone organic solvent, played important but necessary role in assisting in the removal of the remaining dissolved LiCl. In similar experiments of other authors, all the substituted products were washed in water. Acetone was considered by the author to be the appropriate solvent that dissolves all the reactants readily and retained enough water to promote the expulsion of LiCl without being detrimental to the overall process. Later titration, IR, MS, and ¹H-NMR investigations confirmed the wisdom of this procedure. For similar samples in the literature, good repeatability was observed. The following tables (4.3.1) to (4.3.4) summarise the characterisations of these materials and where possible literature sources for evaluation. The characteristics and behaviours of the substituted anions can be seen in tables (4.3.1) to (4.3.4).

Table. (4.3.1)

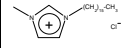
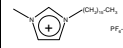
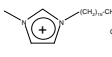
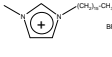
Synthesis : 1- <i>N</i> -hexadecyl-3-methylimidazolium hexafluorophosphate [C ₁₆ -mim] [PF ₆]											
	Name <i>Shorthand</i>	Structure	M: g mol ⁻¹	Melting Point DSC			Mass Spectrometry MS		¹ H-NMR -[C ₁₆ -mim] [PF ₆] Solvent - DMSO		
				K °C	S _A °C	Iso °C	m/z	Fragment	δ - ppm	Splitting	Group
Cation	1- <i>N</i> -hexadecyl-3-methylimidazolium chloride <i>[C₁₆-mim] [Cl]</i>		342.47	-	55.1	66.2	307.1	C ₁₆ -mim ⁺	1.24	singlet	-C ₁₄ H ₂₈ -
							649.7	2(C ₁₆ mim ⁺)Cl ⁻	3.35	singlet	-N-CH-N-
							673.8	2(C ₁₆ -mim ⁺ CH ₃ COO ⁻)	9.10	singlet	-N-CH-N-CH-CH-
Anion	lithium hexafluorophosphate <i>LiPF₆</i>	LiPF ₆	151.90	NA.			N.A.		7.71–7.78	doublet	-N-CH-CH-N-
									0.85	triplet	-CH ₃
									1.78	triplet	-N-CH ₂ -C _x -
Product	1- <i>N</i> -hexadecyl-3-methylimidazolium hexafluorophosphate <i>[C₁₆mim] [PF₆]</i>		452.50	8.2	75.1	125	307.1	C ₁₆ -mim ⁺	4.14	triplet	H ₃ C-N-
							759.8	C ₁₆ -mim ⁺ PF ₆ ⁻			
							649.8	2(Cat ⁺) + Cl ⁻ <i>Very Weak</i>			

Table. (4.3.2)

Synthesis : 1- <i>N</i> -hexadecyl-3-methylimidazolium tetrafluoroborate [C ₁₆ -mim] [BF ₄]											
	Name <i>Shorthand</i>	Structure	M: g mol ⁻¹	Melting Point DSC			Mass Spectrometry MS		¹ H-NMR - [C ₁₆ -mim] [BF ₄] Solvent - DMSO		
				K °C	S _A °C	Iso °C	m/z	Fragment	δ - ppm	Splitting	Group
Cation	1- <i>N</i> -hexadecyl-3-methylimidazolium chloride <i>[C₁₆-mim] [Cl]</i>		342.47	-	55.1	66.2	307.1	C ₁₆ -mim ⁺	1.24	singlet	-C ₁₄ H ₂₈ -
							649.7	2(C ₁₆ mim ⁺)Cl ⁻	3.35	singlet	-N-CH-N-
							673.8	2(C ₁₆ -mim ⁺ CH ₃ COO ⁻)	9.10	singlet	-N-CH-N-CH-CH-
Anion	lithium tetrafluoroborate <i>LiBF₄</i>	LiBF ₄	93.74	NA.			N.A.		7.71–7.78	doublet	-N-CH-CH-N-
									0.85	triplet	-CH ₃
									1.78	triplet	-N-CH ₂ -C _x -
Product	1- <i>N</i> -hexadecyl-3-methylimidazolium tetrafluoroborate <i>[C₁₆-mim] [BF₄]</i>		394.34	-	41.1	81.8	307.1	C ₁₆ -mim ⁺	4.14	triplet	H ₃ C-N-
							701.8	C ₁₆ -mim ⁺ BF ₄ ⁻			
							649.7	2(Cat ⁺) + Cl ⁻ <i>Very Weak</i>			

Tab. (4.3.3)

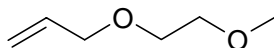
Synthesis : 1- <i>N</i> -hexadecyl-3-methylimidazolium bis-[1,2-benzenediolato(2-)-O,O']borate [C ₁₆ -mim] [H8]											
	Name <i>Shorthand</i>	Structure	M: g mol ⁻¹	Melting Point DSC			Mass Spectrometry MS		¹ H-NMR - [C ₁₆ -mim] [H8] Solvent - DMSO		
				K °C	S _A °C	Iso °C	m/z	Fragment	δ - ppm	Splitting	Group
Cation	1- <i>N</i> -hexadecyl-3-methylimidazolium chloride <i>[C₁₆-mim] [Cl]</i>		342.47	-	55.1	66.2	307.1	C ₁₆ -mim ⁺	1.24	singlet	-C ₁₄ H ₂₈ -
							649.7	2(C ₁₆ mim ⁺)Cl ⁻	3.35	singlet	-N-CH-N-
							673.8	2(C ₁₆ -mim ⁺ CH ₃ COO ⁻) ⁺	9.10	singlet	-N-CH-N-CH-CH-
Anion	lithium bis-[1,2-benzenediolato(2-)-O,O']borate <i>Li [H8]</i>		224.25	246			226.7		7.71–7.79	doublet	-N-CH-CH-N-
							460.1	2(A ⁻) + Li ⁺	0.83	triplet	-CH ₃
							695.3	3(A ⁻) + 2(Li ⁺)	1.78	triplet	-N-CH ₂ -C _x -
Product	1- <i>N</i> -hexadecyl-3-methylimidazolium bis-[1,2-benzenediolato(2-)-O,O']borate <i>[C₁₆-mim] [H8]</i>		524.52	36.1	63.4	97.1	307.1	C ₁₆ -mim ⁺	4.14	triplet	H ₃ C-N-
							841.8	2(Cat ⁺) + A ⁻	6.60	quadruplet	
							649.7	2(C ₁₆ mim ⁺)+Cl ⁻ <i>Very Weak</i>			

Tab. (4.3.4)

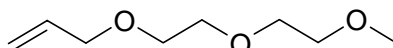
Synthesis : 1- <i>N</i> -hexadecyl-3-methylimidazolium bis-[3,4,5,6-tetrafluoro-1,2-benzenediolato(2-)-O,O']borate [C ₁₆ -mim] [F8]											
	Name <i>Shorthand</i>	Structure	M: g mol ⁻¹	Melting Point DSC			Mass Spectrometry MS		¹ H-NMR - [C ₁₆ -mim] [F8] Solvent - DMSO		
				K °C	S _A °C	Iso °C	m/z	Fragment	δ - ppm	Splitting	Group
Cation	1- <i>N</i> -hexadecyl-3-methylimidazolium chloride <i>[C₁₆-mim] [Cl]</i>		342.47	-	55.1	66.2	307.1	C ₁₆ ⁺ mim ⁺	1.24	singlet	-C ₁₄ H ₂₈ -
							649.7	2(C ₁₆ mim ⁺)Cl ⁻	3.35	singlet	-N-CH-N-
							673.8	2(C ₁₆ -mim ⁺ CH ₃ COO ⁻) ⁺	9.10	singlet	-N-CH-N-CH-CH-
Anion	lithium bis-[3,4,5,6-tetrafluoro-1,2-benzenediolato(2-)-O,O']borate <i>Li [F8]</i>		377.84	180			370.1		7.71–7.78	doublet	-N-CH-CH-N-
							180.7		0.85	triplet	-CH ₃
									1.78	triplet	-N-CH ₂ -C _x -
Product	1- <i>N</i> -hexadecyl-3-methylimidazolium bis-[3,4,5,6-tetrafluoro-1,2-benzenediolato(2-)-O,O']borate <i>[C₁₆-mim][F8]</i>		678.44	-	34.7	71.6	370.9		4.14	triplet	H ₃ C-N-
							370.1				
							749.1	2(A ⁻) + Li ⁺			

4.4. Procedure for the Synthesis (Oligo)ethylen glycol allyl methylethers (EGE)

Synthesis 4,7-Dioxa-1-octen (ethylen glycol allyl methylether) (EGE-A)

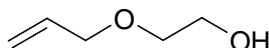


Synthesis 4,7,10-Trioxa-1-undecane (diethylen glycol allyl methylether) (EGE-B)

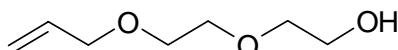


4.4.1. Synthesis of (Oligo)ethylen glycol mono allyl ethers

Synthesis 4-Oxa-5-hexen-1ol (Ethylen glycol mono allyl ether)



Synthesis 4,7-Dioxa-8-nonen-1-ol (Diethylen glycol mono allyl ether)



Part (1)

General product information:

Material	Yield (%)	M. (g mol ⁻¹)	B.P. (°C)	Properties
4-oxa-5-hexen-1ol (ethylen glycol mono allyl ether)	56	102.13	60 (15 Torr)	colourless liquid
4,7-Dioxa-8-nonen-1-ol (diethylen glycol mono allyl ether)	51	146.19	85 (0.1 Torr.)	colourless liquid

Reagents:

potassium hydroxide	[Merck]	97 %	KOH	56.11 g mol ⁻¹
dichloro-methane – dried:	[Merck]	99.98 % dried (25 ppm H ₂ O)	CH ₂ Cl ₂	84.91 g mol ⁻¹
allylbromide (3 brom-1-propane):	[Merck]	98 %	C ₃ H ₅ Br	120.98 g mol ⁻¹
magnesium sulphate	[Merck]	98%	MgSO ₄	120.37 g mol ⁻¹
ethylen glycol dimethylether	[Merck]	99.8 % (60 ppm H ₂ O) dried	C ₄ H ₁₀ O ₂	90.12 g mol ⁻¹
ethylen glycol diethylether	[Merck]	95.8 % (45 ppm H ₂ O) dried	C ₆ H ₁₄ O ₂	118.18 g mol ⁻¹
argon :	[Linde AG]	93% - 7 % H ₂ -mix.	Gas	

Procedure:

In a three necked flask 16.8 g KOH (0.30 mol) is suspended in 0.30 mol of the corresponding amount of (Oligo)ethyleneglycol and stirred with a KPG stirrer until all the KOH is fully dissolved. After complete dissolution of KOH, 36.3 g (0.30 mol 25.4 ml) of distilled allylbromide is added to the mixture and heated and refluxed for three hours at 60 °C. After cooling down 200 ml of dichloromethane is added and the newly formed KBr is extracted by a minimum of four times washing the organic phase with water. The water phase is washed ten times with dichloromethane. The combined organic phases are dried with magnesium sulphate and distilled to a colourless solution. There was good repeatability between the experimental characterisation results and those in the literature ^[28], which are cited in the tables below.

Analysis:

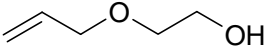
Material Literature ^[29]	¹ H-NMR [CDCl ₃]/TMS 250 MHz			IR	
	δ (ppm)	Splitting	Group	cm ⁻¹	Groups
Section (4.4.1) Part (1)  4-oxa-5-hexen-1-ol (ethyleneglycolmonoallylether)	2.35	singlet	1H, -OH	3081	C-H olef
	3.54 -3.67	triplet	2H, -HOCH ₂ CH ₂ O-	2867	C-H aliph
	3.71-3.78	multiplet	2H, -CH ₂ -CH=CH ₂	1648	C=C
	4.04	doublet doublet	2H, -CH ₂ -CH=CH ₂	1066	C-O-C
	5.22	doublet	1H, -CH ₂ -CH=CH _{cis}		
	5.93	doublet	1H, -CH=CH ₂		

Table. (4.4.1a)

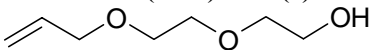
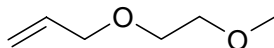
Material Literature ^[29]	¹ H-NMR [CDCl ₃]/TMS 250 MHz			IR	
	δ (ppm)	Splitting	Group	cm ⁻¹	Groups
Section (4.4.1) Part (1)  4,7-Dioxa-8-nonen-1-ol (diethyleneglycolmonoallylether)	2.70	singlet	1H, -OH	3437	O-H
	3.59 -3.74	multiplet	8H, -OCH ₂ CH ₂ O-	3085	C-H
	4.04	doublet doublet	2H, -CH ₂ -CH=CH ₂	2867	C-H
	5.18	doublet triplet	1H, -CH ₂ -CH=CH _{cis}	1645	C=C
	5.27	doublet triplet	1H, -CH ₂ -CH=CH _{trans}	1068	C-O-C
	5.93	doublet	1H, -CH=CH ₂		

Table. (4.4.1b)

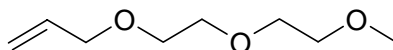
4.4.2.

Synthesis of (Oligo)ethyleneglycolallylmethylethers

Synthesis 4,7-dioxa-1 - octen (ethyleneglycolallylmethylether) (EGE-A)



Synthesis 4,7,10-trioxa-1-undecane (diethyleneglycolallylmethylether) (EGE-B)



Part (2)

General product information:

Material	Yield (%)	M. (g mol ⁻¹)	B.P. (°C)	Properties
4,7-dioxa-1-octen (ethyleneglycolallylmethylether)	75	116.16	127	colourless liquid
4,7,10-trioxa-1-undecane (diethyleneglycolallylmethylether)	88	370.52	85 (5 Torr.)	colourless liquid

Reagents:

sodium hydride	[Merck] 60 %	NaH	15.01 g mol ⁻¹
dichloromethane – dried:	[Merck] 99.5 % analysis	CH ₂ Cl ₂	84.91 g mol ⁻¹
allylbromide (3 brom-1-propane):	[Merck] 98 %	C ₃ H ₅ Br	120.98 g mol ⁻¹
{4.4.1} ethyleneglycolmonoallylether*:	synthesized Dried (35 ppm H ₂ O)	C ₅ H ₁₀ O ₂	102.13 g mol ⁻¹
{4.4.1} diethyleneglycolmonoallylether*:	synthesized Dried (30 ppm H ₂ O)	C ₇ H ₁₄ O ₃	146.19 g mol ⁻¹
argon :	[Linde AG] 93% - 7 % H ₂ -mix.	Gas	

Procedure:

In a three necked flask 8 g NaH (0.20 mol, 60%) is suspended in 100 ml absolute CH₂Cl₂ and cooled in ice. Then 0.20 mol of the corresponding amount of (oligo) ethyleneglycolmonoallylethers* is added to the previous mentioned and stirred with a KPG stirrer while at the same time cooled with ice. Stirring of the solution is continued until all the evolved gas is dissipated. On dispersion of the observed gas 24.2 g (0.20 mol 16.9 ml) of distilled allylbromide in 50 ml CH₂Cl₂ is added under cooling of ice and the combined solutions are refluxed for two hours at 60 °C. After cooling the solution is filtered under vacuum and 75 ml of distilled water is added, where the organic phase is separated from the water phase. The water phase is further washed three times with 50 ml CH₂Cl₂, the combined organic phases are again washed with distilled water, and the separated organic phase is dried

with Na₂SO₄. This solution is vacuum filtered and the organic phase is distilled. The CH₂Cl₂ is first distilled by 38 °C and the required distillate is further distilled under vacuum. A colourless liquid product should be achieved. There was good repeatability between the experimental characterisation results and those in the literature ^[28 - 30], which are cited in the tables below.

Analysis:

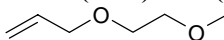
Material (EGE-A) Literature ^[29]	¹ H-NMR [CDCl ₃]/TMS 250 MHz			IR	
	δ (ppm)	Splitting	Group	cm ⁻¹	Groups
Section (4.4.2) Part (2)  4,7-dioxa-1-octen (ethylenglycolallylmethylether)	3.40	singlet	3H, -OCH ₃	3081	C-H olef
	3.54 - 3.67	multiplet	4H, - OCH ₂ CH ₂ O-	2962 - 2876	C-H aliph
	4.04	doublet doublet	2H, -CH ₂ -CH=CH ₂	1648	C=C
	5.21	doublet triplet	1H, -CH ₂ -CH=CH _{cis}	1105	C-O-C

Table. (4.4.2a)

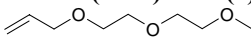
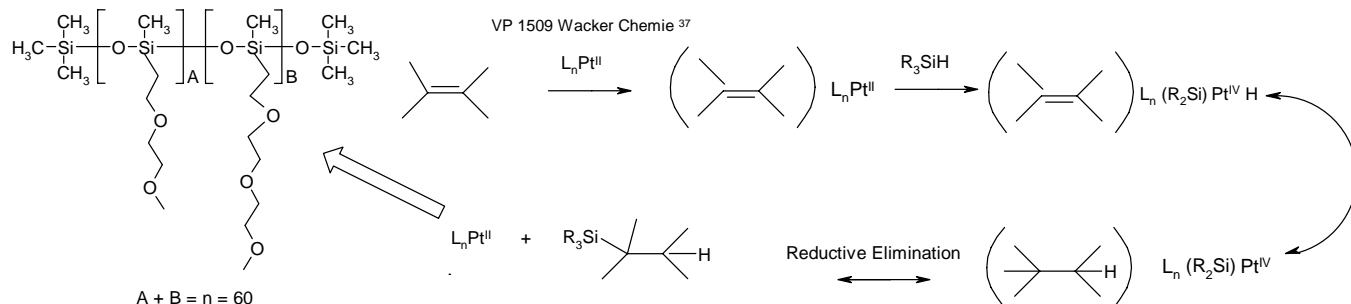
Material (EGE-B) Literature ^[29]	¹ H-NMR [CDCl ₃]/TMS 250 MHz			IR	
	δ (ppm)	Splitting	Group	cm ⁻¹	Groups
Section (4.4.2) Part (2)  4,7,10-trioxa-1-undecane (diethylenglycolallylmethylether)	3.39	singlet	3H, -OCH ₃	3080	C-H olef
	3.54 - 3.73	multiplet	8H, - OCH ₂ CH ₂ O-	2980 - 2873	C-H aliph
	4.04	doublet doublet	2H, -CH ₂ -CH=CH ₂	1647	C=C
	5.18	doublet triplet	1H, -CH ₂ -CH=CH _{cis}	1111	C-O-C
	5.27	doublet triplet	1H, -CH ₂ -CH=CH _{trans}		

Table. (4.4.2b)

4.4.3.

Procedure for the Hydrosilylation of H-Silicone⁶⁰Fig. (4.4.1) Hydrosilylation of H-Silicone with catalyst^{[31] [33]}

General product information:

Material	M. (g mol ⁻¹)	B. P.(°C)	Properties
H-Silicone Hydrosilylation	3767.62 + [(4.4.1) + (4.4.2)] ₆₀	280	Light brown gel to rubbery texture

Reagents:

H-Silicone:	[Wacker]dried (600 ppm H ₂ O)	C ₆₆ H ₂₅₈ O ₆₁ Si ₆₂	3767.62 g mol ⁻¹
tetrahydrofuran (THF): dried	[Merck] analysis Dried (25 ppm H ₂ O)	C ₄ H ₈ O	72.11 g mol ⁻¹
EGE-A – ethylenglycolallylmethylether	synthesised (40 ppm H ₂ O)	C ₆ H ₁₂ O ₂	116.16 g mol ⁻¹
EGE-B – diethylenglycolallylmethylether	synthesised (25 ppm H ₂ O)	C ₈ H ₁₆ O ₃	160.21 g mol ⁻¹
Pt(II)	[Wacker] Trademark	VP1509 ^[31]	Catalyst
argon :	[Linde AG] 93% - 7 %	H ₂ -mix.	Gas

Procedure:

The following is the set procedure followed in the hydrosilylation of H-Silicone⁶⁰ to Fig (4.4.1) with the addition of various concentrations side chain (oligo) ethylenglycol-allylmethylethers* (**EGE-A & EGE-B**). The quantities can be varied according to desired needs. All apparatus were thoroughly dried of water by drying all glassware at approximately 200 °C for 2 days. The constructed apparatus was flushed with nitrogen and evacuated five times before any reagents were injected. Approximately 200 mg of H-Silicone⁶⁰ was injected into the three-necked holding flask in the presence of a continued flow of nitrogen. The appropriate calculated molar quantities of side chain (oligo)ethylenglycolallylmethylethers* is added relative to the weighted amount of previously injected H-Silicone. The added reactants are dissolved in 2.5 ml absolute (THF) and 30 µl of the catalyst Pt(II) VP1509³⁶ is quickly followed in turn. All additions are conducted under the flow of nitrogen. The added solution

36 Pt catalyst Pt(II) VP1509 Wacker Chemie L_nPt^{II} [31]

is then refluxed for 8 - 9 hrs. at 65 °C under a nitrogen environment. Once the procedure is concluded, the THF is evacuated off at 0.5 Torr. at 65 °C for 10 hours. There was excellent repeatability between the experimental characterisation results and those in the literature ^[29 - 30], which are cited in the tables below.

Analysis:

Material Literature ^[29]	¹ H-NMR [CDCl ₃]/TMS 250 MHz			¹³ C-NMR			IR	
	δ (ppm)	Splitting	Group	δ (ppm)	Splitting	Group	cm ⁻¹	Groups
Polymerised Siloxane with Oligo(ethylene)	4.70	singlet	-SiH				2160	-SiH
	0.06	multiplet	-SiCH ₃	-0.15		-SiCH ₃		
	0.5	multiplet	-SiCH ₂	13.27	singlet	-SiCH ₂		
	1.61	multiplet	-SiCH ₂ CH ₂	22.98		-SiCH ₂ CH ₂		
	3.25	singlet	-OCH ₃	58.65	singlet	-OCH ₃		
	2.58 & 2.77	doublet	epoxy -CH ₂	43.85		epoxy -CH ₂		
	3.32 – 3.70	multiplet	-OCH ₂	69.65 – 73.64		-OCH ₂		

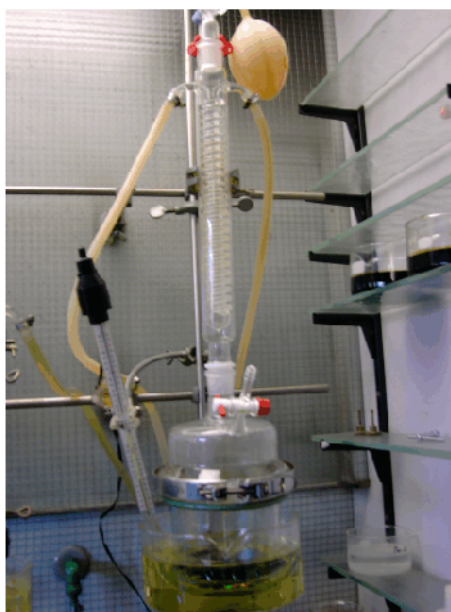
Table. (4.4.3)

4.4.4.

Procedure for the Doping of Poly(siloxane) with Lithium Salts

After the completion of the hydrosilylation procedure as described in section (4.4.3), the indicated lithium salts seen in section (4.1) and table (4.1.1), are doped into the matrix by utilising the following procedure.

The desired quantity of hydrosilylated poly(siloxane) is dissolved at 55 °C in THF in a specially constructed mixing chamber as seen in Pic. (4.4.1). After the dissolution of the polymeric material is achieved the appropriate calculated amount of salt is added and stirred into the mixture for 24 hours and heated to a constant temperature of 55 °C. After 24 hours of refluxing and mixing, the solvate and solvent is permitted to cool down for 2 hrs. The homogenous mixture was dried overnight in standard Schlenk ($\approx 10^{-3}$ atm) and for a further 48 hours over a high vacuum line pumps ($\leq 10^{-6}$ atm).



Pic. (4.4.1) Special glass apparatus employed for the doping of poly(siloxane) and lithium salts. The apparatus is a self contained reflux system, where vapor pressure build-up is reduced by the installation of an expansion balloon. This ensures there is no loss of solvent and the experiment remains inert. The container attached to the reflux column is flat bottomed, this is intended to encourage even mixing and later improved film formation for easier handling.

4.5. Procedure for the Purification of Organic Solvent

Foreword:

During the course of this work a number of solvents played an important role, i.e. during ions exchanges and solvation. It goes without saying that the purity of these solutions is of up most importance concerning the presence of water. Therefore, a number of procedures were performed to mitigate this particular point.

4.5.1. Acetonitrile for Synthesis: CH_3CN

Melting Point - °C	Boiling Point - °C	M.W. - g mol ⁻¹	Water Content - %
-46	81	41.05	0.003

During the synthesis of the imidazolium compounds acetonitrile plays a major role. Acetonitrile as a solvent is highly receptive to mixing with water with a standard off the shelf water content of 0.3%, which for this works purposes, is considered to be still rather high.

The solvent is purified by the addition of 1 g l⁻¹ sodium hydroxide [NaOH] through dispersion and for 10 minutes refluxed and distilled. The distillate is then further purified by the addition of 2 g l⁻¹ of di-phosphor pentoxide [P₂O₅] and is refluxed and stirred for 12 hours under argon. At the end of the procedure, the solvent is once again distilled. The distillate is tested with Karl Fischer³⁷ and the optimal water content of 0.003 % is achieved.

During storage, acetonitrile is stored in a dark place with 3 Å molecular sieves deposited in the container.

³⁷ Karl Fischer (Model CA-02, AbimED Analysen- Technik)

4.5.2.**Acetone for Synthesis: C₃H₆O**

Melting Point - °C	Boiling Point - °C	M.W. - g mol ⁻¹	Water Content - %
-95	56	58.08	0.003 - 0.002

Acetone like acetonitrile as a solvent is particularly difficult in purging water. It is highly receptive to the absorption of water in all forms, due to its frequent use in this work particular attention was allocated to the refinement of this solvent.

The solvent is purified by the addition of 2 g l⁻¹ potassium carbonate (potash) [K₂CO₃] through dispersion and for 6 hours refluxed and distilled. The distillate is then further purified by the addition of 4 g l⁻¹ of di-phosphor pentoxide [P₂O₅] and is refluxed and stirred for 12 hours under argon. At the end of the procedure, the solvent is again distilled. The distillate is tested with Karl Fischer and the optimal water content of 0.003- 0.002 % is achieved.

4.5.3.**Tetrahydrofurane (THF) for Synthesis: C₄H₈O**

Melting Point - °C	Boiling Point - °C	M.W. - g mol ⁻¹	Water Content - %
-108	66	72.11	0.001

THF is highly receptive to the absorption of water in all forms. In the purification of this solvent, 50 % potassium hydroxide [KOH] in solution is shaken, where the water phase turns to a weak brown colour. This procedure is followed by 2 days of vigorous stirring over 2 g l⁻¹ of cuprous chloride [Cu₂Cl₂] and 50 g l⁻¹ of potassium hydroxide [KOH]. The THF is then decanted into a container 10 g l⁻¹ of potassium hydroxide and refluxed for three hours and afterwards distilled. The final procedure requires the insertion of freshly pressed sodium wire and left for two days in darkness before finally distilled and stored in a dark place. The distillate is tested with Karl Fischer and the optimal water content of 0.001 % is achieved.

4.5.4.**Ethyl Acetate for Synthesis: $\text{CH}_3\text{COOC}_2\text{H}_5$**

Melting Point - °C	Boiling Point - °C	M.W. - g mol ⁻¹	Water Content - %
-84	77	76.08	0.01

The delivered ethyl acetate [Merck] with a water content of 0.01 % and purity of 99.5 considered to be adequate for the applications assigned to the solvent.

4.5.5.**1-Ethyl-3-methylimidazol for Synthesis: $\text{CH}_3\text{C}_3\text{H}_3\text{N}_2\text{H}$**

Melting Point - °C	Boiling Point - °C	M.W. - g mol ⁻¹	Water Content - %
-60	198	82.11	0.001

In the literature it is mentioned that 1-ethyl-3-methylimidazol is highly hygroscopic and there is the possibility of oxidation of the cation header group to 1-ethyl-3-methylimidazoxide after prolonged exposure to the atmosphere. Besides this fact with addition of various anions the purity of the material is crucial. Usually the solution has a yellow colour when bought off the shelf. This is due to the presence large amounts of impurities. Therefore 1-ethyl-3-methylimidazolium is refluxed for 24 hours under potassium hydroxide [KOH] and argon (5.0 Linde AG) and is finally distilled. The distillate is tested with Karl Fischer and the optimal water content of 0.001 % is achieved.

References:

1. C. M. Gordon, J. D. Holbrey, A. R. Kennedy and K. R. Seddon, *J. Mater. Chem.*, **8**, 2627 (1998).
2. C. J. Bowlas, D. W. Bruce and K. R. Seddon, *Chem. Commun.*, **14**, 1625 (1996).
3. J. Barthel, R. Buestrich, H. J. Gores, M. Schmidt and M. Wuhr, *J. Electrochem. Soc.*, **144**, 3866 (1997).
4. J. Barthel, H. J. Gores, R. Neueder and A. Schmid, *Pure and Applied Chemistry*, **71**, 1705 (1999).
5. J. Barthel, M. Schmidt and H. J. Gores, *J. Electrochem. Soc.*, **145**, L17 (1998).
6. J. Barthel, M. Wuhr, R. Buestrich and H. J. Gores, *J. Electrochem. Soc.*, **142**, 2527 (1995).
7. J. Barthel, R. Buestrich, E. Carl and H. J. Gores, *J. Electrochem. Soc.*, **143**, 3565 (1996).
8. J. Barthel, R. Buestrich, E. Carl and H. J. Gores, *J. Electrochem. Soc.*, **143**, 3572 (1996).
9. J. Barthel, M. Schmidt and H. J. Gores, *J. Electrochem. Soc.*, **145**, L17 (1998).
10. J. Barthel, A. Schmid and H. J. Gores, *J. Electrochem. Soc.*, **147**, 21 (2000).
11. J. Barthel, A. Schmid and H. J. Gores, *J. Electrochem. Soc.*, **147**, 21 (2000).
12. A. B. McEwen, J. L. Goldman, D. Wasel and L. Hargens, *Proc. - Electrochem. Soc.*, **99-41**, 222 (2000).
13. C. A. Reed and A. S. Larsen, *Abstr. Pap. - Am. Chem. Soc.*, **221st**, IEC (2001).
14. A. Marcinek, J. Zielonka, J. Gebicki, C. M. Gordon and I. R. Dunkin, *Journal of Physical Chemistry A*, **105**, 9305 (2001).
15. P. Wasserscheid and T. Welton, *Ionic Liquids*, Wiley-VCH, (2003)..
16. C. M. Gordon, Section: Synthesis and Purification of Ionic Liquids, *Ionic Liquids in Synthesis*, 7-21 (2002).
17. J. Fuller, A. C. Breda and R. T. Carlin, *Ionic liquid-polymer gel electrolytes*, **144**, No. p. 70 (1997).
18. K. Hoffmann, *Imidazole and Its Derivatives Part I*, **1**, No. p. 445 (1953).
19. T. Ohtake, Y. Takamitsu, K. Ito-Akita, K. Kanie, M. Yoshizawa, T. Mukai, H. Ohno and Kato, Takashi, *Macromolecules.*, **33**, 8109 (2000).
20. K. S. Groß, Title: *Transporteigenschaften des Systems 1-Ethyl-3-methylimidazoliumchlorid/AlCl₃ in Lösungsmitteln verschiedener Klassen im Bereich hoher Verdünnung bis zur reinen Salzschnmelze*, Theoretical & Physical Chemistry, 1-261 (1993).
21. L. Cammarata, S. Kazarin, P. Salter and T. Welton, *Phys. Chem. Chem. Phys.*, **3**, 5192 (2001).
22. J. Fuller, R. T. Carlin, H. C. De Long and D. Haworth, *J. Chem. Soc., Chem. Commun.*, **3**, 299 (1994).
23. V. R. Koch, L. A. Dominey, C. Nanjundiah and M. J. Ondrechen, *J. Electrochem. Soc.*, **143**, 798 (1996).
24. D. R. McFarlane, J. Sun, J. Golding, P. Meakin and M. Forsyth, *Electrochim. Acta.*, **45**, 1271 (2000).
25. J. S. Wilkes and M. J. Zaworotko, *J. Chem. Soc., Chem. Commun.*, 965 (1992).
26. M. Yoshizawa, W. Ogihara and H. Ohno, *Electrochem. Solid-State Letter.*, **4**, E25 (2001).
27. J. S. Wilkes, *Abstr. Pap. - Am. Chem. Soc.*, **221st**, IEC (2001).
28. Z. Zhu, A. G. Einset, C. Y. Yang, W.-X. Chen and G. E. Wenk, *Macromolecules*, **27**, 4076 (1994).
29. A. Merz and H. Bachmann, *J. Am. Chem. Soc.*, **117**, 901 (1995).
30. M. C. Lonergan, M. A. Ratner and D. F. Shriver, *J. Am. Chem. Soc.*, **117**, 2344 (1995).
31. A. J. Chalk and J. F. Harrod, *Journal of the American Chemical Society*, **87**, 16 (1965).
32. www.americanchemsoc.com/reagent-chemicals - search (LiCl titration method)
33. A. F. Hollemann and N. Wiberg, *Lehrbuch der Anorganische Chemie Ed 100st*, Walter de Gruyter, Berlin, (1995).

Chapter 5

Experimental Results

5.1. Poly(siloxane) Polymers

Foreword:

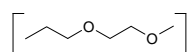
The author intends in this section to present the findings of this work in two separate distinctive sections i.e. {5.1} poly(siloxane) polymers and {5.2}, ionic liquids respectively. This is due to the distinctive nature and behaviour of the materials in question. In section {6}, the author will discuss the implications of these results in more detail and discuss further areas of future interest.

5.1.1. Preparative Work:

5.1.1.1. Review & Strategy Related to Poly(siloxanes)

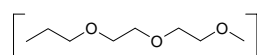
As was already alluded to in section {1} substantial research over the past two decades has been devoted to generating solid polymer electrolytes for use in high density lithium batteries. It was remarked that promising results have been obtained for polymers with highly flexible backbones bearing (oligo)ethyleneglycol side chains³⁸, which were suspected to serve to complex and mobilise the lithium ions in the matrix ^[1]. Numerous articles are cited in section {1} have stated the potential of these materials and their practicality for applications in the area of electrochemistry. The classical disadvantages of developing polymeric electrolytes are their tendency to exhibit an affinity to charge localisation of substrate such as lithium ions, which are often trapped at the ether group. Moreover, the existence of tight ion

³⁸ In the case of this work:



4,7-dioxa-1-octen (ethyleneglycolallylmethylether)

(EGE-A)



4,7,10-trioxa-1-undecane (diethyleneglycolallylmethylether)

(EGE-B)

pair formation, which in turn significantly reduces the number of available charge-conducting ions within the presented electrolyte ^[2].

In order to alleviate such potential drawbacks; this work has taken two approaches in polymer electrolyte design (see section {1}) and has combined them into one concerted approach. The first is the selection of lithium salts, which should have low lattice energies and a polymer that is flexible enough when polymerised to permit a reduced T_g with the additional factor of improved mobility of solvated salts within the polymer matrix. Such a polymeric material is H-silicone. This form of poly(siloxane) is reputed to have a highly flexible backbone as well as low glass transition temperatures and displays large free volumes ^[3]. The author presumed therefore that they should be good hosts for lithium ion transport. This is also complemented with the substitution/insertion of (EGE)'s side chains to form a comb-like structure. This is done to reduce the glass transition temperature of the materials, which can be added accordingly to permit the fine turning of the desired physical consistence of the test electrolyte i.e. in gels. This is important since the (EGE)'s are expected to significantly decrease inter-chain interactions that often lead to undesired chain cross-linking with the subsequent consequence of reduced conductivities ^[4].

The second approach is the careful selection of a lithium salt that reduces ion pairing using weakly basic and sterically hindered anionic charge centres. The lithium salts utilised for this work were chosen specifically to fulfil this role. These salts comprise of molecular anions with covalent bonds of high thermal and chemical stabilities (i.e. +320 – +350 °C), have large radii and hence have lower lattice energies in lithium salts leading to low polarisability, especially when per-fluorinated due to the low polarisability and electron withdrawing capability of fluorine. This is expected to lead to reduced ion paring; large charge delocalisation resulting in excellent electrochemical stability and weak anion lithium ion interactions leading in turn to greater conductivities. With these considerations in mind, all experimental endeavours progressed with relative success to this aim.

5.1.1.2.

Hydrosilylation insertion of (oligo)ethylenglycolallylmethylethers side chains (EGE) & Selection

The author performed over 140 investigations in attempting to modify poly(siloxane) polymers as described in section {4.4.} through the hydrosilylation insertion of two (oligo)ethylenglycolallylmethylethers (**EGE**)'s of different chain lengths. This procedure was carried further through the doping of the newly formed poly(siloxanes) with three new recently synthesised lithium salts ^[5 - 9], seen in table (5.1.1). As aforementioned the branched side chains poly(siloxanes) were found to have lower glass transition θ_g temperatures than their corresponding linear counterparts as seen in table (5.1.2). This maybe attributed to the branched side chains offering an increase in the free volume leading to a lower θ_g . This event was also assisted by the majority presence of α^* (**EGE-B**) as seen from in table (5.1.3). This is mainly attributable to reduced cross-linking between the side-chains due to their increased steric hindrance, this is later offset with increasing concentrations of (**EGE-A**) i.e. δ to $\mathbf{1}$ in table (5.1.3) due to elevated side-chain cross-linking that can be interpreted from the θ_g and impedance data which will be discussed later in section {6}.

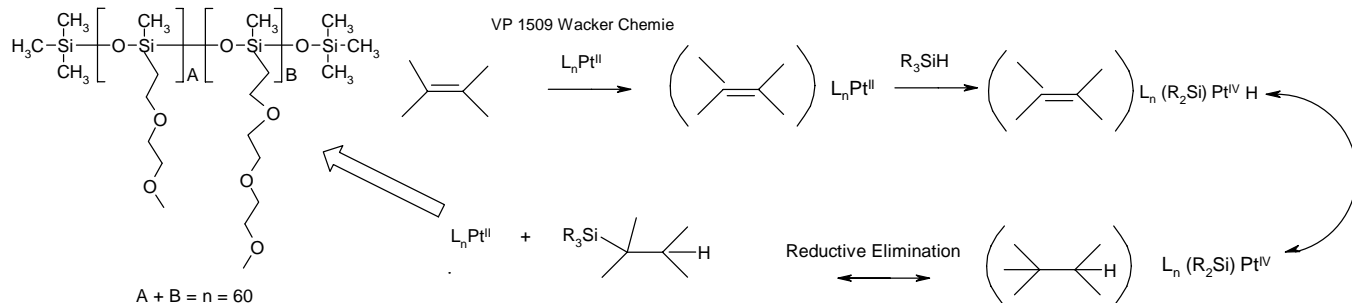


Fig. (5.1.1) Hydrosilylation reaction between allyl(EGE)'s [(EGO-A) (EGO-B)] molecule and poly(siloxane).

The preparation of the substituted poly(siloxanes) is generally carried out as described in section {4.4} via hydrosilylation reaction between the precursor allyl(**EGE**)'s molecules in the presence of a platinum catalyst ^[41] where the synthesis is outlined in Fig. (5.1.1) (see section {4.4.3}). The success of the hydrosilylation process was determined by the presence or lack of presence of any remaining Si-H functional groups along the backbone of H-siloxane⁶⁰ observed in IR ($\nu = 2160 \text{ cm}^{-1}$) and ^1H NMR (chemical shift 4.70 ppm) measurements. Nevertheless residual Si-H groups were often evident from IR and NMR spectra and the author estimated their presence to be $\geq 5 \%$. To remedy this situation; the residual groups were in most circumstances eliminated with the readdition of fresh catalyst and further

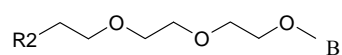
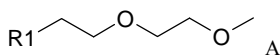
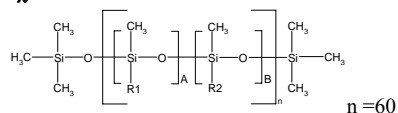
synthesis leaving an estimated 0.2 % Si-H groups unreacted. The presence of unreacted Si-H groups made complete control of the stoichiometry of the poly(siloxanes) difficult as was also similarly reported by Lonerger and co-workers [2].

The tables in the appendix³⁹ section show the experiments carried out by this author with the intent to establish the optimal reaction ratio and physical consistency of poly(siloxane) to (**EGE**) side-chains in order fulfil the requirement of designing a polymer electrolyte. The marked columns were of particular interest to this author due to their physical behaviours and consistencies. As one will notice from the summarised results in table (5.1.2) a general trend in the physical behaviours and consistencies of the experiments can be discerned. The longer chain length (**EGE-B**) seems to dominate the physical behaviour of the product material that in the literature was similarly noted by a number of authors [2] [10 - 11]. As the molar fraction (**EGE-A**) increases and (**EGE-B**) decreases correspondingly the product material takes on an ever more crystalline behaviour from an initial gel-like consistency to a powdery crystal α (A6:B54-10%:90%) and finally to τ (A60:B0-100%:0%) respectively seen in table (5.1.2) and in the appendix section⁴⁰. Since the desired characteristics for this work are that the materials should be gel-like in nature most concentrated samples in both ends of the (**EGE**) stoichiometry spectrum for which only a glass transition was observed, the polymer gels exhibited glass and melt transitions θ_g and θ_m table (5.1.3). The test samples in most circumstances tended to be colourless or a light brown gels and ranged from soft to tar-like gels. The author concentrated all further work in the cells that have been highlighted and marked with an asterisk(*) as seen in table (5.1.3). For the ease in further explanation; this author will from this point onwards refer to these specifically chosen and marked poly(siloxane) samples as α , β , and χ ⁴¹. More on these observations, behaviours will be discussed in detail later in section {6}.

39 See appendix

40 See appendix

41 α	A6:B54-10%:90%	H-Siloxane ⁶⁰	(A+B) = n = 60
β	A12:B48-20%:80%	H-Siloxane ⁶⁰	(A+B) = n = 60
χ	A18:B42-30%:70%	H-Siloxane ⁶⁰	(A+B) = n = 60



Structure	Name	Short-hand	g mol ⁻¹
	lithium bis - [3,4,5,6 – tetrafluoro – 1,2 – benzenediolato (2-) –O,O']borate	Li [F ₈]	377.84
	lithium bis-[3- fluoro-1,2-benzenediolato (2)-O,O']borate	Li [F ₂ H ₆]	269.90
	lithium bis-[1,2-benzenediolato(2-)-O,O']borate	Li [H ₈]	233.92

Table (5.1.1) Table of lithium salts synthesised (see section 4.1}) and utilised during this work.

No.	Mole Fraction <i>A : B</i>	H-Silicone <i>n</i>	θ_g °C	θ_m °C	Properties <i>Observation</i>
α^*	A6:B54-10%:90%	60	-79.4	-45,8	Light gel
β^*	A12:B48-20%:80%	60	-66.4	-23.5	Thick gel
χ^*	A18:B42-30%:70%	60	-59.2	-	Soft rubber – waxy
ϵ	A54:B6-90%:10%	60	-15.7	-	Brittle crystalline material
ϕ	A48:B12-80%:20%	60	-22.1	-	Brittle crystalline material
γ	A42:B18-70%:30%	60	-25.6	-	Crystalline

Table (5.1.2)

<p>H-Siloxane</p>					
<p>Ethylenglycolmonoethylether = 120,00 mol⁻¹</p>			<p>Diethylenglycolmonoethylether = 166,13 mol⁻¹</p>		
No.	Mole Fraction <i>A : B</i>	H-Siloxane <i>n</i>	Polymer <i>g</i>	Consistence <i>Observation</i>	Comments <i>JDR</i>
α^*	A6:B54-10%:90% *	60	0.212	Light gel	Desired *
β^*	A12:B48-20%:80%*	60	0.327	Thick gel	Desired *
χ^*	A18:B42-30%:70%*	60	0.288	Soft rubber – waxy	Desired *
ϵ	A54:B6-90%:10%	60	0.188	Brittle crystalline material	Interest – not further studied
ϕ	A48:B12-80%:20%	60	0.247	Brittle crystalline material	Interest – not further studied
γ	A42:B18-70%:30%	60	0.222	Crystalline	Interest – not further studied
η	A60:B0-100%:0%	60	0.241	Powdery crystal	Interest – not further studied
ι	A0:B60-0%:100%	60	0.264	Turbid liquid	Interest – not further studied

Table (5.1.3) Summarised test results between polymerised H-siloxane and (EGE)'s with marked cells further studied.

5.1.1.3.

Solvation of the polymer matrix and doping with lithium salts

The second approach in designing a gel-like electrolyte referred to by the author concerned the application of the lithium salts. The poly(siloxane) samples were doped in the presence of THF solvent at elevated temperatures [as described in section {4.4.4}] with the three different lithium salts as seen in table (5.1.1) Li [F8], Li [F2H6], and Li [H8]. Similar to the previous section the author will refer to a shorthand form of the salts under discussion to assist in explanation as seen in table (5.1.1). The author encountered considerable difficulty in the re-solvation of the poly(siloxane) during initial experiments due to the high polarisability of the (EGE) side groups. A further difficulty of this procedure is to ensure the thorough mixing of the lithium salts within in the polymer matrix, while at the same time ensuring the convenient formation of a film for later ease of transfer to the electrolyte test cell. This was achieved by the construction of a special glass apparatus as seen in Pic. (4.4.1) in section {4.4.4} seen previously, which ensured a large surface area for even mixing. Thereby, encouraging easier drying and later removal of the sample when in non-gel form. A great deal of time was invested in the removal of THF solvent from the polymer salt mix as already described in detail in section {4.3}. This was due to the tendency of THF to entrap and impregnate itself within the polymer matrix. Such incidences were reduced to the lowest possible level by instigating an extensive and tougher drying procedure [section {4.4.4}]. The finished samples were transferred to an argon-filled glove box where the newly formed film or gel material was removed and placed in the electrolyte test cell as described in detail in section {3.3}.

5.1.1.4. (O:Li) ratio doping with lithium salts

In order to understand the conductive patterns and behaviours of poly(siloxane) and lithium salt mixtures a wide doping range of (O:Li) were employed:

$$\begin{array}{cccc} & & \text{(O:Li)} & \\ \text{(16:1)} & \text{(24:1)} & \text{(32:1)} & \text{(64:1)} \end{array}$$

These particular ratio ranges were chosen in reference to similar ratio ranges employed in the literature ^[10 - 11]. The initial preliminary measurements were performed over all the above ranges with each lithium salt [table (5.1.1)]; to firstly determine the optimal doping concentration and secondly to determine the effect of ion-ion interactions in the form of charge delocalisation with the increasing presence of fluorine. Each poly(siloxane) complex was studied with varying lithium salt concentrations (O:Li) at a temperature of 20 °C. The results of conductivity *vs.* (Li/O) [O:Li] can be seen in Fig. (5.1.2). Similar to other authors for comb-like poly(siloxanes) the conductivity increased with increasing lithium salt content to a maximum and then gradually tailed away due to ion-ion interactions. When large enough concentrations of lithium salt are present, the viscosity usually increases and the ion mobility decreases to such an extent that a maximum in conductivity versus salt concentration occurs, a phenomenon that has been reported for salt containing networks based on PEO and PPO. It is suggested by Torell *et al* ^[42] that the conductivity drop at higher salt concentrations is due to reduced ion mobility but also to the formation of ion pair and higher aggregates. The presence of neutral ion pairs usually implies a decreased number of charge carriers and hence reduced conductivity. When one ignores the side chain variance (i.e. the different poly(siloxanes) α , β , χ), there is either a relative stable conductivity at low lithium salt concentrations as observed in the case of sample χ - Li [F2H6] and α - Li [H8] or a maximum α - Li [F8] for (32:1). These results indicate that the effects of increasing carrier density are overcome by the accompanying decrease in segmental mobility as seen in Fig. (5.1.2). There is a general decrease in conductivity due to the increase of θ_g with increasing (EGE-A) concentration see table (5.1.2). This effect is reduced in magnitude by the increased lithium ion concentrations from the doped salts that seem to probably reduce ion pairing and are promoting anion and cation dissociation with especial reference to the Li [F8] salt. The author suspects this may not be due to typical cross linking between the (EGE) substitutes, which usually results in the decreasing of conductivity with increasing salt concentrations but more with ion-pair

formation and weakening cation-anion interactions due to charge delocalisation of the anion as seen later in table (6.1.1)⁴². In Fig. (5.1.4a) which is the graph of the three poly(siloxane) mixtures α , β , and χ with Li [F8], there is an obvious trend to be observed.

Although all polymers are doped with Li [F8] over the same (O:Li) ratio the χ polymer dopant exhibits a much lower average conductivity (10^{-6} to 10^{-8} S cm⁻¹) over the complete doping range. This implies that the side chains are the deciding factor in the conductivity within each salt group. In reference to the other graphs Fig. (5.1.4b) and (5.1.4c) a similar scenario is played out in their conductive behaviours. If one studies the relationships of each polymer α , β , and χ individually with each salt as seen in Fig. (5.1.4 d e f). An expected pattern emerges where their conductivity responses are ordered by their ability to delocalise the charge within the matrix; hence with Li [F8] logically exerting the greatest influence. The Li [F8] salt demonstrates consistently the highest over-all conductivities in all side-chain variances table (5.1.2.) and (5.1.4a). The worst performing poly(siloxane) mix, is χ Li [H8], this is mainly due to the combination in the one hand of high polarisability plus weak delocalisation effects of the anion and in the other hand considerable side-chain cross-linking with quasi-crystalline regions forming and hence impeding ion transport of the poly(siloxane). Observations by Barthel and co-workers^[9] indicated that increasing ionic radius and fluorination of the presented salts initiated a parallel increase in the conductivities of the samples. This increased conductivity could be directly attributed to suppressed the ion pair formation due to the strong charge delocalisation effects of the anion itself toward the surrounding polymeric matrix; this hypothesis seems to hold true for these experiments and will be further discussed in section {6}.

The 3D graphs seen in Fig. (5.1.3 a b c) are a useful means of conceptualising the triple relationship of the percentage of polymer side chain (**EGE-A**) (x-axis) relative to (**EGE-B**) content, molar ratio of lithium to oxygen (y-axis), and conductivity (z-axis) at 20 °C. They show a clear plateau formation in the presence of Li [F8] in Fig. (5.1.3a) with the best conductivity response at 10 % (**EGE-A**) at molar ratios (32:1) and (24:1). Similar was seen for Fig. (5.1.3b) in the presence of Li [F2H6]. A plateau was observed in the same (O:Li) region. The figure (5.1.3c) in the presence of Li [H8] showed an unusual conductive response as compared to the other two data sets. At 10 % (**EGE-A**), there is no typical high

⁴² See page 212

conductivity plateau, but there is a shift to the 20 % (**EGE-A**) concentration in the same (O:Li) region of (32:1) and (24:1).

This could tentatively be explained from the salt coming to a sterically better accommodation with the polymer matrix as compared the other salts of the same region and more shall be commented on this point later. The figures (5.1.3 a – c) and (5.1.4a - f) show clearly the conductive behaviours of these materials for various (O:Li) concentrations at 20 °C. As this author has already alluded to the fact that in most data sets there is a trend to a particular maximum of conductivity vs. [Li/O] (O:Li), (or sterically convenient) range for the poly(siloxane) dopant mixture at ratios of (32:1) and (24:1). This was a rather surprising development, therefore the author decided to investigate these two particular data sets in more detail and over a wider temperature range from +15 °C to +100 °C, where the results of these investigations can be seen in Fig. (5.1.6)⁴³, (5.1.7)⁴⁴, (5.1.8 a – f)⁴⁵, (5.1.9a - f)⁴⁶ and (5.1.10a - f)⁴⁷. The author explored these higher conductivity salt concentrations in the belief that θ_g would reach a maximum. In addition, the increase of the lithium salt content would not only increase the ion mobility but should also simultaneously increase the freedom of the small cations such as Li^+ to move independently of their surroundings^[12].

Graph of combined poly(siloxanes) with different doped lithium salts at 20 °C

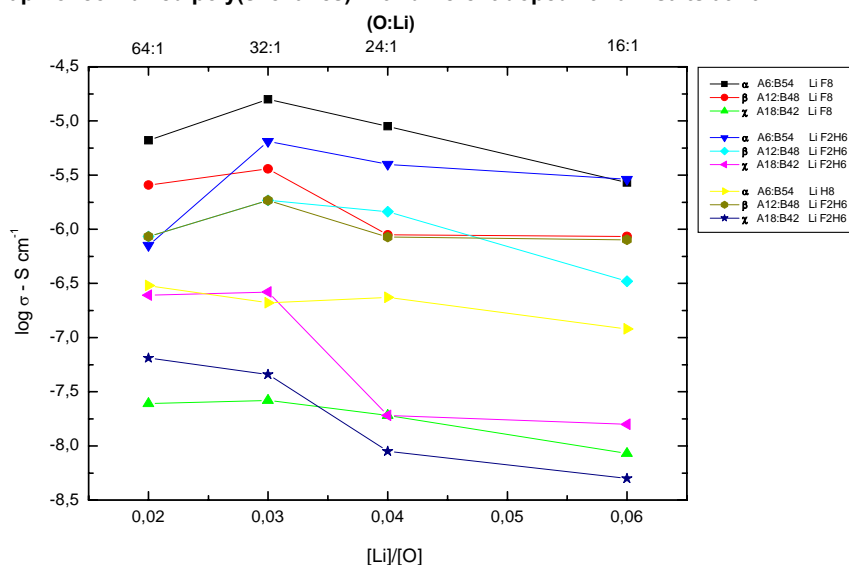


Fig. (5.1.2)

43 Combined graph's of poly(siloxane) doped with various lithium salts to: (O:Li) – (1:32) 15 °C – 100 °C

44 Combined graph's of poly(siloxane) doped with various lithium salts to: (O:Li) – (1:24) 15 °C – 100 °C

45 3D Graphs of the relationship of conductivity, temperature, and percentage of (**EGE-A**) at ratios (32:1) and (24:1) respectively.

46 Graphs of poly(siloxane) for each lithium salt to: (O:Li) - (32:1) & (24:1) 15 °C – 100 °C

47 Graphs of various lithium salts per poly(siloxane) variance: (O:Li) - (32:1) & (24:1) 15 °C – 100 °C

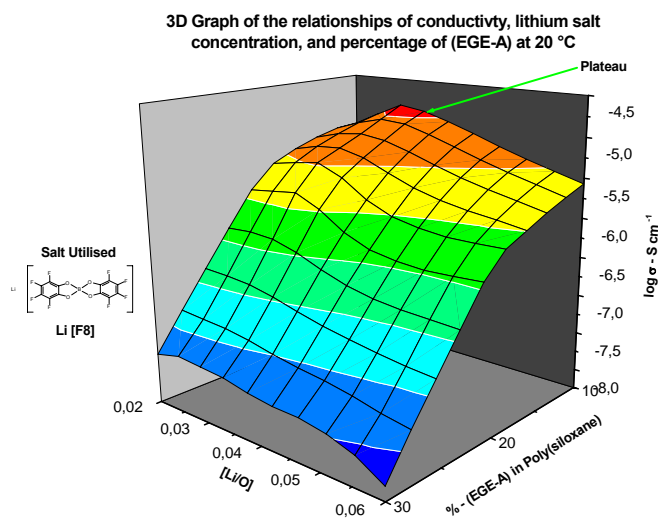
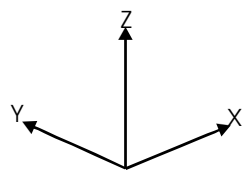


Fig. (5.1.3a)

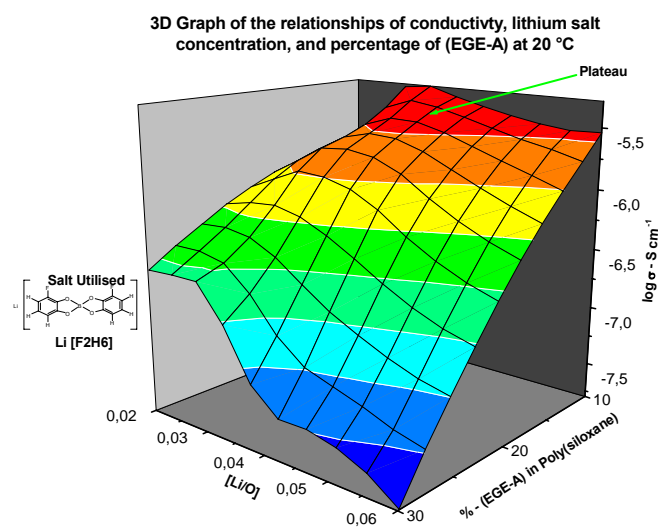


Fig. (5.1.3b)

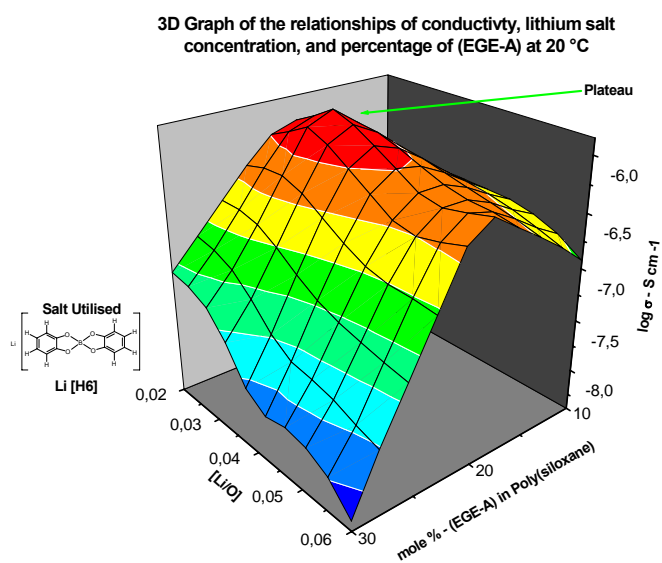


Fig. (5.1.3c)

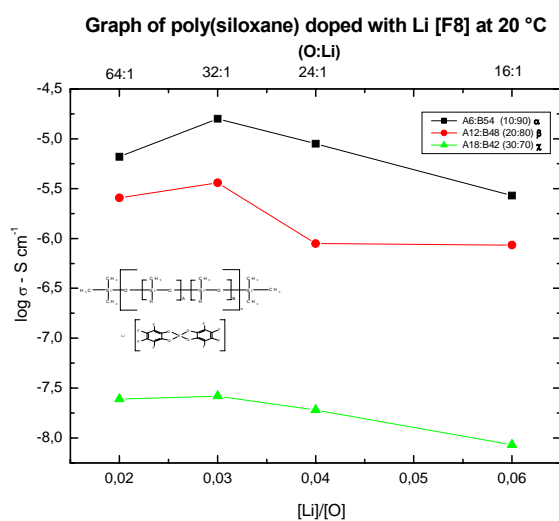


Fig. (5.1.4 a)

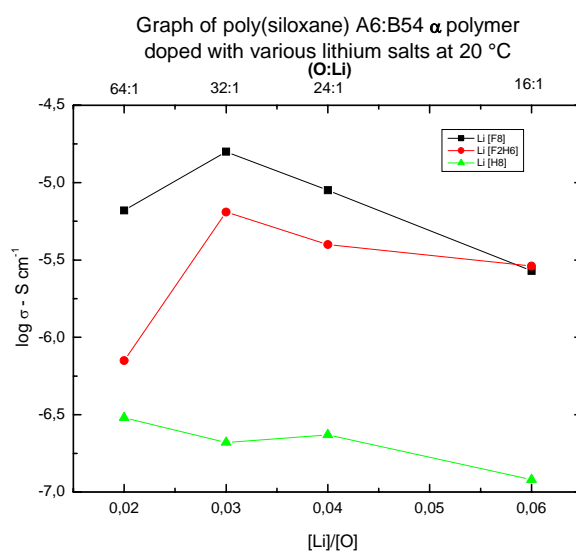


Fig. (5.1.4 d)

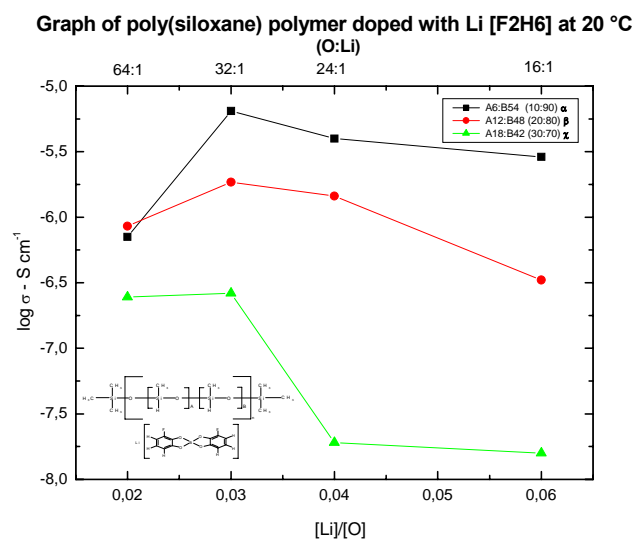


Fig. (5.1.4 b)

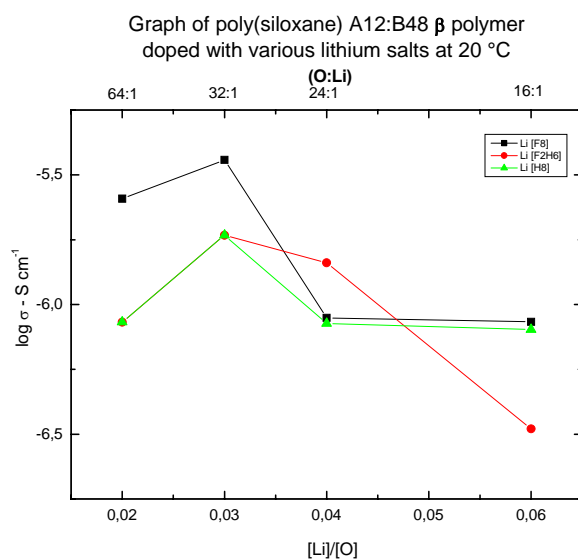


Fig. (5.1.4 e)

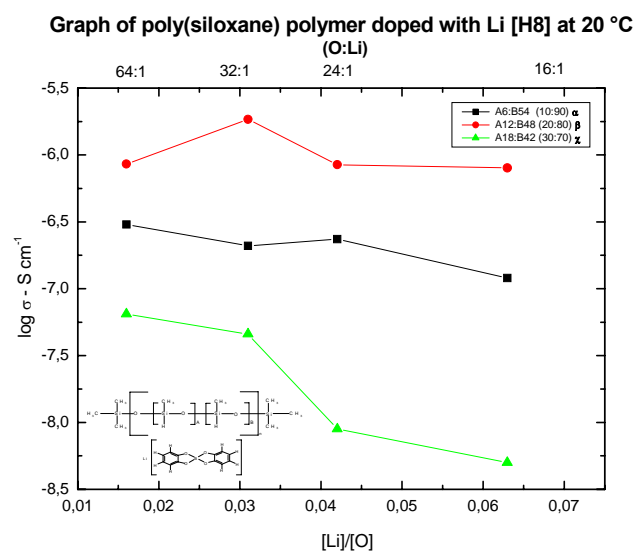


Fig. (5.1.4 c)

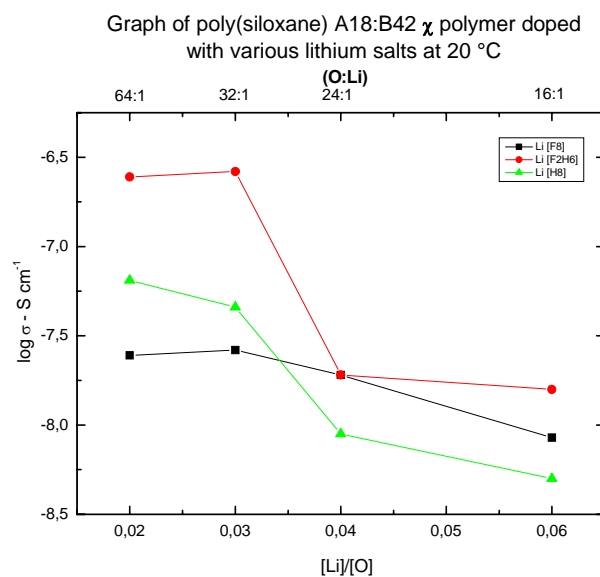


Fig. (5.1.4 f)

5.1.2.

Poly(siloxane) polymers and lithium salt mixtures at ratios of (O:Li) – (32:1) & (24:1):

The ionic conductivity of all synthesised poly(siloxane) polymer doped electrolytes were determined by means of electrical impedance spectroscopy (EIS) utilising the in-house designed thermostat previously discussed in section {3.2} and the electrolyte cell as described in sections {2.4}, {3.1}, and {3.3}. The conductivities of all samples were measured at regular intervals at temperatures of 20 °C, 40 °C, 60 °C, 80 °C, and 100 °C and the results are summarised in the tables (5.1.4) and (5.1.5) for (O:Li) : (32:1) and (24:1) respectively⁴⁸. The Nyquist plot example in Fig. (5.1.5) illustrates the complex plane impedance spectra obtained at three different temperatures for the sample α Li [F8]. A straight line appears in the low frequency range due to the diffusion impedance at the electrolyte/electrode interface^[13], followed by a semicircle with Z' intercept in the higher frequency range. Similar behaviour was observed for all the samples tested and will be discussed in more detail in section {6} later. The experimental data was fitted with a “simplified” equivalent circuit similar to the one shown within Fig. (5.1.5). The symbol R_l stands for the polymer electrolyte resistance, C_l is the double layer capacitance of the polymer electrolyte interface and C_2 describes the deviation of the low frequency slope from the 90° rise in the Nyquist plot that seems to be lithium salt concentration dependent. From the Z' vs. Z'' plot the ionic conductivities were calculated at each temperature from the intercept of the curve of the real axis as previously described in section {2.4}. The temperature dependence of the ionic conductivities of the various chosen polymer salt mixtures is shown in Fig. (5.1.7) and (5.1.8) for (32:1) and (24:1) ratios respectively. The average for the conductivities at ambient temperatures (20 °C) for all salts lie in the range of $(4.58 \times 10^{-8} \text{ S cm}^{-1} \chi - \text{Li [H8]})$ to $(1.57 \times 10^{-5} \text{ S cm}^{-1} \alpha - \text{Li [F8]})$ and $(8.89 \times 10^{-9} \text{ S cm}^{-1} \chi - \text{Li [H8]})$ to $(1.96 \times 10^{-6} \text{ S cm}^{-1} \alpha - \text{Li [F8]})$ for (32:1) and (24:1) respectively. These results were in a similar range and order to other studies^[14 - 16], the maximum ambient temperature conductivity was reached at an optimum doping level of (32:1) and in some cases (24:1) (O:Li) ratio. The conductivity of the salt in polymer reached a maximum near (O:Li) (32:1) because the θ_g of the material rises rapidly with salt content as seen in table (5.1.6), therefore causing a decrease in ionic mobility that is offset by the effects of increasing charge carrier concentration seen in Fig. (5.1.7) and (5.1.8).

48 See appendix

Conductivity Table of Poly(siloxane) Polymers α , β , χ , doped with Lithium Salts at (0:Li) – (32:1)

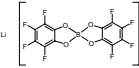
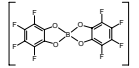
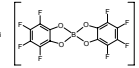
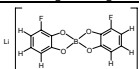
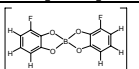
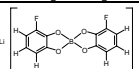
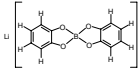
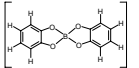
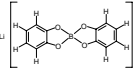
(0:Li) (32:1)		Siloxane Polymer α A6:B54-10%:90%			Siloxane Polymer β A12:B48-20%:80%			Siloxane Polymer χ A18:B42-30%:70%		
Celsius.	Kelvin	Ohms	σ	$\log \sigma$	Ohms	σ	$\log \sigma$	Ohms	σ	$\log \sigma$
$^{\circ}\text{C}$	1000/K	Ω	S cm^{-1}	$\log \text{Scm}^{-1}$	Ω	S cm^{-1}	$\log \text{Scm}^{-1}$	Ω	S cm^{-1}	$\log \text{Scm}^{-1}$
		Li [F8]			Li [F8]			Li [F8]		
										
20	3,41	6,37E+04	1,57E-05	-4,80	2,77E+05	3,61E-06	-5,442	3,83E+07	2,61E-08	-7,58
40	3,19	5,35E+03	1,87E-04	-3,73	1,76E+04	5,67E-05	-4,246	1,06E+06	9,42E-07	-6,03
60	3,00	6,76E+02	1,48E-03	-2,83	4,08E+03	2,45E-04	-3,610	1,18E+05	8,50E-06	-5,07
80	2,83	1,72E+02	5,80E-03	-2,24	1,06E+03	9,48E-04	-3,023	2,01E+04	4,98E-05	-4,30
100	2,68	5,35E+01	1,87E-02	-1,73	1,29E+02	7,75E-03	-2,111	4,72E+03	2,12E-04	-3,67
		Li [F2H6]			Li [F2H6]			Li [F2H6]		
										
20	3,41	1,56E+05	6,42E-06	-5,19	5,41E+05	1,85E-06	-5,733	3,83E+06	2,61E-07	-6,58
40	3,19	5,43E+03	1,84E-04	-3,74	5,35E+04	1,87E-05	-4,728	5,40E+05	1,85E-06	-5,73
60	3,00	3,67E+02	2,73E-03	-2,56	1,16E+04	8,64E-05	-4,063	1,54E+05	6,47E-06	-5,19
80	2,83	1,09E+02	9,16E-03	-2,04	5,35E+03	1,87E-04	-3,728	2,88E+04	3,47E-05	-4,46
100	2,68	6,25E+01	1,60E-02	-1,80	2,43E+03	4,12E-04	-3,385	5,00E+03	2,00E-04	-3,70
		Li [H8]			Li [H8]			Li [H8]		
										
20	3,41	4,76E+06	2,10E-07	-6,68	5,41E+05	1,85E-06	-5,733	2,19E+07	4,58E-08	-7,34
40	3,19	2,81E+05	3,56E-06	-5,45	3,22E+04	3,11E-05	-4,507	3,02E+06	3,31E-07	-6,48
60	3,00	5,10E+04	1,96E-05	-4,71	2,51E+03	3,98E-04	-3,400	6,71E+05	1,49E-06	-5,83
80	2,83	5,62E+03	1,78E-04	-3,75	4,95E+02	2,02E-03	-2,695	1,27E+05	7,89E-06	-5,10
100	2,68	1,19E+03	8,37E-04	-3,08	1,16E+02	8,63E-03	-2,064	9,90E+04	1,01E-05	-5,00

Table (5.1.4)

Conductivity Table of Poly(siloxane) Polymers α , β , χ , with doped Lithium Salts at (0:Li) – (24:1)

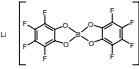
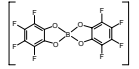
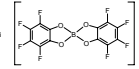
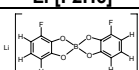
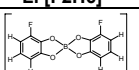
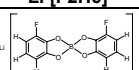
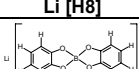
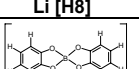
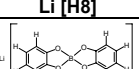
(0:Li) (24:1)		Siloxane Polymer α A6:B54-10%:90%			Siloxane Polymer β A12:B48-20%:80%			Siloxane Polymer χ A18:B42-30%:70%		
Celsius.	Kelvin	Ohms	σ	$\log \sigma$	Ohms	σ	$\log \sigma$	Ohms	σ	$\log \sigma$
$^{\circ}\text{C}$	1000/K	Ω	S cm^{-1}	$\log \text{Scm}^{-1}$	Ω	S cm^{-1}	$\log \text{Scm}^{-1}$	Ω	S cm^{-1}	$\log \text{Scm}^{-1}$
		Li [F8]			Li [F8]			Li [F8]		
										
20	3,41	5,10E+05	1,96E-06	-5,71	5,59E+06	1,79E-07	-6,747	5,65E+07	1,77E-08	-7,75
40	3,19	3,52E+04	2,84E-05	-4,55	2,29E+05	4,37E-06	-5,360	1,02E+06	9,80E-07	-6,01
60	3,00	4,26E+03	2,35E-04	-3,63	1,91E+04	5,23E-05	-4,281	9,80E+04	1,02E-05	-4,99
80	2,83	1,14E+03	8,80E-04	-3,06	5,00E+03	2,00E-04	-3,699	3,57E+04	2,80E-05	-4,55
100	2,68	5,35E+02	1,87E-03	-2,73	1,17E+03	8,55E-04	-3,068	1,40E+04	7,12E-05	-4,15
		Li [F2H6]			Li [F2H6]			Li [F2H6]		
										
20	3,41	5,38E+05	1,86E-06	-5,73	1,83E+06	5,45E-07	-6,264	2,04E+07	4,89E-08	-7,31
40	3,19	3,65E+04	2,74E-05	-4,56	1,77E+05	5,66E-06	-5,247	1,27E+06	7,88E-07	-6,10
60	3,00	5,95E+03	1,68E-04	-3,77	1,61E+04	6,23E-05	-4,206	1,44E+05	6,95E-06	-5,16
80	2,83	1,45E+03	6,88E-04	-3,16	2,80E+03	3,57E-04	-3,447	2,01E+04	4,97E-05	-4,30
100	2,68	4,45E+02	2,25E-03	-2,65	8,13E+02	1,23E-03	-2,910	6,07E+03	1,65E-04	-3,78
		Li [H8]			Li [H8]			Li [H8]		
										
20	3,41	4,26E+06	2,35E-07	-6,63	1,18E+06	8,45E-07	-6,073	1,12E+08	8,89E-09	-8,05
40	3,19	8,77E+05	1,14E-06	-5,94	3,08E+05	3,25E-06	-5,489	1,20E+07	8,30E-08	-7,08
60	3,00	2,53E+05	3,96E-06	-5,40	1,14E+05	8,79E-06	-5,056	1,38E+06	7,25E-07	-6,14
80	2,83	6,86E+04	1,46E-05	-4,84	5,15E+04	1,94E-05	-4,712	2,58E+05	3,88E-06	-5,41
100	2,68	4,22E+04	2,37E-05	-4,63	3,44E+04	2,91E-05	-4,536	9,90E+04	1,01E-05	-5,00

Table (5.1.5)

But the conductivities overall were significantly higher in the presence of Li [F8] lithium salt as compared to similar conditions for the other lithium salt substitutes i.e. Li [F2H6] and Li [H8]. The Li [F8] salt exhibited the most significant conductive behaviour. This enhanced conductivity being attributed to changes in mobility and carrier concentration as a well as to a larger extent due to the dissociation driven presence of the fluorinated anion. It was observed in some cases the ionic conductivities increased with temperature, values in the order of ($10^{-2} \text{ S cm}^{-1}$) at temperatures of 100°C see Fig. (5.1.10a - f) and (5.1.11a – f).

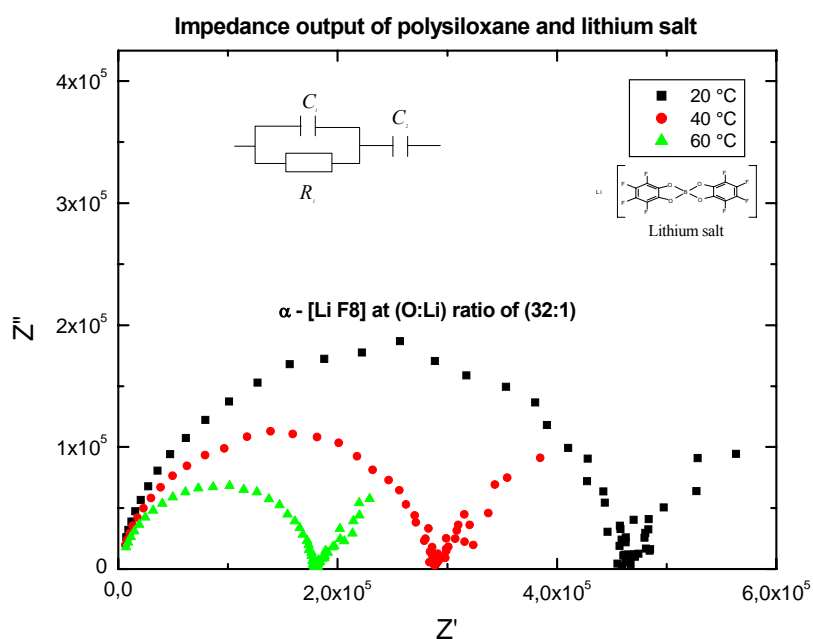


Fig. (5.1.5) Impedance spectroscopy analysis with simplified equivalent circuit

Polymer No.	Lithium Salt	Ratio (O:Li)	θ_g °C	Conductivity at 20 °C $\sigma - \text{S cm}^{-1}$
α^*	Li [F8]	(32:1)	-53.2	1.57×10^{-5}
		(24:1)	-48.8	1.95×10^{-6}
		(16:1)	-31.5	8.58×10^{-7}
α^*	Li [H8]	(32:1)	-18.8	2.10×10^{-7}
		(24:1)	-18.1	2.35×10^{-7}
		(16:1)	-15.7	8.00×10^{-9}

Table (5.1.6) Table of θ_g 's and ionic conductivities of polymers

Combined graph's of poly(siloxane) polymers doped with different lithium salts
(O:Li) = (32:1)

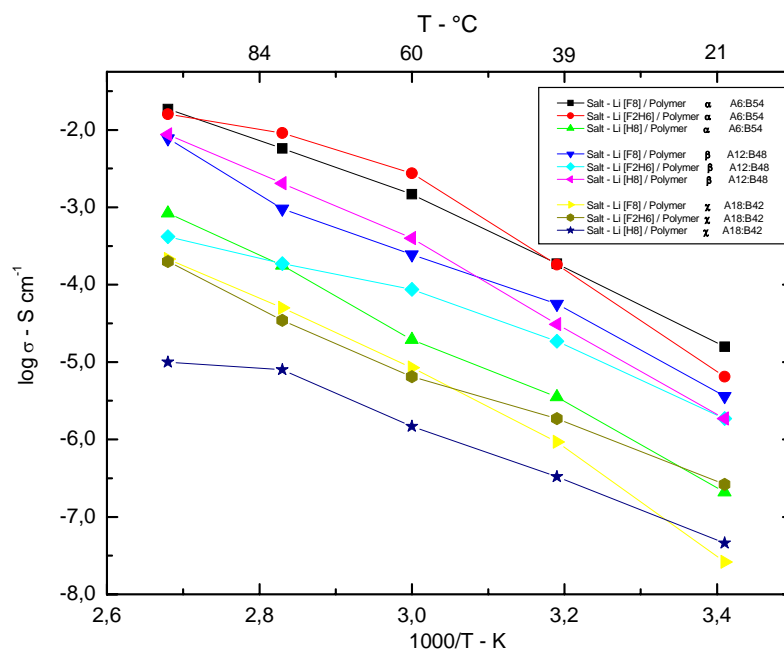


Fig. (5.1.7)

Combined graph's of poly(siloxane) polymers doped with different lithium salts
(O:Li) = (24:1)

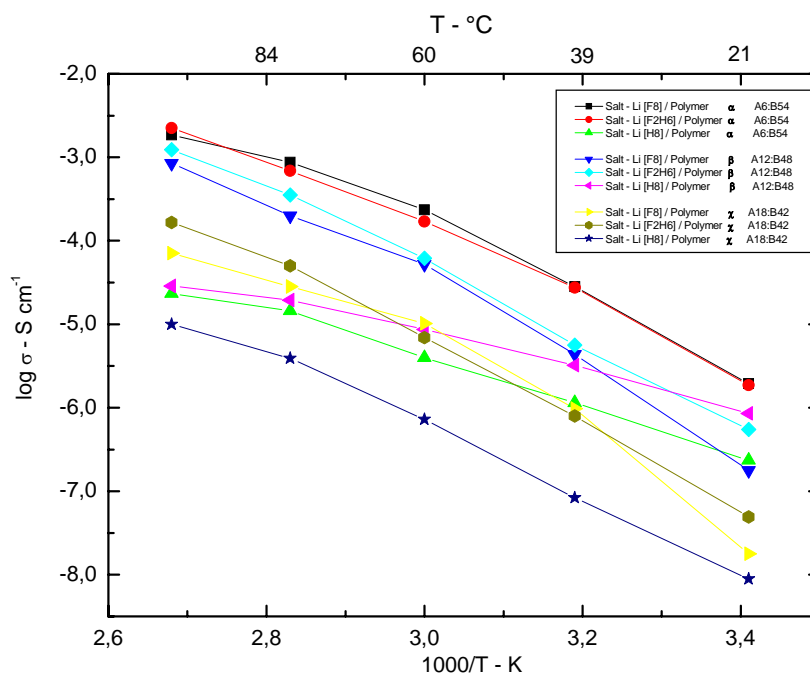


Fig. (5.1.8)

It is obvious from the results that in these comb-link poly(siloxane) polymers the role played by the salt is critical. In addition, further factors can be considered and extracted from the data, the ionic conductivity increases with increasing numbers of (**EGE-B**) units ^{[1 - 2] [13]} ^[17]. Plus the length of the (**EGE**)'s combined with the respective concentration of certain (**EGE**)'s [i.e. (**EGE-A**)] increase the capability to develop crystallinity (table 5.1.3⁴⁹) which increases at the same time as there is a decrease in ion mobility and thus ionic conductivity [(Fig. (5.1.7) & (5.1.8)]. These results are in general well within the range of ionic conductivities of polymer electrolytes reported in the literature according to Acosta ^[13].

The 3D graphs seen in Fig. (5.1.9 a b c) and Fig. (5.1.9 d e f) show the relationships of conductivity (z-axis), temperature (y-axis), and the percentage of (**EGE-A**) doped with different salts (x-axis) for the ratios (32:1) and (24:1) respectively. The figure. (5.1.9 a b) and (5.1.9 d e) generally exhibit a non-linear behaviour over the full temperature range for the salt Li [F8] and Li [F2H6]. However, if one examines Fig. (5.1.9c) and (5.1.9f), one observes that the conductivity vs. temperature at high concentrations of (**EGE-A**) i.e. (20%) for both ratios is non-linear. Such behaviour would be difficult to observe, if such data were plotted in the conventional 2D form as seen in Fig. (5.1.10 a – f) and Fig. (5.1.11 a – f). It is generally observed that the $\log \sigma$ vs. $1/T$ conform to one of the two following types of behaviours or in some cases a mixture of both depending on the temperature one concentrates:

- (a) Vogel-Tamman-Fulcher (VTF) behaviour equation either throughout the temperature range or in limited ranges ^[18] see section {2.3.2.1}
- (b) Arrhenius behaviour similarly throughout the temperature range or in limited ranges.

The practical implications of these two dependencies have been discussed in detail in section {2.3} and their relevance in practice will be discussed in detail in the next section {6}. Nevertheless, at this point it is safe to comment that non-linear VTF behaviour is observed in most of the polymer salts, but seems to break down for the Li [H8] mixtures as seen in Fig. (5.1.9 c) and (5.1.10f); where the line takes a linear form and moves away from the VTF “ideal” form. The ion transport seems to be dependent on the segmental motion of the (**EGE**) chains.

⁴⁹ See appendix

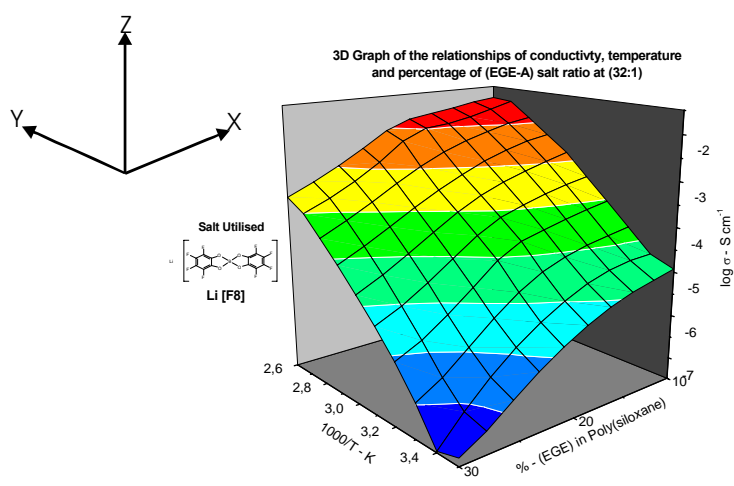


Fig. (5.1.9a)

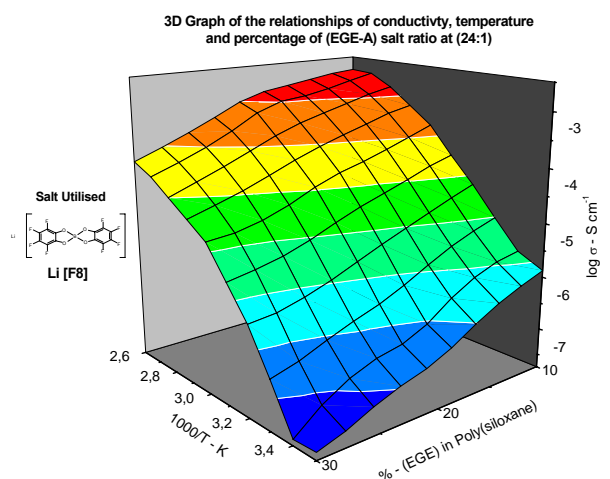


Fig. (5.1.9c)

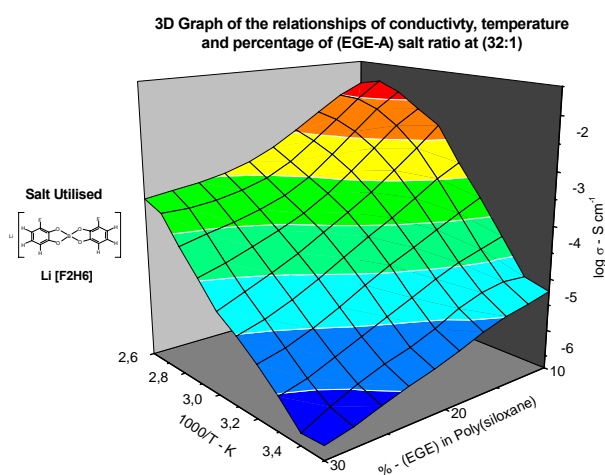


Fig. (5.1.9b)

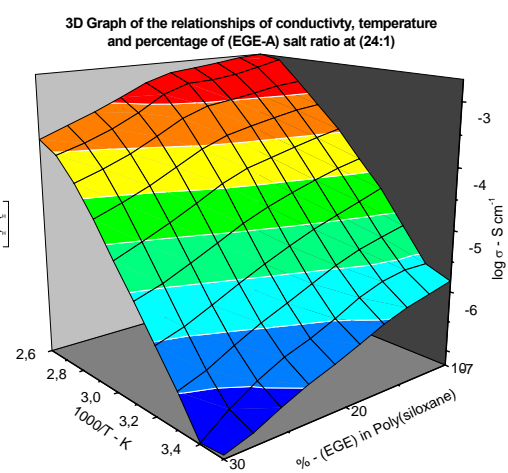


Fig. (5.1.9e)

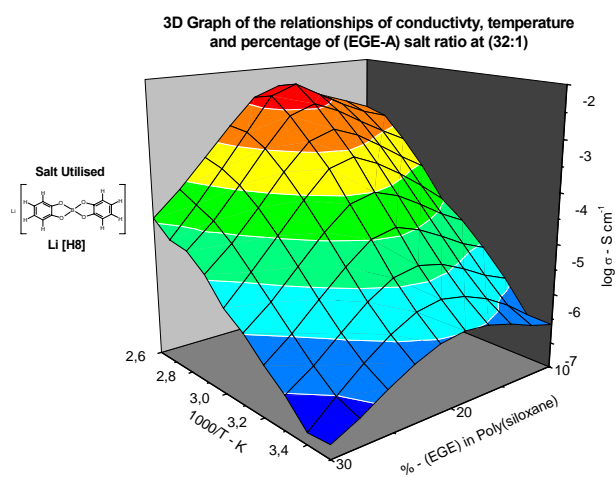


Fig. (5.1.9c)

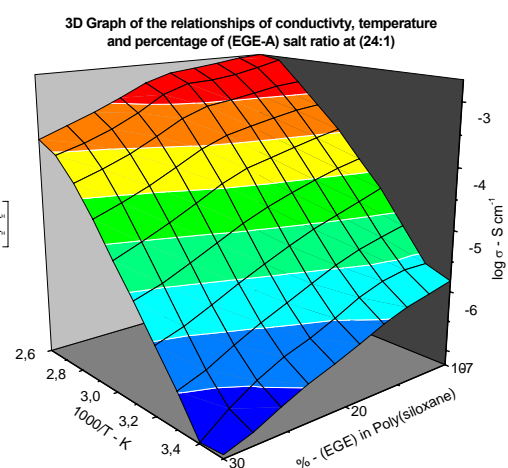


Fig. (5.1.9f)

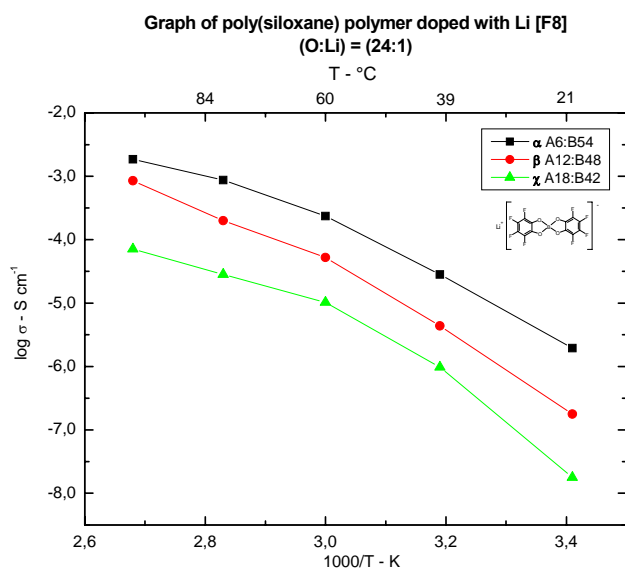


Fig. (5.1.10a)

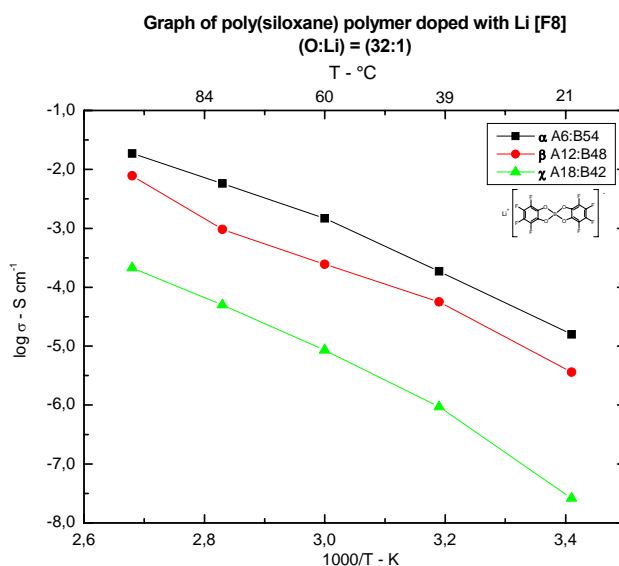


Fig. (5.1.10c)

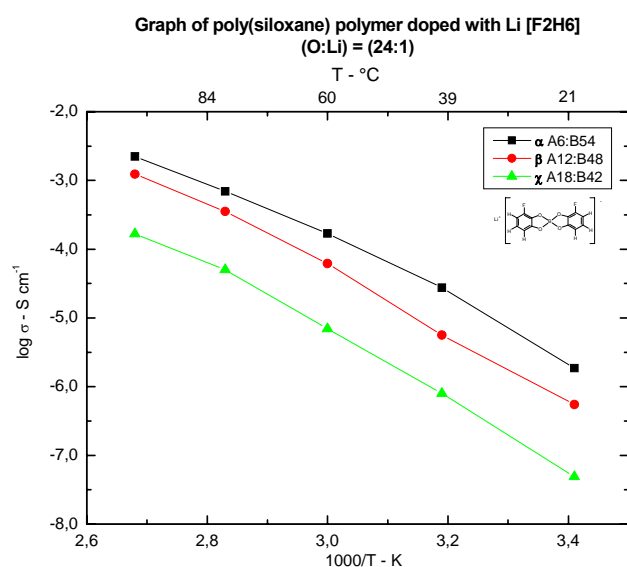


Fig. (5.1.10b)

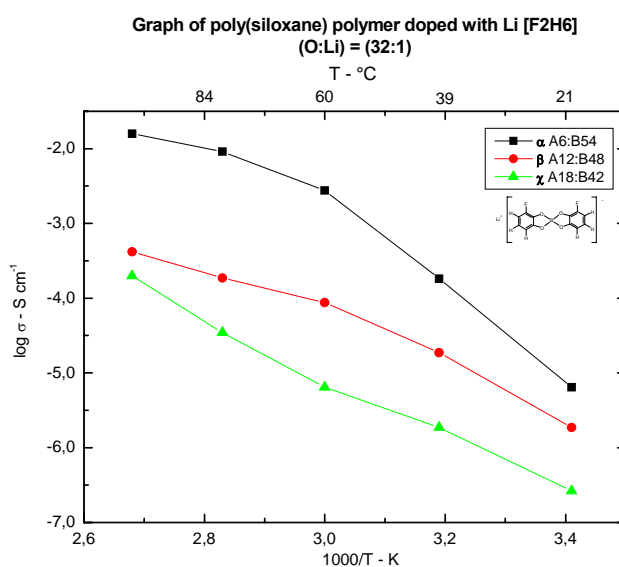


Fig. (5.1.10e)

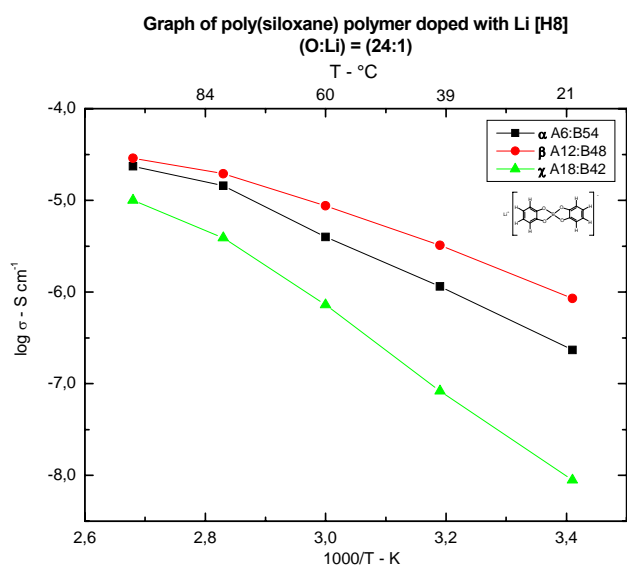


Fig. (5.1.10c)

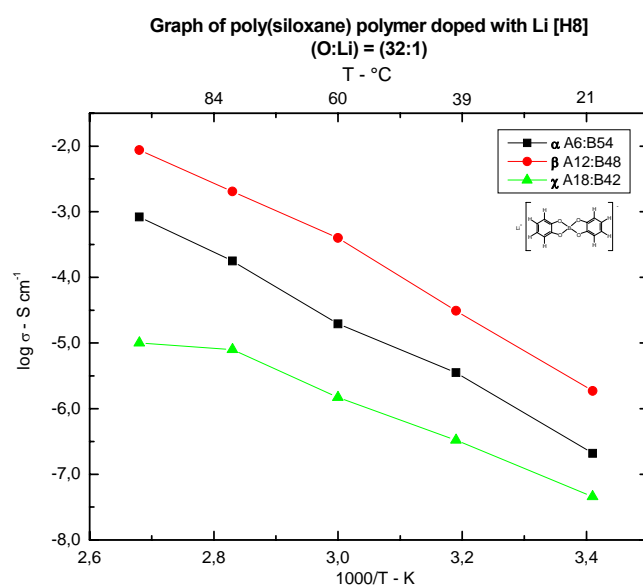


Fig. (5.1.10f)

Graph of poly(siloxane) polymer α A6:B54 doped with various lithium salts
(O:Li) = (24:1)

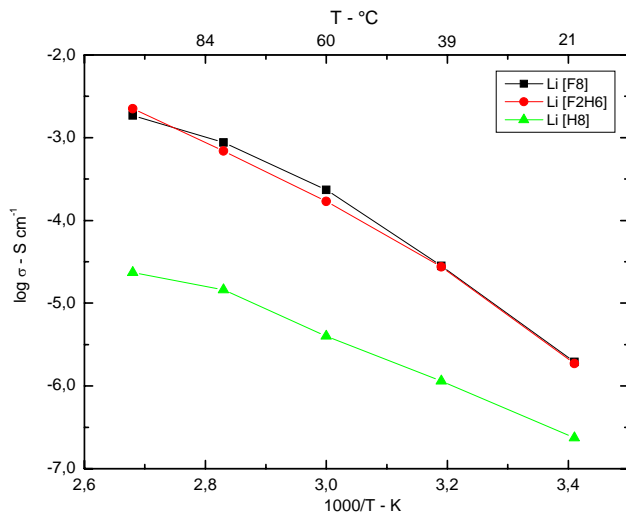


Fig. (5.1.11a)

Graph of poly(siloxane) polymer α A6:B54 doped with various lithium salts
(O:Li) = (32:1)

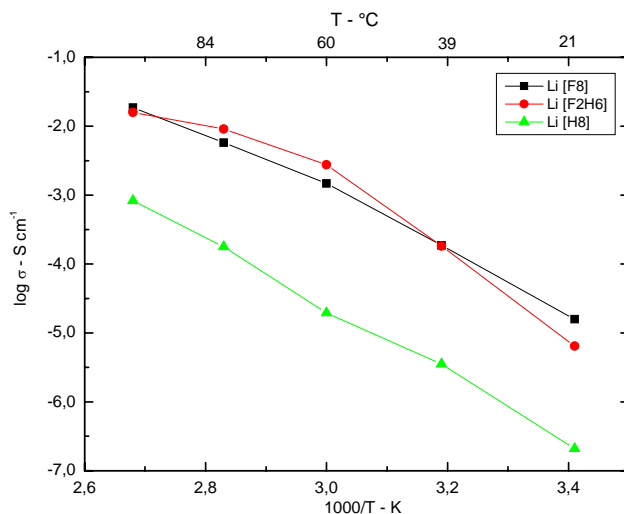


Fig. (5.1.11d)

Graph of poly(siloxane) polymer β A12:B48 doped with various lithium salts
(O:Li) = (24:1)

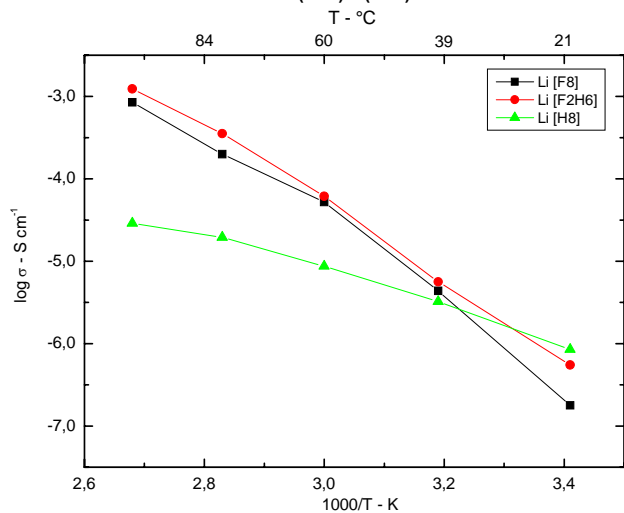


Fig. (5.1.11b)

Graph of poly(siloxane) polymer β A12:B48 doped with various lithium salts
(O:Li) = (32:1)

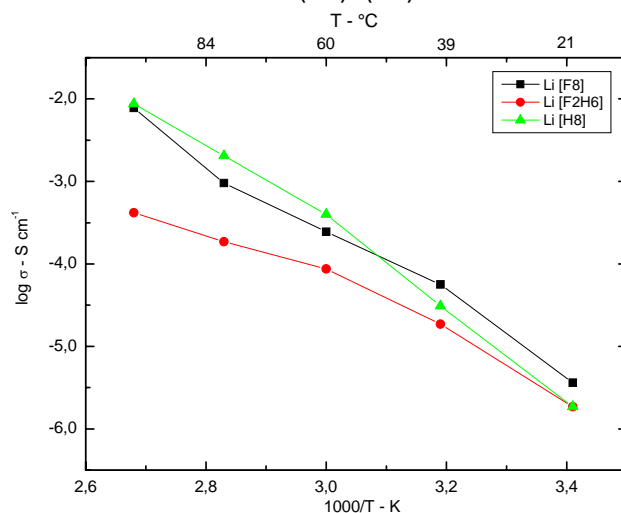


Fig. (5.1.11e)

Graph of poly(siloxane) polymer χ A18:B42 doped with various lithium salts
(O:Li) = (24:1)

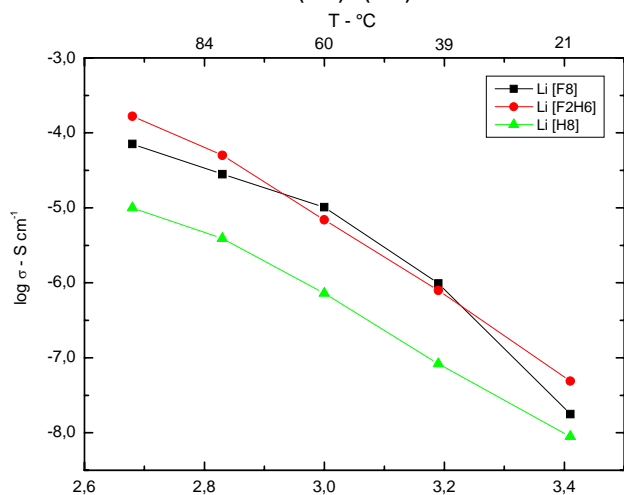


Fig. (5.1.11c)

Graph of poly(siloxane) polymer χ A18:B42 doped with various lithium salts
(O:Li) = (32:1)

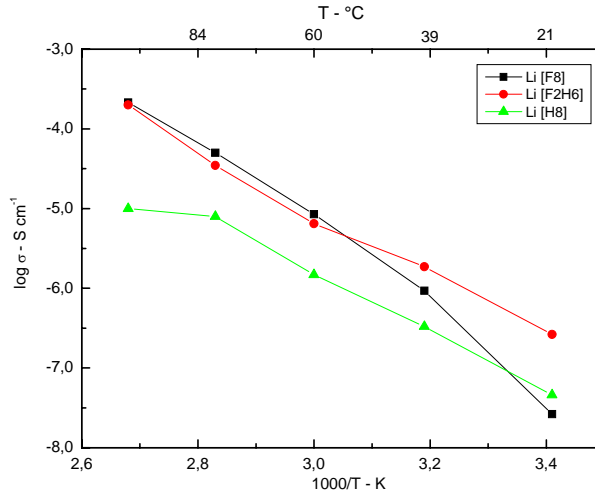


Fig. (5.1.11f)

Therefore the viscosity of the materials at defined temperatures play a crucial role in the conductive behaviours of the materials and in fact is greatly emphasised for the later discussions concerning the ionic liquids.

The highest ambient temperature conductivity at 20 °C for these mixtures was determined to be $1.57 \times 10^{-5} \text{ S cm}^{-1}$ i.e. { Li [F8] (32:1) } at {molar fraction α -A6:B54-10%:90% for poly(siloxane) to (**EGE-A**) and (**EGE-B**) respectively}. Similar to previous commentary the longer (**EGE-A**) chain dictated the physical characteristics of the sample and with increasing concentration of (**EGE-A**) [i.e. table (5.1.2)] conductivities dropped correspondingly indicating increased flexibility constriction of the side chains with the added fact of becoming ever more viscous and rubbery. In respect to the presence of the other lithium salts Li [F₂H₆] and Li [H₈] with their corresponding (**EGE**)'s, they also showed similar conductive behaviours, but where significantly lower conductivities as was expected from previous discussions indicated in section {1}. They exhibited generally higher θ_g 's, indicating a lesser degree of motional freedom of the polymer chains and reflecting their reduced ability to suppress cross-linking due to weaker charge delocalisation of the anion cores as in Table (5.1.6).

5.1.3.

Final commentary:

As aforementioned, a variety of substituted and comb-like polymers with different side-chains attached to a siloxane backbone has been prepared and their conductivity was measured when doped with lithium salts. The comb-like polymers exhibited low glass transition temperatures (T_g) that rose slowly with increasing salt content. The highest ambient temperature conductivity was determined to be between (24:1) and (32:1) ratios for most polymers prepared. The author would also like to add that these results are open to question when one considers that despite extensive attempts to dry the H-siloxane backbone base material before polymerisation, it was observed from IR and ¹H NMR spectra that there remained estimated 1 to 2 % water trapped within the polymer matrix. Plus there was the added issue of residual THF solvent trapped within the matrix estimated to be 0.5% of the total mass. The procedures employed in the removal of these impurities have already been discussed in section {4.4.4}. However, bearing such facts in mind the true validity of the presented results must permit the factoring in of an error from the undesired presence of water molecules.

5.2. Ionic Liquids – Imidazolium Salts

Foreword:

This work had two requirements; firstly the synthesis of novel electrolytes that exhibit gel-like behaviours and secondly to investigate the synthesised materials with EIS. Ionic liquids or room-temperature molten salts are currently of interest, due to their unique chemical and physical properties. Much has been discussed in recent years about their potential applications as electrolytes, a number of investigations have been concerned with the characterisation of these materials and in particular the determination of their conductivities ^[19 - 22]. Some studies are concerned with the understanding of the conductive nature and structure of these materials. Much is known about their structure and behaviours under various thermal conditions, but little is known of their ion-ion interactions and how their conductive pathways function under an applied voltage.

5.2.1.

Preparative Work:

5.2.1.1.

Choice of Cation Salt

The first element to consider in ionic liquids is the core that bears the ionic charge and serves as the locus for the second element, i.e. the substituent group. The core cation may be as simple as a single atom such as nitrogen, phosphor, or sulphur in the form of ammonium, phosphonium, or sulfonium ions respectively. Alternatively, the core may be a heterocyclic such as imidazolium or pyridinium as was discussed in detail in section {1}. The choice made in this regard plays an important role in determining both the chemical and physical properties of the resulting salts. The second element of general importance in the synthesis of such materials is the source of the functional group that is to be incorporated. The key to success here is the identification of the appropriate characteristics desired. By the selective addition of linear alkyl substituents, which have many rotational degrees of freedom ^[23], it is possible to predict and thereby design ionic liquids with alkyl chains that melt at low temperatures and may be easily super-cooled and that demonstrate solid-solid polymorphic transitions.

The first endeavour of this exercise was fulfilled by the selection of the ionic liquid based on imidazolium compounds, whose basic fundamental structure can be seen in Fig. (5.2.1). The selection of the synthesised salts based on this particular cation, is not only

promoted due to its high thermal stability, but also due to its relatively low melting points when compared to other similar salts who were tested by Hirao and co-workers^[19]. The author Hirao^[19] synthesised numerous ammonium, imidazolium, and phosphonium cations and followed by extensive studies of their conductivities (σ), glass transitions (θ_g), and melting transitions (θ_m). Their 1-*N*-methyl-ethyl-imidazolium tetrafluoroborate, turned out to have the best characteristics for electrolyte applications; with an θ_m of 36.9 °C. In addition, earlier investigations in Aberdeen had proved promising and merited further investigation utilising the new lithium salts. Therefore, the imidazolium cation was considered the main target molecule for these investigations. As aforementioned, it is important to choose the appropriate imidazolium salt. It is well known that the characteristic properties of the ionic liquids vary with the choice of anion and cation^[24].

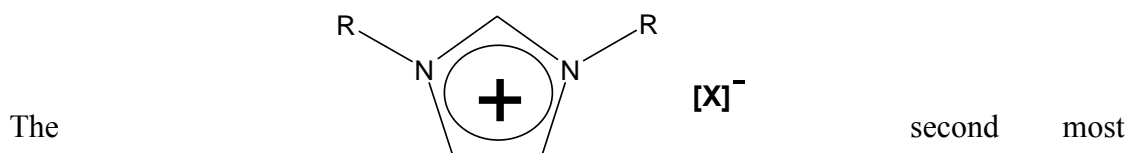


Fig. (5.2.1) Imidazolium cation in the presence of an undefined anion.

$R = C_nH_{2n+1}$; $n \in I [1 - 18]$, $X^- = Cl^-, BF_4^-, PF_6^-$, etc.

important factor after the selection of the appropriate cation, is the selection of the suitable functional group that is to be incorporated. The structure of an ionic liquid directly affects upon its properties, in particular at the melting and liquidus ranges. The Fig. (5.2.2) illustrates the changes in melting points that are observed by changing the symmetry of the imidazolium cation header group if the typical ethyl and butyl groups are respectively exchanged for generic linker alkyl function R (where $R = C_nH_{2n+1}$; $n \in I [1 - 18]$). Therefore a series of cations are generated, all of which can be utilised as the basis of ionic liquids^[25]. As one sees in figure (5.2.2); the manipulation of the alkyl chain can induce a considerable alteration in the melting points and in the tendency of the ionic liquids to form glasses rather than crystalline solids. It is immediately noticeable that an increase in the substituent chain length initially reduces the melting point of imidazolium cation that tends towards glass formation on cooling for $n = 4 - 10$. On extending the alkyl chain lengths beyond i.e. (8 – 10) carbons of alkyl chain lengths; the melting point of the salts start to increase again. This can be explained due to the increasing chain length, as Van der Waal interactions between the long hydrocarbon chains contribute to the local structure by the induction of “microphase” separation between the covalent hydrophobic alkyl chains and the charged ionic regions of the molecule.

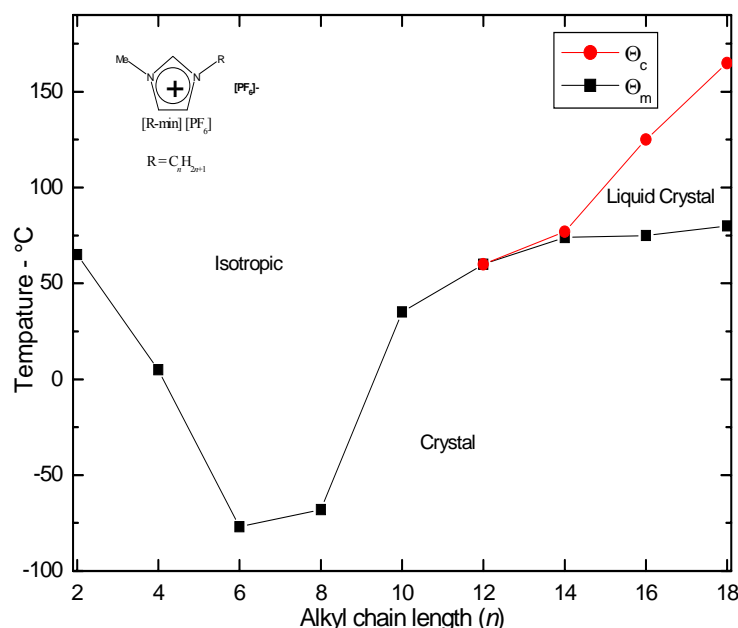


Fig. (5.2.2) Melting point phase diagram for [R-min] $[\text{PF}_6]$ ionic liquids as a function of alkyl chain length n showing the phase changes for the melting transitions (θ_m) from crystalline materials (■), and the clearing transition (θ_c) of the liquid crystalline phase (●)^[24 - 26]

For $n = 12$ and upwards there seems to be a divergence or “split” of the melting points, which increases accordingly to n . This permits the formation of a phase window i.e. a window of two transition phases; a melting transition phase and the clearing transition phase; θ_m and θ_c respectively. This window describes the liquid crystalline phase, which is precisely the region the author intends to exploit for further by EIS investigations. Within this range of $n = 14$ to 18, there is a wide smectic A phase $[\text{S}_A]$ ^{50 [27]}. The author similarly to the work conducted in Aberdeen chose the $n = 16$ chain length for further investigation as seen in Fig. (5.2.3). This was due to its comparatively large $[\text{S}_A]$ window and relatively low θ_m . The other chain lengths of $n = 12$ or less; exhibited no presence of liquid crystalline phase behaviour or were liquids at ambient temperatures as reported by the author^{[23] [28]}. It was intended in this work to substitute into the imidazolium salt matrix various lithium anions; as was discussed previously in section {1}, this would lead to an expected disruption of the packing layers, whereby reducing the θ_c to ambient temperatures to form a gel-like material leading to enhanced conductivities.

50 Smectic A phase $[\text{S}_A]$ is a liquid crystal phase in which the molecules are arranged in layers^[27]

5.2.1.2. Choice of Anion Salt

As already alluded to in earlier sections; the choice of the anion ultimately intended to be an element of the ionic liquid is perhaps more than any other single factor of particular importance. In this work, it will become increasingly clear that the anion within ionic liquid exercises a significant degree of control over the ionic solvent. As was previously mentioned; increases in anion size gave rise to reductions in melting points of salts through a reduction of the Coulombic attraction contributions to the lattice energy of the crystal. In ionic liquids generally, increasing anion size results in lower melting points, (but this is not always the case as will be demonstrated later). The charge and distribution of the charge on the respective ions are the main factors that influence the melting points of the salts, as generic classes. Within similar series of salts as seen in table (5.2.1), small changes in the shape of the uncharged, covalent regions of the ions can have a considerable influence on the melting points of the salts and in turn on the conductivity. The dominant force in ionic liquids is Coulombic attraction between ions. This in turn leads to the next point, i.e. the of the overall lattice energies of ionic liquids, which according to Wasserscheid^[24] depend on:

- (i) the product of the net ion charges.
- (ii) ion-ion separation.
- (iii) packing efficiency of the ions.

Thus low melting from this interpretation should be most preferred when charges on the ions are ± 1 and when the sizes of the ions are large, thus ensuring that the inter-ion separation r is also large. In addition, as was stated consistently up to this point, large ions permit greater charge delocalisation, especially when substituted with electron withdrawing substituents such as $-\text{F}$, $-\text{CF}_3$, $-\text{SO}_2\text{CF}_3$. Such ions further reduce the overall charge density, assists in promoting greater charge mobilities by reducing the formation of large neutral aggregates and in turn increasing their respective conductivities as often cited by authors,. To achieve this aim as was already developed in section {1}, for an ionic salt to melt at room temperature, the anion would have to have a radius in excess of about $3.4 - 4 \text{ \AA}$ ^[24]. This target is achieved by the utilisation of the Regensburg salts synthesised by Barthel and co-workers^{[5 - 9] [29 - 33]}, that are well above this stated size seen in table (5.2.1). Similar behaviours are observed with increasing cation size as was already indicated in the

previous section {5.2.1.1} on moving down the periodic table for example. The lithium salts tend to be higher melting than their sodium or caesium analogues, which is well documented in the literature^[34]. If the charge on the ion can be delocalised or if the charge bearing regions can be effectively isolated in the interiors of the ionic moiety, then the Coulombic terms are further reduced. Therefore in summarised form, the reduction in the melting points can be achieved by increasing the size of the anion, or the cation and through the manipulation of the substituted functional groups i.e. alkyl chain lengths as already discussed in detail in sections {1} and {5.2.1.1}. The implications of manipulating these variables will become obvious in later sections.

Structure	Name IUPAC	Short-hand	M g mol ⁻¹	Calculated Radius r – Å ⁵¹
$\text{Li}^+ [\text{Cl}]^-$	lithium chloride	Li [Cl]	42.39	1.7
$\text{Li}^+ \left[\begin{array}{c} \text{F} \\ \\ \text{F}-\text{P}-\text{F} \\ \\ \text{F} \end{array} \right]^-$	lithium hexafluorophosphate	Li [PF₆]	151.90	2.41
$\text{Li}^+ \left[\begin{array}{c} \text{F} \\ \\ \text{F}-\text{B}-\text{F} \\ \\ \text{F} \end{array} \right]^-$	lithium tetrafluoroborate	Li [BF₄]	93.75	2.32
$\text{Li}^+ \left[\begin{array}{c} \text{H} \quad \text{H} \\ \quad \\ \text{C} \quad \text{C} \\ \quad \\ \text{H} \quad \text{H} \end{array} \text{O} \text{B} \text{O} \begin{array}{c} \text{H} \quad \text{H} \\ \quad \\ \text{C} \quad \text{C} \\ \quad \\ \text{H} \quad \text{H} \end{array} \right]^-$	lithium bis-[1,2-benzenediolato(2-)-O,O']borate	Li [H8]	233.92	4.21
$\text{Li}^+ \left[\begin{array}{c} \text{F} \quad \text{F} \\ \quad \\ \text{C} \quad \text{C} \\ \quad \\ \text{F} \quad \text{F} \end{array} \text{O} \text{B} \text{O} \begin{array}{c} \text{F} \quad \text{F} \\ \quad \\ \text{C} \quad \text{C} \\ \quad \\ \text{F} \quad \text{F} \end{array} \right]^-$	lithium bis - [3,4,5,6 – tetrafluoro - 1,2 – benzenediolato (2-) -O,O']borate	Li [F8]	377.84	4.20

Table (5.2.1) Table of lithium salts utilised during this work dissolved in liquids.

51 These anion radii data were sourced from Welton^[24] and MOPAC

5.2.2.

Synthesis & Salt Substitution:

The synthesis of the ionic cationic liquid imidazolium header group with the relevant alkyl functional is achieved by mixing of equimolar quantities of the appropriate amine and chloroalkane as described in detail in section {4.2}. The substitution procedure of the various lithium salts utilised for this work can also be read in section {4.3}. The synthesis and subsequent substitution of the referred to materials under investigation is summarised in Fig. (5.2.4).

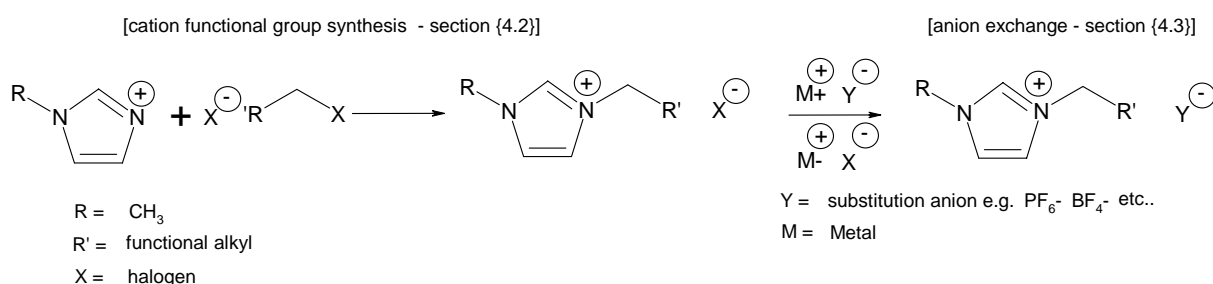


Fig. (5.2.4) The general synthesis of ionic liquid 1-*N*-alkyl-3-methylimidazolium and anion exchange

The imidazole employed was 1-methylimidazole chloride. To this reagent was selectively attached 1-chlorohexadecane [$\text{C}_{16}\text{H}_{33}\text{Cl}$] forming 1-*N*-hexadecyl-3-methylimidazolium chloride [$\text{C}_{16}\text{-min}$] [Cl] as seen in Fig. (5.2.5). In general, it is well known that the halide salts become less hygroscopic as the alkyl chain increases in length. The lithium salts as seen previously in table (5.2.1) reacted with their respective imidazolium salt by means of an anion exchange in the presence of acetone solvent yielding scarcely soluble LiCl and the imidazolium salt. The characterisation of these materials can be seen in section {4.3} and are briefly summarised in table (5.2.2).

In addition to the substitution of the various lithium salts, the substituted salts were further doped with their respective generic lithium salt. This procedure was initiated to establish if the conductivities of the samples could be further increased through the presence of the lithium salt and to study the movements of the ions through the matrix itself. Four systems were selected for this procedure i.e. [$\text{C}_{16}\text{-min}$] [PF_6], [$\text{C}_{16}\text{-min}$] [BF_4], and [$\text{C}_{16}\text{-min}$] [F8] which were doped with lithium hexafluorophosphate **Li** [PF_6], lithium tetrafluoroborate **Li** [BF_4], lithium bis-[1,2 benzenediolato(2-)-O,O']borate **Li** [**H8**], and lithium bis - [3,4,5,6 – tetrafluoro - 1,2 – benzenediolato (2-) -O,O']borate **Li** [**F8**] respectively. The author in

Aberdeen [28] previously tested the first system [C₁₆-min] [PF₆], but the later systems have to this point not been investigated.

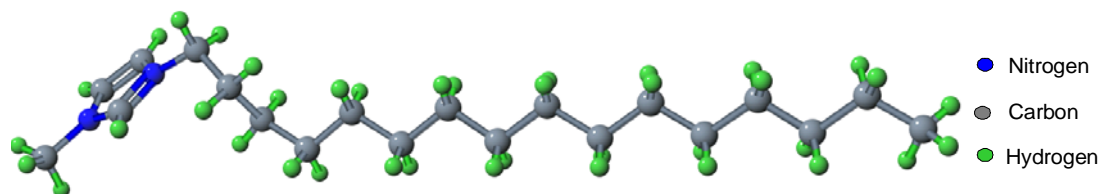


Fig. (5.2.5) 1-*N*-hexadecyl-3-methylimidazolium cation [C₁₆-min]⁺

Shorthand	Name	Structure	M g mol ⁻¹	Phase Transitions		
				C _H - °C	S _A - °C	Iso - °C
[C ₁₆ -min] [Cl]	1- <i>N</i> -hexadecyl-3-methylimidazolium chloride		342.97	-	55.1	66.2
[C ₁₆ -min] [PF ₆]	1- <i>N</i> -hexadecyl-3-methylimidazolium hexafluorophosphate		452.50	16.2	75.1	125
[C ₁₆ -min] [BF ₄]	1- <i>N</i> -hexadecyl-3-methylimidazolium tetrafluoroborate		394.34	-	41.1	81.8
[C ₁₆ -min] [H8]	1- <i>N</i> -hexadecyl-3-methylimidazolium bis-[1,2-benzenediolato(2-)-O,O']borate		524.52	36.1	63.4	97.14
[C ₁₆ -min] [F8]	1- <i>N</i> -hexadecyl-3-methylimidazolium bis-[3,4,5,6-tetrafluoro-1,2-benzenediolato(2-)-O,O']borate		678.44	-	34.7	71.6

Table (5.2.2)

5.2.3.

Structural Analysis of [C₁₆-min] in the presence of anion:

Before detailed discussions ensue concerning the conductive behaviours of the presented materials, it is important to understand the structure of the materials at an inter-molecular level. The following discussions will draw on cited evidence from two papers of X-ray crystallography measurements and other supporting evidence ^[23] ^[26] ^[28]. The proposals from these papers have been added to and reinforced in the light of new evidence of recent investigations.

The author has already presented in Fig (5.2.5) the crystalline structure of typical 1-*N*-3-methyl-imidazolium salt at ambient temperatures. From the cited evidence ^[23] ^[26] the structure consists of discrete cations and anions separated by at least Van der Waals distances. The molecular ring is planar. The straight chain nature of the alkyl side chain groups is disrupted close to the ring where it adopts a bent conformation seen in Fig. (5.2.5). The chain configuration and the lack of any disorder in the structure appears to be the consequence of interdigitated molecular packing as seen in Fig. (5.2.6). The ionic liquids presented in this work suggest a helix configuration of the alkyl chains packed together in a tight manner with each imidazolium header intertwined at 180° to its partner along the *n*-alkyl chains as a helix seen in Fig. (5.2.6) and (5.2.7). These structures are irregular liquid like confirmations or possibly with persistent helical sense mounted on a crystalline to liquid crystalline superstructure. The spacing between each lamella layer was measured to be 26.5 Å for [C₁₆-min] [PF₆] and can be assumed to be holding true for all other substituted lithium salts. The alkyl chains are tilted relative to the layers of the cation and anions in a manner similar seen in Fig. (5.2.6) and (5.2.7).

In the cited evidence and with the knowledge of these investigations the anions are inserted between the imidazolium header groups and the twisted chains as indicated in Fig. (5.2.8). The gap between the header group and the twisted chains has been calculated to be 3.108 Å and should be noted for future reference by comparing the anion size already shown in table (5.2.1) seen earlier. The anions occupy the 2-dimensional helical spaces as seen in Fig. (5.2.8). This premise can be supported by observations of the presented materials under a POM (Polarised Optical Microscope)⁵² and in particular samples [C₁₆-min] [Cl], [C₁₆-min]

⁵² POM instrument supplied with kind gratitude by Prof. Prof. Dr. A. Pfitzner Institut für Anorganische Chemie, Universität Regensburg.

[BF₄], and [C₁₆-min] [PF₆] where focal-conic bire-fringent or liquid crystalline phase changes were observed [see Fig. (5.2.10)] at elevated temperatures of 66.12 °C, 81.88 °C and 75.19 °C for [C₁₆-min] [Cl], [C₁₆-min] [BF₄], and [C₁₆-min] [PF₆] respectively. An interesting observation was noted for salts [C₁₆-min] [H8] and [C₁₆-min] [F8], where these samples did not exhibit the typical pattern of behaviours for ionic liquids of this family. At elevated temperatures the typical smectic A [S_A] character expected did not occur for Li [F8], but instead the sample on melting went straight from crystalline to the isotropic phase i.e. non-birefringence was stated. There was no discernable liquid crystalline phase observed. It is proposed by this author that these particular anions [H8] and [F8] are too large for full stoichiometric occupancy of the inter-helical spaces and therefore take up less energetically advantageous orientations within the matrix in which more will be said later.

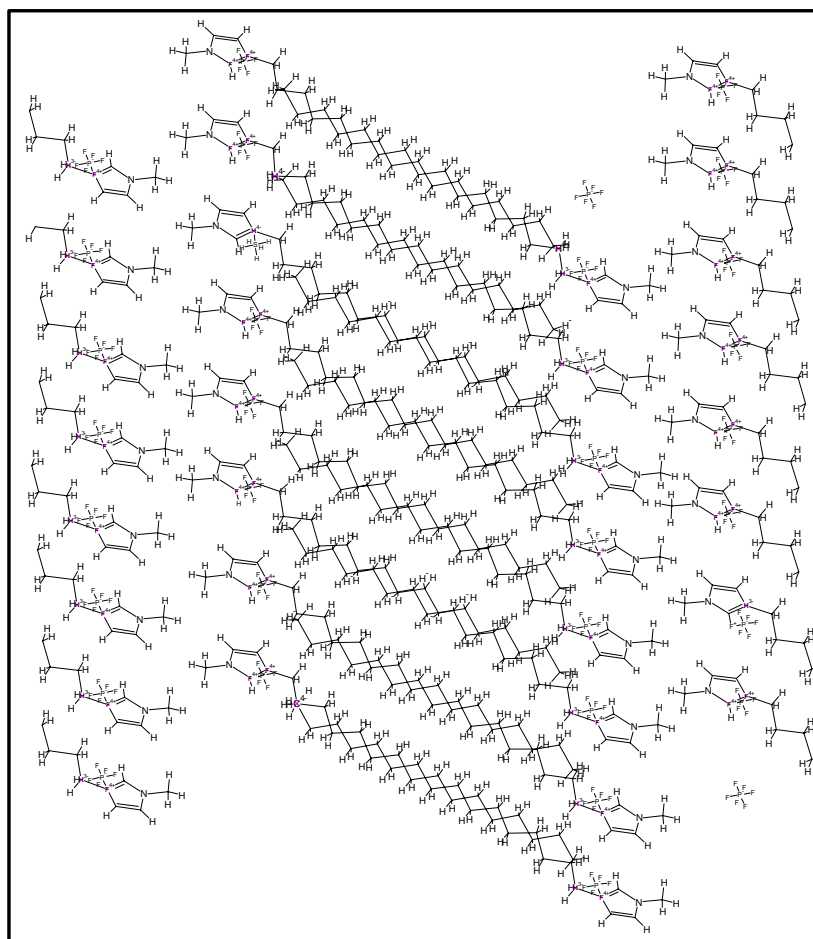


Fig. (5.2.6) Over view of lattice conformation for [C₁₆-mim] [PF₆].

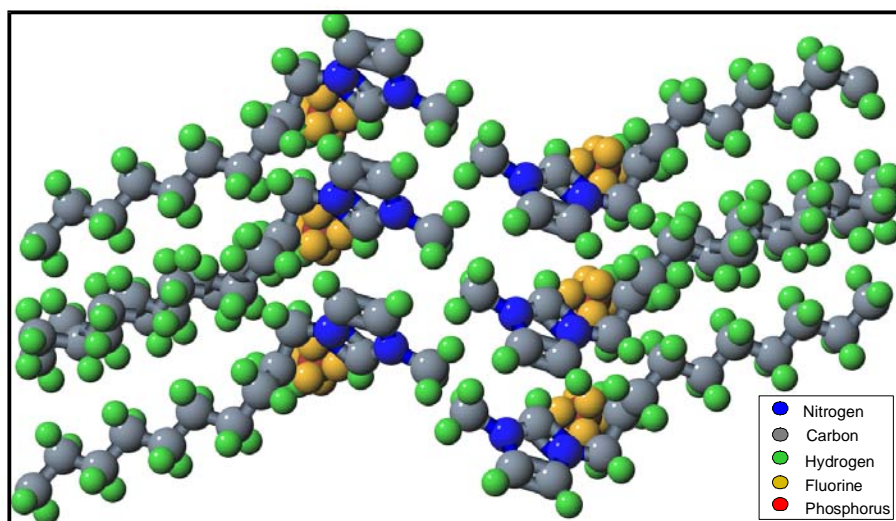


Fig. (5.2.7) [C₄mim][PF₆] interdigitated molecular packing

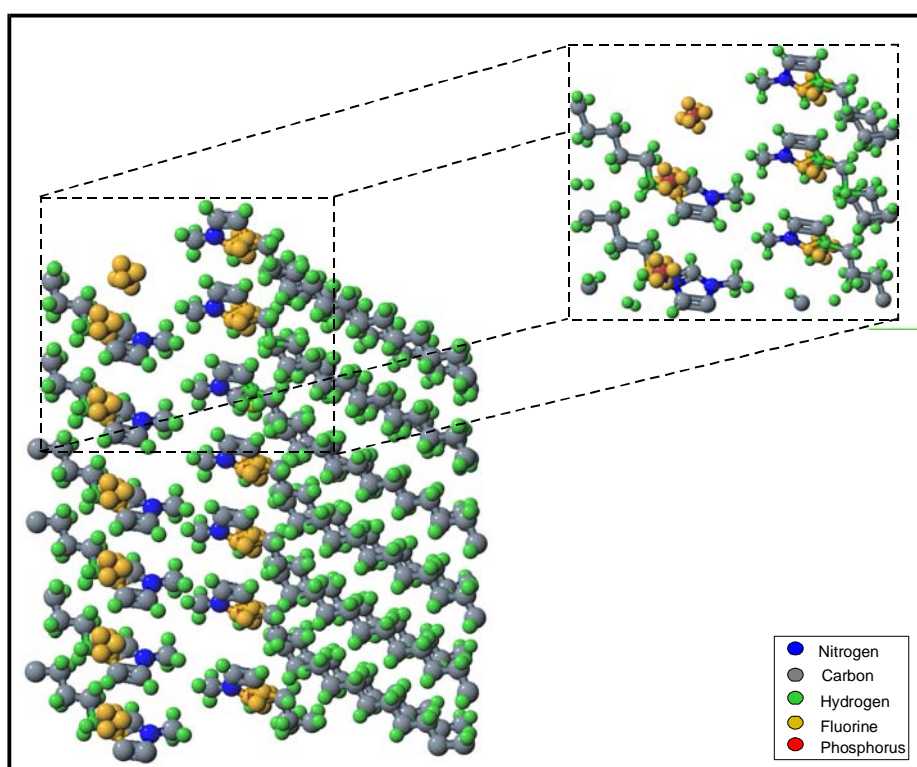


Fig. (5.2.8) [C₄mim][PF₆] - Here one sees the anions are inserted between the imidazolium header groups and the twisted chains.

5.2.4.

DSC Analysis of [C₁₆-min] in the presence of different anions:

The application of DSC and DTA methods is an integral part of the analysis of ionic liquids. There is a close relationship between the thermal behaviours of the materials and their conductivities. On heating the typical sample [C₁₆-min] [PF₆] from – 40 °C to +140 °C, three distinct exothermic phase peaks are observed as seen in Fig. (5.2.11a). All DSC plots presented are from the second heating cycle Fig. (5.2.11a-e). On the second DSC cycle the temperatures of the peaks are usually 1 to 2 °C lower than the initial cycle. The first cycle can be considered the residual morphological “fingerprint” of the solvent utilised in the sample synthesis and preparation and involves association between the n-alkyl chains, where as the second cycle exposes the true nature of the materials i.e. any discrepancies can be assigned to random encounters between the segments during various phase transitions. On cooling of all samples, the phase transition peaks are generally 10 °C lower than their corresponding heating curve, this can be attributed to super-cooling and is a common phenomenon in such systems [24] [43 - 45]. Supercooling is an important and common feature of these materials, and complicates the calorimetry. Many DSC experiments demonstrated a delayed melting endotherm, due to the failure of the sample to crystallise quick enough. A suggestion by Mutch & Wilkes [35] proposed that the sample could be reliably crystallised by cooling as rapidly as possible (ballistic cooling) in the DSC cell. The author experimented with such a technique with good success, since slow cooling invariably resulted in supercooling. The implications for such ionic liquids could mean electrolytes functioning at substantially below its melting point θ_m .

In reference to the particular sample [C₁₆-mim] [PF₆], once can see three exothermic peak at 8.11 °C, 75.19 °C and 125.56 °C which are assigned the [C_I – C_{II}], [C_{II} – S_A], and [S_A – Iso] phase transitions respectively. The phase transitions that are common to such media are the two transitions [C_{II} – S_A] and [S_A – Iso]. On cooling from the isotropic phase [Iso] (clearing temperature) to the smectic A phase [S_A] at 125.56 °C, the sample coalesce to give a focal conic fan texture⁵³ {see Fig. (5.2.9)} that was observed under the POM. This phase is commonly known as the mesophase, which on further cooling the sample passes through a

⁵³ In most case the layers of smectic A phases are not flat, but rather are distorted. As fig. (5.2.9a) indicates, the layers may be rolled enrolled to give cylindrical structures. If the cylinders themselves are bent and there are many layer, the so-called anchor-ring arises in Fig. (5.2.9b), which has two geometrical lines of maximum distortion of the structure: a straight line and a circle, both of which are visible in the respective textures because they are places of maximum light scattering under a POM. If the anchor is slightly deformed, the so called “Dupin cyclide” is existing as seen in Fig. (5.2.9c). In the texture containing cyclides known as “focal conic” branches of hyperbolas and ellipses exist as geometrical places of maximum deformation and are visible in special formations [36].

new to phase transition $[C_{II} - S_A]$ at 75.19 °C yielding a characteristic crystalline texture which is assigned the $[C_{II}]$. The lower temperature phase transition at 8.11 °C is associated with a change in the texture of the crystal phase. De Roche mentioned it & Imrie^[23] that this transition was not previously been reported for the $[C_{16}\text{-mim}] [PF_6]$ salts. What actually occurs to the sample as it passes from one phase to another has also important implications for the conductivities of the material, which will be discussed in the next section. As was aforementioned, three phase transitions are observed for the $[C_{16}\text{-mim}] [PF_6]$, and similar behaviours are observed for the other anions. In all samples except $[C_{16}\text{-mim}] [Cl]$ observations under the POM indicated the presence of focal-conic fan texture as seen in Fig (5.2.10). The larger anions $[C_{16}\text{-mim}] [H8]$ and $[C_{16}\text{-mim}] [F8]$ reduced the $[C_{II} - S_A]$ and $[S_A - Iso]$ phase transitions considerably in the case of $[C_{16}\text{-mim}] [F8]$, to 34.71 °C and to 71.62 °C for the phase transitions $[C_{II} - S_A]$ and $[S_A - Iso]$ respectively. This is a particularly important development, because we have brought the liquid crystalline phase down to near ambient temperatures without requiring the need to dope the material first, while at the same time retaining a wide mesophase of 28 °C. It has already been discussed in section [1] that by doping the ionic liquid, one can reduce the θ_m and θ_c through disrupting the lamella pathways and favouring energetically less stable structures and hence lowering the phase transitions. By doping $[C_{16}\text{-mim}] [F8]$ with Li $[F8]$ the conductivities should from previous experience be enhanced. The crystal to isotropic phase transition should be reduced even further to already near ambient temperatures.

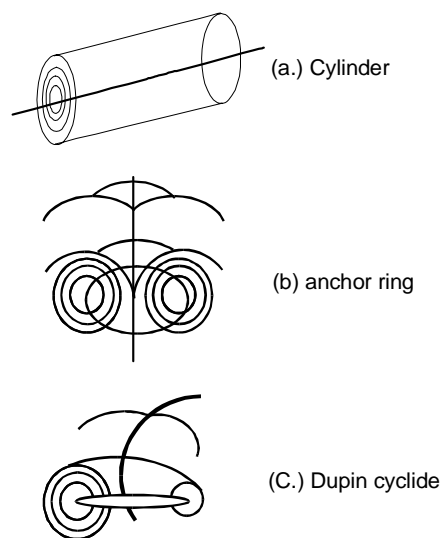
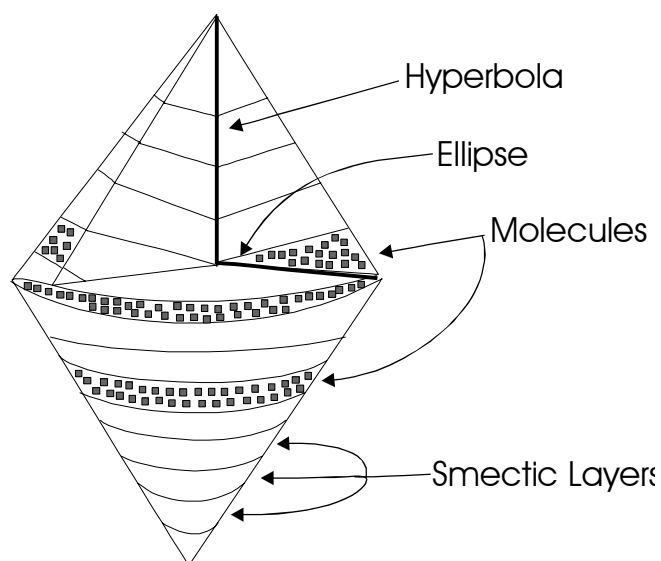
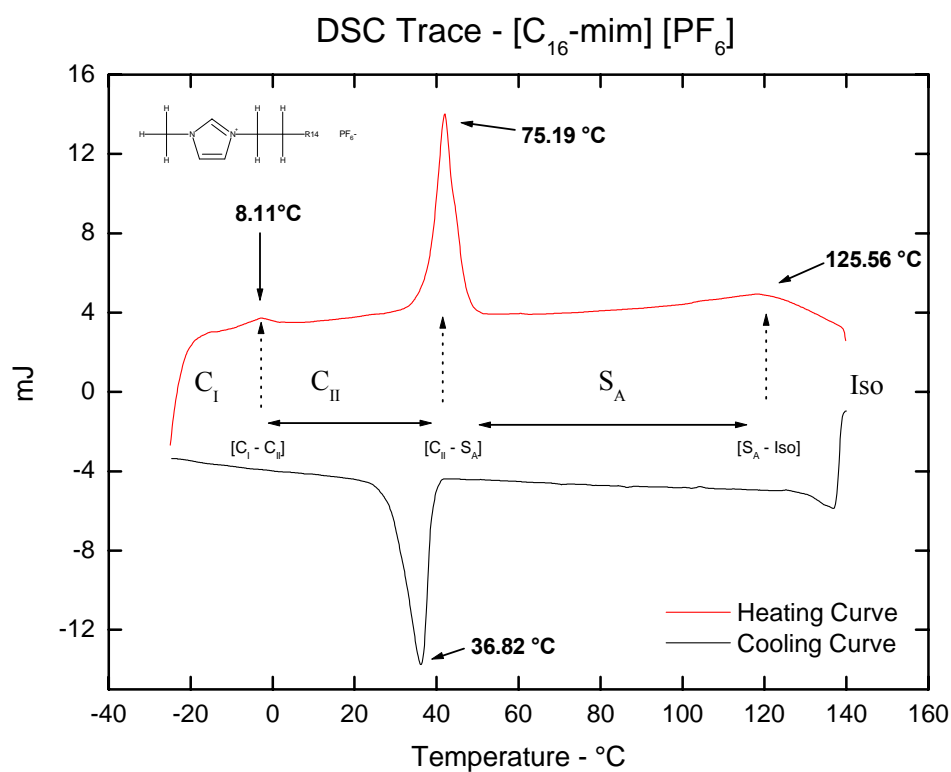


Fig. (5.2.9) Defects in smectic A phases^[36].

Fig. (5.2.10) Depiction of focal-conic domain ^[28]Fig. (5.2.11a) DSC trace of [C₁₆-mim] [PF₆] with indicated phase transitions

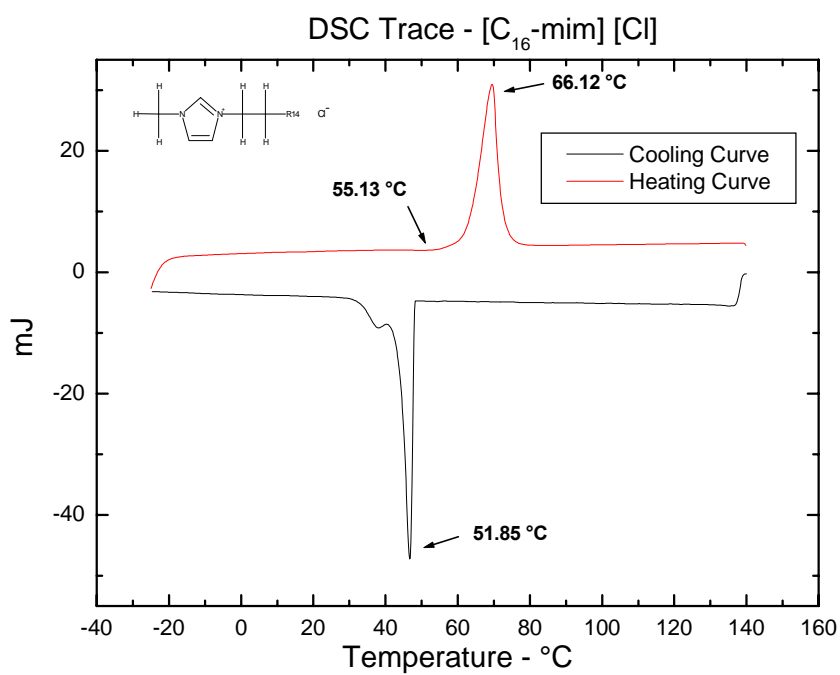


Fig. (5.2.11b)

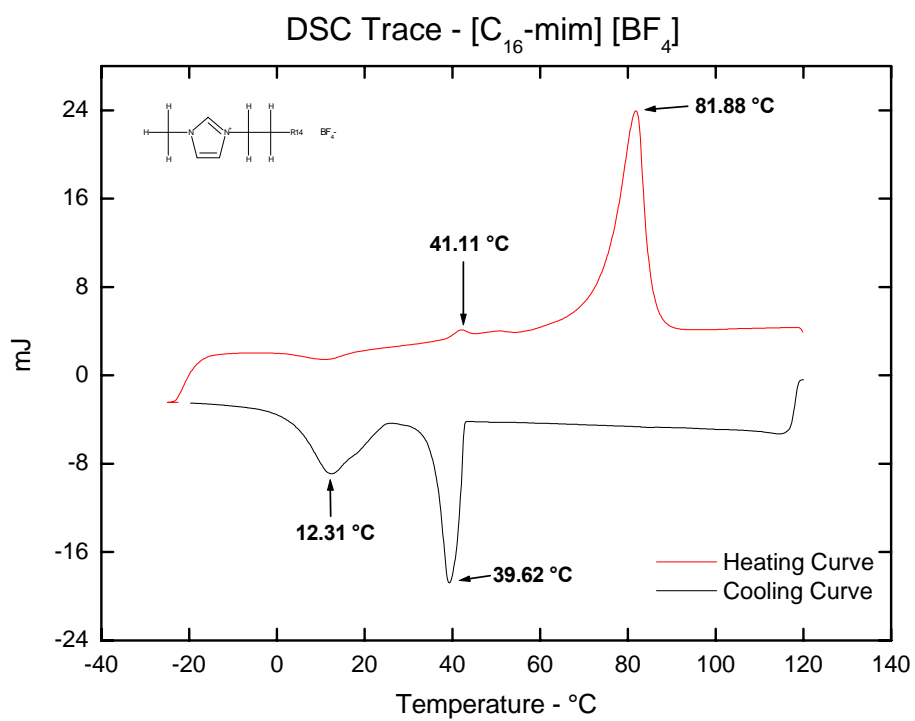


Fig. (5.2.11c)

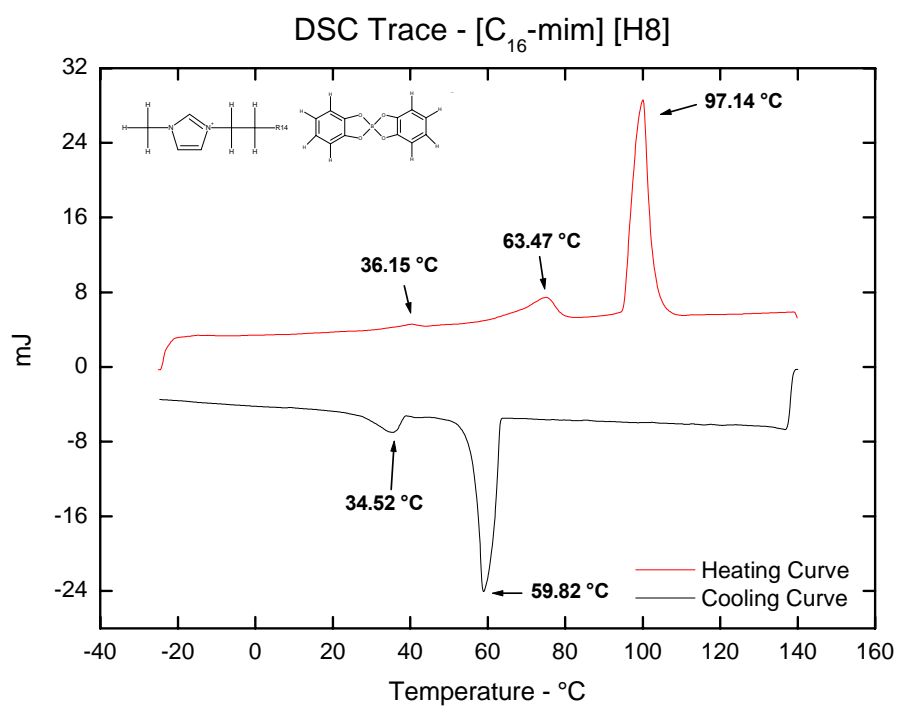


Fig. (5.2.11d)

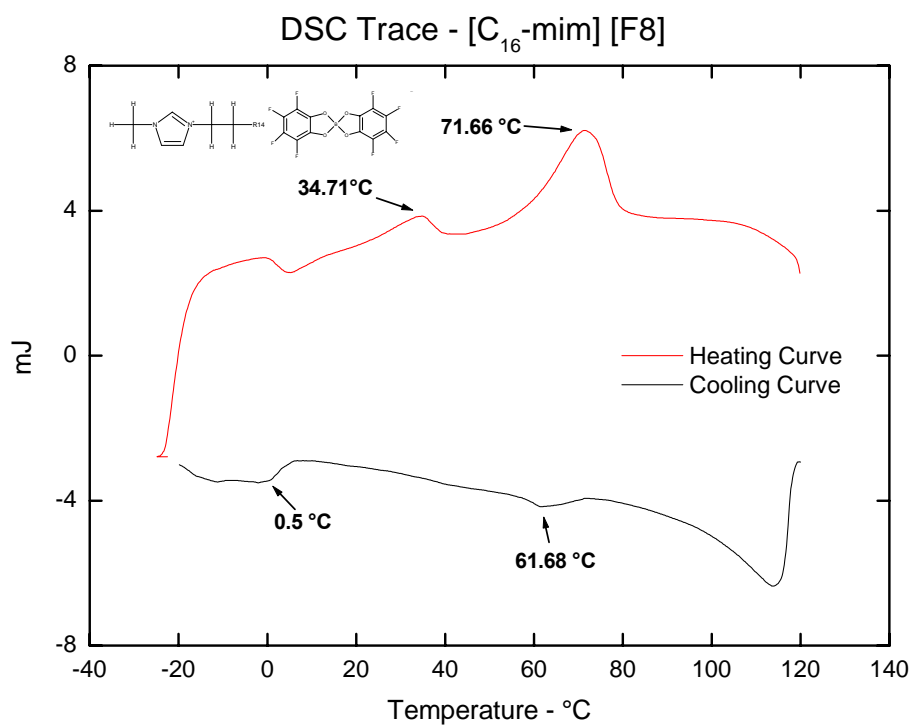


Fig. (5.2.11e)

5.2.5.

EIS investigations of $[C_{16}\text{-mim}]^+$ in the presence of anion:

5.2.5.1.

Phase Transitions:

The EIS investigations of the presented materials brought forth a number of newly observed conductivity phenomena. The data was acquired by the usual means and is presented in the classical Arrhenius format. Most measurements are assumed to be conducted over a temperature range of $-10\text{ }^{\circ}\text{C}$ to $140\text{ }^{\circ}\text{C}$ unless otherwise stated. The Fig. (5.2.14a-e) summarises the conductive behaviours of the samples utilised. The samples were subjected to a vigorous testing routine over a period of predefined days (1, 3, 6, and 9 days), this was intended to establish a understanding of the conductive stabilities of the investigated samples under at elevated temperatures. From the presented data, it is obvious that the conductive behaviours reflect either the morphological behaviour of the samples i.e. phase transitions and or the relative sizes and charge densities of the substituted anions. For all samples, there is a surprisingly close correlation between the DSC exotherms and their respective conductivity seen in Fig. (5.2.13a-e).

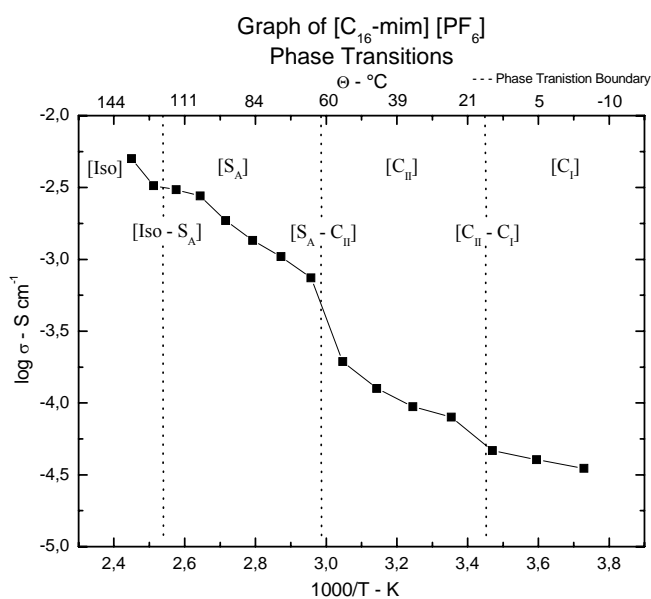


Fig. (5.2.12 i) Three phase transition

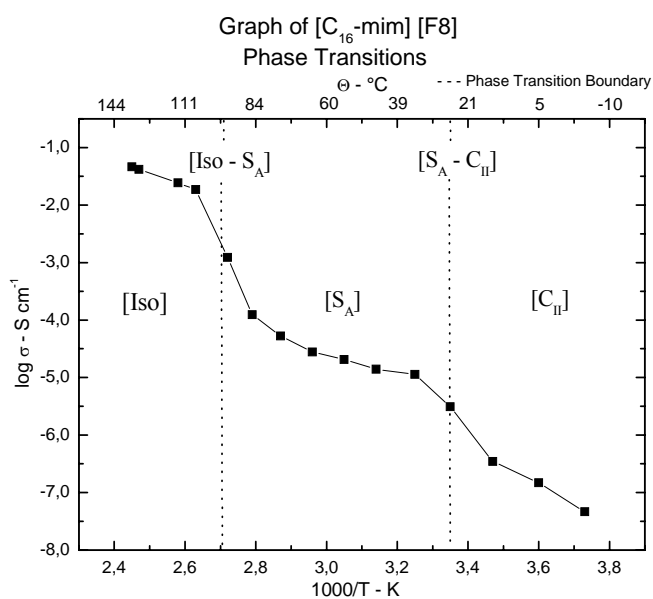


Fig. (5.2.12 ii) Two phase transition

If we now take a closer examination of the data sets [C₁₆-mim] [PF₆] and [C₁₆-mim] [F8] in figure (5.2.12 i) and (5.2.12 ii) respectively; one can clearly see within the data output in both situations the outline of conductivity dependent steps or “jumps”. The figure (5.2.12 i) shows for [C₁₆-mim] [PF₆] a clearly discernable large conductivity elevation attributed to the [C_{II} - S_A] phase transition. In the case of all presented samples, if one examines Fig. (5.2.14a-e) there is a significant change in the conductivity associated with the melting of the sample from the [C_{II}] to the [S_A] phases. In figure (5.1.12 i) and (5.1.12 ii); it is interesting to note that the crystal phase [C_{II}] demonstrates considerable levels of conductivity implying greater ion mobility in the solid state^{[23][28]}. In the case of figure. (5.2.12 i) for the sample [C₁₆-mim] [PF₆], three phase transitions are observed. On heating from low temperatures the first phase transition is the [C_I - C_{II}] the dramatic decrease in conductivity for this sample which was reported by De Roche and Imrie^[28] is not observed in the data. Instead the [C_I - C_{II}] phase transition is active in a region of relatively high conductivity at the temperatures less than 5 °C, which is the region where the [C_I] phase is suspected to be present. Where this author reports conductivities of $\sigma = 4.036 \times 10^{-5} \text{ S cm}^{-1}$ at 5 °C, which is considerably better than those reported by De Roche^{[23][28]} previously. The results are compared in Fig. (5.2.13). From the graph one sees that there is no dramatic decrease in conductivity below the [C_I - C_{II}] phase transition as was previously reported. The low temperature [C_I] phase can be described as a region, where the ionic motion is constricted by the lattice extreme rigidity. The phase transition [C_I - C_{II}] is relatively small, suggesting that the [C_{II}] phase permits better ionic motion of the anions and a slight losing of the alkyl side chains. Their smaller size, when compared to the larger imidazolium cations, permits their easier movement and greater flexibility within the suggested lamella matrix. The DSC data for this sample exhibit a similar barely detectable exotherm indicating no radical structural alterations within the matrix.

On increasing the temperature even further and passing through the [C_{II} - S_A] phase transition, there is a large jump in conductivities on passing through the [S_A] phase transition, i.e. for 80 °C a conductivity of $\sigma = 1.356 \times 10^{-3} \text{ S cm}^{-1}$ [C₁₆-mim] [PF₆] once again there is a correspondingly large endotherm observed in the DSC plot in the same region see Fig. (5.2.14b). This region and in particular the conductivity step is attributed to the melting of the alkyl side chains. This in turn permits a greater degree of freedom for the anions to move about within the matrix through increased free volume leading to higher ionic mobility. The final phase transition observed exhibits a smaller increase of the conductivity jump for [S_A - Iso] phase transition i.e. for 135 °C a conductivity of $\sigma = 3.471 \times 10^{-3} \text{ S cm}^{-1}$ [C₁₆-mim] [PF₆].

The ionic environment changes little during this particular phase transition and can be considered the final organisational gasp of the matrix as large ionic aggregates persist where the free volume change is smaller over the transition. The Fig. (5.2.15) is a schematic summarising the structural changes that the sample undergoes as it proceeds from one phase transition to another. A similar explanation has recently proposed to rationalise the low values of ΔS [S_A - Iso] for similar length alkyl chains liquid crystals, whereby the hydrogen bonded aggregates are proposed to exist in the isotropic phase ^[23] ^[46]. In a further comment, concerning the comparison of the conductive measurements between the presented work and similar measurements in Aberdeen ^[23] ^[28] for $[C_{16}\text{-mim}][PF_6]$, one sees in Fig. (5.2.13) much improved conductivities at lower temperatures and clear evidence of a third phase transition below ambient temperatures. This as previously indicated can be attributed to more advantages measuring conditions available to this author during investigations in Regensburg, where all preparations and measurements were conducted in an inert environment (as previously described in detail in section {3.3}).

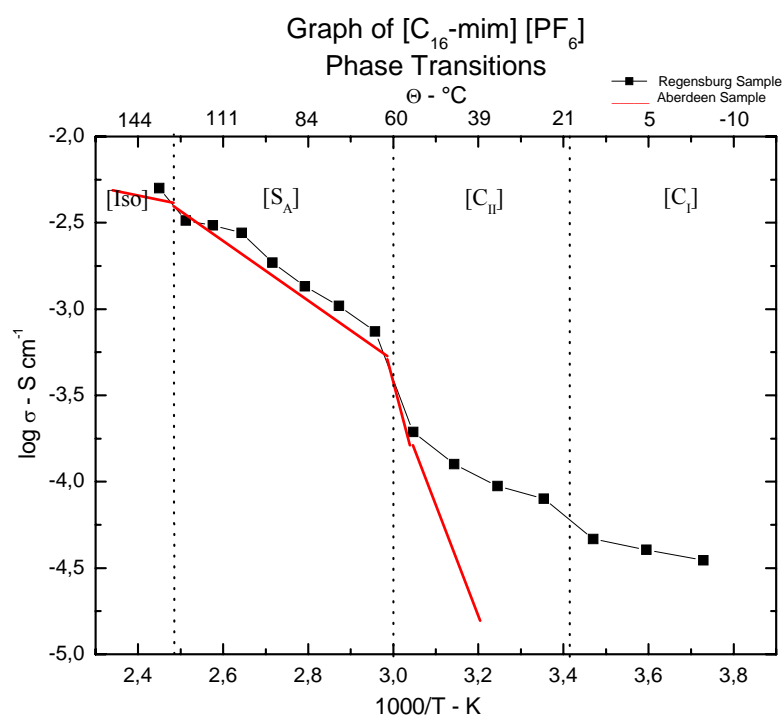


Fig. (5.2.13) Comparison of conductive data plots between Regensburg and Aberdeen ^[23] ^[28] for sample $[C_{16}\text{-mim}][PF_6]$.

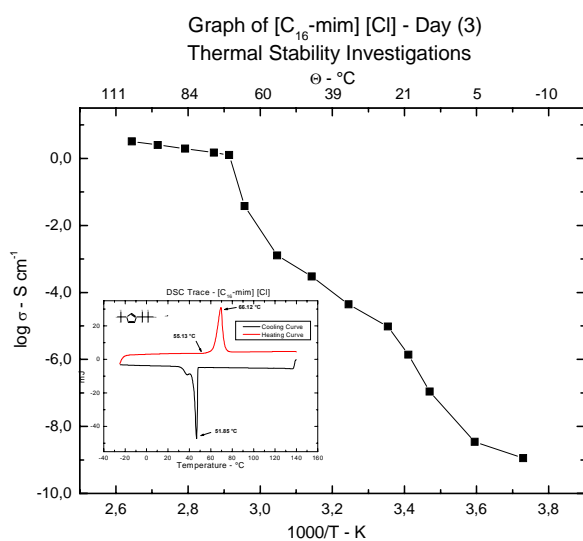


Fig. (5.2.14a)

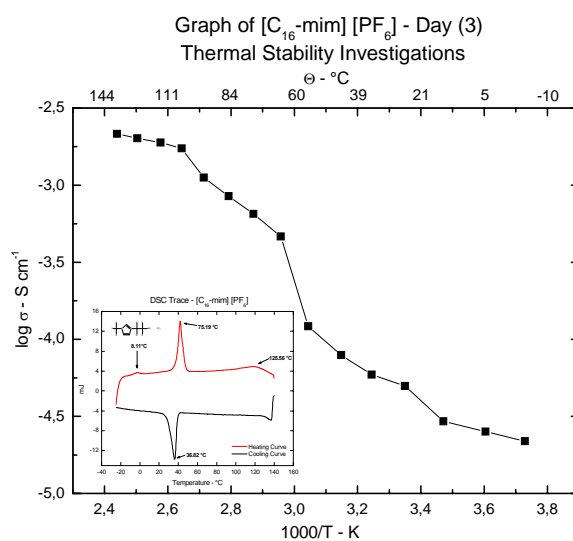


Fig. (5.2.14b)

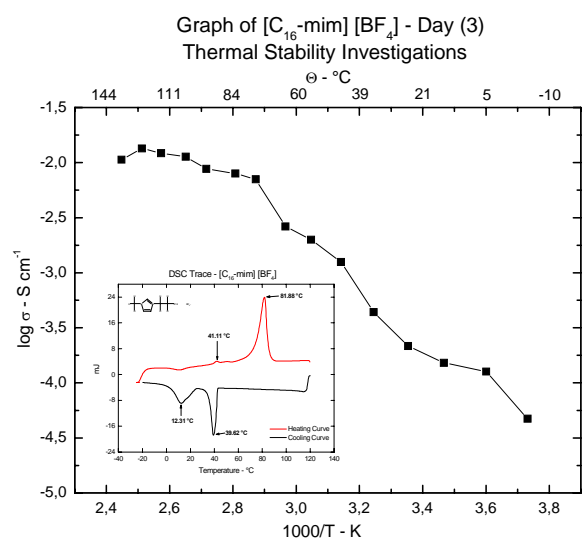


Fig. (5.2.14c)

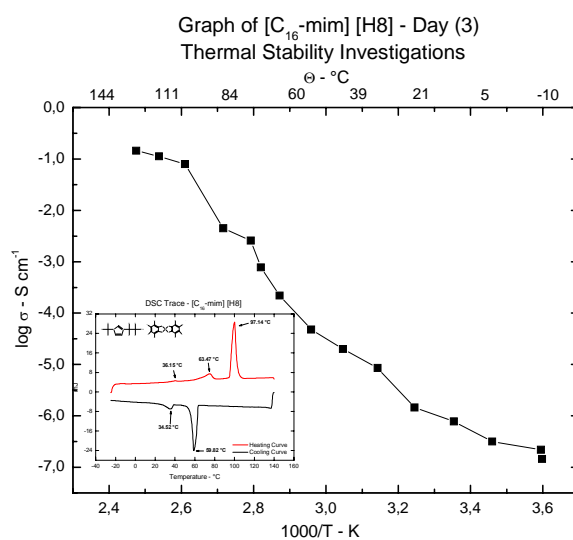


Fig. (5.2.14d)

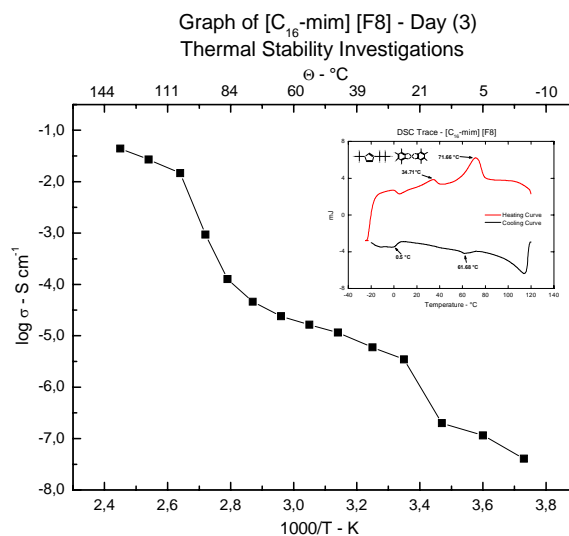


Fig.(5.2.14e)

Consequently the Fig. (5.1.12 ii) for sample $[C_{16}\text{-mim}][F8]$ the conductivity measurements behaved in similar manner to the $[C_{16}\text{-mim}][PF_6]$ in Fig. (5.1.12 i). Only two phase transitions are observed; the $[S_A - C_{II}]$ and $[Iso - S_A]$, which occur at 34.1°C and 71.66°C respectively. The disappearance of the $[C_I]$ may be attributed to the reduced free volume within the matrix due to the presence of the large anions. Only at Θ_m near the $[C_{II} - S_A]$ phase transition is there any notable change in conductivities, which can be attributed to the melting of the alkyl salts. It is clear that from initial comparisons of samples, that “size does matter” and that the predicated charge delocalising properties of the anions have less impact on the conductivities of the samples materials in contrast to the poly(siloxane) based solid polymer electrolytes presented in the previous section {5.1}.

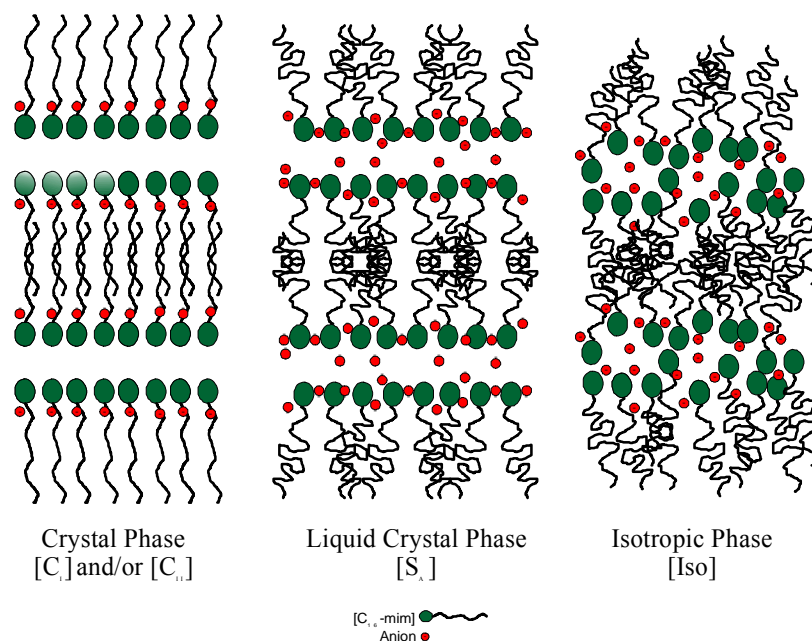


Fig. (5.2.15) Schematic of the phase transitions of the undoped $[C_n\text{-mim}][X^-]$ systems. Increasing temperatures permit great ionic mobility due to the decreasing rigidity of the system.

5.2.5.2.**Suspected Decomposition of [PF₆] anion due in the presence of unsolved LiPF₆:**

This author in previous conductivity investigations in Aberdeen [28] reported that the sample [C₁₆-mim] [PF₆] exhibited generally lower conductivities after a number of thermal cycles. This drop in conductivity between cycles was particularly evident between the first and second thermal cycle (day 3). Only after the third cycle on day 6 did the conductivities stabilise as seen in Fig. (5.2.16b). This occurrence was suspected to be one of two possibilities:

- (i) that the morphology of the residual solvent “fingerprint” hindered the optimal structure of the self-organising materials i.e. therefore; inadvertently depressing the true conductivity of the sample.
- (ii) that the anion [PF₆] decomposes above 65 °C due to the presence of still unsolved LiPF₆; which is well documented [37].

If it was a factor of structural reorganisation of the material to a more optimal orientation relative to the cell electrodes, then the further question must be asked why did the conductivity decrease and not increase as seen in Fig. (5.2.16b). In the initial investigations of the [C₁₆-mim] [PF₆], particularly during the refinement of the substitution procedure small amounts of LiPF₆ were still trapped in the matrix and did not fully dissociate. In addition, very low amounts of water were present. In later synthetic batches after better refinement techniques were applied the aforementioned conductivity drop did not occur. This implies that the initial morphology played little or no role in the overall drop in conductivities of the [C₁₆-mim] [PF₆] sample as was suspected from the measurements in Aberdeen [28] and now in Regensburg. This reported drop in conductivity can be attributed to the decomposition of unsolvated LiPF₆ within the samples, yielding a scarcely soluble LiF and PF₅ i.e. two non-conducting materials.



The author conducted IR measurements to prove the occurrence of the above reaction. The author observed for PF_5 two strong fundamental bands in the IR spectrum at 947 cm^{-1} and 575 cm^{-1} . Further evidence of the presence of HF formation, was collaborated from the corroded condition of the stainless steel electrodes. This is not the case in all samples, but this development further reinforces the important point mentioned in section {4.3} concerning the importance of successful purification of the salts before electrochemical studies can be initiated. It is important to note that LiPF_6 is widely used as a salt in conductivity investigations by many work-groups and is often underestimated as to its disadvantages in high temperature applications. The DSC plots indicated no evidence of structural changes in the phase transition shifts which further emphasises the complementary roles that both methods play in similar investigations

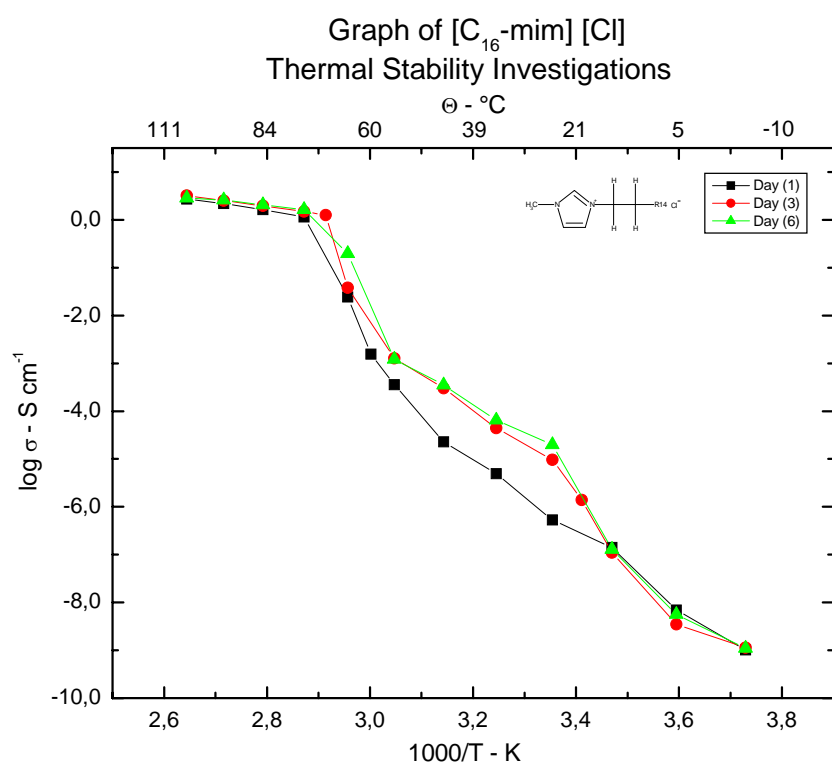


Fig. (5.2.16a)

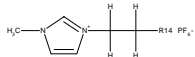


Fig. (5.2.16b)

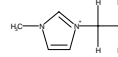


Fig. (5.2.16c)

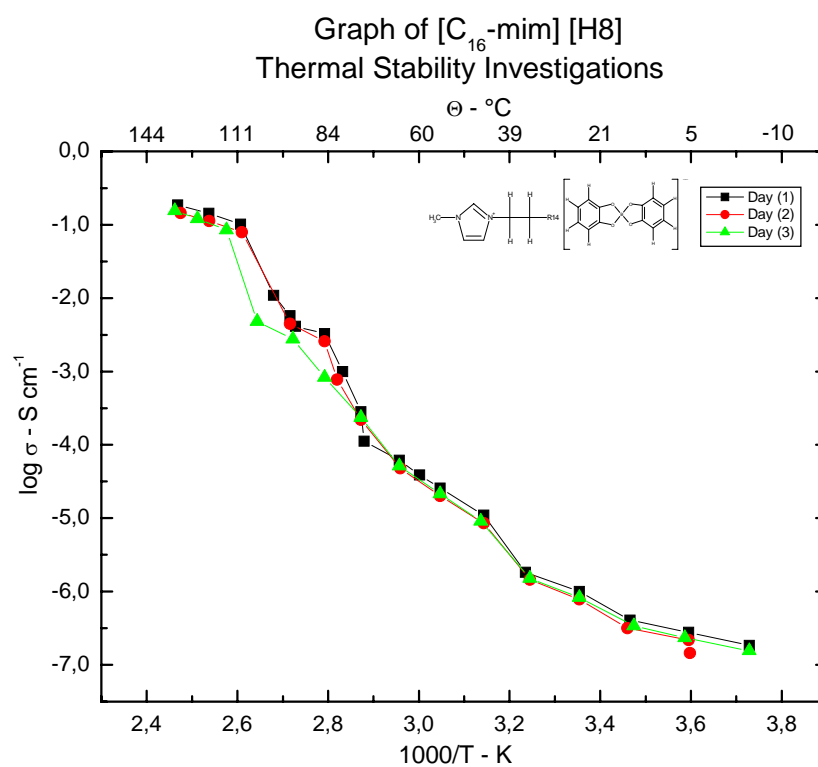


Fig. (5.2.16d)

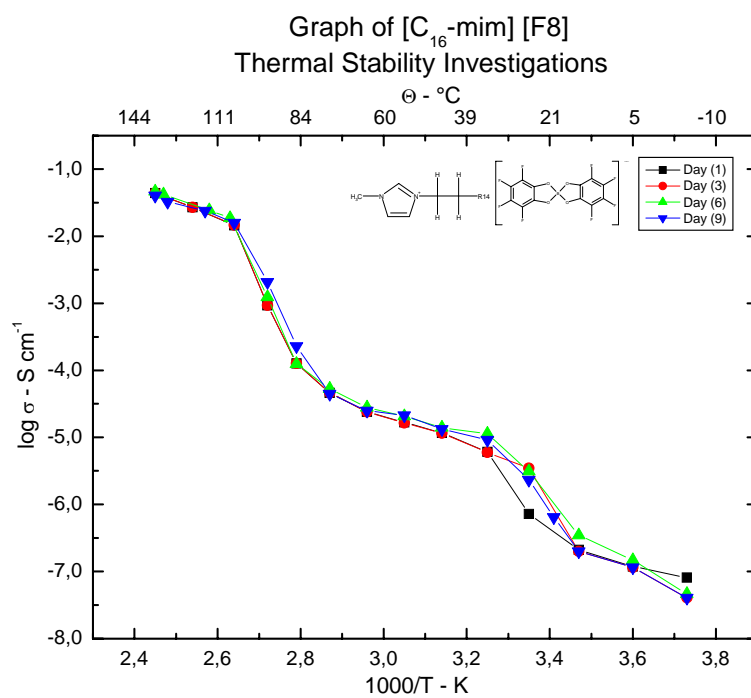


Fig. (5.2.16e)

5.2.5.3.

Undoped [C₁₆-mim] [X⁻]:

If the reader examines the data for samples [C₁₆-mim] [H8] and [C₁₆-mim] [F8] in Fig. (5.2.17); which combines one data set for each sample investigated, both referred to samples have generally lower overall conductivities as would be expected for such ions in other situations, although their conductive behaviours are replicated comparatively well in their DSC plots as seen previously in Fig. (5.2.14d) and Fig. (5.2.14e). Surprisingly their conductivities are subdued at lower temperatures as compared to the other smaller anions [Cl], [BF₄], and [PF₆]. Only after passing through the [S_A – Iso] phase transition in the high temperature range do they surpass the conductivities of the smaller ions. Only in the upper [S_A] and through out the [Iso] regions do the larger ions have complete freedom of movement within the disbanded matrix. The salts with larger anions exhibit superior conductivities in these regions (i.e. for [C₁₆-mim] [F8] at 125 °C - $\sigma = 2.693 \times 10^{-2} \text{ S cm}^{-1}$ and [C₁₆-mim] [H8] at 125 °C - $\sigma = 1.441 \times 10^{-1} \text{ S cm}^{-1}$) due to their charge delocalising effect, that was previously at lower temperatures suppressed due to their confinement within the rigid crystalline matrix. The charge delocalising attributes of these ions could effect little influence in the prevention of the formation of ion aggregates, which were previously alluded to concerning the hydrogen bonded aggregates which were proposed to exist in the isotropic phase^{[23] [46]}. This is most likely due to their constrained configurations within the matrix of the crystalline samples. On melting of the chains, the salts acquired enough freedom of movement within the matrix to influence the overall behaviours and conductivities of the sample. The weaker delocalising and smaller ions such as the mentioned [Cl], [BF₄], and [PF₆] anions have the advantage at lower temperatures to achieve higher ionic mobility through their ability to maximise their stoichiometric occupancy of the available sites along the helix alkyl chains near the header groups as previously depicted in Fig. (5.2.8).

The smaller anions [Cl], [BF₄], and [PF₆], probably offer a more stable configuration i.e. the anions fit more snugly in conjunction to the chains and header groups. They probably are hindered to a much lesser extent the ionic transport and charge movement through the system along the lamella phases or conductive “channels”. The larger anions [H8] and [F8] firstly pushed further away by their dissociative nature and secondly by their large size. As was previously mentioned the large anions are suspected at least partially occupying the lamella layers as seen in Fig. (5.2.18). This would firstly explain the disappearance of the [C_I] phase in the DSC plots for these samples. Secondly the conductivity step seen for the [S_A –

Iso] phase transition in Fig. (5.2.17) is considerably greater in intensity for the larger anions when compared to the smaller [Cl], [BF₄], and [PF₆] anions, probably due to their more disruptive nature within the matrix.

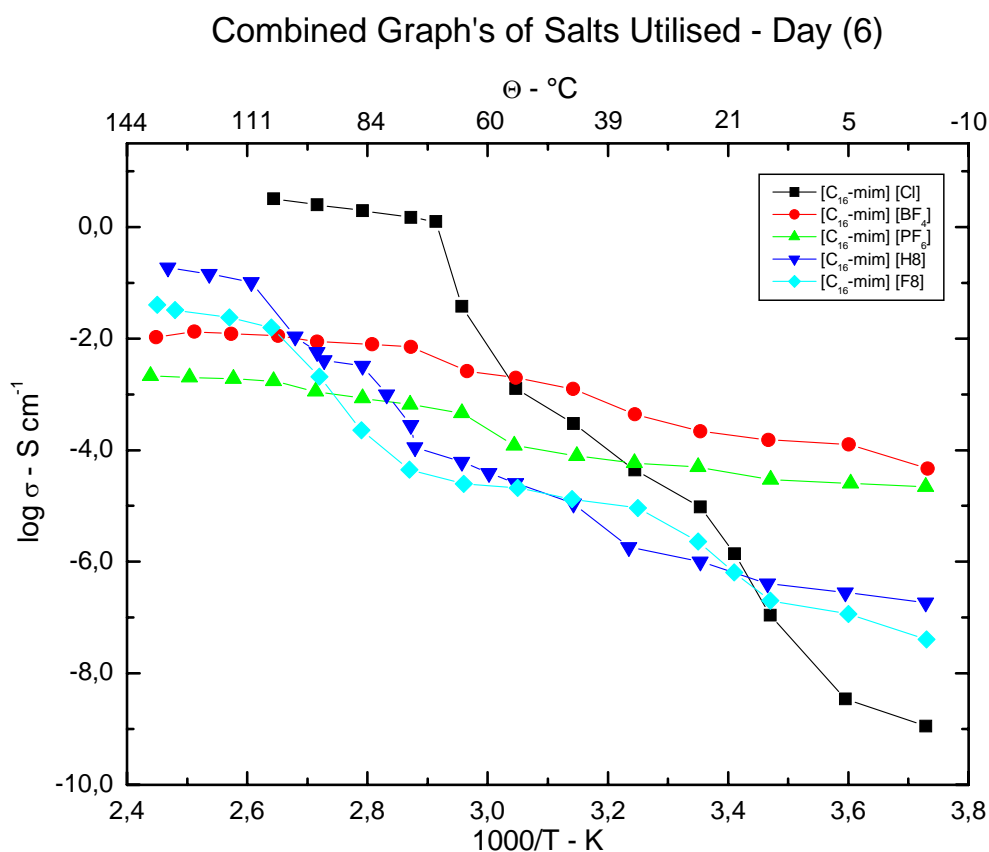


Fig. (5.2.17)

This indicates their freer movement on passing through the [S_A – Iso] phase transition. These results also lend support the proposal of Holbery^[26] and Ohlin^[38] that in the absence of lithium ions, the mobile species in such systems are the anions. In addition, it was observed over a number of days for the sample [C₁₆-mim] [BF₄] in the complex plane plots, there was a shift in resistance from the bulk semi-circle (i.e. decreasing semi-circle), while at the same time an increase in the low frequency capacitance “spike” at the sample electrode as seen in Fig. (2.5.19). These phenomena will be dealt with in more detail in the next section {6}.

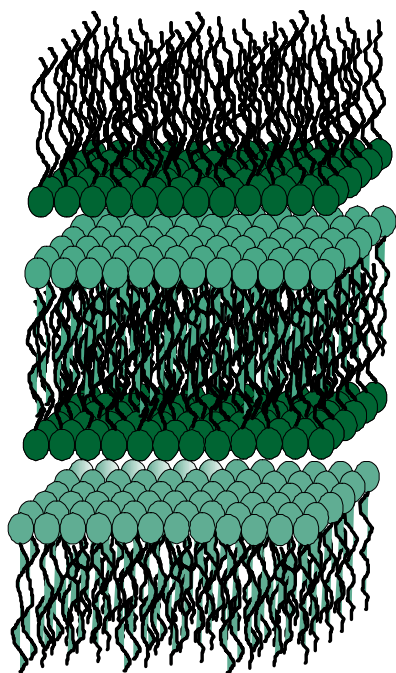


Fig. (5.2.18)
Schematic illustration of self-organising ion conductive materials containing stacked lamella phases, where the lamella planes lie normal to the direction of the stress

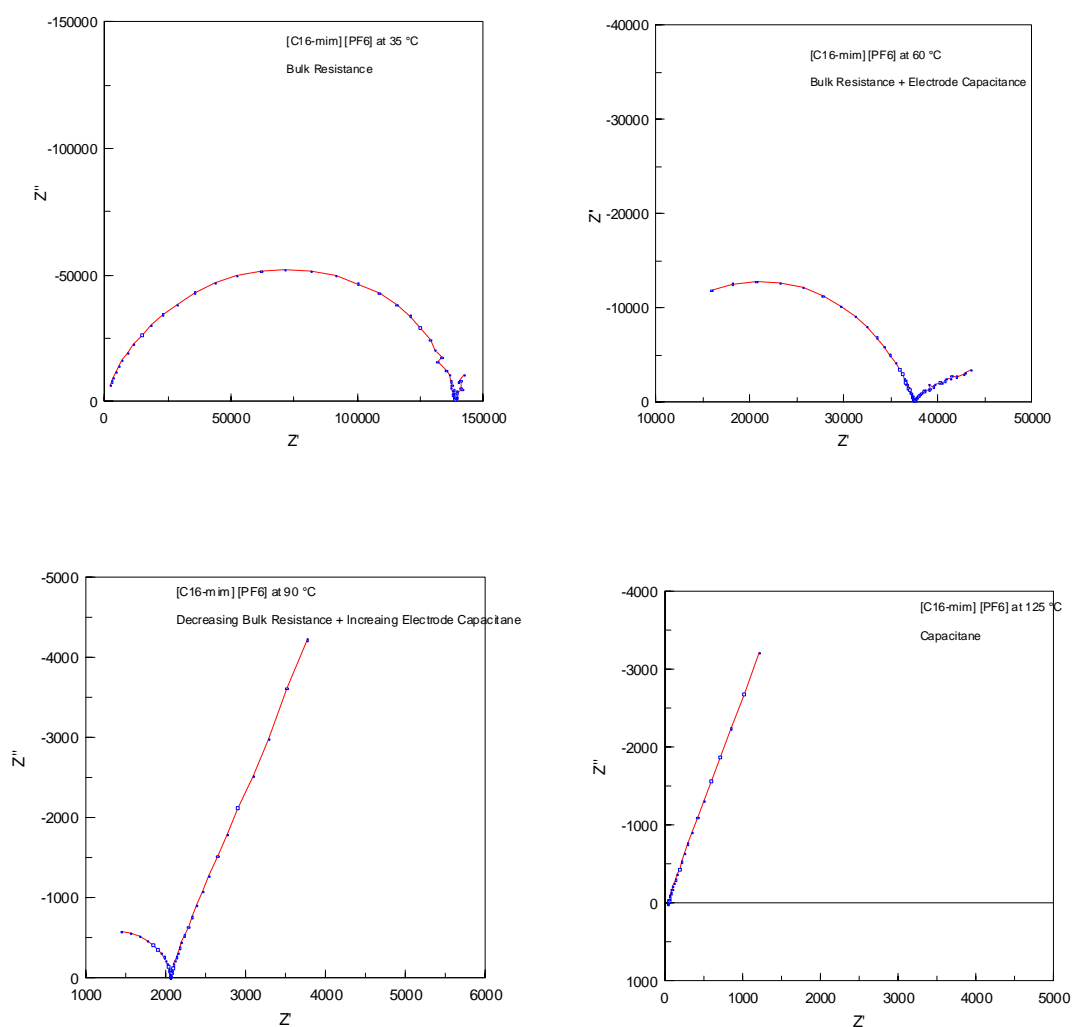


Fig. (5.2.19) Complex plane plots of $[C_{16}\text{-mim}][PF_6]$ with increasing temperature.

5.2.5.4.**[C₁₆-mim] [X⁻] Doped with 0.1 – 0.5 MF Li [X⁻]:**

In order to understand the transport properties of the materials under investigation, the [C₁₆-mim] cations were doped with their respective lithium salts seen in table (5.2.3a-d). None of the samples were doped in excess of molar fraction 0.5 MF of lithium salt. Previous experiments in Aberdeen ^[28] had shown that high concentrations of dopant were detrimental to the conductive behaviours of the samples and therefore experiments were confined to 0.5 MF and below. These investigations indicated that the excess lithium ions moved within the lamella phase boundaries or “channels” seen in Fig. (5.2.20). The presence of the lithium salt generally improved the overall conductivities of the samples above the undoped samples as can be seen in Fig. (5.2.21 a–c) for the samples [C₁₆-mim] [PF₆], [C₁₆-mim] [BF₄], and [C₁₆-mim] [F8] respectively. There is also evidence of limitations to the maximum substitution of lithium salts “stuffing limiting factor” similar to comments by Torell ^[42] ^[47] concerning high concentration of added salts. The systems toleration for each salt had a maximum capacity to which they can absorb and solvate salts before the beneficial effects of the salt are mediated by overloading of the system. In case of the [C₁₆-mim] [PF₆] above 0.5 MF doping with LiPF₆, the conductivities drop considerably. The [C₁₆-mim] [BF₄] system showed no improved conductive qualities until the concentration of doped LiBF₄ was above 0.4 MF. This sort of behaviour can not be directly likened to the poly(siloxane) system described in the previous section {5.1}.

It is true that at larger concentrations of dopant the ionic mobility decreased to such an extent that a maximum in conductivity versus salt occurs and phenomenon which has been reported for salt containing networks based on PEO and PPO⁵⁴. In these circumstances, it was suggested that the conductivity drop at higher salt concentrations is not only due directly to reduced ion mobility from chain entanglements, but also on the formation of large ion aggregates. In the case of the ionic liquids presented chain entanglements at elevated temperatures play a much reduced if any role. The formation of ion aggregates such as ion pairs, triple or higher aggregates are not such a large factor and take a secondary role. The main disruptive feature of these salts lies in their occupation of the lamella phases through which most of the ionic activity is occurring. An additional factor is observed, once the larger [H8] and [F8] have entered the isotropic phase the conductivities are considerably better than expected as they fulfil their role in reducing ion-pair formation.

⁵⁴ poly(propylene oxide)

The phase transitions were disrupted with a general shift in the phase transition steps to lower temperatures. In most samples at high concentrations of doped salt, the mesophase disappears when observed under a POM. In such systems only two phases are observed, the [C_{II}] and the [Iso]. This indicates the the lamella phase can only sustain limited disruption. This cannot be considered a negative development. The phase transitions have shifted toward ambient temperatures. In addition, there is an increase in the conductivities of the doped samples as compared to the undoped samples at the same respective temperature. In the case of the doped [C₁₆-mim] [F8] sample in Fig. (5.2.21c), rather surprising results were observed on increasing the concentrations of Li [F8]. The conductivities increased considerably and there was the expected drop of the [C_{II} - Iso] phase transition from 83 °C to 35 °C for MF 0.2 MF Li [F8]. This shift is well above expectations. For the doped sample at 25 °C the conductivity is ($\sigma = 5.493 \times 10^{-6} - \text{S cm}^{-1}$) for 0.2 MF Li [F8] as opposed to ($\sigma = 4.493 \times 10^{-7} - \text{S cm}^{-1}$) for the undoped sample at the same temperature see Fig. (5.2.21c). The delocalising nature of the large anion assisted the improved conductivities of the system by promoting the movement of the lithium ions and limiting the formation of aggregates at elevated temperatures.

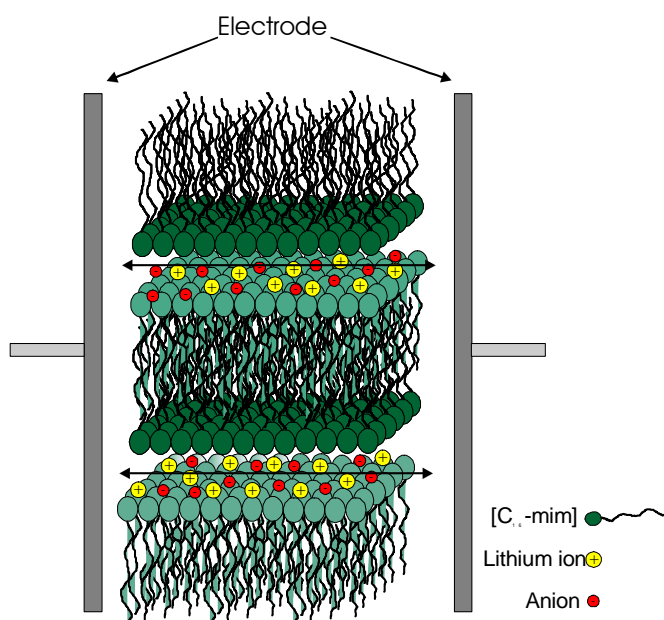


Fig. (5.2.20) Schematic of a doped crystal lamella phase, where the lamella planes lie normal to the direction of the electrodes

[C₁₆-mim] [PF₆] doped with Li [PF₆] salt

Salt Mole Fraction	Salt Moles	Salt g	Cation g	Cation Moles	Cation Mole Fraction
0,5	6,71E-04	0,102	0,300	6,59E-04	0,5
0,4	5,33E-04	0,081	0,360	7,90E-04	0,6
0,3	3,75E-04	0,057	0,390	8,56E-04	0,7
0,2	2,37E-04	0,036	0,420	9,22E-04	0,8
0,1	1,18E-04	0,018	0,480	1,05E-03	0,9

Table (5.2.3a)

[C₁₆-mim] [BF₄] doped with Li [BF₄] salt

Salt Mole Fraction	Salt Moles	Salt g	Cation g	Cation Moles	Cation Mole Fraction
0,5	3,73E-04	0,035	0,180	4,53E-04	0,5
0,4	3,20E-04	0,030	0,180	4,53E-04	0,6
0,3	2,67E-04	0,025	0,280	7,05E-04	0,7
0,2	2,13E-04	0,020	0,280	7,05E-04	0,8
0,1	1,49E-04	0,014	0,380	9,56E-04	0,9

Table (5.2.3b)

[C₁₆-mim] [F₈] doped with Li [F₈] salt

Salt Mole Fraction	Salt Moles	Salt g	Cation g	Cation Moles	Cation Mole Fraction
0,5	1,85E-04	0,070	0,150	2,21E-04	0,5
0,4	1,32E-04	0,050	0,150	2,21E-04	0,6
0,3	7,94E-05	0,030	0,150	2,21E-04	0,7
0,2	5,29E-05	0,020	0,150	2,21E-04	0,8
0,1	2,65E-05	0,010	0,150	2,21E-04	0,9

Table (5.2.3c)

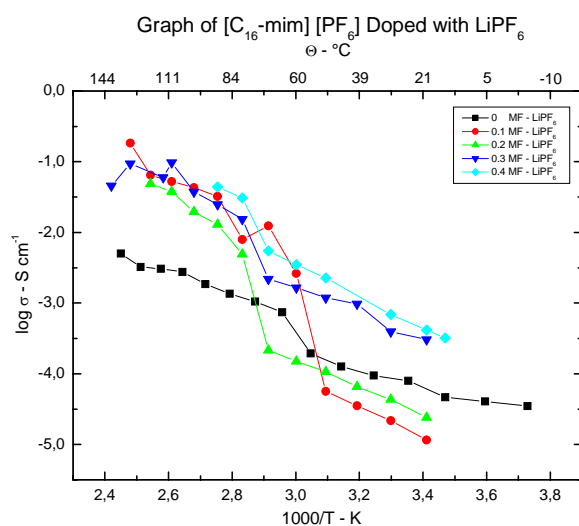


Fig. (5.2.21a)

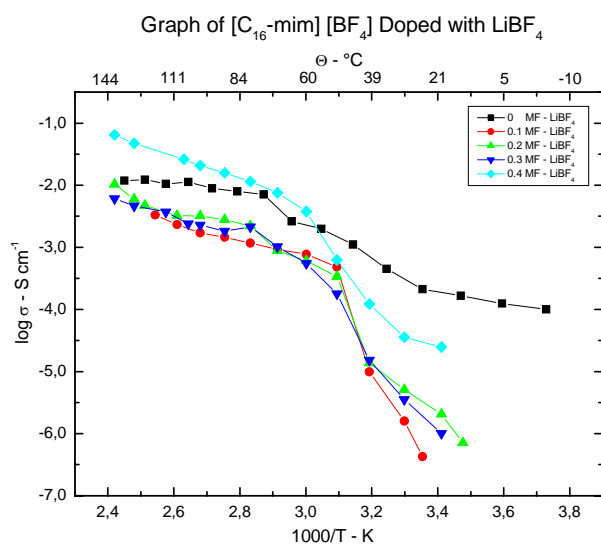


Fig. (5.2.21b)

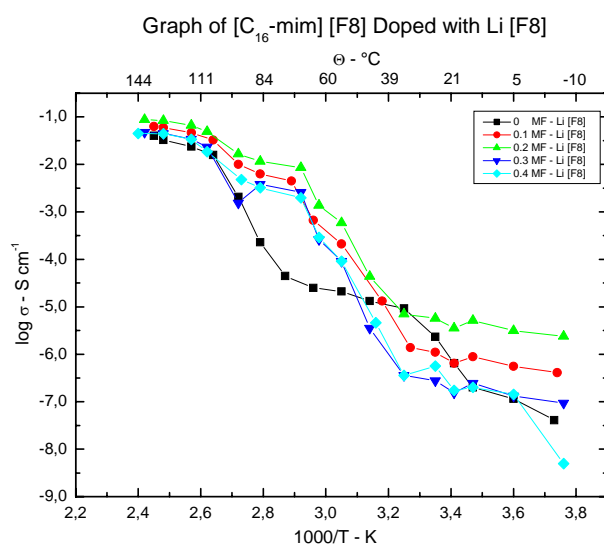


Fig. (5.2.21c)

The lamella structures previously mentioned are crucial in delivering the conductive pathways, which allow ionic motion to occur even within the rigid crystalline phase. The lamella layers are suggested to lie parallel to the electrodes and the helix alkyl chains axes. This conformation should be beneficial to the conductivity across the cell Fig. (5.2.20). In doped systems the changes in the form of the complex plane plots Z'' vs. Z' following the thermal treatment of the samples reflects the change in the internal structure of the material as the new interfaces are formed. The Fig. (5.2.22a-c) shows the 3D graphical relationship of conductivity (z-axis), temperature (y-axis), and molar fraction of dopant (x-axis) added. Such graphical depictions are useful in discovering conductive plateaus or “islands” of conductive stability. The familiar and expected capacitance “spike” at low frequencies of the cation, anion, and lithium ion mixtures do not develop immediately as one elevates the temperature seen in Fig. (5.2.23). But instead the bulk semi-circle progressively bends over with increasing temperature to become a new semi-circle and later disappears, the closer the system progresses towards the $[C_{II} - \text{Iso}]$ phase transition. Once through the $[C_{II} - \text{Iso}]$ phase transition the capacitance spike reappears and takes on its familiar form. This form of impedance behaviour clearly indicates the presence of Warburg impedance. This behaviour is typical of Li [F8] and perhaps reflects the transformation of the system to a Maxwell two-phase series of multi-layered dielectrics ^[39]. More shall be discussed on this topic in section {6}.

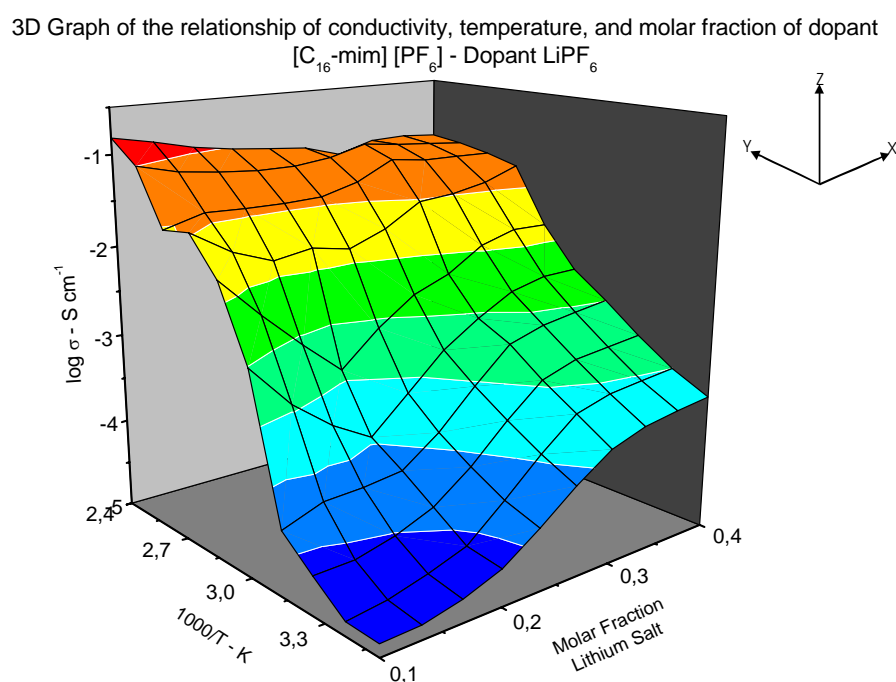


Fig. (5.2.22a)

3D Graph of the relationship of conductivity, temperature, and molar fraction of dopant
 $[C_{16}\text{-mim}][BF_4]$ - Dopant $LiBF_4$

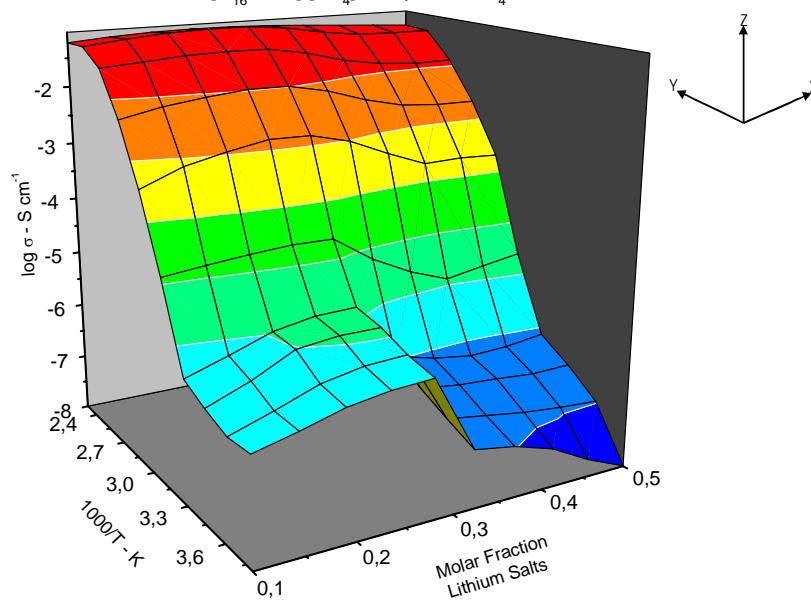


Fig. (5.2.22b)

3D Graph of the relationship of conductivity, temperature, and molar fraction of dopant
 $[C_{16}\text{-mim}][F8]$ - Dopant $Li[F8]$

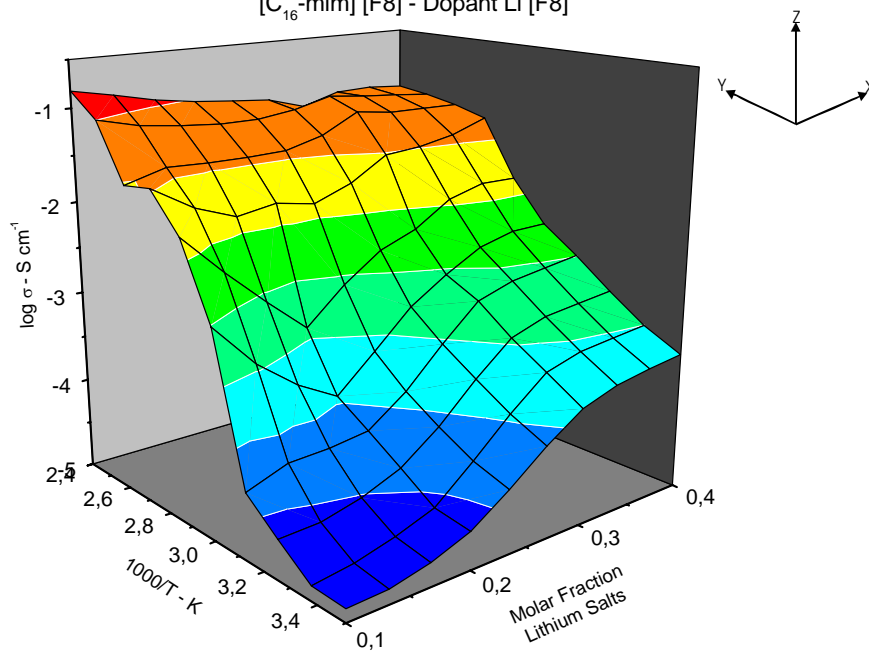


Fig. (5.2.22c)

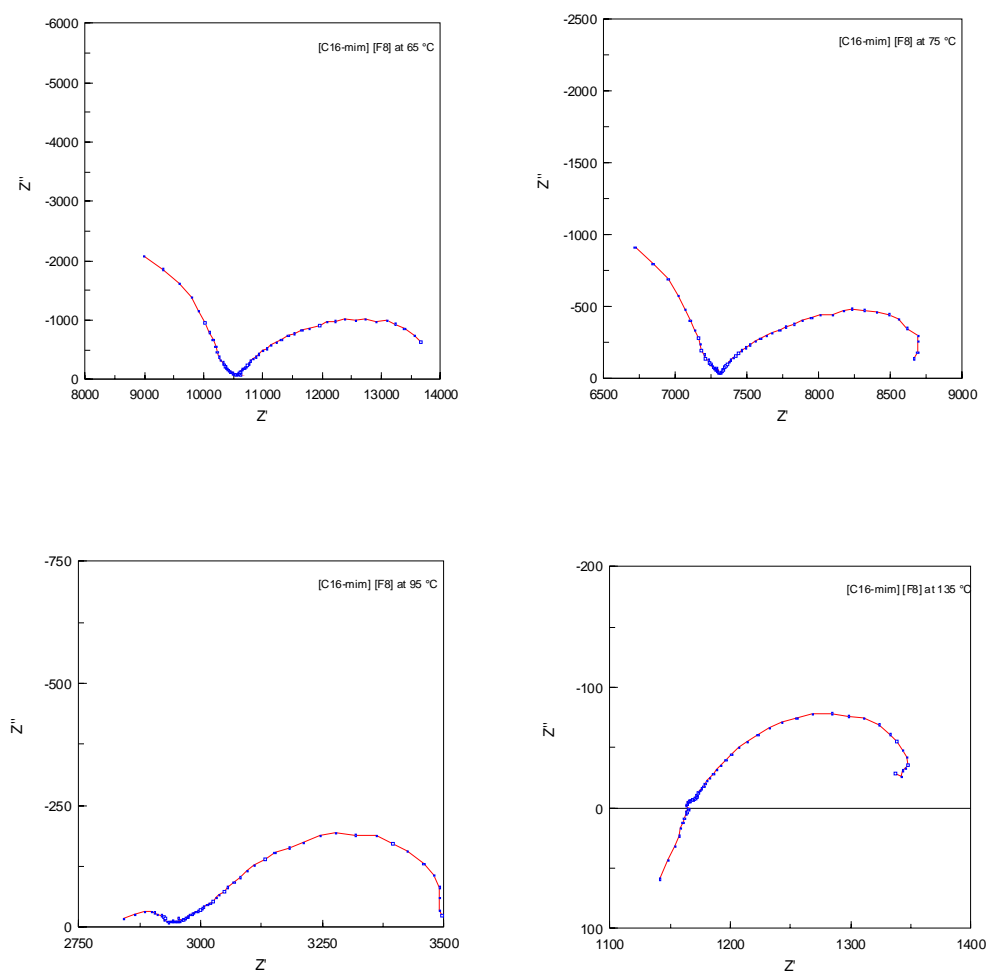


Fig. (5.2.23) Formation of double semi-circle in [C16-mim][F8] for Li [F8] 0.2 MF, indicating the presence of Maxwell dielectrics ^[39]

5.2.6.

Final Commentary:

The presented systems could be described as “polymer-in-salt” systems, which was coined by Angell ^[48]. These are systems, that are from mechanical and fabrication standpoints dimensionally stable gel-like electrolytes possessing the conductive properties at elevated temperatures similar to liquids ^[40]. Recent work has shown, for example that contamination with chloride ions increases ionic liquid viscosity while contamination with moisture decreases viscosity, and hence ionic liquid viscosity is strongly coupled to ionic conductivity. Therefore, every precaution was taken to eliminate the possibilities of such impurities having an adverse affect on the EIS measurements. Interestingly, it was often found, that the correlation between the anion type or size and the ionic liquid conductivity is very limited. In this work, similar results were observed for the larger ions at lower temperatures and mainly below the crystal to isotropic phase transition phase boundary. The delocalising effects of the large [F8] anion did not demonstrate significant improved conductivities at lower temperatures, where the ionic liquid is crystalline and rigid.

The Arrhenius approach and the VTF approach cannot be applied to explain all the behaviours of the presented systems. There are multiple phase transitions to be noted and if one intends to describe the ion-ion interactions of these systems by means of the equivalent circuit method, a new strategy is required. Each phase has its own behaviour that has crystal, liquid crystal, and liquid properties. Therefore, each phase must be understood as an independent system in itself. It is not practical to try to impose one equivalent circuit form for the whole system as could be done for other simpler systems as seen in section {5.1}. The next section will examine the implications of the phase transitions on the conductivities and will propose possible scenarios for the ion-ion interaction that are occurring within the presented systems.

References:

1. A. Merz and H. Bachmann, *J. Am. Chem. Soc.*, **117**, 901 (1995).
2. M. C. Lonergan, M. A. Ratner and D. F. Shriver, *J. Am. Chem. Soc.*, **117**, 2344 (1995).
3. C. A. Angell, *J. Phys. Chem.*, **70**, 3988 (1966).
4. A. Reiche, T. Cramer, G. Fleischer, R. Sandner, B. Sandner, F. Kremer and J. Kaerger, *J. Phys. Chem. B.*, **102**, 1861 (1998).
5. J. Barthel, H. J. Gores and L. Kraml, *J. Phys. Chem.*, **100**, 3671 (1996).
6. J. Barthel, R. Buestrich, E. Carl and H. J. Gores, *J. Electrochem. Soc.*, **143**, 3572 (1996).
7. J. Barthel, R. Buestrich, H. J. Gores, M. Schmidt and M. Wuhr, *J. Electrochem. Soc.*, **144**, 3866 (1997).
8. J. Barthel, M. Schmidt and H. J. Gores, *J. Electrochem. Soc.*, **145**, L17 (1998).
9. J. Barthel, A. Schmid and H. J. Gores, *J. Electrochem. Soc.*, **147**, 21 (2000).
10. Z. Zhu, A. G. Einset, C. Y. Yang, W.-X. Chen and G. E. Wenk, *Macromolecules*, **27**, 4076 (1994).
11. R. Hooper, L. J. Lyons, D. A. Moline and R. West, *Silicon Chemistry*, **1**, 121 (2002).
12. C. A. Angell, C. Liu and E. Sanchez, *Nature (London)*, **362**, 137 (1993).
13. E. Morales and J. L. Acosta, *Electrochimica Acta*, **45**, 1049 (1999).
14. P. H. de Souza, R. F. Bianchi, K. Dahmouche, P. Judeinstein, R. M. Faria and T. J. Bonagamba, *Chem. Mater.*, **13**, 3685 (2001).
15. G. B. Zhou, I. M. Khan and J. Smid, *Macromolecules*, **26**, 2202 (1993).
16. H. R. Allcock, M. E. Napierala, D. L. Olmeijer, C. G. Cameron, S. E. Kuharcik, C. S. Reed and S. J. M. O'Connor, *Electrochim. Acta*, **43**, 1145 (1998).
17. T. F. Yeh, Y. Okamoto and T. A. Skotheim, *Mol. Cryst. Liq. Cryst.*, **190**, 205 (1990).
18. G. S. Fulcher, *Journal of the American Chemical Society*, **8**, 339 (1925).
19. M. Hirao, H. Sugimoto and H. Ohno, *J. Electrochem. Soc.*, **147**, 4168 (2000).
20. M. Hirao, K. Ito and H. Ohno, *Electrochim. Acta*, **45**, 1291 (2000).
21. A. B. McEwen, E. L. Ngo, K. LeCompte and J. L. Goldman, *J. Electrochem. Soc.*, **146**, 1687 (1999).
22. H. L. Ngo, K. LeCompte, L. Hargens and A. B. McEwen, *Thermochimica Acta*, **357-358**, 97 (2000).
23. J. De Roche, C. M. Gordon, C. T. Imrie, M. D. Ingram, A. R. Kennedy, F. Lo Celso and A. Triolo, *Chemistry of Materials*, **15**, 3089 (2003).
24. P. Wasserscheid and T. Welton, *Ionic Liquids*, Wiley-VCH, (2003)..
25. J. D. Holbrey and K. R. Seddon, *Clean Products and Processes*, **1**, 223 (1999).
26. C. M. Gordon, J. D. Holbrey, A. R. Kennedy and K. R. Seddon, *J. Mater. Chem*, **8**, 2627 (1998).
27. C. Imrie, Section: Liquid Crystals - The world of liquid crystals. *Chem* 161-180 (1999).
28. J. De Roche, Thesis: Liquid Crystalline Electrolytes, University of Aberdeen Department of Chemistry, 1-185 (2000).
29. J. Barthel, A. Schmid and H. J. Gores, *J. Electrochem. Soc.*, **147**, 21 (2000).
30. J. Barthel, R. Buestrich, E. Carl and H. J. Gores, *J. Electrochem. Soc.*, **143**, 3565 (1996).
31. J. Barthel, M. Wuhr, R. Buestrich and H. J. Gores, *J. Electrochem. Soc.*, **142**, 2527 (1995).
32. J. Barthel, R. Buestrich, H. J. Gores, M. Schmidt and M. Wuhr, *J. Electrochem. Soc.*, **144**, 3866 (1997).
33. J. Barthel, M. Wuhr, R. Buestrich and H. J. Gores, *J. Electrochem. Soc.*, **142**, 2527 (1995).
34. F. B. Dias, S. V. Batty, A. Gupta, G. Ungar, J. P. Voss and P. V. Wright, *Electrochim. Acta*, **43**, 1217 (1998).
35. M. L. Mutch and J. S. Wilkes, *Electrochemical Society Proceedings*, **98**, 254 (1998).
36. R. Zentel, Section: Liquid Crystalline Polymers, *Liquid Crystals*, 103-139 (1994).
37. V. R. Koch, L. A. Dominey, C. Nanjundiah and M. J. Ondrechen, *J. Electrochem. Soc.*, **143**, 798 (1996).
38. C. M. Gordon, C. A. Ohlin and C. Ritchie, *Abstr. Pap. - Am. Chem. Soc.*, **221st**, IEC (2001).
39. I. N. Shtennikova, *Liquid-Crystal Polymers*, No. p. 455 (1993).
40. J. Fuller, A. C. Breda and R. T. Carlin, *Ionic liquid-polymer gel electrolytes*, **144**, No. p. 70 (1997).
41. A. J. Chalk and J. F. Harrod, *Journal of the American Chemical Society*, **87**, 16 (1965).

42. L. M. Torell and C. A. Angell, *Br. Polym. J.*, **20**, 173 (1988).
43. K. Hoffmann, *Imidazole and Its Derivatives Part 1*, **1**, No. p. 445 (1953).
44. Zbigniew and Stojek, Section: Experimental, *Electrochemical Methods - Guide to Experiments and Applications*, 300-305, Ed. Scholz, S., Springer, London, (2002).
45. C. M. Gordon, Section: Synthesis and Purification of Ionic Liquids, *Ionic Liquids in Synthesis*, 7-21, Ed. Wasserscheid, P. & Welton, T., Wiley-VCH, (2002).
46. F. Chia, Y. Zheng, J. Liu, N. Reeves, G. Ungar and P. V. Wright, *Electrochimica Acta*, **48**, 1939 (2003).
47. S. Schantz and L. M. Torell, Section: Light Scattering in Polymer Electrolytes, *Polymer Electrolyte Reviews (2)*, 1-42 (1989).
48. C. A. Angell, C. Liu and E. Sanchez, *Nature (London)*, **362**, 137 (1993).

Chapter 6

Discussion

6.1. Poly(siloxane) Polymers

Foreword:

In the previous section {5}, the author presented the results of EIS and DSC investigations of both poly(siloxane) and ionic liquid systems. The preliminary observations indicated a number of interesting behaviours that deserve closer examination. The author is now in the position in following elaboration to give a more detailed understanding of the conductive pathways and ion-ion interactions of the presented systems.

6.1.1.

Discussion of structural & conductive behaviours of doped poly(siloxanes):

6.1.1.1.

Polymer Gels:

The figure (6.1.1) is a proposed schematic of the poly(siloxane) systems, which is intended to convey a simplified representation of the polymer matrix and the relationships between its constituents. The schematic envisages doped salts highly solvated by strongly polar side chains attached to a flexible backbone with large anions immobilised within the matrix while free charge carrying cations are mobile. The schematic representation is not a definitive model, but in the following discussion, it will be used to tie together a number of the behaviours that will shortly be considered. But before we delve too deep at this point in our discussion a short recapitulation of the synthetic procedure of the presented systems is essential to convey some of the approaches that will be considered with reference to the schematic depiction in Fig. (6.1.1). The H-siloxane is mixed and polymerised with various stoichiometrically controlled (oligo)ethylenglycol (EGE) side chain units to form a comb-like structures seen in Fig. (6.1.1.). The poly(siloxane) is solvated and mixed with a controlled amount of lithium salt seen previously in table (5.1.1). The large lithium anions are suspected

of exerting a strong charge delocalisation influence in the surrounding matrix and encourage the formation of free ions. It will be shown that in certain types of lithium salts, the Li^+ ion becomes the main charge carrier. Therefore, the author intends to examine the proposed conductive hypothesis depicted in the schematic Fig. (6.1.1).

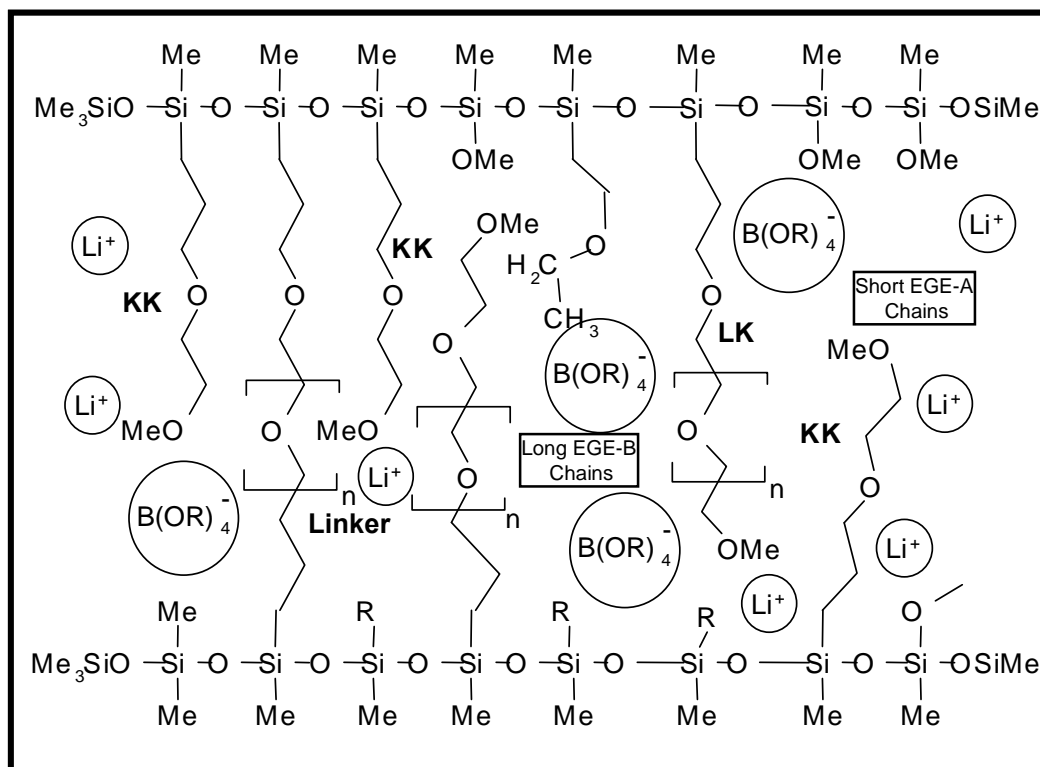


Fig. (6.1.1) Schematic of the proposed structure poly(siloxane) polymers with different stoichiometric EGE side chain units (see table 5.1.2) doped with different lithium salts seen in table (5.1.1)⁵⁵.

It is well known that lithium ion conduction takes place predominately in the amorphous domain and the segmental motion of the polymer (i.e. T_g) is an important factor in determining the ionic mobility ^[1 - 4]. According to Morales ^[4] the best means of achieving this aim is to synthesise comb-like polymers by attaching short side chain units that will sequence to an existing amorphous polymer backbone. This is undertaken by means of utilising poly(siloxanes) as the flexible backbone polymer as is the case in this work. Cameron & Ingram *et.al.* ^[5], who worked on alkali metal thiocyanates in liquid copolymers EO and PE, commented that such aforementioned amorphous regions within the polymer matrix are attributable to the segmental motions of the side chain units. They go on to propose that these motions are liquid like in character and usually demonstrate temperature dependence in the form of the VTF approach. This mentioned amorphicity often leads to the formation of gel-

55 Schematic courtesy of Prof. Dr. Andres Merz Organic Chemistry, Universität Regensburg.

like electrolytes and can be described as a method of gelation. Other authors such as Hikmet & Petters^[6] working with gel-like materials, polyethylene glycol diacrylates (PEGDA) systems doped with LiPF_6 added considerable quantities of solvent to the polymer with the objective of obtaining gels with enhanced mechanical stabilities and at the same time the limiting of excessive flow due to the polymer matrix. This method of consistency control “gelation” reported by Hikmet & Petters^[6] lead to a large decrease in conductivity of the gels when compared with the solutions of the salt. Such decreases are often associated with reduced ionic mobility as a result of increased glass transition temperatures of the system once polymerised. In this work in order to avoid the negative aspects of gelation, a more refined method was utilised. The employment of (oligo)ethylenglycol (EGE) as side chain units offered an ideal solution to this predicament. These systems provided an excellent solvent-like diffusion zone and improved the efficiency of polymer support^[7 - 8]. The (oligo)ethylenglycols due to the oxygens along their chains have a large polarisability and encourage in turn lower glass transitions temperatures according to Ito^[9]. Ito emphasises that (oligo)ethylenglycols chains are capable of dissolving considerable quantities of salt which accordingly dissociate ions into the more desirable free ions.

The current investigations revealed some dynamical properties of the presented polymer/gel electrolytes by expressing three conductivity-determining mechanisms in these systems:

- I. Firstly, all systems demonstrated the “classical” dependence of doped lithium salt concentration and the mobility of charge carriers by means of the typical conductivities. To emphasise this reported dependence, the figures (6.1.2a & b) show the conductivity dependence of the lithium salt concentration with the selected polymer side chain unit preparations (α) and (χ) and their relative effect on the overall conductance respectively.
- II. Secondly, a strong dependence was observed in the conductivities of the presented systems with relation to the delocalising effect from increasing molar quantities of fluorine attached to the anion part of the inserted lithium salt, i.e. $\text{Li} [\text{F2H6}]$ & $\text{Li} [\text{F8}]$ see table (5.1.1). The EIS measurements showed significantly improved conductivity values of the sample that contained fluorinated anions over those that were non-fluorinated (i.e. $\text{Li} [\text{H8}]$). The

positive aspect of this dependence was attributable to considerable improved charge delocalisation within the polymer matrix, thereby suppressing or relaxing ion pairing and higher aggregate formation. The figures (6.1.3a & b) provided a good example of the general respective influence of anionic fluorination on the net conductivity of the selected poly(siloxane) systems of side chain unit preparations (α) and (χ) at molar ratio (O:Li) – (24:1).

- III. Finally, there is a clear relationship between conductivity and the different stoichiometric proportions of EGE side chain units along the comb-branch polymer, which can be seen in Fig (6.1.4a & b). The figures (6.1.4a & b) show the conductivity dependence of the side chain units with different lithium salt concentrations for the samples Li [H8] and Li [F8] respectively. The proportion of the side chain units i.e. (EGE-A and EGE-B) along the H-siloxane backbone played a key role in the behaviours of glass transition (T_g) temperatures of the presented systems and consequently on their conductive performance.

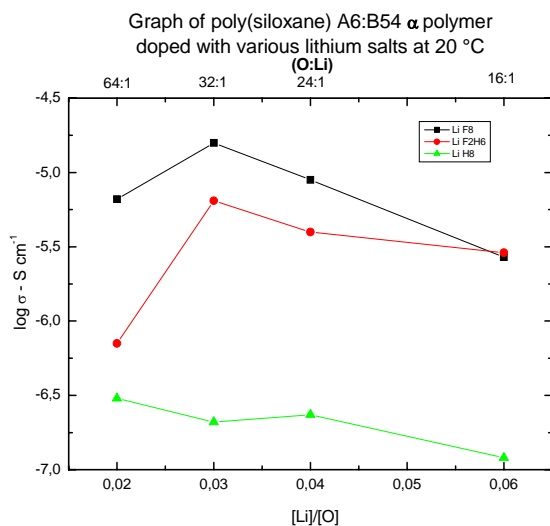


Fig. (6.1.2 a)

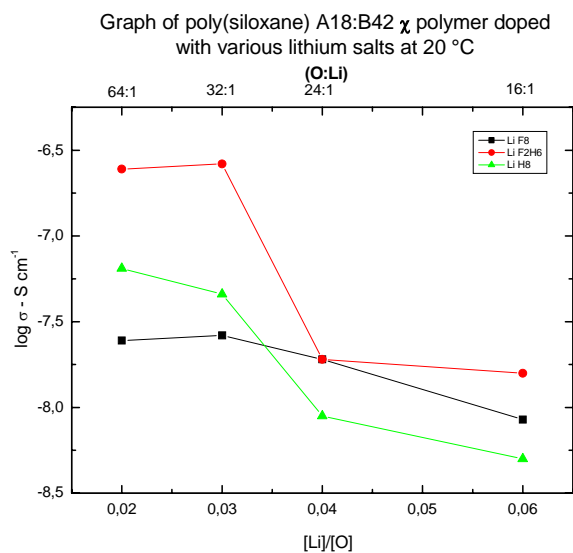


Fig. (6.1.2 b)

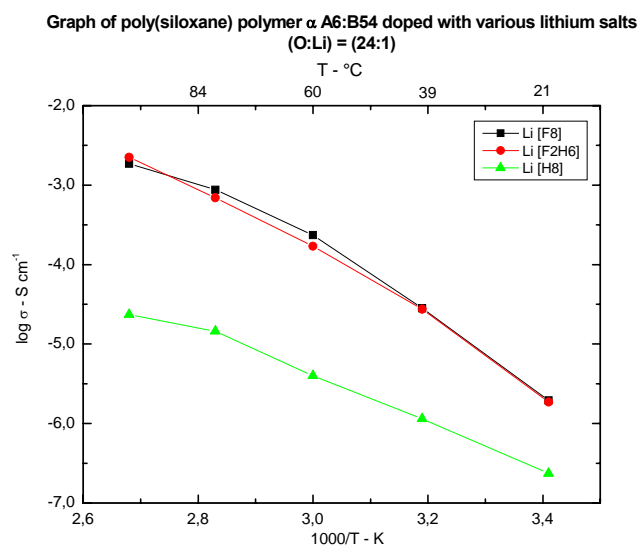


Fig. (6.1.3a)

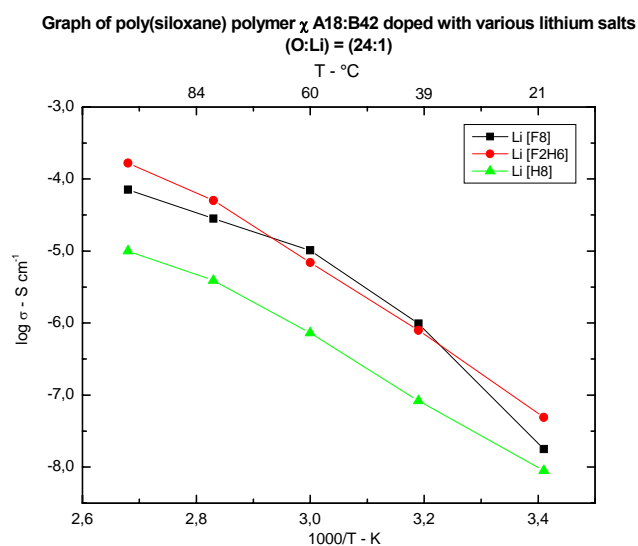


Fig. (6.1.3b)

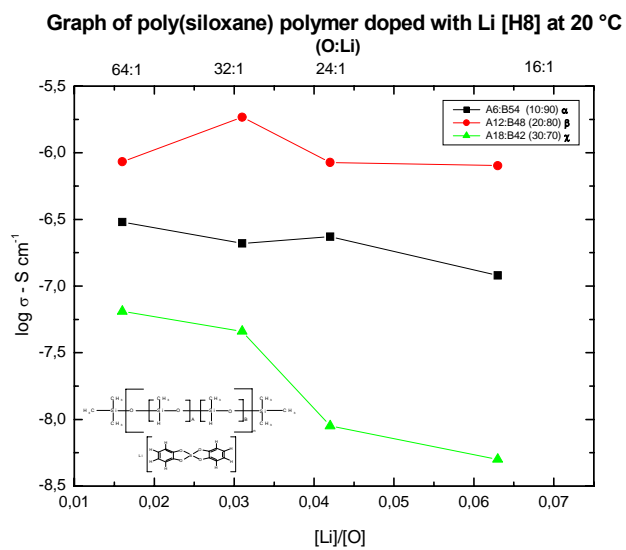


Fig. (6.1.4a)

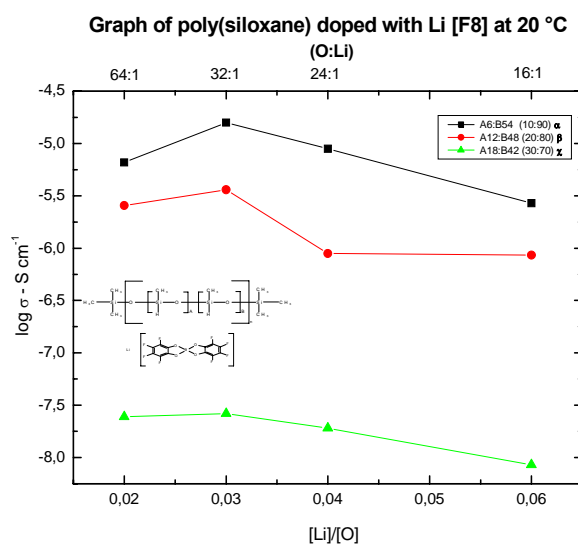


Fig. (6.1.4b)

6.1.1.2.

Effect of Lithium Salt Concentration:

On considering the first point, concerning the dependence of the salt concentration and conductivity, the doping of the presented systems exhibited a “classical” conductivity response with respect to increasing salt concentration, hence influencing T_g and viscosities of the system. If one examines the figures Fig. (6.1.2a) and (6.1.2b), one observes a conductive pattern that is consistent to similar preparations of other authors^{[5][9 - 12]}. In taking an example of similar findings, the workers Ito & Ohno^[9], who investigated the bulk ion conduction of several kinds of charged groups (i.e. carboxylate, sulfonate, benzenesulfonate, sulfonamide, pyridinium, and triethylammonium) introduced into the terminal of poly(ethylene oxide) (PEO) oligomers. The authors^[9] like many others before them observed that the ionic conductivity of the polymers for salts increased with increasing dissociation constant owing to the increase in the number of charge carrier ions for the same molecular weight of the PEO part. At the same time, the ionic conductivity of the polymer decreased at a high salt concentration after reaching a maximum. In a similar situation for this work at low molar ratios of (O:Li) – (64:1) the conductivity is generally low but the matrix still has the potential to accept and solvate more salt. On increasing to the salt doping concentration to (O:Li) – (32:1) and in some cases (24:1), the conductivity reaches a maximum see the [quasi- plateau previously in the 3D plots for conductivity, Fig. (5.1.3a-c)]. On further increasing the salt doping concentration, the conductivity of the systems fell sharply. Over the years there have been a number of conflicting arguments in scientific circles as to explain this phenomenon. A number of authors attempted to apply the Debye-Hückel theory^[13] that had its origins in liquid electrolyte systems, which was later proved inadequate⁵⁶. The current most popular explanation was proposed by Angell^[14] based on Adam-Gibbs theory^[15]. A number of authors have developed this theory of conductivity further such as Bruce & Vincent^[16 - 17] with their two papers concerning theoretical explanations of ion association behaviours. Investigations by Cameron & Ingram^[5] of solutions of alkali metal thiocyanates in liquid ethylene oxide-propylene oxide (EO-PO) copolymers noted behaviours within their so-called “amorphous” systems, suggesting at lower molar conductivity extensive ion pairing with a subsequent rise in the molar conductivity explained in terms of the formation of triple ions. On again further increasing salt concentrations the molar conductivity decreases again with an associated rise in viscosity. In respect to the presented systems extreme ion pairing can be ruled out but the formation of triple ions and large aggregates cannot be ruled out. The table

⁵⁶ Please see section {2.1}

(6.1.1) shows the glass transition temperatures θ_g of the investigated poly(siloxane) polymers at different molar ratios of oxygen to lithium ions. One observes that with increasing salt concentrations the θ_g values increase accordingly and hence greater viscosity should be observed. It should be noted that the salt concentration is not the only factor that influences the viscosity. The configuration of the side chains unit also plays an important if not crucial role in dictating the physical properties of the sample of which more shall be said shortly.

Polymer No.	Lithium Salt Shorthand	Ratio (O:Li)	θ_g °C	σ at 20 °C S cm ⁻¹
α^*	Li [F8]	(32:1)	-53.2	1.57×10^{-5}
		(24:1)	-48.8	1.95×10^{-6}
		(16:1)	-31.5	8.58×10^{-7}
α^*	Li [H8]	(32:1)	-18.8	2.10×10^{-7}
		(24:1)	-18.1	2.35×10^{-7}
		(16:1)	-15.7	8.00×10^{-9}

Table (6.1.1) Table of θ_g 's and ionic conductivities of polymers

The aforementioned 3D plots of conductivity (z), reciprocal temperature (y), and percentage of (EGE-A) side chain units seen previously in Fig. (5.1.3 a –b –c) for each of the respective lithium salts indicated the presence of a possible conductivity maximum. On examining the data more closely the salt doping concentrations of oxygen to lithium at (O:Li) – [(32:1) and (24:1)] offered the highest conductivities at ambient temperatures of 1.57×10^{-5} S cm⁻¹ for sample (α) – Li [F8] and 1.96×10^{-6} S cm⁻¹ for sample (χ) - Li [F8] respectively see Fig. (6.1.2a). Consequently the following lithium salt concentrations of oxygen to lithium were chosen for more detailed EIS investigations: (32:1) and (24:1).

6.1.1.3.

Effect of Lithium Salt Fluorination at the Anion:

The complementary process mentioned previously is the relative increase of conductivity of the samples due to the increasing fluorination of the anion part of the lithium salt when doped with Li [H8], Li [F2H6], and Li [F8] respectively. Zhou ^[53] suggested that in most polymer electrolytes both the anions and the cations are mobile. Zhou ^[53] showed by means of transport number measurements that “anions frequently are the carriers of the bulk current due to the complexation of the cations with chelating polymer substituents. We know from a number of authors such as Izo ^[9] that if the conductivity is to be enhanced by some means in any system it must not come at the expense of the cations. The cations should be favoured above all else as the charge “carrier”. We know anions and larger aggregates often induce polarisation which interferes with the cation migration. Investigations by Hikmet ^[6] ^[19] on ion conducting gels produced from photo-polymerisation of acrylates in the presence of lithium hexafluorophosphate LiPF_6 in various solvents, showed that strong interactions within the gel matrix influenced the motions of the LiPF_6 . The Li^+ ions had a lower conductivity due to the poor ion disassociation of the salt. Therefore according to Lee ^[18] and what's more is the opinion of the author, the task is to find and utilise a salt of large anionic radii and delocalising negative charge leading to reduced ion-ion interactions (i.e. reduce ion pairs and other larger aggregates and promote the formation of mobile free ions).

The lithium salts presented in the table (5.1.1) previously provided a good opportunity to test this hypothesis. According to Hikmet ^[6] ^[19] the process of polymerisation leads to a large decrease in the conductivities of gels. This is often associated with reduced mobility in connection to increased glass transition temperatures of the systems upon polymerisation. Likewise, the diffusion coefficients of the ions falls during polymerisation. The presented lithium salts are known to have a good charge delocalising characteristics, firstly, due to their relatively large size, which reduces their mobility, and secondly their strong electronegative nature permits greater cation freedom, hence better charge carrier mobility. Furthermore, the large delocalising strength of the anions leads to greater dissociation constants. Ito ^[9] found from transport number measurements that the anion conductivity decreased with increasing anion radius, in accordance with Stokes law. Through the application of the newly synthesised salts reported earlier, the current investigations demonstrated the expected “encouragement” of charge delocalisation of the matrix, which in turn encourages the

reduction of ion aggregate formation. The charge delocalisation affects the electrochemical stability vs. oxidation because of increasing fluorination ^{[20] [21]}.

The advantages allotted to large anions in addition to their respective delocalisation strengths becomes less noticeable with respect to the free volume when the system moves above a certain concentration maximum. Adam & Gibbs ^[15] who wrote an early ground breaking paper concerning the issue of “the temperature dependence of cooperative relaxation properties in glass-forming liquids” developed the theoretical foundation of the modern interpretation of the structural behaviours of polymeric systems by explaining the temperature dependence of the relaxation behaviour in glass-forming liquids in terms of the temperature variation of the size of the cooperatively rearranging region. “The size of this cooperatively rearranging region is determined by configuration restrictions in the glass-forming liquids and is expressed in terms of their configurational entropy” ^[15]. Angell ^[22] later wrote a review paper discussing the importance of free volume and its implications for the variables of viscosity and segmental motion by implying that the “rapidly lengthening timescale for diffusional and/or reorientational motion ... provokes the glass transition, ...and is examined within the framework of the “strong” and “fragile” classification of both liquids and plastic crystals”. It is important to note that the free volume theory does not take into account the specific interactions within the system, such as the preferential co-ordination of the lithium ion ^{[6] [19]}. Therefore, one must on the one hand strike a balance between the maximum possible salt concentrations while on the other hand extracting the maximum number of free cation charge carriers.

The data presented earlier in Fig. (5.1.2) proves that ion pairing can be reduced significantly by the addition of sufficiently strong delocalising anions in the form of lithium salts that are thermally stable, have large radii, and lower lattice energies leading to reported good solubilities ^{[23] [24]}. The special factor concerning these presented lithium salt dopants is their “excellent stability and weak anion lithium ion interactions entailing higher conductance despite lower mobility of the larger anion” as reported by Barthel & Gores ^[25]. An example taken from Fujinami & co-workers ^[24], who investigated “the molecular design of inorganic-organic hybrid polyelectrolytes to enhance lithium ion conductivity, showed that the concepts of molecular design are very important for complex large sized anionic structures such as the “ate” complex structures (e.g. aluminate, borate)”. They found similar to this work and as postulated by Barthel & Gores ^[21] that ionic conductivity was enhanced by the introduction of

Lewis acid groups, which reduced the charge on the aluminate or borate complexes and weakened ion pairing between the lithium ion and the immobilized anion. Likewise in this work the ionic conductivity was found to be dependent on the length and structure of the oligo(ether) chains. In addition, the introduction of bulky groups onto the polymer backbone in the region of the oligo(ether) chain restricted the mobility of the latter. Therefore, there is evidence from the current investigations that lithium salts can be ordered in increasing order of conductivity $\text{Li [H8]} < \text{Li [F2H6]} < \text{Li [F8]}$ with respect to their extent of fluorination see Fig. (5.1.2). This behaviour between fluorinated and non-fluorinated samples is unsurprising and confirms the complementary and critical role that the dopant lithium salt design plays in the overall conductivity behaviour of the tested systems.

As alluded to earlier, we have of course cannot forget the conflicting role of high concentrations of lithium salts play in the system. The 3D-plots shown in Fig. (5.1.3a-b-c) earlier highlight the continuing discontinuity of the salt concentration and the conductivity similarly reported by Torell ^[26] ^[27]. Most significantly the concentration and the size of the anion itself was already discussed and can either suppress or promote crystallisation, thereby in turn altering the glass transition temperature. The development of intentional or unintentional crystallisation regions can on the one hand improve the mechanical properties of the system as was the case in this work for the samples (χ), (δ) and (ϵ)-poly(siloxane) polymers seen in table (5.1.3) in section {5.1.1.}, while on the other hand such developments usually impede ionic transport.

A paper by Imrie & Ingram *et.al.* ^[28] related a new class of polymer electrolyte (MeOCnGm polymer-LiClO₄) tailored to polyether backbones and pendent mesogenic groups systems. They found that increased salt concentrations within the polymer matrix suppressed T_g due to the slower progress of gel formation in the presence of extra salt as seen for the thermal results in table (6.1.1). The table shows the influence of salt concentration on the T_g values for (α) - Li [H8] and (α) - Li [F8], where the T_g values increase with increasing salt concentration, hence the conductivity of the same samples decreasing as the polymeric samples drift towards crystallinity. There is often the danger that high concentrations of salt particularly in gel-like materials encourage migration and an accumulation of salt at the electrolyte/electrode interface. The figure (6.1.5) shows the complex impedance plot for (α) - poly(siloxane) Li [H8] over a number of days measured at the same temperature. One observes a growing capacitance “spike” at the low frequency capacitance range. Initial

investigations of the (α) - poly(siloxane) systems showed no formation of a low frequency capacitance spike that was typically observed for the other more crystalline materials. This development indicates the presence of a good contact at the electrolyte/electrode interface. The greater the molar volume of the longer side chain unit EGE-B present, the more the polymer matrix proceeded towards crystalline type structure with an accordingly well define bulk semi-circle and an ever present low frequency capacitance spike. Therefore the lower the T_g values i.e. more gel-like, the greater is the chance of charge build-up at the polymer electrode interface otherwise known as polarisation.

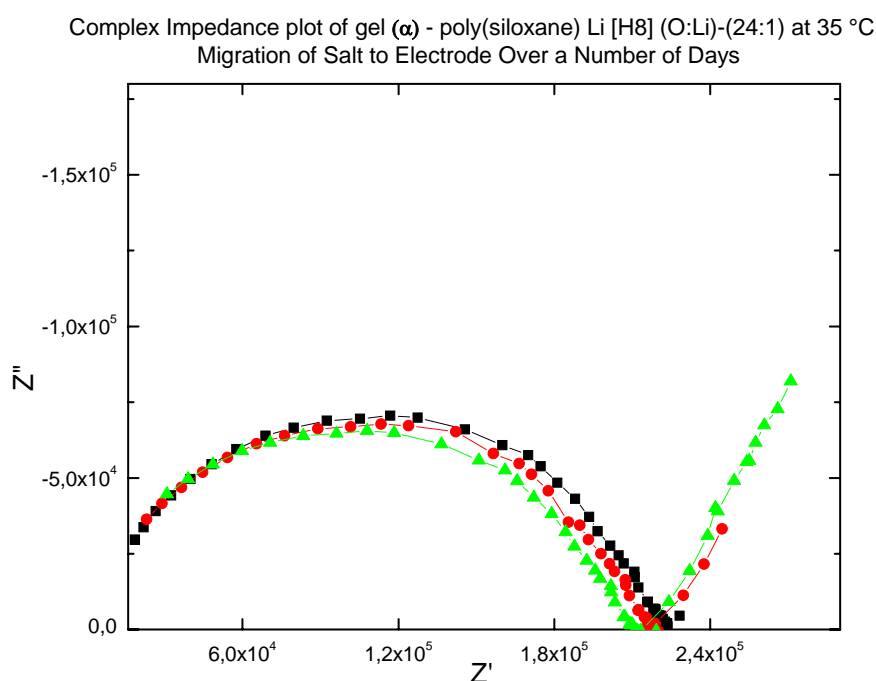


Fig.(6.1.5) Example of salt migration and lithium salt build up at the electrolyte/electrode interface over a number of days (■) – Day (1), (●) – Day (6), and (▲) – Day (17).

6.1.1.4.

Effect of Side Chain Units:

The final piece of the puzzle in our journey to understand the ion-ion interactions of the presented systems concerns the movement of the ions along the side chain units. The (oligo)ethylenglycol (EGE) side chain units coincided with the synthetic efforts to prepare polymers of highly solvating side chain units that deviated from the typically reported EO and PO⁵⁷ side units which predominate current investigations ^[29 - 31]. The negative aspect of solvated ions is the occurrence of ion pairing, particularly at elevated temperatures. The remedy to this occurrence according to Loneragan ^[32] is “through the use of weakly basic and sterically hindered anionic centres and a highly solvating solvent like diffusion zone”. The charge carrier diffusivity and hence the conductivity are closely related. Ogumi & co-workers ^[33] who worked with polyvinylidene fluoride (PVdF) and oligo(ethleneglycol) dimethyl ether (OEGDME) systems commented that as the molecular weight of the polymers increases, the temperature dependence of ionic conductivity becomes that of VTF type. The author in this work noted the bulk conductivity was revealed to be greatly influenced by the molecular weight of the side chain units, since the ion mobilities are related to the segmental motion of the polymer. Hence, ionic transport of such systems are considerably influenced by the degree of cross-linking that may be occurring through out the matrix from neighbouring side chains and opposite backbone side chains. The issue of cross-linking of the side chains is a well known phenomenon, for example Cameron & Ingram ^[5] discussed the onset of cross-linking, causing the inevitable loss of segmental mobility, thereby higher viscosity and a corresponding fall in conductivity. Similar to this work the large viscosities of the samples make the transfer of Li⁺ ions between electrodes more difficult thus leading to higher activation energies ^[33]. The behaviours of these materials are not only dictated by the concentration of the side chain units but also on the length of the side chains themselves. There is countless evidence in the literature of the effects of (oligo)ethylenglycol (EGE) chain on both the viscosities and the ionic conductivities of their respective systems ^{[7] [34 - 37]}. Fujinami ^[24] referred to earlier, who worked on siloxyaluminate-oligo(ether) co-polymers doped with LiAlH₄ and/or LiBH₄, found the ionic conductivity to be dependent on the length of the oligo(ether) side chain unit chain length. Partial crystallinity of the polymer and accordingly reduced the ionic conductivity as was observed by this author. The (oligo)ethylenglycols due to the oxygens along their chains having large dipole moments and encouraged in turn lower glass transitions temperatures according to Ito ^[9]. Ito emphasises

⁵⁷ PO - propylene oxide

that (oligo)ethylenglycols chains are capable of dissolving considerable quantities of salt which accordingly dissociate to free ion.

In the absence of lithium salts partially crystalline samples are obtained for high concentrations of EGE-A i.e. for greater than 40 % of the total side unit positions see table (5.1.3). The degree of crystallinity increases according to the increasing proportion of the shorter chained EGE-A. The dipole moment of such chains is weaker than their longer chained cousins (EGE-B) and hence more cross-linking occurs ^[9]. This observed behaviour is reflected in the θ_g data seen in the table (6.1.1), where θ_g values progressively increase with increasing proportions of EGE-A side chain units. The sample (α) - poly(siloxane) undoped polymers accordingly exhibit the lowest θ_g values and has a gel-like texture. The improved conductivities of the (α) - poly(siloxane) remains a common theme once the samples are doped by the appropriate lithium salt as seen in the example of Fig. (6.1.3b) earlier. On closer examination of the (32:1) and (24:1) lithium salt concentrations with different side chain unit proportions previously seen in section {5.1} in Fig. (5.1.7) and Fig. (5.1.8) respectively. The above described dependence for the side chain unit proportions is consistent with less ionic cross-linking in the EGE-B dominant poly(siloxane) salt mixes. This can be attributed to greater segmental motion. The conductivity of the polymer with the highest proportion of EGE-B is plotted against the reciprocal of temperature for different salt concentrations Fig. (6.1.6a –b).

The dependence of the glass transition temperatures of the presented systems can be also attributed to the weaker-binding of the ions to the two polymer side chain units and hence is greatly reduced for high concentrations of EGE-B in the (α) - poly(siloxane) system. The initial conductivity measurements of the presented data do not reveal significant improvements in conductivities over those reported in the literature ^{[32] [35 – 36] [39 – 40]}. The mechanical properties of the presented polymers systems are strongly influenced by the side chain units determined from the changes in their glass transitions. The lithium salts play a lesser role in the mechanical properties of the systems and has an impact that is more direct on the conductive behaviour of system.

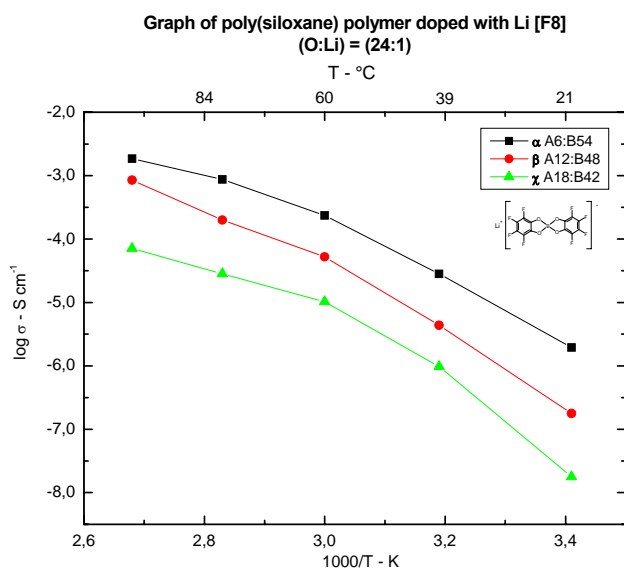


Fig. (6.1.6a)

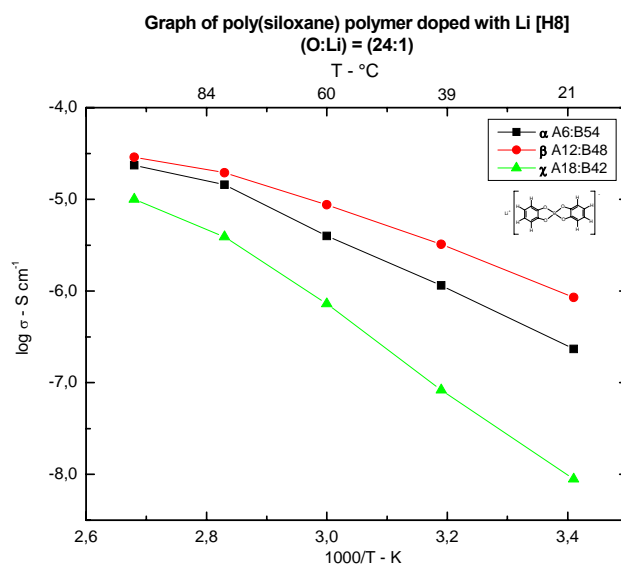


Fig. (6.1.6b)

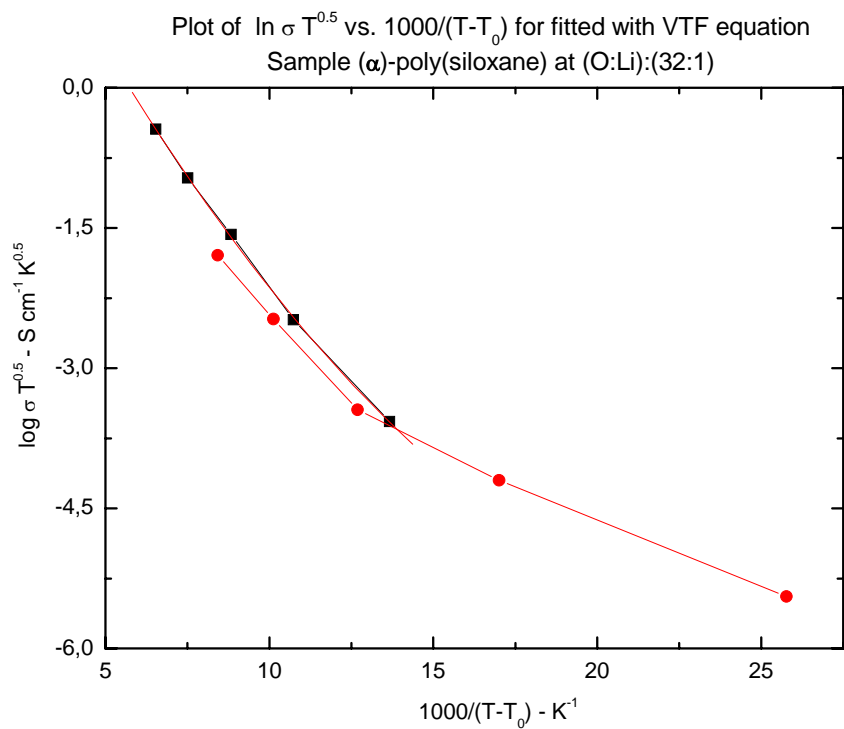


Fig. (6.1.7) Graph of VTF behaviour of the samples fitted to the equation Equ. [2.3.2].
Where (■) Li [F8] and (●) Li [H8] are fitted (-) fit line

6.1.1.5.

Arrhenius & VTF Approaches:

The temperature dependence of ionic conductivity suggested that the migration of ions was controlled by the segmental motion of the polymer particularly amorphous samples (α)-poly(siloxane) and (β)-poly(siloxane)], since almost linear curves were obtained in VTF plots. In section {5.1} we have already seen the temperature dependence of conductivity of the doped samples (32:1) and (24:1) in Fig. (5.1.7) and Fig. (5.1.8) respectively. In most samples, a curvature characteristic of polymer assisted ion motion described by Hooper^[41] is observed. The poly(siloxane) samples that are doped with fluorine containing salts and that have high proportions of EGE-B side chain units [i.e. (α)-poly(siloxane)] exhibited weak VTF behaviour⁵⁸ and were fitted by the formula Equ. [2.3.2] accordingly see Fig. (6.1.7). The non-fluorinated salt Li [H8] mixed with a low proportion of EGE-B (χ)-poly(siloxane) at oxygen to lithium concentrations (32:1) and (24:1) displayed at ambient temperatures (20 °C) disappointingly low conductivities of $4.58 \times 10^{-8} \text{ S cm}^{-1}$ and $8.89 \times 10^{-9} \text{ S cm}^{-1}$ respectively. In addition to its conductive deficiencies, these samples showed poor application to the VTF approach. The ambient temperature conductivities for all polymers are summed up in

$\theta = 20^\circ\text{C}$	Li [F8]	Li [F2H6]	Li [H8]	$\theta = 20^\circ\text{C}$
Poly(siloxane)	σ	σ	σ	Mole Ratio
Mole Fraction	S cm^{-1}	S cm^{-1}	S cm^{-1}	(O:Li)
(α) – poly(siloxane)	1.57×10^{-5}	6.42×10^{-6}	2.10×10^{-7}	(32:1)
(β) – poly(siloxane)	3.61×10^{-6}	1.85×10^{-6}	1.85×10^{-6}	(32:1)
(χ) – poly(siloxane)	2.61×10^{-8}	2.61×10^{-7}	4.58×10^{-8}	(32:1)
(α) – poly(siloxane)	1.96×10^{-6}	1.86×10^{-6}	2.35×10^{-7}	(24:1)
(β) – poly(siloxane)	1.79×10^{-7}	5.45×10^{-7}	8.45×10^{-7}	(24:1)
(χ) – poly(siloxane)	1.77×10^{-8}	4.89×10^{-8}	8.89×10^{-9}	(24:1)

Table (6.1.2) Table of the conductivities of poly(siloxanes) mixed with lithium salts at 20 °C at molar ratio (32:1) and (24:1) respectively.

⁵⁸ Please see section {2.3}

table (6.2). The longer side chained EGE-B i.e. (α)-poly(siloxane) and (β)-poly(siloxane)] containing three oxygens demonstrated consistently better conductivities. Where T_o is fixed at 20 K° below T_g . The data indicated that the mechanism of diffusion of the lithium (Li^+) ion is strongly coupled to the motion of the host polymer referred to earlier. In summary high concentrations of long side, chained units such as EGE-B for gels offered a good fit to the VTF approach defined by equation [2.3.2]. As the system drifts towards crystallinity the VTF approach (i.e. EGE-A above 30%) begins to break down.

In most circumstances in polymeric systems at low temperatures, the free ions are trapped or confined and devoid of ionic mobility where they have reduced contact with other ionic species. As the temperature increases and proceeds above a certain critical point, the increased free volume of the system i.e. greater ionic mobility within the system. Initially the conductivity increases in proportion to the increase in temperature and the free ions become highly mobile due to the loosening of the matrix itself. The conductivity on reaching a maximum either is observed to stall or decreases beyond a certain critical temperature. The free ions achieve sufficient mobility within the matrix, where they acquire the opportunity to interact with other free ion species to form either neutral ion pairs or other higher aggregates, thereby leading to a fall in conductivity due to the lower availability of free ions for ionic transport. What develops above and below a certain critical temperature is a non-linear relationship that deviates greatly from the VTF approach. This is especially applicable to systems that have large association constants ^[11]. Therefore, the VTF approach is often applied and confined to certain temperature and salt concentration ranges. In the case of the presented data, there are indications within the limited temperature range measured that large numbers of free ions are present even at ambient temperatures and above due to the steep elevation of the conductivity slopes of the for the (β)-poly(siloxane) seen in Fig. (6.1.8). The non-fluorinated Li [H8] salt has relatively weak temperature dependence of conductivity and exhibits a more linear conductivity behaviour more in akin to Arrhenius behaviour defined by equation Equ. [2.3.1]. The Coulomb interactions between mobile carriers and the fixed anionic centres are more likely to introduce correlation effects.

All the factors discussed, lithium salt concentrations, lithium salt type utilised, and side chain unit proportion come together to form a complicated web of interactions that define the nature of each sample. The empirical evidence presented in this discussion suggests the strongest facet dictating the conductivities of the systems is the proportion of relative side

chain units followed by the lithium salt concentration. The type of lithium salts utilised with respect to the degree of fluorination has a significant part to play conductively, in their role as limiting factors against the formation of ionic pairs and larger aggregates, which have been consistently alluded to in this discussion. However, their charge delocalising attributes are limited within the specific system in accordance to the side chain unit proportion. The temperature dependence of ionic conductivity obey the VTF approach in all of the fluorinated and gel-like samples but on application of the non-fluorinated lithium salts and when the samples takes on a rubbery consistency the Arrhenius approach takes precedence.

6.1.2.

Application of Equivalent Circuit Methodology:

The next and final step in our discussion is to utilise the information in our current discussion to construct a picture of the ion-ion interactions within the presented systems. In the literature, the application of equivalent circuit methodology for EIS investigations to polymeric systems is a common feature. Many authors apply the equivalent circuit technique in a very haphazard manner. In many instances there are liberal interpretations of the processes involved for charge transport, where on equivalent circuit is proposed on the foundation of data sources that that are not based on conductivity data or if conductivity data are available no fitting procedures are attempted ^{[4] [33]}. Therefore, in the following discussion the author will avoid such shortcomings by drawing on empirical data from other techniques and by the utilisation for the latest fitting methods⁵⁹. Previously we have at length defined and discussed the equivalent circuit elements can be directly related to the electrochemical parameters of the system⁶⁰. In this work, the impedance data of ionically conducting polymers are analysed based on a modified Voigt equivalent circuits of which an example can be seen below in Fig. (6.1.9).

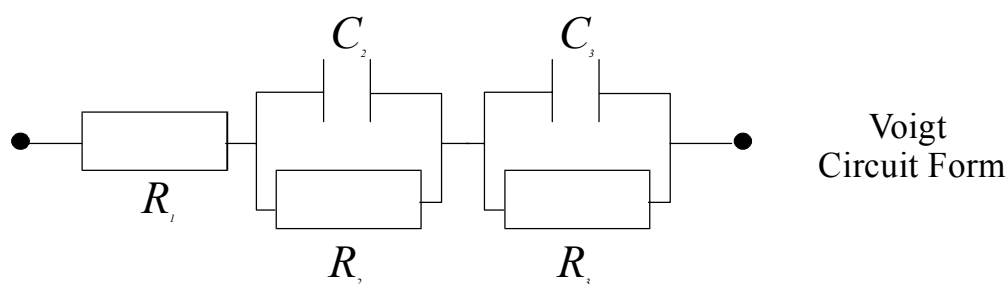


Fig. (6.1.9) Voigt circuit type

⁵⁹ See section {2.4.4}, {3.1.3}, and {3.1.5}

⁶⁰ See Chapter (2)

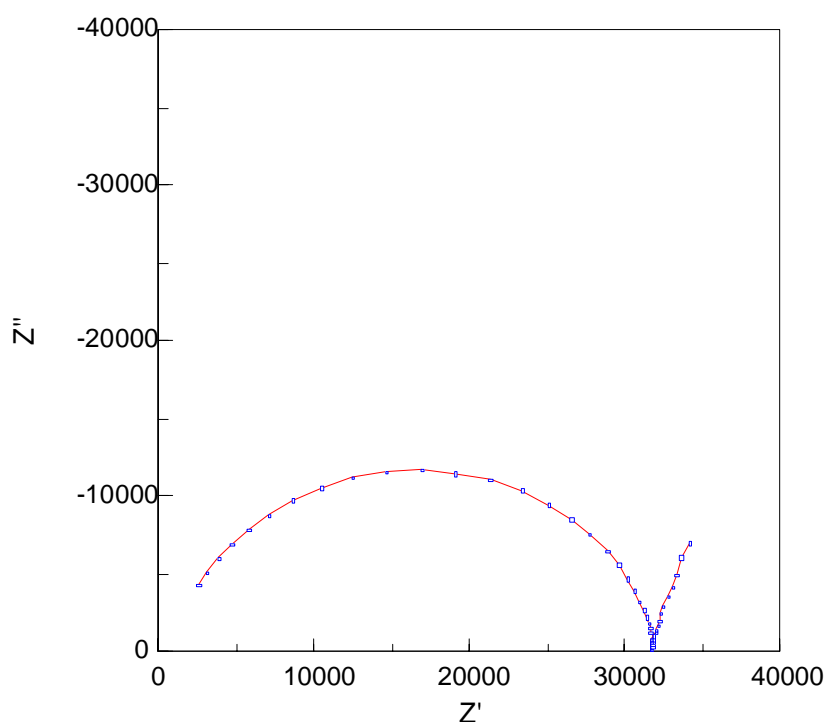


Fig. (6.1.10) Typical impedance output for all samples
(α)-poly(siloxane) Li [F8] (O:Li) – (24:1) at 40 °C.

The figure (6.1.10) shows a typical sample of a complex plane plot measured with the EIS method. A straight line at the low frequency range, this is mainly due to diffusion processes occurring at the electrolyte/electrode interface followed by a well defined but depressed semi-circle in the high to middle frequency range along the Z' real resistance axis. Similar behaviour was observed for all other samples and for ease and convenience in our further discussions the sample (α)-poly(siloxane) Li [F8] (O:Li) – (24:1) at 40 °C will be dissected in detail in furthering our understanding of the ion-ion interactions of the presented systems. Deviations from the described impedance behaviour were only observed for the systems of high viscosity and high concentration of lithium salt in the form of migration that will be discussed later and which was previously shown in Fig. (6.1.5). This aforementioned deviation was attributed to polarisation effect build up at the electrolyte/electrode interface.

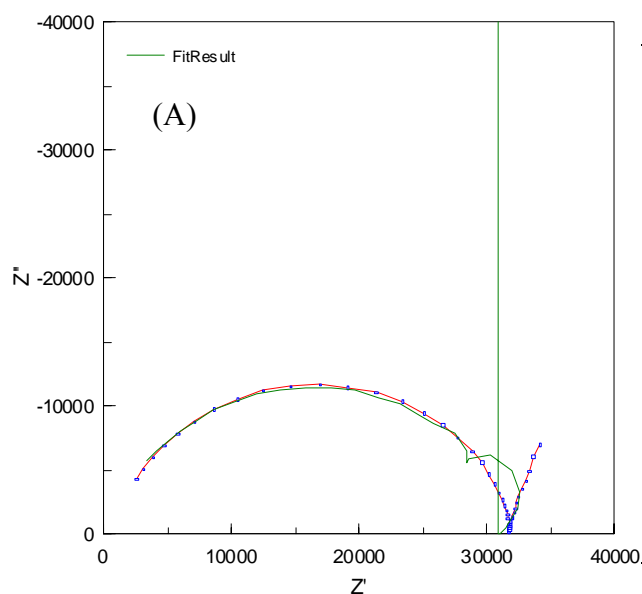
The author with the assistance of bode plot presented in Fig.(6.1.11) and (6.1.12) permitted the analysis of the real systems for high and low frequency regions. The author first attempted at fitting the real data to the equivalent circuit utilising the Warburg impedance Z_W element seen in Fig. (6.1.11b). The Voigt modified circuit, where R_I is the sum of the electrolyte resistance and the ionic polymer electrolyte similar to example provided by

Macdonald ^[41]. The elements C_{DL} and R_{CT} are the double layer capacitance of the polymer intergrain interfaces and the charge transfer resistance respectively. Both elements combined describe the semi-circle i.e. bulk resistance. The element Z_W , R_{WE} , and C_{WE} describe the finite diffusion process occurring near the electrolyte/electrode interface, the finite resistance and the finite capacitance occurring at the electrolyte/electrode interface respectively. The Warburg element Z_W was previously defined in section {2.4.3.1}:

$$Z_W = \frac{\sigma}{\omega^{1/2}} - j \frac{\sigma}{\omega^{1/2}} \quad \text{Equ. [2.4.48]}$$

We know from previous discussions in section {2.4.3.1} that the Warburg element describes a finite diffusion process in a homogenous system with a reflective boundary at the coordinate $x = 1$, $(dc/dx)_{x=1}$, where c is the concentration of the diffusing species ^[42 - 43]. This is mathematically analogous to the diffusion of a wave in the finite distributed RC transmission line ^[44]. The present circuit is widely utilised in systems where ionic and electronic diffusion occurs ^[45 - 47]. Nevertheless, the circuit shown in Fig. (6.1.11) for the real data proved to be a poor fit indicating that the conductivity is not electronic or diffusion based but more in the form of migration. Therefore, a new stratagem must be adopted.

(α)-poly(siloxane) Li [F8] (O:Li) – (24:1) at 40 °C.



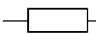

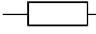



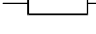

Element	Freedom	Value	SI-Units	Symbol
R_I	Fixed	0.25	Ω	
C_{DL}	Fixed	2.584×10^4	pF	
R_{CT}	Fixed	0.709	Ω	
Z_{W-R}	Fixed	5.550×10^5	Ω	
Z_{W-C}	Fixed	4.117×10^{-5}	pF	
Z_{W-P}	Fixed	0.78		
R_{WE}	Fixed	3.275×10^4	Ω	
C_{WE}	Fixed	1.034×10^{-5}	pF	

Table of fitted values the Voigt circuit in (B)

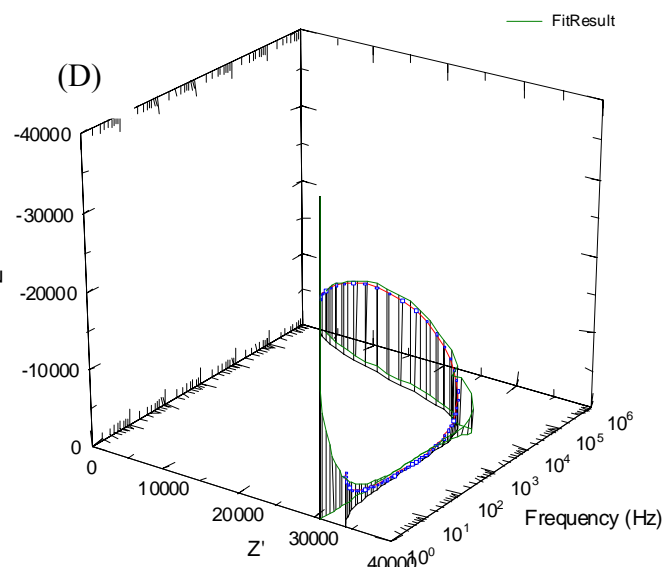
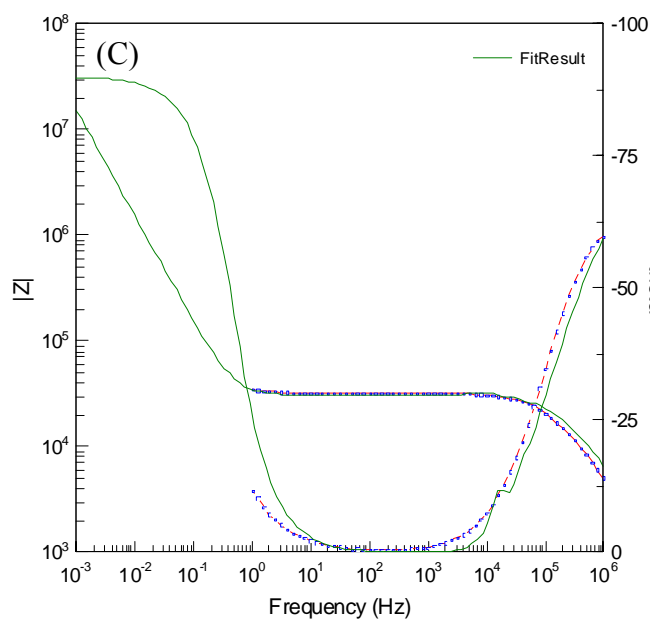
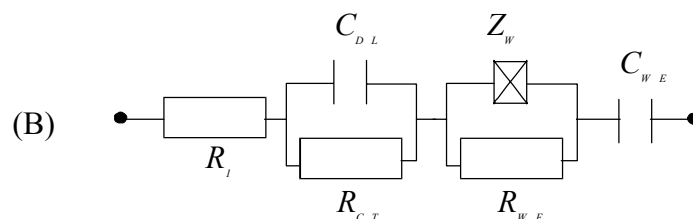


Fig: (6.1.11) Example of fitting of real data (A) with the proposed Voigt equivalent circuit at (B) utilising the Warburg element Z_W . The Bode plot (C) and the 3D plot (D) show clearly the poor fit of this circuit proposal which does not take into consideration the ion diffusion process it only considers the charge transfer.

The real system has to be analysed by breaking down the Warburg impedance Z_W element previously discussed in section {2.4.3.1} into a sub-circuit containing all the necessary resistances, capacitances and Warburg elements. The refinement of the Warburg element can be seen in Fig. (6.1.12b). The Fig. (6.1.12b) is again a further refinement of the Voigt circuit, which compensates for the Warburg elements failure to fit the real system in Fig. (6.1.11) previously, where the energy dissipation processes are lower than the 45° Warburg straight line and pseudocapacitance straight line towards the real axis as seen in Fig. (6.1.11a). Therefore the circuit element that substitutes the Warburg element can be identified as the Constant Phase Element (CPE) Z_{CPE} . A single circuit seen in Fig. (5.1.12b) can be proposed to fit the system over the complete frequency range utilising the new element. This element has already been discussed in detail in section {2.4.3.3} and takes into consideration the deviation of the real system from ideal behaviour:

$$\frac{1}{Z} = Y_{CPE}^* = A(j\omega)^{-n} \quad \text{Equ. [2.4.53]} \\ 0 \leq n \leq 1$$

In figure (6.1.12b) the first CPE, Z_{CPE-1} compensate for the inhomogeneities of the ionic charge transport occurrence in the bulk. This scenario is highly dependent on the previous discussed variables of segmental motion, salt concentration, and anionic charge and size. The second CPE, Z_{CPE-2} can be described as the representation of the charge carrier build-up at the electrolyte/electrode interface. The origin of the CPE can probably be attributed to the presence of a particular type of interionic morphology with grain boundaries and are not necessary for the characteristic of the CPE ^[48 - 49]. The CPE can be regarded as being a relaxation process of the polymer/gel materials in space charge regions and the discontinuity of the thermal expansion i.e. free volume and free ion mobility ^[50]. By this statement, the author implies that the systems free volume pulls ahead of the ionic mobility of the free ions. Therefore the charge is able to move quicker though the system as the temperature increases because the mobility of the free ions are still hindered, but they behave more like amorphous materials, in such circumstances there are no clean grain boundaries for the charge to pass through, but instead exist conductive voids.

(α) -poly(siloxane) Li [F8] (O:Li) – (24:1) at 40 °C.

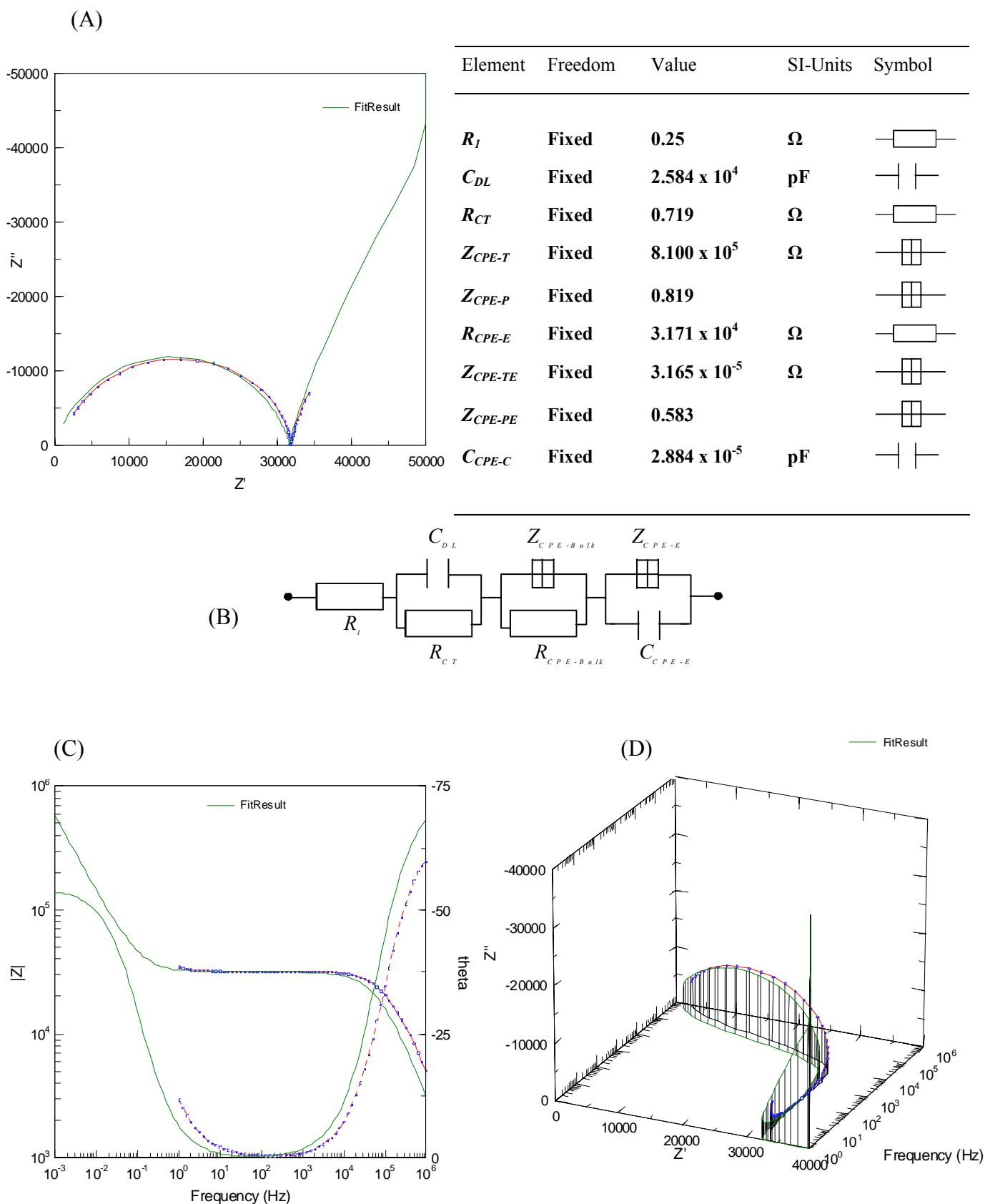


Fig: (6.1.12) Example of fitting of real data (A) with the proposed Voigt equivalent circuit at (B) utilising the Constant Phase Element Z_{CPE} . The Bode plot (C) and the 3D plot (D) show clearly a good fit of this circuit proposal which takes into consideration the ion diffusion process and charge transfer process.

In reference to the earlier mentioned polarisation effects at low frequency in the (α)-poly(siloxane) polymers, such events can be attributed to the ionic migration of the lithium salts to the electrolyte/electrode interface. A passivation layer can be ruled out since this usually involves the formation of a second low frequency semi-circle. This is not the case as seen in Fig. (6.1.13). The polarisation takes the form of an increasing low frequency capacitance spike that is indicated in Fig. (6.1.13). The bulk impedance remains constant and only the electrode impedance changes and it highlighted in the broken box in Fig. (6.1.13). In general, the proposed electrical equivalent circuit model based on impedance behaviour can only express the total electrical properties of the electrolyte system. Therefore, a single element of the system does not always represent a real physical property of the system. Nevertheless, comparisons of impedance behaviours plus armed with T_g values it seems reasonable to assume that the addition of relatively simple circuits permits an explanation of the physical nature of the interfaces involved. The procedure proposed for fitting of poly(siloxanes) polymers for the proposed systems successfully accounted for the deviations from ideal behaviour. The procedure can be successfully applied to obtain electrical parameters effects of various salts doped within the system.

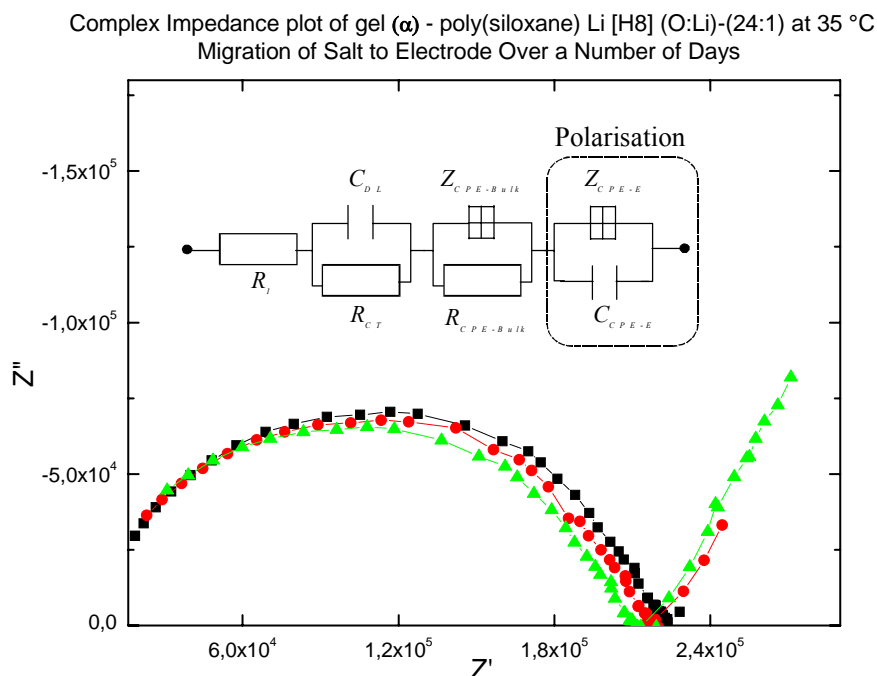


Fig.(6.1.13) Example of salt migration and lithium salt build up at the electrolyte/electrode interface over a number of days (■) – Day (1), (●) – Day (6), and (▲) – Day (17).

Summary:

The schematic of the proposed structure poly(siloxane) polymers with different stoichiometric side chain units seen in Fig. (6.1.1) seems to hold up well in most aspects. The table (6.1.4) shows the best conductivity results at 25/75 °C for this work and are compared with a number of selected poly(siloxane) containing systems investigated by other authors. The presented table (6.1.3) shows a number routes followed by different work groups in their attempts to improve the overall conductivities of poly(siloxane) system. Generally, the trend over the last 15 years is towards gel like systems and because of this trend the conductivities have improved accordingly. Our results seem to mirror this general improvement but only in the high temperature region. The sample No. 1 in table (6.1.3) shows a comparable conductivity range at 70 °C to the most recent investigations of similar systems seen in No. 4 table (6.1.3) for the author Hooper^[41]. At ambient temperatures, all the presented samples operated within the conductive parameters of previous investigations. The other samples prepared in this work seen in No. 2 and No. 3 table (6.1.3) show disappointingly poor conductivities at ambient and elevated temperatures and lie in the range of previous investigations, mostly likely because of their low ion mobilities. We saw previously in Table (5.1.6) an increase in T_g with increasing salt concentration was attributable to the formation of ion-dipole cross-linking. It is not clear to what degree the non-polar siloxane backbone may be impeding the movement of ions among the (oligo)ethylenglycol side chains.

In retrospect to other investigation seen in table (6.1.3) this work was successful in increasing the conductivity through suppression of crystallisation of the polymer chains and hence improved chain mobility. Other investigations have had considerably more difficulty in achieving this aim ^[52 - 53]. The conductive advantage that our salts have over previous investigations is their ability to increase the carrier concentration. Similar to the effects observed for the ionic liquids later, the Li [F8] consistently demonstrated better conductivities particularly at elevated temperatures. Indicating that the charge delocalising effects of the salts plays an important role once sufficient free volume is available at elevated temperatures. The poorer performance of the other salts No. 2 and 3 in table (6.1.3) may be due to the strong localisation of the cation about the immobile anionic site. The authors cited in table (6.1.3) encounter similar problems in their investigations. The salt Li [H8] exhibited the poorest relative conductivity amongst all the other samples, indicating the localisation of the charge and tight ion pairing which significantly reduces the number of available pairs. The

localisation effect may be considered in terms of more general correlation effect resulting according to Dupon^[87] from the Coulombic attraction between the cation and the anion. To date, there have been few direct investigations of the effect of salt size and charge delocalisation effects in the presented systems.

The conductivities of the samples are dependent on temperature particularly at low salt concentrations, whose curvatures are characteristic of amorphous/polymer salt complexes^[52]. The temperature dependence of ionic conductivity suggested that the migration of ions was controlled by segmental motion of the polymer, since linear curves were obtained in VTF plots similarly reported by Yeh & co-workers^[54]. Yeh^[54] reported flexible polymeric siloxane main chains and the anion source bonded on it, such that only the cation could migrate. In summation, the ionic conductivity has been shown for these poly(siloxanes) systems to increase as a direct result to the proportions of side chain units added. The longer the side chain unit and the more present leads to lower glass transition temperatures with a corresponding increase in conductivity. The conductivity is confined largely above the glass transition temperature considered by Andreev^[55] to be most advantageous, and is related to the unique conduction mechanism involving the creation of free volume, arriving from the dynamics of the polymer chains. In the presented systems, crystallinity is suppressed and segmental motion maximised. The influence of the lithium salts was most significant in respect to their direct concentration within the system and is typical for all polymeric systems i.e. conductivity maximums are observed. The most notable and obvious facet of these systems is the interaction of lithium salt and the polymer matrix itself. The delocalisation effect of the anions of the salts played an important role in reducing the formation of large numbers of ion pairs and other neutral species. In previous studies, the cations are often located within the helix of the PEO side chains. The lithium salt Li [F8] exerted a particularly positive influence on the overall conductivities due to its large size and many electronegative F-substituents. If the author compares the value acquired for the presented systems and those for similar systems in the literature^{[4] [32] [41]}, our electrolytes have better thermal stabilities and better overall conductivities at ambient and elevated temperatures.

The only significant question to these results remains the issue of water when one considers that after extensive attempts to dry the H-siloxane backbone base material before polymerisation. Previously reported current densities by Merz^[7] measured by means of cyclic voltammetry must be considered with caution. All samples were measured in aqueous and

acetonitrile solution. It was observed for the IR and NMR spectra of the starting reagent H-siloxane that there remained estimated 1 to 2 % water trapped within the polymer matrix. Moreover, there was the added issue of residual THF solvent trapped within the matrix estimated to be 0.5% of the total mass. The procedures employed in the removal of these impurities have already been discussed. Nevertheless, bearing such facts in mind the true validity of these presented results must permit the unfortunate factoring of a error from the undesired presence of water molecules that with certainty interferes with the highly sensitive doped lithium salts.

No.	Polymer/Gel	Salt	$\theta = 25\text{ }^{\circ}\text{C}$ $\sigma = \text{S cm}^{-1}$	$\theta = 70\text{ }^{\circ}\text{C}$ $\sigma = \text{S cm}^{-1}$	Reference
1	α -Poly(siloxane)	Li [F8] (O:Li) (32:1)	1.57×10^{-5}	3.80×10^{-3}	Presented Work 2003
2	α -Poly(siloxane)	Li [F2H6] (O:Li) (32:1)	6.42×10^{-6}	9.10×10^{-3}	Presented Work 2003
3	α -Poly(siloxane)	Li [H8] (O:Li) (32:1)	2.10×10^{-7}	8.34×10^{-5}	Presented Work 2003
4	(double-comb) poly(siloxane) with branched oligoethyleneoxide	LiTFSI	2.99×10^{-4}	10^{-3}	Hooper & Lyons ^[41] 2002
5	poly(methylalkoxysiloxane) PHMS oligo-oxyethylene side chains	LiClO ₄	3×10^{-5}	10^{-4}	Morales & Acosta ^[4] 1999
6	poly {poly { [.omega.- methoxypoly(oxyethylene)]propyl } methylsiloxane } - co-[3-(3,5-di-tert-butyl-4- hydroxyphenyl)butyl]methylsiloxane }	Na(OC(CH ₃) ₃ 2 % Na / ethylene oxide	1.4×10^{-6}	1.68×10^{-5}	Lonergan & Ratner ^[32] 1995
7	poly(hydromethylsiloxane) (PHMS)	vinyl-contg. cyclic carbonate in acetonitrile	1×10^{-7}	1×10^{-5}	Zhu & Zhenya ^[52] 1994
8	comblike poly(siloxane) with oligo(oxyethylene) side chains and pendent sulfonate groups polyethylene glycol allyl Me ether and allyl glycidyl ethe	NaHSO ₃	2×10^{-5}	10^{-4}	Zhou & Bin ^[53] 1993
9	Poly(siloxane) with PEO side chains		2×10^{-4}		Hall & Davies ^[56] 1986

Table (6.1.3) Comparative table of the conductivities at the indicated temperatures for a range of poly(siloxane) based systems

6.2. Ionic Liquid Electrolytes

Foreword:

In the following presented work the author intends to move away from “empirical knowledge and feel”, strategies^[57] pursued over the years by researchers in the field of room temperature molten salts. Instead to deliver a more concrete understanding of the ion-ion interactions within such systems by means of detailed EIS analysis, that is currently underdeveloped in this field. This work has electrochemically studied the bulk properties at a microscopic level (in the form of ion-ion interaction, conductive pathways, and ionic transport) the molecular properties at a macroscopic level (in the form of solvation effects, hydrogen bonding, liquid structure, etc.).

6.2.1.

Discussion of Structural & Conductive Behaviours of Ionic Liquids:

6.2.1.1.

A multiphase “lamella bilayer” System:

According to Every^[50] “room temperature molten salts (ionic liquids) are one of the most concentrated electrolytic fluids possessing a high number of charge carriers per unit volume”. Furthermore “... these carriers are mobile with very high conductivities possible”. The above statements attributed to Every^[50] can be considered an imprecise generalisation to a very broad subject, when taken in the light of the present investigations. The investigated ionic liquid systems shown in table. (5.2.2) earlier presented us with the unique, and until now, unrecognised opportunity to study so-called self-organising systems^[58 - 60]. This aforementioned system exhibits three different types of well known and studied electrolyte systems all rolled into the confines of one system. In the order of increasing temperature, the first system can be described as “plastic crystal” electrolyte^{[1] [22] [61]}, the second system can be described as the “amorphous” “salt-in-polymer” electrolyte^[28] and finally the third system can be described as “viscous liquid electrolyte”^{[12] [62 - 63]}. In the course of our discussion each of the proposed electrolyte systems will be discussed in the context of their ion-ion interactions with the assistance of the equivalent circuit method already developed and utilised in section {6.1}.

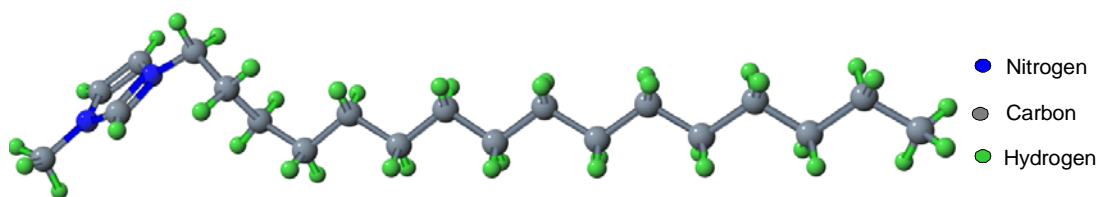


Fig. (6.2.1) 1-n-hexadecyl-3-methylimidazolium cation [C_{16} -mim]

The author has already alluded to in section {5.2.3} the existence of “novel architecture”^[59] for the ionic transport of the presented systems at different temperatures in table (5.2.2). Therefore all further discussions will assume awareness of the knowledge and conclusions from our previous structural commentary discussed earlier in section {5.2.3}. The previously outlined and cited experiential data^[64 - 65] has indicated the existence of two-dimensional conductive pathways characteristic of “lamella bilayers”^[52]. These systems are usually structured by self-assembly of molecules through hydrogen interactions to form “super-molecular” structures. A simplified example of such a system can be seen in Fig. (5.2.6)^[66]. Dias & co-workers^[52], who investigated polymers with different alkyl chain lengths ($R = -C_{16}H_{33}$ or $-C_{12}H_{25}$) that were synthesised and mixed with several salts of Li^+ , Na^+ , and Mg^+ . Dias^[52] reported similarly to this work that the salts complexed to form “two dimensional helical poly(ether) backbone layers” which separated into hydrocarbon layers that can be best described as lamella bilayers. Diaz^[52] goes on to indicate that the alkyl side chain lengths ($R = -C_{16}H_{33}$ & $-C_{18}H_{37}$) exhibited liquid crystal phases with independent extensive self-organising qualities that made them highly conductive at elevated temperatures. More recent cited evidence from Chia *et al*^[67], who investigated three component low dimensional polymer electrolyte complexes of blends in amphiphilic helical polymers with ($R = -C_{16}H_{33}$) chain lengths also encountered well defined lamella morphology with good conductivities ($1 \times 10^{-3} \text{ S cm}^{-1}$ at $\theta = 20^\circ \text{C}$) when doped with $LiBF_4$. The main force behind such self-assembling structures in the solid and liquid crystalline states is hydrogen bonding^[58]. The author suggests the reason for such high conductive properties of the long alkyl ($R = -C_{16}H_{33}$) chain lengths systems arises from ionic mobility within the relatively unimpeded spaces between the well organised complex molecules and molecular aggregates.

The presented systems have exhibited excellent conductive properties at ambient temperatures for the bulk phase seen previously in Fig. (5.2.17). On doping the ionic liquid with the appropriate lithium salt at ambient temperatures and below, the salt mixtures mainly

exhibited lithium “fast ion” conduction see Fig. (5.2.21a) (5.2.21c) ^{[2] [61] [68]}. Examples of materials with similar characteristics are glasses and ceramic systems, which are reputed to conduct via the fast ion conduction mechanism. The lithium ions move within an essentially static framework ^[61]. On the other hand as the salt mixtures enter into the amorphous polymer-in-salt system at elevated temperatures the motion of the ions in such polymer systems is similar to that of solvent based systems i.e. their motion is mediated by the dynamics of the host polymer.

Structure	Name	Short-hand	M g mol ⁻¹	Calculated Radius r – Å ⁶¹
$\text{Li}^+ [\text{Cl}]^-$	lithium chloride	Li [Cl]	42.39	1.7
$\text{Li}^+ \left[\begin{array}{c} \text{F} \\ \\ \text{F}-\text{P}-\text{F} \\ \\ \text{F} \end{array} \right]^-$	lithium hexafluorophosphate	Li [PF₆]	151.90	2.41
$\text{Li}^+ \left[\begin{array}{c} \text{F} \\ \\ \text{F}-\text{B}-\text{F} \\ \\ \text{F} \end{array} \right]^-$	lithium tetrafluoroborate	Li [BF₄]	93.75	2.32
$\text{Li}^+ \left[\begin{array}{c} \text{H} \quad \text{H} \\ \quad \\ \text{C} \quad \text{C} \\ \quad \\ \text{H} \quad \text{H} \end{array} \right]^-$	lithium bis-[1,2-benzenediolato(2-)- O,O']borate	Li [H8]	233.92	4.21
$\text{Li}^+ \left[\begin{array}{c} \text{F} \quad \text{F} \\ \quad \\ \text{C} \quad \text{C} \\ \quad \\ \text{F} \quad \text{F} \end{array} \right]^-$	lithium bis - [3,4,5,6 – tetrafluoro - 1,2 – benzenediolato (2-) -O,O']borate	Li [F8]	377.84	4.20

Table (6.2.1) Table of lithium salts utilised during this work dissolved in liquids.

The table (6.2.1) is inserted to remind us of the lithium salts substituted into the ionic liquid matrix seen in Fig. (5.2.21a) - (5.2.21c). The relationship of conductivity and the reciprocal of temperature obtained from EIS measurements can be seen in Fig. (5.2.17). shown previously. All samples exhibited rather unusual conductive behaviours at elevated temperatures. In the following discussion the samples [C₁₆-mim] [PF₆] and [[C₁₆-mim] [F8]] will be utilised as our benchmarks to attain a general overview of the materials under investigation. The figures (6.2.2a) & (6.2.2b) show the previously indicated phase transitions detected in both EIS and DSC thermal investigations respectively. Similarly the schematic of the structural behaviours of the sample for each respective phase transition can be seen in Fig. (5.2.15) and will be referred to in their course of our discussion.

61 These anion radii data were sourced from Welton ^[69] and MOPAC atom calculator.

$[C_I]$	Pre-ordered crystal phase	{ “ <i>plastic crystal</i> ” system }
$[C_{II}]$	Side chain relaxation phase	{ <i>relaxed “plastic crystal”</i> system }
$[S_A]$	Liquid crystal phase	{ <i>amorphous polymer-in-salt</i> system }
$[Iso]$	Isotropic phase	{ <i>viscous liquid electrolyte</i> system }

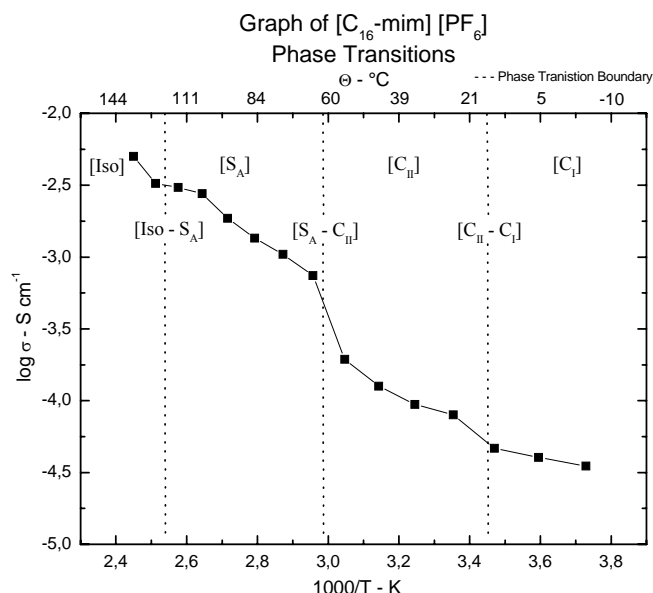


Fig. (6.2.2 a) Three phase transition Arrhenius conductivity plot

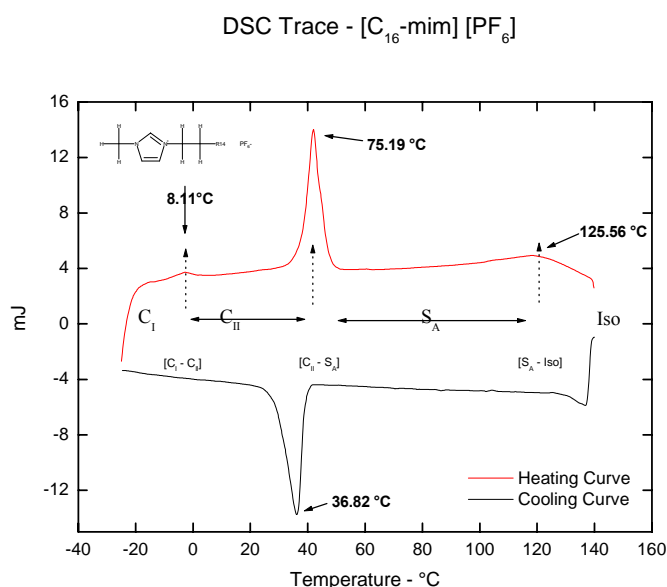


Fig. (6.2.2 b) Three phase transition DSC thermal plot

6.2.1.2.

Pre-ordered Crystal Phase / $[C_I] - [C_{16-mim}] [PF_6]$:

In commencing our discussion, we shall take the sample $[C_{16-mim}] [PF_6]$ as our starting point. This system provides an excellent example of a multiphase system that covers all three electrolyte characteristics alluded to in section {6.2.1.1}. The author has already in numerous occasions stated that the presented systems are far more complex than other electrolyte systems thus far presented. This is mainly due to their temperature dependent multiphase character. The aforementioned multiphase character makes a generalised interpretation of their conductive behaviours difficult. Mainly for this very reason most authors have avoided direct investigations of the ion-ion interactions of ionic liquids. Therefore the author intends to back-engineer the presented systems to their fundamental “constituent parts” in order to ascertain a more detailed understanding of the structural and conductive behaviours.

The first phase encountered $[C_I]$ is rather unusual and was first reported by De Roche & Imrie *et.al.* ^[64] working with similar samples. The phase can be considered a pre-ordered high density and structurally rigid structure similar to a “plastic-polymer” electrolyte seen in the proposed schematic in Fig. (6.2.3g) ^[61]. The crystalline state of such substances is typically fully ordered at low temperatures. The exhibited conductivities operate in the range, where they can be described according to West ^[70] and Irvine ^[71] as emulating polycrystalline materials with fast ion conduction ^{[2][72]}. Electronic conductivity can be ruled out since we are well above the glass transition point at this temperature range (-5 to +20 °C). According to MacFarlane ^[61] conductivity “can be polycrystalline in nature typical of the bulk materials creating grain interior resistances and capacitances which lower the overall conductivities”. At the temperature $\theta = 0$ °C the conductivity for the sample was about $1 \times 10^{-7} \text{ S cm}^{-1}$ although quite a poor result, it was considerably better than $1 \times 10^{-9} \text{ S cm}^{-1}$ at similar temperatures previously reported by De Roche & Imrie *et.al.* ^[64], owing probably to better measuring conditions. The low temperature $[C_I]$ phase can be described as a region, where the ionic motion is constricted by the lattices extreme rigidity. The conductivity mechanism in this region can be considered a very constricted form of ionic conductivity. The application of the equivalent circuit method for such systems is relatively simple. The figure (6.2.3a) shows the complex impedance plot for the sample $[C_{16}\text{-mim}][\text{PF}_6]$ at $\theta = 0$ °C. The figure shows a good semi-circle and is characteristic of a single phase microstructure described by Macdonald ^[42]. The semi-circle is remarkably round. This indicates the highly organised nature of the microstructures with few anomalies.

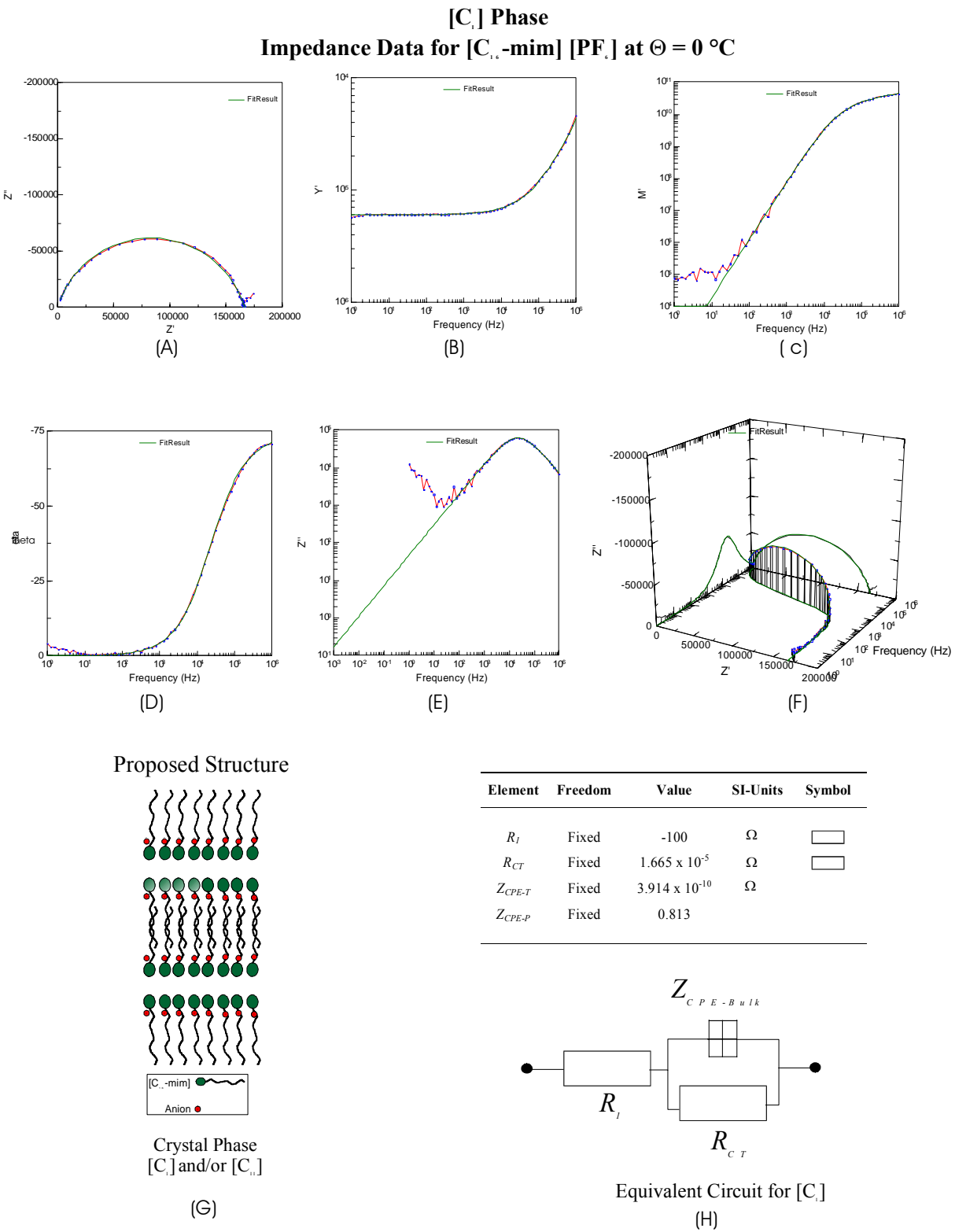
The fitting of the system for the equivalent circuit seen in Fig. (6.2.3h), like the previous poly(siloxane) systems, the R_I element is the sum of the resistances and the electronic resistances. The elements R_{CT} and $Z_{CPE-Bulk}$ are the elements corresponding to the charge transfer resistance and the complex impedance response of the grain interiors respectively. The bode-modulus plot shown in Fig. (6.2.3c) confers the relative homogeneity and the continuity of the sample which in this case is very good. The straying of the data at the low frequency region can be attributed to the electrode roughness. The level of agreement between the experimental and the simulated fitting is quite satisfactory for the grain interiors in terms of the shape and distribution of the frequency arcs fitted to the phase angle plot seen in Fig. (6.2.3d). The phase angle plot is a useful plot in exposing any hidden microstructures or interfaces that often go unnoticed in the complex plane plots. The 3D plot perspective offers additional back-up to expose any unusual structural and conductive anomalies that

often go unregistered in the normal complex plane plots Z , Y , M , and ε . The Z' vs. frequency plot shown Fig. (6.2.3e) puts greater emphasis on the internal resistance of the system and is very useful in displaying which part of the system dominates the overall resistivity. In the case of this system at $\theta = 0$ °C the bulk resistance dominates the conductive nature of the sample.

6.2.1.3.

Crystal Phase / [C₁₁] – [C₁₆-mim] [PF₆]:

On increasing the temperature of the [C₁₆-mim] [PF₆] sample to $\theta = 25$ °C, a small but still significant conductivity jump is observed coinciding with the DSC phase transitions in Fig. (6.2.2a) & (6.2.2b) respectively. Overall, the systems remain rigid and organised at the micro-structural level. The endotherm for this phase transition seen in Fig. (6.2.2b) is quite small, employing that the structural change to the matrix is limited. The authors De Roche & Imrie *et al* ^[64] postulated that this phase transition is a direct response to greater ionic motion and/or flexibility of the anions by means of the slight losing of the alkyl side chains. We are aware from collected X-ray crystallography results that the anions in this state are found inserted between the cation header groups and the twisted alkyl chains shown previously in Fig. (5.2.7) (5.2.8) ^[65 - 65]. Their smaller size, when compared to the larger imidazolium cations, permits their easier movement and greater flexibility within the suggested lamella matrix, similarly to the opinion of the author Chia ^[67] working with similar systems who concluded that these systems could provisionally be labelled “relaxed” plastic-polymer electrolytes. The measured impedance data indicated no significant change in the microstructure. Only in the Z' vs. frequency plot can one observe the beginnings of a low frequency event in Fig. (6.2.4e). The author believes that those anions nearest the electrolyte/electrode interface after achieving their newly discovered greater mobility (permitted by the alkyl chain loosening) start to accumulate at the electrolyte/electrode interface. This salt accumulation is not occurring in significant enough quantities to merit serious concern. The conductivity of the system is still



predominately by the bulk, this statement is reinforced from evidence concluded from the well formed semi-circle in the complex impedance plot seen shown in Fig. (6.2.4a). Furthermore the system remains well structured and organised cited from evidence from the Bode-modulus plot seen in Fig. (6.2.4c), where no unusual anomalous events are observed. The system is still dominated by limited ionic conductivity and perhaps only extremely limited anionic conductivity occurring directly at the electrode/electrolyte interface. The equivalent circuit presented previously for $[C_I]$ in Fig. (6.2.3h) is still applicable in the current system shown in Fig. (6.2.4h). The level of agreement between the experimental and the simulated fitting satisfactorily fitted for the grain interiors in terms of the shape and distribution of the frequency arcs fitted to the phase angle plot in Fig. (6.2.4d).

6.2.1.4.

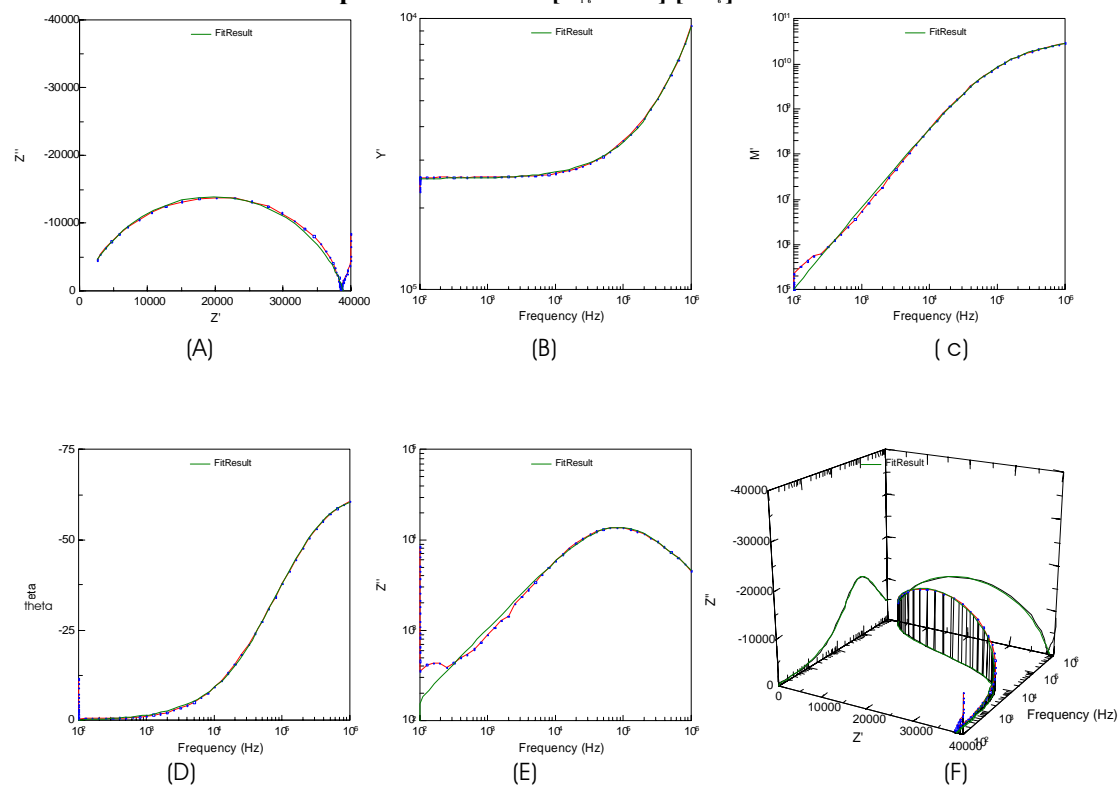
Crystal to Liquid Crystal Phase transition / $[C_{II}] - [S_A] - [C_{16}\text{-mim}] [PF_6]$:

The crystal to liquid crystal phase transition $[C_{II}] - [S_A]$ that occurs at $\theta = 75^\circ\text{C}$ in the $[C_{16}\text{-mim}] [PF_6]$ sample is a highly complex phase transition. This is the phase transition region in which the highly organised crystalline structure gives way to a locally organised amorphous “polymer-in-salt” structure proposed by Angell ^[82]. The figure (6.2.5g) shows the schematic representation of the sample changing from a highly organised rigid structure to a more flexible and considerably more conductive material. The figures (6.2.2a) and (6.2.2b) showed a large conductivity jump and endotherm in this temperature region respectively. This region and in particular the conductivity step is directly attributable to the melting of the alkyl side chains. This in turn permits a greater degree of freedom (free volume) ^[88] for the anions to move about within the matrix through increased free volume leading to higher ionic mobility ^[64]. At this point in the conductivity measurements of the aforementioned lamella phases become more evident and will shortly be commented upon.

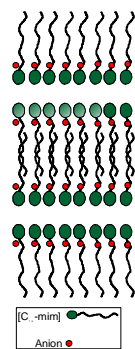
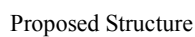
The helical axis is suspected of lying normal to the lamellae layer obtained from previous evidence cited by the authors Hashimoto ^[73] ^[76], who have studied crystalline polymers. In the complex impedance plot seen in Fig. (6.2.5a) one large rounded semi-circle and one small compressed semicircle is observed in the high and low frequency regions respectively. The familiar low frequency initially capacitance spike touched on in the previous section {6.2.1.3} is not seen in the complex plane plots but observed in the Bode plots.

[C₁₁] Phase

Impedance Data for [C₁₆-mim] [PF₆] at Θ = 25 °C



Element	Freedom	Value	SI-Units	Symbol
R_I	Fixed	420	Ω	<input type="text"/>
R_{CT}	Fixed	3.847×10^4	Ω	<input type="text"/>
Z_{CPE-T}	Fixed	7.291×10^{-10}	Ω	
Z_{CPE-P}	Fixed	0.7963		



Crystal Phase
[C_i] and/or [C_{ii}]

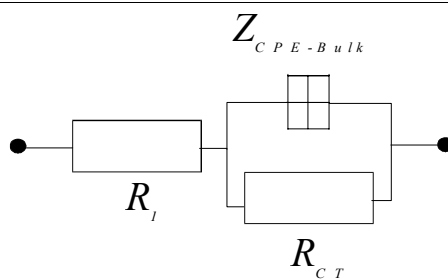


Fig. (6.2.4)

The high frequency semi-circle progressively bends over to a new semi-circle with increasing temperature between 60 °C to 80 °C, which is precisely the start and end of the phase transition registered in both EIS and DSC measurements seen in Fig. (6.2.2 a) and (6.2.2 b). This behaviour is typical of polymorphic systems ^[74] showing the transformation and existence of two phases. In addition the author MacFarlane^[61], who studied similar ionic liquid [bis(trifluoromethane-sulphonil) imideazolium – C₁₂H₂₇] materials prepared by doping Li₂SO₄ salt to “plastic crystal matrix” that exhibited fast lithium ion motion due to rotational disorder and the existence of vacancies within the lattice. They reported conductivities as high as $2 \times 10^{-4} \text{ S cm}^{-1}$ at $\theta = 60^\circ\text{C}$, which compares most favourably to our results of $3.15 \times 10^{-4} \text{ S cm}^{-1}$ at $\theta = 60^\circ\text{C}$ for the longer chained [C₁₆-mim] and the weakly coordinating [PF₆] anion. The authors Chia & co-workers ^[67] who investigated three component low dimensional polymer electrolytes similar in structure to the sample presented in this work, attributes the appearance and short lifespan of the second semi-circle to that of phase behaviours of Maxwell two-phase series dielectrics. Evidence of two phases coinciding together can be seen in the Bode-modulus plot seen in Fig (6.2.5c). There is a palpable link to be observed in the plots middle to low frequency range that was previously not noted in earlier data sets. This illustrates that the system is much less homogenous and is undergoing radical structural alterations. If one compares previously Fig. (6.2.5c) the similar plot in the lower temperature range, the bend in the line seems to be shifting downwards towards the low frequency region. The Z' vs. frequency plot in Fig. (6.2.5e) shows a similar shift of the arcs with the formation of a second hump at the low frequency region that was previously not present in earlier plots. Furthermore the phase angle plot seen in Fig. (6.2.5d) exposed a conductive event that was not present in any of the previous plots at lower temperatures. This indicates that the bulk resistance is losing dominance and the resistance is shifting towards the low frequency region near the electrode.

During the fitting of such data a number of compromises must be made owing to systems phase transformation within the defined temperature region. The equivalent circuit shown in Fig. (6.2.5h) presents a complex nine element circuit. The first three elements we have already encountered and describe both double layer capacitive C_{DL-1} and resistive R_{CT-1} response of the first semi-circle in the intergrain region discussed earlier. This is followed by the second double layer capacitive C_{DL-2} and resistive R_{CT-2} response of the second smaller semi-circle which the author attributes to the grain boundary region. This grain boundary region is suspected to be the product of two sets of globular lamellar “microdomains” ^[75 - 77]

with identical spacing meeting. This region can be equated to the disjointed nature of the sample as the intermolecular contacts (along/between the alkyl side chains) weaken and lose their rigidity seen in the schematic Fig. (6.2.5g). At this point the anions (now main the charge carriers) become much more mobile and start to migrate into the lamella interphase channels. The conduction in the present state is “facilitated by the presence of well defined conduction channels” between the lamellar phases ^[60]. It should be added that the anions can not diffuse across or tunnel through the membranes but stay confined along the channels. This is mainly owing to the strong polarity of the imidazolium cation header groups ^{[57] [78]}. The second last circuit element pair $Z_{CPE-Bulk}$ and $R_{CPE-Bulk}$ describes the correction factor that must be included for the suppressed nature of the second semi-circle seen in Fig. (6.2.5a). Similar to the poly(siloxane) in the previous section {6.1}, the free volume of the system pulls quicker ahead of the actual conductive capacity of the charge carriers (i.e. the anion charge carriers). This is mainly due to the fact that the mobilities of the charge carriers are still hindered by the residual structure (i.e. lamella phase) maintained by the mobility restricted imidazolium cationic header groups. The final two highlighted circuit elements in Fig. (6.2.5h) Z_{CPE-E} and C_{CPE-E} describe the growing capacitance spike and anionic charge carrier build-up at the electrolyte/electrode interface. The fitting of the circuit in this circumstance was more difficult due to the disordered nature of the system within rapid structural changes that were occurring within this temperature range. The sample was at this temperature and time in a state of structural metamorphous. The level of agreement between the experimental and the simulated data “roughly” fitted for the grain interior, grain boundary, and electrode impedances in terms of the shape and distribution of the frequency arcs fitted for the phase angle plot also seen in Fig. (6.2.5d).

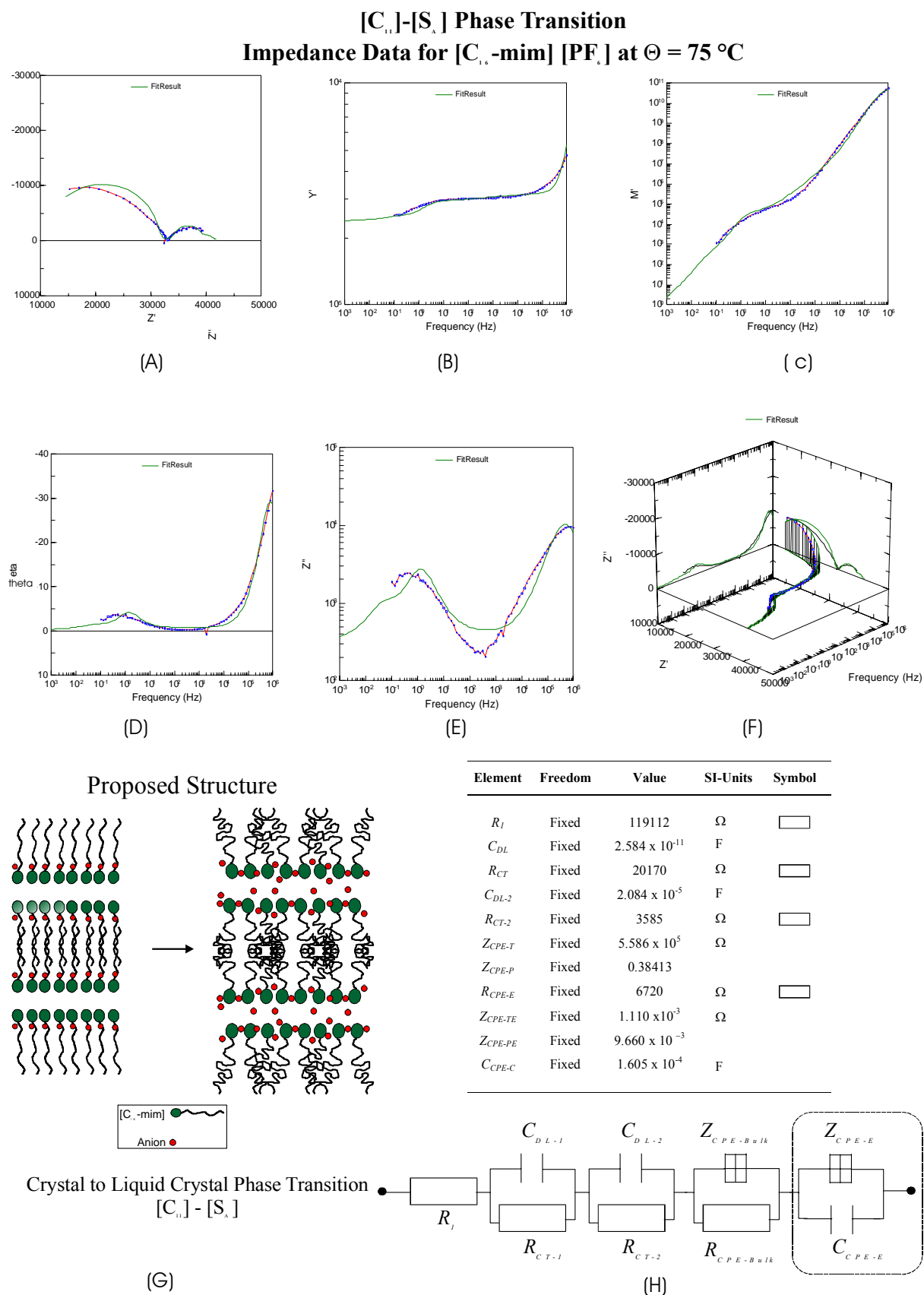


Fig. (6.2.5)

6.2.1.5.

Liquid Crystal Phase / $[S_A] - [C_{16}\text{-mim}] [PF_6]$:

For the sample $[C_{16}\text{-mim}] [PF_6]$ the liquid crystal phase $[S_A]$ exists between $\theta = 75^\circ\text{C}$ to 125°C for the presented sample. This phase is highly unusual and its structural and conductivity behaviours are extremely temperature responsive and dependent respectively. In this phase region the anions dominate the conductive nature of the sample. They become increasingly mobile with increasing temperature. The complex plane plot seen in Fig. (6.2.6a) shows a considerably truncated high frequency semi-circle and greatly extended low frequency capacitance spike for the sample measured at $\theta = 105^\circ\text{C}$. As the temperature increases and moves away from the $[C_{II}] - [S_A]$ phase transition, the bulk semi-circle at the high frequency region progressively disappears while similarly the low frequency capacitance spike increases in extent. In the figure (6.2.6g) the schematic provides a good overview of what is occurring within the microstructure. The alkyl chains have already melted and have become highly flexible; the anions are now mobile both between the helical side chains and the lamella plane channels. At such high temperatures the hydrogen bonding previously indicated by Karle^[58] as the main organisational force in maintaining the molecular superstructures starts to fail. The majority of the charge carriers now reside in the lamella plane channels, where they accordingly migrate towards the electrode. The structural referred to lamella channels are maintained by the strongly polar cations^{[57] [89]}. With increasing temperature they begin to lose their structural integrity and likewise start to shift and bend. The bulk resistance becomes a residual factor in the overall conductivity of the system. This is attested by examining the Bode-modulus and Z' vs. frequency plots in figures (6.2.6c) & (6.2.6e) respectively. The lines have in both cases shifted downwards to the low frequency electrode active region. In this state the system can be effectively considered a amorphous “polymer-in-salt” electrolyte previously described by the authors Angell^[82] and Imrie^[28].

The data of the presented system was fitted according to the equivalent circuit shown in Fig. (6.2.6h). In comparison to the previous phase transition equivalent circuits seen previously in Fig. (6.2.5h), the circuit has become considerably simpler. The intergrain double layer capacitive C_{DL-1} and resistive R_{CT-1} response has now given way to the grain boundary double layer capacitive C_{DL-2} and resistive R_{CT-2} response (i.e. residual lamellar microdomains)^[75 - 77]. The inhomogeneity within the residual bulk structure is compensated by utilising CPE responses of $Z_{CPE-Bulk}$ and $R_{CPE-Bulk}$ due once again to the noted suppressed nature of the semi-circle in Fig. (6.2.6a). The highlighted final circuit pairs elements Z_{CPE-E}

and C_{CPE-E} in Fig. (6.2.6h) again describe the growing capacitance spike and anionic charge carrier build-up at the electrolyte/electrode interface that now dominates the conductive parameters of the system. The level of agreement between the experimental and the simulated data excellently fitted for the grain boundary and electrode impedances in terms of the shape and distribution of the frequency arcs fitted for the phase angle plot also seen in Fig. (6.2.6d).

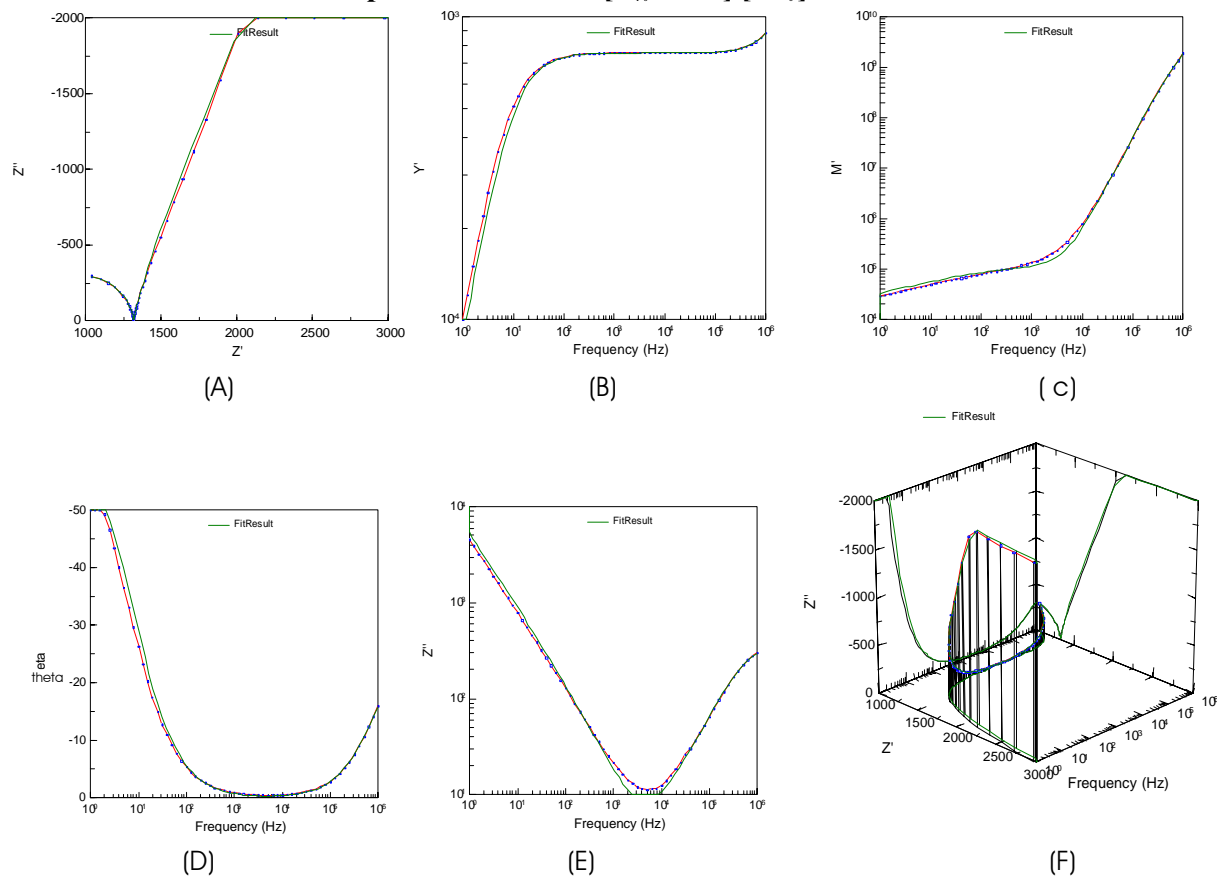
6.2.1.6.

Isotropic Phase – [Iso] / [C₁₆-mim] [PF₆]:

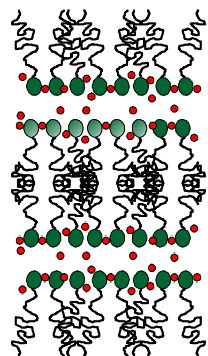
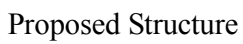
The final phase to be discussed is the isotropic phase that occurs at $\theta \geq 125^\circ\text{C}$ for the sample [C₁₆-mim] [PF₆]. In the Fig. (6.2.7a) the bulk semi-circle double layer capacitive C_{DL-I} and resistive R_{CT-I} response have disappeared altogether. What remains is a low resistance high capacitance spike. The structure has devolved to effectively a viscous liquid electrolyte or a truly “molten salt” state, where the residual organisation that the structure retained from the cation “polarity” of the imidazolium header groups has now dissolved and only a pure capacitance between the two electrodes remains. The Fig. (6.2.7g) shows the proposed schematic of the system. The alkyl side chains have long since melted and the imidazolium header groups have now become highly mobile charge carriers similar to the anions.


The equivalent circuit seen in Fig. (6.2.7h) represents the capacitance which exists at the electrodes. The resistor R_I element is the residual resistance of the interionic contacts that are still occurring between the mobile charge carriers. The elements Z_{CPE-E} and C_{CPE-E} represent the pure capacitance between the electrodes. The level of agreement between the experimental and the simulated fit data for the electrode impedances in terms of the shape and distribution of the frequency arcs fitted for the phase angle plot also seen in Fig. (6.2.7d) is satisfactory. There is a point of note concerning these systems, when they are compared to typical liquid/polymer electrolytes, as the presented systems deviated in their conductive behaviours at high temperature. We are already familiar with the example provided by Gerber ^[11] concerning the temperature dependence of LiBF₄ in dimethoxyethane, a solvent of low dielectric permittivity, the conductivity of lithium salts can in certain situations exhibit a negative temperature dependence of conductivity. Such solutions of salts in solvents of low permittivity show particular properties which can be attributed to the formation of ion pairs, triple-ions or large ionic aggregates that hinder and reduce the number charge carriers in solution.

[S_A] Phase Transition

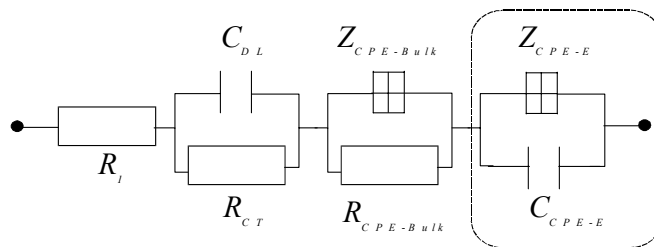


Element	Freedom	Value	SI-Units	Symbol
R_I	Fixed	612,5	Ω	<input type="text"/>
C_{DL}	Fixed	3.882×10^4	F	<input type="text"/>
R_{CT}	Fixed	7.865×10^{-8}	Ω	<input type="text"/>
Z_{CPE-T}	Fixed	7.454×10^{-10}	Ω	<input type="text"/>
Z_{CPE-P}	Fixed	0.907		<input type="text"/>
R_{CPE-E}	Fixed	707	Ω	<input type="text"/>
Z_{CPE-TE}	Fixed	4.016×10^{-5}	Ω	<input type="text"/>
Z_{CPE-PE}	Fixed	0.6740		<input type="text"/>
C_{CPE-C}	Fixed	6.887×10^{-6}	F	<input type="text"/>




 Liquid Crystal Phase
 $[S_A]$

(G)

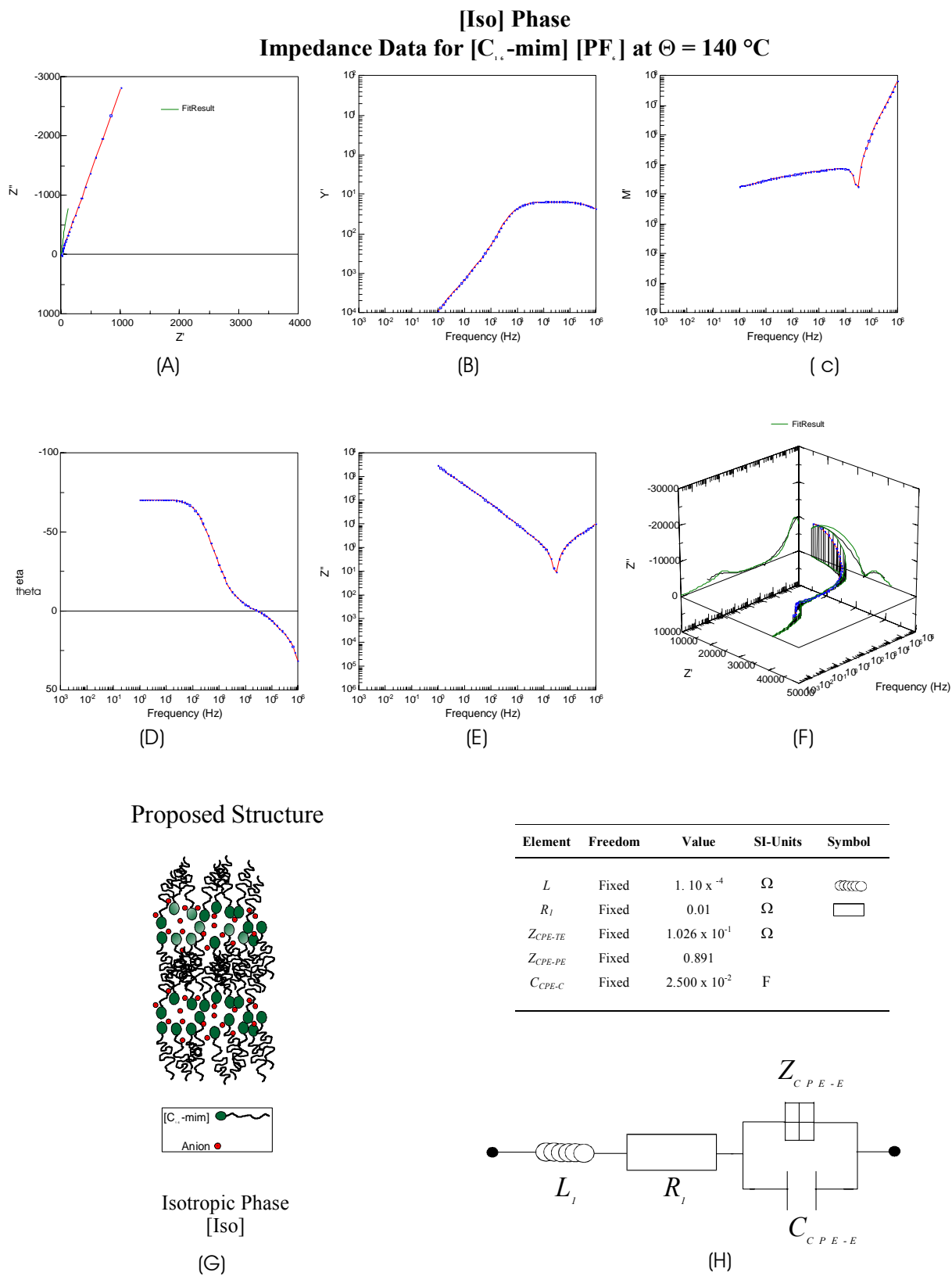


Equivalent Circuit for $[S_A]$ Phase Transition

(H)

Fig. (6.2.6)

In the presented systems this response was not observed. Even in the isotropic state the conductivities did not drop due to the formation of ion pairs discussed in the previous section {6.1}. Greater charge carrier stability can be attributed to the relative large size of the respective ionic constituents. The large imidazolium cationic header group with its long alkyl chains reduced the possibility of formation of large aggregate interactions that would hinder ionic mobility. The larger anions such as Li [F8] at higher conductivities played a significant role but will be commented on at a later point. Generally the conductivity was dictated by the morphology of the system which in turn was dictated by the temperature.



6.2.1.7.

Phase Transitions of [C₁₆-mim] [F8]:

In the previous section {6.2.2}, we have successfully fitted the proposed equivalent circuits to the multiphase sample [C₁₆-mim] [PF₆]. Now we will discuss the application of the proposed equivalent circuits to our newly synthesised lithium salt samples with different anionic centres. Therefore a good candidate is the sample [C₁₆-mim] [F8]. The figures (6.1.8a) & (6.1.8b) show the previously indicated phase transitions detected in both EIS and DSC thermal investigations for the sample [C₁₆-mim] [F8] respectively. The graphs in Fig. (6.2.9a-f) are the various already seen complex plane, bode, and 3D plots for the sample [C₁₆-mim] [F8] over the complete measuring temperature from $\theta = -5\text{ }^{\circ}\text{C}$ to $105\text{ }^{\circ}\text{C}$. Similar to all samples in Fig. (6.2.9a) in the complex plane plot, with increasing temperature the bulk (semi-circle) resistance decreases due the structural changes occurring within the matrix previously discussed. The Bode-admittance plot vs. frequency is an excellent plot in showing major conductive alterations in the form of capacitance changes within the matrix. One can observe that there is an obvious jump in capacitance of the samples between the temperatures $25\text{ }^{\circ}\text{C}$ and $55\text{ }^{\circ}\text{C}$ which corresponds to the similar conductive jump of the [C_{II}] to [S_A] phase transition seen in Fig. (6.2.9a) in the same temperate range. In the crystalline region below $35\text{ }^{\circ}\text{C}$ one can observe in the low frequency region a large capacitance spike indicating that there is already a large charge build-up at the electrolyte/electrode interface. This can be attributed to the large size of the anion radius, compared to the smaller [PF₆] and [BF₄] anions, whereby being unable to fit sufficiently energetically within the helix and the cationic header groups, is pushed into the lamella channels. Therefore, more accessible near the electrode. The phase angle plot in Fig. (6.2.9d) shows at the high temperature low frequency region is the development of a noticeable hump as the sample shifts from a plastic-crystal in which the charge transport is polycrystalline to a polymer-in-salt system. Here the anions become mobile as previously discussed and ionic transport increasingly takes over as the anionic charge carriers already highly dissociated due to the large electronegative delocalising charge start to migrate towards the electrode. At elevated temperatures a second but smaller capacitance jump in the mid-frequency range can be observed in figures. (6.2.9b) and (6.2.9d) between $65\text{ }^{\circ}\text{C}$ and $75\text{ }^{\circ}\text{C}$. This jump is the [S_A] to [Iso] phase transition and similarly corresponds to the conductivity vs. reciprocal of temperature plot seen in Fig. (6.2.8a). The Fig. (6.2.10a-c) shows the complex plane and Bode plots of the sample at selected temperatures covering the whole phase transition range. The level of agreement between the

experimental and the simulated data excellently fitted to proposed equivalent circuit in Fig. (6.2.10) in terms of the shape and distribution of the frequency arcs fitted for the phase angle plots. The Fig.(6.2.11) summarises in schematic the structural changes occurring parallel to the proposed equivalent circuit for each phase transition. On cooling of all systems the structure reverted back to their original order and hydrogen bonding take permanence in the form of re-establishing the lamellar layers. There was no permanent conductive alteration within the system in the later heating cycles.

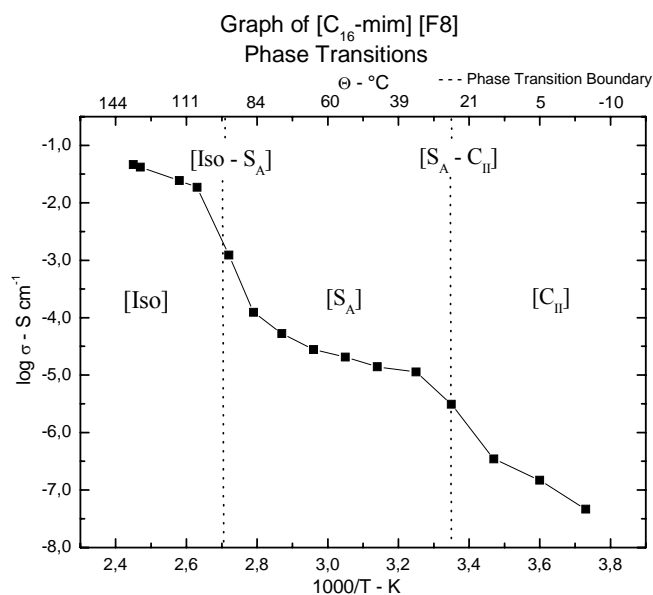


Fig. (6.2.8 a) Three phase transition Arrhenius conductivity plot

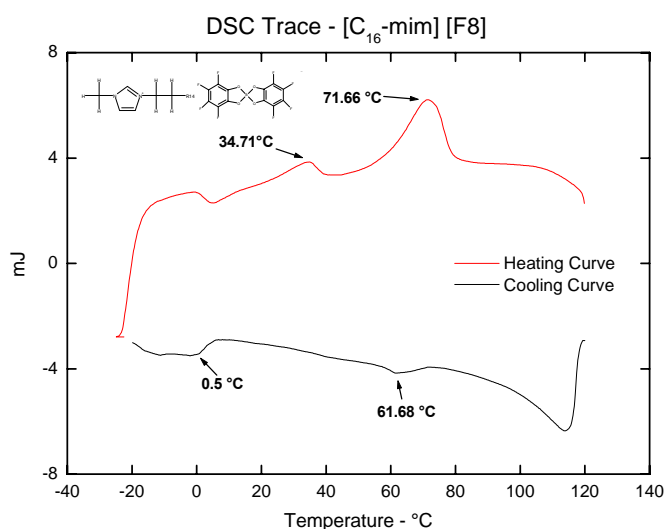


Fig. (6.2.8 b) Three phase transition DSC thermal plot

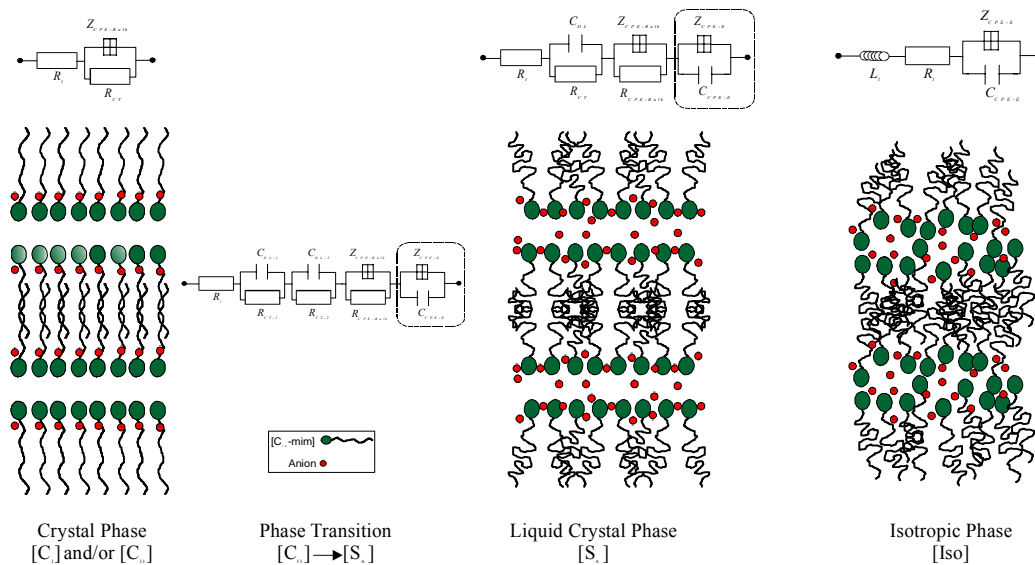


Fig. (6.2.11) Summarises the form of a schematic the structural changes occurring parallel to the proposed equivalent circuit for each phase transition.

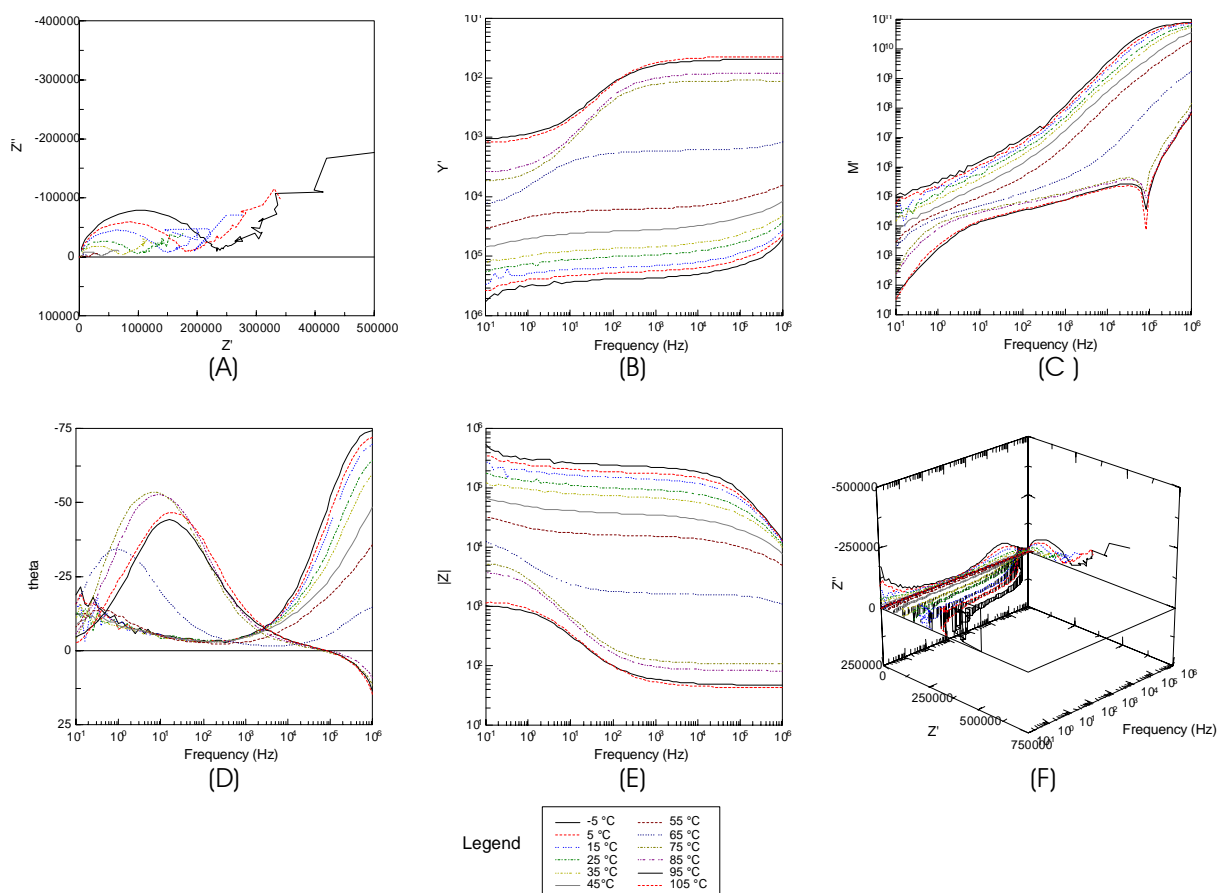


Fig. (6.2.9) Complex plane, Bode, and 3D plots of $[C_{11}\text{-mim}] [F8]$ from $\Theta = -5^\circ\text{C}$ to 105°C

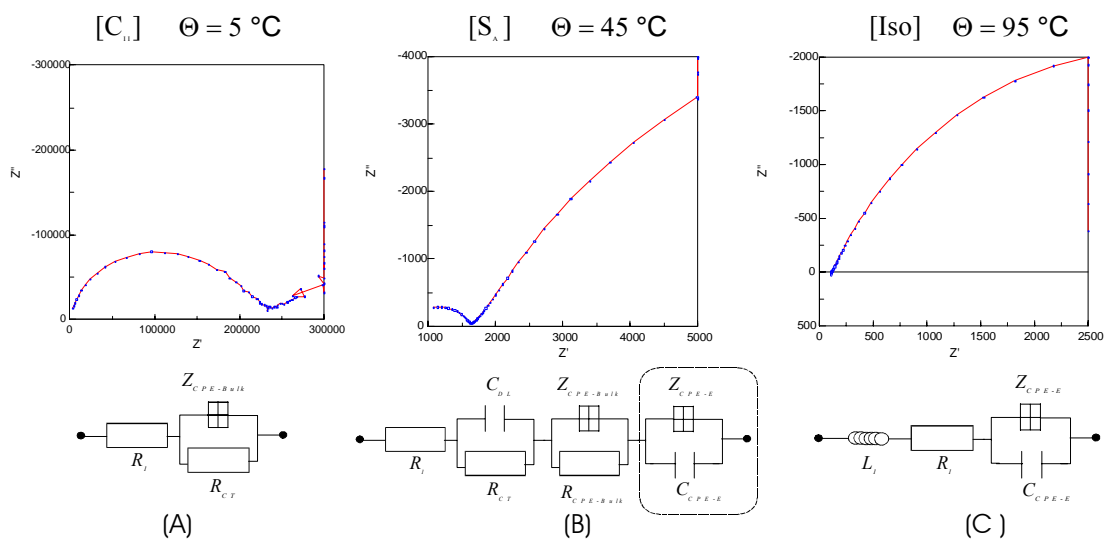


Fig. (6.2.10) Complex plane plots and their proposed equivalent circuits for the sample $[C_{11}\text{-mim}] [F8]$ at $\Theta = 5^\circ\text{C}$, 45°C , and 95°C for the crystal, smectic A, and isotropic phases respectively.

6.2.2.

Influence of Anion Salt Size on the Structural & Conductive Behaviours of Ionic Liquids:

We discussed in section {6.2.1} by means of equivalent circuit methodology how the presented systems responded conductively under thermal stress. Our next task is to discuss in more detail the implications of salt type and in particular the implications of anionic salt size. Similarly to the poly(siloxane) systems discussed in section {6.1}, ionic liquids are greatly influenced by the anion radii and charge delocalisation effects that go along with these salts. As a result the melting points and general conductive characteristics of these systems are greatly influenced by the aforementioned attributes^[50]. The author Every^[50] commented that the “melting points of the ionic liquids are determined by the ionic shape and their interactions”. This leads in turn to the conclusion that the energy associated with melting is dominated by the entropy of the ordered lattice^[50]. The substitution of salts in ionic liquids with the intent of manipulation of the polycrystalline architecture has been pursued in recent years as a method to enhance ion dissociation^[79]. In general according to Forsyth^[79] the presence of regularly spaced anionic charges in close proximity to the alkyl side chains leads to poor ion dissociation and poor solubility due to their strong Coulombic repulsions. By the application of fluorinated anionic salt groups, they should help in improving the dissociating ability by weakening the direct anion alkali metal interactions that will crop up concerning the lithium ion later when the systems are doped. The problem of anion repulsion still remains and particularly so for fluorinated anions salts such as PF_6^- and BF_4^- , which according to Carmichael^[50] are weakly coordinating anions. However even in the weakly coordinating systems important interactions are at work and a number of unfavourable conditions can be observed.

Therefore it was the opinion of the author that through the application of the newly synthesis salts Li [F8] and Li [H8] previously seen in table (6.2.1), that some of the more negative aspects referred to above could be mitigated. Their large radii and greater charge delocalisation attributes with particular reference to Li [F8] was seen as a promising means achieving that aim. It was hoped that through the application of these salts a reduction of the melting point could be achieved by increasing the ion size and perhaps shifting the highly conductive mesogenic phase down to ambient temperatures.

If the reader examines the data for samples [C₁₆-mim] [H₈] and [C₁₆-mim] [F₈] in Fig. (5.2.17); which combines one data set for each sample investigated, both referred to samples generally have lower overall conductivities as would be expected for such ions in other situations, although their conductive behaviours are replicated comparatively well in their DSC plots as seen previously in Fig. (5.2.14e) and Fig. (5.2.14f). Surprisingly their conductivities are subdued at lower temperatures as compared to the other smaller anions [Cl], [BF₄], and [PF₆]. Only after passing through the [S_A – Iso] phase transition in the high temperature range do they surpass the conductivities of the smaller ions. Only in the upper [S_A] and throughout the [Iso] regions do the larger ions have complete freedom of movement within the disbanded matrix. The larger ions exhibit superior conductivities in these regions (i.e. for [C₁₆-mim] [F₈] at 125 °C - $\sigma = 2.693 \times 10^{-2} \text{ S cm}^{-1}$ and [C₁₆-mim] [H₈] at 125 °C - $\sigma = 1.44 \times 10^{-1} \text{ S cm}^{-1}$) due to their charge delocalising effect, that was previously at lower temperatures suppressed due to their confinement within the rigid crystalline matrix. The charge delocalising attributes of these ions could effect little influence in the prevention of the formation of ion aggregates, which were previously alluded to concerning the hydrogen bonded aggregates that were proposed to exist in the isotropic phase ^{[64] [67]}. This is most likely due to their constrained configurations within the matrix of the crystalline samples. On melting of the chains, the salts acquired enough freedom of movement within the matrix to influence the overall behaviours and conductivities of the sample. The weaker delocalising and smaller ions such as the mentioned [Cl], [BF₄], and [PF₆] anions have the advantage at lower temperatures to achieve higher ionic mobility through their ability to maximise their stoichiometric occupancy of the available sites along the helix alkyl chains near the header groups depicted in Fig. (5.2.7) and (5.2.8).

The smaller substituted anions [Cl], [BF₄], and [PF₆] seem to offer a more stable configuration since the anions fit more efficiently in conjunction to the chains and the header groups seen in Fig. (6.2.18b). Yoshizawa ^[85], who worked on “new ionic liquids prepared by neutralising five different imidazole derivatives with two imidzolium type acids” such as bis(trifluoromethanesulfonyl)imide and bis(perfluoroethyl-sulfonyl)-imide. Yoshizawa ^[85] found that the imidazolium compounds overall conductivity depended directly on the size of the anion radii i.e. increasing anion size caused decreasing conductivity. They were unable to report with certainty if this was the case due to close proximity in anionic radii of [BF₄] and [PF₆]. However, in the light of newly presented evidence in this work, this is the case seen

from the EIS since anions of our salts Li [F8] and Li [H8] have considerably large radii than anions in Li [BF₄] and Li [PF₆].

The reason for this system response is mainly due to the smaller anions for example [BF₄] being hindered to a much lesser extent in its ionic transport and charge movement through the system along the lamella phases or conductive “channels”. The larger anions [H8] and [F8] are firstly pushed further away by their disassociate nature and secondly by their larger size. As previously mentioned the larger anions are suspected at least partially occupying the lamella layers as seen previously in Fig. (5.2.6). This would firstly explain the disappearance of the [C_I] phase in the DSC plots for these samples. Secondly the conductivity steps for both salts seen for the [S_A – Iso] phase transition in (5.2.14e) and Fig. (5.2.14f). are considerably greater in intensity for the larger anions when compared to the smaller [Cl], [BF₄], and [PF₆] anion, highlighting their more disruptive nature within the matrix. This indicates their freer movement on passing through the [S_A – Iso] phase transition. These results also lend support to the proposal by Holbery^[65] that in the absence of lithium ions, the mobile species in such systems are the anions. In addition, it was observed that the complex plane plots, shifted in resistance from the bulk semi-circle (i.e. decreasing semi-circle), while at the same time there was an increase in the low frequency capacitance “spike” at the sample electrode as seen and discussed previously is observed. The figure (6.2.12) shows the relationship of conductivity to the anion salt size at different temperatures. As one observes there is a obvious relationship between anionic size and conductivity. At low temperatures, the small salts are able to move more easily in the constrained environment and therefore have the advantage of achieving surprisingly high conductivities at low temperatures. However, once the larger anion containing ionic liquid samples pass into the isotropic phase (i.e. above 116 °C) the advantageous charge delocalising effects of the larger fluorinated ions takes hold and their conductivities overtake those of the small ions at the same temperature.

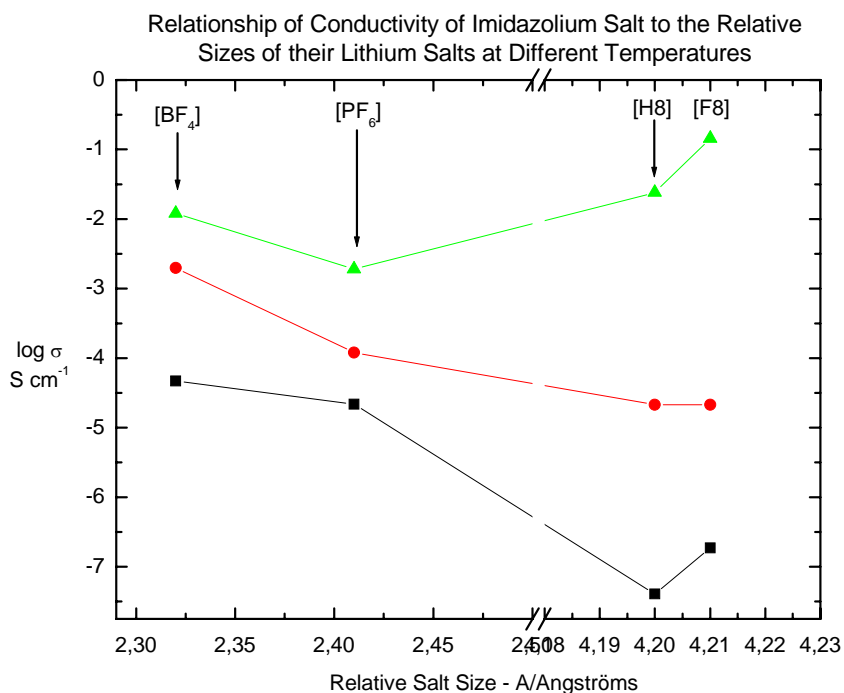


Fig. (6.2.12) Relationship of imidazolium salt conductivity to lithium anion radii at different temperatures.
 (▲) 115 °C (●) 55 °C (■) -5 °C

6.2.3.

Influence of Doped Lithium Salt on the Structural & Conductive Behaviours of Ionic Liquids:

Previous experiments in Aberdeen ^[80] had shown that high concentrations of dopant were detrimental to the conductive behaviours of the samples and therefore experiments were confined to 0.5 Molar Fraction and below. These investigations indicated that the excess lithium ions moved within the lamella phase boundaries or “channels” seen in Fig. (6.2.13). The ionic liquid matrix contained the same anions hence doping can be considered as cation substitution. The presence of the lithium salt generally improved the overall conductivities of the samples above the undoped samples as can be seen in Fig. (5.2.21 a–c) for the samples [C₁₆-mim] [PF₆], [C₁₆-mim] [BF₄], and [C₁₆-mim] [F8] respectively. There is also evidence of limitations to the maximum substitution of lithium salts “stuffing limiting factor” similar to

comments by Torell ^[26 - 27] concerning high concentration of added salts. The systems toleration for each salt had a maximum capacity to which they can absorb and solvate salts before the beneficial effects of the salt are mediated by overloading of the system. In case of the [C₁₆-mim] [PF₆] above 0.5 MF doping with LiPF₆, the conductivities drop considerably. The [C₁₆-mim] [BF₄] system show no improved conductive qualities until the concentration of doped LiBF₄ was above 0.4 MF. This sort of behaviour can not be directly likened to the poly(siloxane) system described in the previous section {5.1}.

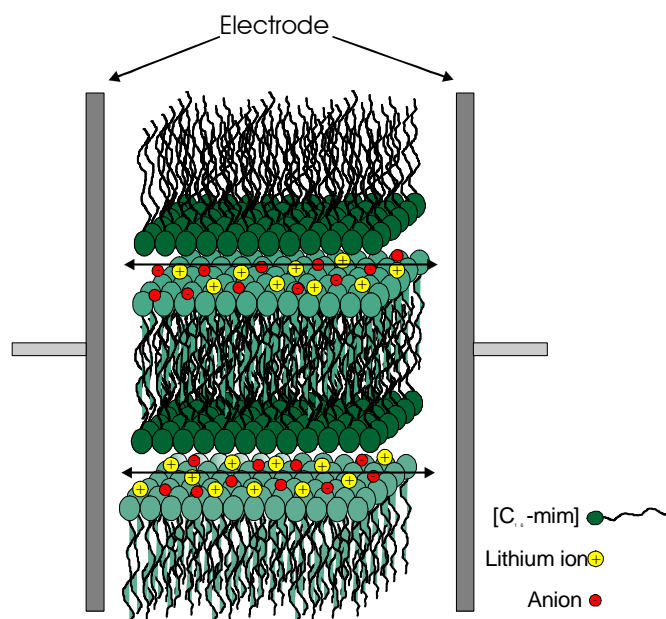


Fig. (6.2.13) Schematic of a doped crystal lamella phase, where the lamella planes lie normal to the direction of the electrodes

It is true that at larger concentrations of dopant the ionic mobility decreased to such an extent that a maximum in conductivity versus salt occurs and is a similar phenomenon which has been reported for salt containing networks based on PEO and PPO⁶² ^[81]. In these circumstances, it was suggested that the conductivity drop at higher salt concentrations is not only due directly to reduced ion mobility from chain entanglements, but also to the formation of large ion aggregates. In the case of the ionic liquids, presented chain entanglements at elevated temperatures play a much reduced if any role. The formation of ion species such as ion pairs, triple ions or higher aggregates are not such a large factor and take a secondary role. The main disruptive feature of these salts lies in their occupation of the lamella phases though which most of the ionic activity is occurring. An additional factor is observed, once the larger [H8] and [F8] have entered the isotropic phase the conductivities are considerably better than

expected as they fulfil their role in reducing higher ion species formation and promoting dissociation from the metal ion ^{[52] [54] [79]}. The application of the equivalent circuit models proposed earlier was relatively simple. The insertion of the lithium salt promoted the conductivity and made more charge carriers available. The conductive behaviours of the samples were relatively similar at low salt concentrations. Therefore, the direct application of the model was possible for each phase.

The phase transitions were disrupted with a general shift in the phase transition steps to lower temperatures. In most samples at high concentrations of doped salt, the mesophase disappears when observed under a POM. In such systems only two phases are observed, the [C_{II}] and the [Iso]. This indicates that the lamella phase can only sustain limited disruption. This cannot be considered a negative development as the phase transitions have shifted towards ambient temperatures. In addition, there is an increase in the conductivities of the doped samples as compared to the undoped samples at the same respective temperature. In the case of the doped [C₁₆-mim] [F8], sample in Fig. (5.2.21c), rather surprising results were observed on increasing the concentrations of Li [F8]. The conductivities increased considerably and there was the expected drop of the [C_{II} - Iso] phase transition from 83 °C to 35 °C for MF 0.2 MF Li [F8]. This shift is well above expectations. For the doped sample at 25 °C the conductivity is ($\sigma = 5.493 \times 10^{-6} \text{ S cm}^{-1}$) for 0.2 MF Li [F8] as opposed to ($\sigma = 4.493 \times 10^{-7} \text{ S cm}^{-1}$) for the undoped sample at the same temperature see Fig. (5.2.21c). The delocalising nature of the large anion assisted the improved conductivities of the system by promoting the movement of the lithium ions and limiting the formation of aggregates at elevated temperatures. The lamella structures previously mentioned is crucial in delivering the conductive pathways, which allow ionic motion to occur even within the rigid crystalline phase. The lamella layers are suggested to lie parallel to the electrodes and the helix alkyl chains axes. This conformation should be beneficial to the conductivity across the cell Fig. (5.2.13). The familiar and expected capacitance “spike” at low frequency of the salt mixtures do not develop immediately as one elevates the temperature. But instead the bulk semi-circle progressively bends over with increasing temperature to become a new semi-circle and later disappears, the closer the system progresses towards the [C_{II} – Iso] phase transition this behaviour has already been explained by grain boundary microdomains of lamellar layers interacting with one another. Once through the [C_{II} – Iso] phase transition the capacitance spike reappears and takes on its familiar form. This form of impedance behaviour clearly indicates the presence of a diffusion process (Warburg impedance). This behaviour is typical

of Li [F8] and perhaps reflects the transformation of the system to a Maxwell two phase series of multi-layered dielectrics ^[90].

Summary:

The presented systems could be described as “polymer-in-salt” system particularly in their liquid crystal [S_A] phase system ^[82]. These are systems, which are from mechanical and fabrication, standpoints dimensionally stable gel-like electrolytes possessing the conductive properties similar at elevated temperatures to liquids ^[83]. It was shown that these systems retained the unique characteristics of three different electrolyte type systems that were possible to study in a methodical ways by means of EIS. Direct comparisons with similar previous investigations are difficult. For the most part most investigations are concerned with the characterisation of these system types. Therefore, previous data relating to the presented systems are non-existent. Currently many authors are starting to design ionic liquids that are integrated into the polymer, which is considered by many as the next greater step for ionic liquid electrochemistry. The table (6.2.2) shows a range of ionic liquids and their conductivities at selected temperatures from a number of selected authors. Largely there are very few conductivity measurements of ionic liquids with similar long side chain lengths i.e. C₁₆. Chia ^[67] previously discussed electrochemical investigated [C₁₆] chains lengths mixed with poly(tetramethyleneoxide) polymer and discovered two-dimensional lamella phases with relatively high conductivity at ambient temperatures see table (6.2.2). Most current investigations have concentrated in alkyl chain length shorter then (n = 8). Many authors favour the shorter chain lengths, because the ionic liquids exist in liquid phase at ambient temperatures.

Overall, the conductivities of the presented sample at ambient temperature remained subdued and only after the liquid crystal to isotropic phase transition do significant conductivities come into play. The conductivity for the sample [C₁₆-mim] [PF₆] reported by the author is 10 times better than those reported by De Roche ^[64] at similar temperatures see table (6.2.2). The first system was described as “plastic crystal” electrolyte ^{[1] [22] [61]} see table (6.2.3), the second system was described as a “amorphous” “salt-in-polymer” electrolyte ^[28] ^[82] and finally the third system was described as a “viscous liquid electrolyte” ^{[12] [62 – 63]}. Their ion-ion interactions were established by means of EIS measurement utilising the equivalent circuit method. These systems showed remarkable thermal stability and durability

after numerous thermal stress measurements. The dependence of conductivity and lithium salt size was also demonstrated to play a crucial role in the overall conductivities of the samples. The delocalising effects of the large [F8] anion did not demonstrate significant improved conductivities at lower temperatures, where the ionic liquid is crystalline and rigid. But on increasing the temperature to above the isotropic phase transition significant improvements were observed indicated its role in reducing ion pairs due to its strong charge delocalising effect is proved without doubt.

The Arrhenius approach and the VTF approach cannot be applied to explain all the behaviours of the presented systems. There are multiple phase transitions to be noted and if one intends to describe the ion-ion interactions of these systems by means of equivalent circuit method a new strategy is required. Each phase has its own behaviour that has crystal, liquid crystal, and liquid properties. Therefore, each phase must be understood as an independent system in itself as already indicated. It is not practical to try to impose one equivalent circuit form for the whole system as can be attempted for other simpler systems as seen in section {5.1}.

No.	Ionic Liquid	Salt	$\Theta = ^\circ\text{C}$ $\sigma = \text{S cm}^{-1}$	$\Theta = ^\circ\text{C}$ $\sigma = \text{S cm}^{-1}$	Reference
1	[C ₁₆ -mim]	[BF ₄] ⁻	21 °C 2.15 x 10 ⁻⁴	111 °C 1.2 x 10 ⁻²	Presented Work 2003
2	[C ₁₆ -mim]	[PF ₆] ⁻	21 °C 6.3 x 10 ⁻⁵	111 °C 1.89 x 10 ⁻³	Presented Work 2003
3	[C ₁₆ -mim]	[H8] ⁻	21 °C 2.0 x 10 ⁻⁶	111 °C 2.3 x 10 ⁻²	Presented Work 2003
4	[C ₁₆ -mim]	[F8] ⁻	21 °C 9.7 x 10 ⁻⁷	111 °C 0.1023	Presented Work 2003
5	[C ₁₆ -mim]	[PF ₆] ⁻	21 °C 6.1 x 10 ⁻⁶	111 °C 2.7 x 10 ⁻⁴	De Roche & Imrie ^[64] 2003
6	alpha., omega.-Diimidazoliumalkylene salts (C _n (ImX) ₂ ; n = 2-8)	LiTFSI	20 °C 10 ⁻³	—	Ito & Nishina ^[84] 2000
7	1-methyl-3-ethylimidazolium	bis(trifluoromethanesulfonyl)imide	20 °C 10 ⁻²	—	Every & Bishop ^[50] 2000
8	two imide-type acids such as bis(trifluoromethanesulfonyl)imide and bis(perfluoroethylsulfonyl)imide		25 °C 7 x 10 ⁻³	—	Yoshizawa & Oghihara ^[85] 2001
9	C _n Alkylmethylpyrrolidinium (n= 12)	Lithium bistrifluoromethanesulfonyl	60 °C 2 x 10 ⁻⁴	—	MacFarlane, & Douglas ^[61] 1999
10	C ₁₆ Poly(tetramethyleneoxide) – co- dodecamethylene	Li BF ₄	25 °C 10 ⁻³	—	Chia, & Zheng ^[67] 2003,

Table (6.2.2) Comparative table of the conductivities at the indicated temperatures for a range of poly(siloxane) based systems

6.3. Conclusion

In conclusion, to our discussion a number of interesting issues have been addressed and expanded upon. We have discussed at length the conductive investigations of two different potential electrolyte systems. If we remember from our earlier discussions, Andreev^[55] elegantly stated, “gel electrolytes are liquid electrolytes entrapped in a polymer matrix”. The conclusion from the presented evidence suggests some truth in this statement. The presented poly(siloxane) systems enjoy all the advantages and disadvantages of liquid electrolytes.

We observed by altering the constitution of the (oligo)ethyleneglycol side chain units, we could suppress and control to an extensive degree the crystallisation process of the polymer matrix. This in turn assisted in improved chain mobility. Hence, the temperature dependence of ionic conductivity suggested that the migration of ions was controlled by the segmental motion of the polymer due to the linear tendency of the curves in the VTF plots. We also observed the relationship between salt concentration and conductivity plus the detrimental effects of excess salt concentrations can have on the respective conductivity of systems which can also be said of the ionic liquids. This work proved the close relationship of conductivity and salts with anions of delocalising electronegative charges that influenced the dissociation of the salts with the matrix. The Li [F8] exerted a particularly positive influence on the overall conductivities due to its large size and many electronegative F-substituents. The author was successfully able to apply the equivalent circuit methodology to the investigation of the mechanism of the ionic transport of the indicated systems. Through the manipulation of such parameters the author managed to obtain a good, enough understanding of the ionic transport mechanism to design a equivalent circuit. At low viscosity and hence low T_g substantial ionic migration towards the electrode was observed and the application of ZwinTM equivalent circuits permitted a good fit to the proposed model. The author did not manage to achieve two of the three aims proposed in section {1} in the design considerations of a polymer electrolyte. Firstly, we managed to increase significantly the mobility of the side chain units by controlled and selective substitution of (oligo)ethyleneglycol side chain units hence regulated crystallisation process. Secondly, we increased the charge carrier mobility by means of mixing large F-substituents that were strongly charge delocalising and dissociative towards the cation, hence producing more charge carrying free ions. The third and least

successful aspect of the work was the appearance and development polarisation at the electrolyte/electrode interface. This indicated the probable migration of both anion and cation toward the electrode; therefore the author was unsuccessful in immobilising the anion itself. The conductivities on comparison with similar systems in the literature were not vastly improved when compared at ambient temperatures. Nevertheless, the samples did show a significant conductivity response at elevated temperatures that was comparable if not better than those found in the literature results. The issue of trapped water within the matrix played a major part in offering only a qualified commentary to the absolute conductive nature of the presented samples.

The second system showed results that are far more promising. As previously mentioned we had the unique opportunity to study the effective conductivity of three electrolyte systems contained within one material. We saw that at elevated temperatures the presented ionic liquid systems exhibited polymer-in-salts behaviour. Through the application of the equivalent circuit methodology, we were able to construct a detailed conductive picture of the ionic transport mechanisms of the three phase transitions present that has to date not been attempted. The author was with good success able to apply the fitting parameters to the respective phase. This procedure permitted a clearer understanding of suspected multi-domain lamella structures that take shape below the isotropic phase transition. The mechanism of transport was suspected to be by means of channels held open by the large polar-polar repulsion of the imidazolium header groups. At elevated temperatures above 50 °C the imidazolium header group order themselves as loosely packed, large surface area, bilayers held together by short range Coulombic forces and long range Van der Waals forces in multi-domains. It was observed that these self-organising systems could be disrupted and manipulated through their melting points by varying both the salt type and concentration. The large lithium salts Li [H8] and Li [F8] significantly affected the conductivities and melting points of the presented ionic systems. Due to their large physical size they were unable to fit comfortably at low temperatures within the 3D structure and therefore reducing considerably the conductivity of the crystal phase compared to the other smaller salt such as Li [PF₆] Li [BF₄]. At elevated temperatures above the isotropic phase, the salts with larger anions have far superior conductivities as the latent charge delocalisation effects of the salt come into play, previously suppressed due to the rigid crystalline structure. Hence encouraging greater free ion development.

In considering future work for the presented systems, the author can foresee a combination of the best aspects of the poly(siloxane) highly flexible backbone and the highly conductive and self-organising ionic liquids. Currently ionic liquids are of great interest (see section {1}) due to their relatively low melting points, vapour pressures, and novel architectures. In addition these materials demonstrate good characteristics such as non-volatility, thermal stability, non-flammability, extremely high ionic conductivity these systems could be applied for polymer electrolytes. Recent work Imrie & Ingram ^[28] have focused on aligning and organising the polymer chains in order to enhance the levels of ionic conductivity. The authors ^[28] concentrated on the liquid crystalline state to force solvating polymer conformations that was dictated by the liquid crystal part. The result is a partial decoupling of the conductivity from the glass-transition temperature of the polymer. The conductivity of such liquid crystalline chain polymers is low at room temperature, but reaches liquid like values at high temperature or when kept under polarisation, and therefore remains so upon cooling to room temperature. Since we know from our discussions that ionic liquids migrate along with the potential slope, it is assumed that the transport numbers of the target ions are low ^[86]. Ohno ^[86] stated “the lack of selectivity in the target ion transport is also a critical problem of these systems”. Taking these two characteristics in to account, a new type of ionic liquid could be designed for better ionic conductivity, hence polymerisation of ionic liquids. Recently the author Ohno ^[86] developed a series of new salts in which cationic unit was covalently tethered with anionic one. These salts are called “zwitterionic salt” ^[86] and are expected not to migrate under potential gradient even under melt conditions. These zwitterionic salts that are in the opinion of this author the ideal materials as non-volatile solvent for polymer electrolytes. In summation this work has opened the possibility for the further development of combining poly(siloxane) with imidazolium by means of polymerisation for applications as electrolytes. Every day there is a growing number of ionic liquids and equally researchers are now starting to go beyond the main occupation of characterisation of ionic liquids and are currently exploring new ways of combining the best attributes of both systems presented in this work.

The author is in a position to report the following new findings:

- The author reports new conductivity data for polymer-in-salt ionic liquid system for the recently newly synthesised lithium salts lithium bis-[3,4,5,6-tetrafluoro-1,2-benzenediolato(2-)-O,O']borate, lithium bis-[3-fluoro-1,2-benzenediolato (2)-O,O']borate, and lithium –bis-[1,2-benzenediolato(2-)-O,O']borate previously unreported in the literature. In addition, the author reports improved conductivity values of lithium hexafluorophosphate salt at ambient and sub-ambient temperatures ^[64] for the presented ionic liquid system over previously reported literature values. Similarly new conductivity values are reported for the poly(siloxane) gel-like systems.
- The author has proven the close correlation between the conductivity and thermal analysis measurements in the form of phase transitions in DSC data plots for the presented ionic liquid systems. This was previously reported by De Roche ^[64] for PF₆⁻ containing ionic liquids, but was never confirmed with other salts.
- The author reports improved conductivity values for the sample 1-*N*-hexadecyl-3-methylimidazolium hexafluorophosphate at ambient and sub-ambient temperatures compared to those reported by De Roche at Aberdeen ^[64].
- The presented conductivity results have proved the dependence of ionic mobility and hence conductivity with respect to the dissociative strength of F-substituted lithium salts lithium bis-[3,4,5,6-tetrafluoro-1,2-benzenediolato(2-)-O,O']borate, and lithium –bis-[1,2-benzenediolato(2-)-O,O']borate in both poly(siloxane) and ionic liquid systems. This dependence was previously proposed by Barthel and co-workers ^[91 - 92] for aforementioned lithium salts. In addition to their highly dissociative and charge delocalising nature, within ionic liquid systems their relative size hindered the movement of charge and charge carriers between the lamella channels at low temperatures. Only at elevated temperatures above the isotropic phase transition did their conductivities surpass previously reported conventional salts.
- The author reports for the first time a successful previously unattempted equivalent circuit analysis that interprets ionic conductive behaviours of multiphase ionic liquids systems utilising a modified Voigt equivalent circuit model. An individual model was developed for each phase transition, which accurately mimicked the behaviour of the system. Similarly a common model was proposed for the poly(siloxanes) investigated.

- The author reports the successful application of a newly in-house designed electrolyte cell for soft-polymer and gel-like electrolytes.
- Finally, the author reports a simpler and more refined method of synthesising long chained 1-*N*-3-methy-imidazolium ionic liquids over previously reported literature procedures.

References:

1. C. A. Angell, *Solid State Ionics*, **18-19**, 72 (1986).
2. C. A. Angell, *Solid State Ionics*, **9-10**, 3 (1983).
3. T. Fujinami, M. A. Mehta, K. Sugie and K. .. Mori, *Electrochim. Acta*, **45**, 1181 (2000).
4. E. Morales and J. L. Acosta, *Electrochimica Acta*, **45**, 1049 (1999).
5. G. G. Cameron, J. L. Harvie, M. D. Ingram and G. A. Sorrie, *Br. Polym. J.*, **20**, 199 (1988).
6. R. A. M. Hikmet and M. P. J. Peeters, *Solid State Ionics*, **126**, 25 (1999).
7. A. Merz and H. Bachmann, *J. Am. Chem. Soc.*, **117**, 901 (1995).
8. A. Reiche, T. Cramer, G. Fleischer, R. Sandner, B. Sandner, F. Kremer and J. Kaerger, *J. Phys. Chem. B.*, **102**, 1861 (1998).
9. K. Ito and H. Ohno, *Electrochim. Acta*, **43**, 1247 (1998).
10. S. W. Martin and C. A. Angell, *J. Am. Ceram. Soc.*, **67**, C148 (1984).
11. J. Barthel, R. Gerber and H. J. Gores, *Ber. Bunsen-Ges. Phys. Chem.*, **88**, 616 (1984).
12. G. G. Cameron and M. D. Ingram, Section: Liquid Polymer Electrolytes, *Polymer Electrolyte Reviews* (2), 168-190, Ed. Mac Callum, J.R. & Vincent, C.A., (1989).
13. H. Weingartner, V. C. Weiss and W. Schroer, *J. Chem. Phys.*, **113**, 762 (2000).
14. C. A. Angell and J. C. Tucker, *J. Phys. Chem.*, **84**, 268 (1980).
15. G. Adam and J. H. Gibbs, *J. Chem. Phys.*, **43**, 139 (1965).
16. P. G. Bruce and C. A. Vincent, *J. Electroanal. Chem. Interfacial Electrochem.*, **225**, 1 (1987).
17. P. G. Bruce, M. T. Hardgrave and C. A. Vincent, *J. Electroanal. Chem. Interfacial Electrochem.*, **271**, 27 (1989).
18. K. H. Lee, K. H. Kim and H. S. Lim, *J. Electrochem. Soc.*, **148**, A1148 (2001).
19. R. A. M. Hikmet, *Solid State Ionics*, **127**, 199 (2000).
20. J. Barthel, A. Schmid and H. J. Gores, *J. Electrochem. Soc.*, **147**, 21 (2000).
21. J. Barthel, M. Wuhr, R. Buestrich and H. J. Gores, *J. Electrochem. Soc.*, **142**, 2527 (1995).
22. C. A. Angell, *J. Non-Cryst. Solids*, **131-133**, 13 (1991).
23. J. Barthel, H. J. Gores, R. Neueder and A. .. Schmid, *Pure and Applied Chemistry*, **71**, 1705 (1999).
24. M. A. Mehta, T. Fujinami, S. Inoue, K. Matsushita, T. Miwa and T. Inoue, *Electrochim. Acta*, **45**, 1175 (2000).
25. J. Barthel, M. Wuehr, R. Buestrich and H. J. Gores, *J. Electrochem. Soc.*, **142**, 2527 (1995).
26. L. M. Torell and C. A. Angell, *Br. Polym. J.*, **20**, 173 (1988).
27. S. Schantz and L. M. Torell, Section: Light Scattering in Polymer Electrolytes, *Polymer Electrolyte Reviews* (2), 1-42, Ed. Mac Callum, J.R. & Vincent, C.A., (1989).
28. C. T. Imrie, M. D. Ingram and G. S. McHattie, *J. Phys. Chem. B*, **103**, 4132 (1999).
29. M. M. Doeff, P. Georen, J. Qiao, J. Kerr and L. C. De Jonghe, *J. Electrochem. Soc.*, **146**, 2024 (1999).
30. J. B. Kerr, G. Liu, L. A. Curtiss and P. C. Redfern, *Electrochimica Acta*, **48**, 2305 (2003).
31. N. Yoshio, Section: Lithium-Ion Secondary Batteries with Gelled Polymer Electrolytes, *Advances in Lithium-Ion Batteries*, 233-249, Ed. Van Schalkwijk, W.A. & Scrosati, B., Kluwer Academic / Plenum Publishers, (2002).
32. M. C. Lonergan, M. A. Ratner and D. F. Shriver, *J. Am. Chem. Soc.*, **117**, 2344 (1995).
33. Z. Ogumi, T. Abe, Ohkubo, T, I. Yamada, Y. Iriyama and M. Inaba, *Journal of the Electrochemical Society Proceedings*, **21**, 388 (2000).
34. Y. Zheng, F. Chia, G. Ungar, T. H. Richardson and P. V. Wright, *Electrochim. Acta*, **46**, 1397 (2001).
35. W. u. Xu, J.-P. Belieres and C. A. Angell, *Chem. Mater.*, **13**, 575 (2001).
36. A. Reiche, T. Cramer, G. Fleischer, R. Sandner, B. Sandner, F. Kremer and J. Kaerger, *J. Phys. Chem. B.*, **102**, 1861 (1998).
37. M. McLin and C. A. Angell, *Polym. Prepr. (Am. Chem. Soc., Div. Polym. Chem.)*, **30**, 439 (1989).
38. W. u. Xu, J.-P. Belieres and C. A. Angell, *Chem. Mater.*, **13**, 575 (2001).
39. J. J. Xu and G. C. Farrington, *J. Electrochem. Soc.*, **145**, 744 (1998).

40. S. S. Zhang and C. A. Angell, *J. Electrochem. Soc.*, **143**, 4047 (1996).
41. R. Hooper, L. J. Lyons, D. A. Moline and R. West, *Silicon Chemistry*, **1**, 121 (2002).
42. J. R. Macdonald, *Impedance Spectroscopy*, No. p. 344, John Wiley & Sons, New York, (1987).
43. P. Ferloni, M. Mastragostino and L. Meneghello, *Electrochimica Acta*, **41**, 27 (1996).
44. P. H. Smith, *Electronics*, **17**, 318 (1944).
45. G. Lang, J. Bacskaï and G. Inzelt, *Electrochimica Acta*, **38**, 773 (1993).
46. S. H. Glarum and J. H. Marshall, *Journal of the Electrochemical Society*, **127**, 1467 (1980).
47. C. Ho, I. D. Raistrick and R. A. Higgins, *Journal of the Electrochemical Society*, **127**, 343 (1980).
48. anonymous, www.comulrsr.com/resources/eis/cpe1.htm, (2002).
49. G. J. Brug, A. L. G. Van Den Feden, M. Sluyters-Rehbach and J. H. Sluyters, *Journal of Electroanalytical Chemistry*, **176**, 275 (1984).
50. H. Every, A. G. Bishop, M. Forsyth and D. R. MacFarlane, *Electrochim. Acta.*, **45**, 1279 (2000).
51. A. Watts, R. D. Hopwood, T. J. VanderNoot and Y. Zhao, *J. Electroanal. Chem.*, **433**, 207 (1997).
52. Z. Zhu, A. G. Einset, C. Y. Yang, W.-X. Chen and G. E. Wnek, *Macromolecules*, **27**, 4076 (1994).
53. G. B. Zhou, I. M. Khan and J. Smid, *Macromolecules*, **26**, 2202 (1993).
54. T. F. Yeh, Y. Okamoto and T. A. Skotheim, *Mol. Cryst. Liq. Cryst.*, **190**, 205 (1990).
55. Y. G. Andreev and P. G. Bruce, *Electrochim. Acta*, **45**, 1417 (2000).
56. P. G. Hall, J. E. Davies, J. M. McIntyre, I. M. Wards, D. J. Bannister and K. M. F. Le Brocqu, *Polymer Communications*, **27**, 98 (1986).
57. A. J. Carmichael, C. Hardacre, J. D. Holbrey, K. R. Seddon and M. Nieuwenhuyzen, *Journal of the Electrochemical Society Proceedings*, **99**, 209 (2000).
58. I. L. Karle, D. Ranganathan and V. Haridas, *J. Am. Chem. Soc.*, **118**, 7128 (1996).
59. F. B. Dias, S. V. Batty, A. Gupta, G. Ungar, J. P. Voss and P. V. Wright, *Electrochim. Acta*, **43**, 1217 (1998).
60. G. S. McHattie, C. T. Imrie and M. D. Ingram, *Electrochim. Acta*, **43**, 1151 (1998).
61. D. R. MacFarlane, J. Huang and M. Forsyth, *Nature (London)*, **402**, 792 (1999).
62. C. A. Angell, *J. Chem. Phys.*, **46**, 4673 (1967).
63. J. Barthel and H. J. Gores, *Liquid nonaqueous electrolytes*, No. p. 97, (1999).
64. J. De Roche, C. M. Gordon, C. T. Imrie, M. D. Ingram, A. R. Kennedy, F. Lo Celso and A. Triolo, *Chemistry of Materials*, **15**, 3089 (2003).
65. C. M. Gordon, J. D. Holbrey, A. R. Kennedy and K. R. Seddon, *J. Mater. Chem*, **8**, 2627 (1998).
66. K. M. Lee, C. K. Lee and I. J. B. Lin, *Chem. Commun.*, **9**, 899 (1997).
67. F. Chia, Y. Zheng, J. Liu, N. Reeves, G. Ungar and P. V. Wright, *Electrochimica Acta*, **48**, 1939 (2003).
68. H. Ohno and K. Ito, *Chem. Lett.*, 751 (1998).
69. P. Wasserscheid and T. Welton, *Ionic Liquids*, Wiley-VCH, (2003).
70. A. R. West, *Basic Solid State Chemistry*, No. p. 480, Wiley, (1996).
71. J. T. Irvine, D. C. Sinclair and A. R. West, *Materials Chemistry*, **2**, 132 (1990).
72. A. Hamnett, Section: Transport Properties Chapter 8, *Solid State Chemistry Techniques*, 279-321, Ed. Cheetham, A.K. & Day, P., Clarendon Press, Oxford, (1987).
73. L. Soubiran, E. Staples, I. Tucker, J. Penfold and A. Creeth, *Langmuir*, **17**, 7988 (2001).
74. N. Nakashima, Y. Yamaguchi, H. Eda, M. Kunitake and O. Manabe, *J. Phys. Chem. B*, **101**, 215 (1997).
75. S. Koizumi, H. Hasegawa and T. Hashimoto, *Macromolecules*, **27**, 4371 (1994).
76. T. Hashimoto, S. Koizumi and H. Hasegawa, *Macromolecules*, **27**, 1562 (1994).
77. T. Hashimoto, K. Yamasaki, S. Koizumi and H. Hasegawa, *Macromolecules*, **26**, 2895 (1993).
78. S. Shinkai and T. Kajiyama, *Pure Appl. Chem.*, **60**, 575 (1988).
79. M. Forsyth, J. Sun, F. Zhou and D. R. MacFarlane, *Electrochimica Acta*, **48**, 2129 (2003).
80. J. De Roche, Title: *Liquid Crystalline Electrolytes*, University of Aberdeen Department of Chemistry, 1-185 (2000).
81. P. C. Trulove and R. A. Mantz, Section: Electrochemical Properties of Ionic Liquids, *Ionic Liquids in Synthesis*, 109-123, Ed. Wasserscheid, P. & Welton, T., Wiley-VCH, Weinheim, (2003).
82. C. A. Angell, C. Liu and E. Sanchez, *Nature (London)*, **362**, 137 (1993).

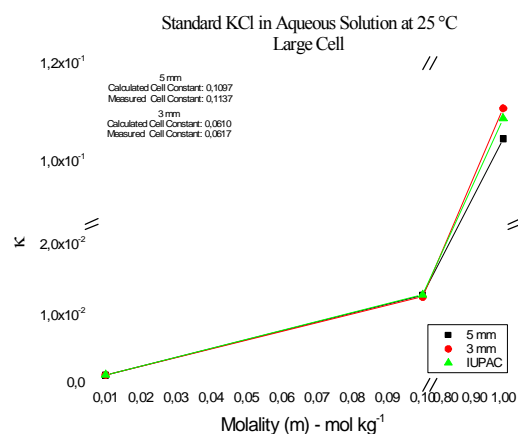
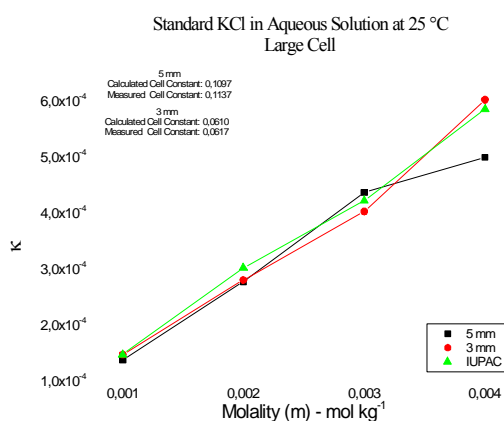
83. J. Fuller, A. C. Breda and R. T. Carlin, *Ionic liquid-polymer gel electrolytes*, **144**, No. p. 70,(1997).
84. K. Ito, N. Nishina and H. Ohno, *Electrochim. Acta*, **45**, 1295 (2000).
85. M. Yoshizawa, W. Ogihara and H. Ohno, *Electrochem. Solid-State Lett.*, **4**, E25 (2001).
86. H. Ohno, M. Yoshizawa and W. Ogihara, *Electrochimica Acta*, **48**, 2079 (2003)
87. R. Dupon, B. L. Papke, M. A. Ratner, D. H. Whitmore and D. F. Shriver, *J. Am. Chem. Soc.*, **104**, 6247 (1982).
88. C. A. Angell, *J. Phys. Chem.*, **70**, 3988 (1966).
89. N. A. Hamill, K. R. Seddon, A. Stark and M. J. Torres, *Abstr. Pap. - Am. Chem. Soc.*, **221st**, IEC (2001).
90. I. N. Shtennikova, *Liquid-Crystal Polymers*, No. p. 455, Plenum Press, New York, (1993).
91. J. Barthel, H. J. Gores and L. Kraml, *J. Phys. Chem.*, **100**, 3671 (1996).
92. J. Barthel, H. J. Gores and L. Kraml, *J. Phys. Chem.*, **100**, 1283 (1996).

Appendix

Data tables of testing and calibration of electrochemical test cell

Large Cell – Gap Piece 5 mm							
Calculated Cell Constant	Measured Cell Constant	Gap Piece	Potassium Chloride Millipore Water				
0,1097 cm ⁻¹	0,1137 cm ⁻¹	5 mm					
Conc.	Resistance	Conductance G	Measured κ	IUPAC κ	Measured Cell Constant	Calculated Cell Constant	Deviation
Molality	Ω	Ω ⁻¹	Ω ⁻¹ cm ⁻¹	Ω ⁻¹ cm ⁻¹	Ω ⁻¹ cm ⁻¹	cm ⁻¹	%
0,001	796,26	1,256E-03	1,378E-04	1,470E-04	0,117	0,1097	6,7
0,002	395,36	2,529E-03	2,775E-04	3,018E-04	0,119	0,1097	8,8
0,003	251,39	3,978E-03	4,364E-04	4,220E-04	0,106	0,1097	-3,3
0,004	198,56	5,036E-03	5,525E-04	5,860E-04	0,116	0,1097	6,1
0,01	80	1,250E-02	1,371E-03	1,408E-03	0,1126	0,1097	2,7
0,1	8,6	1,163E-01	1,276E-02	1,282E-02	0,1103	0,1097	0,5
1	1,05	9,524E-01	1,045E-01	1,086E-01	0,1141	0,1097	4,0

Large Cell – Gap Piece 3 mm							
Calculated Cell Constant	Measured Cell Constant	Gap Piece	Potassium Chloride Millipore Water				
0,0610 cm ⁻¹	0,0617 cm ⁻¹	3 mm					
Conc.	Resistance	Conductance G	Measured κ	IUPAC κ	Measured Cell Constant	Calculated Cell Constant	Deviation
Molality	Ω	Ω ⁻¹	Ω ⁻¹ cm ⁻¹	Ω ⁻¹ cm ⁻¹	Ω ⁻¹ cm ⁻¹	cm ⁻¹	%
0,001	414,73	2,411E-03	1,471E-04	1,470E-04	0,0610	0,0610	0,0
0,002	217,5	4,598E-03	2,805E-04	3,018E-04	0,0656	0,0610	-7,1
0,003	151,47	6,602E-03	4,027E-04	4,220E-04	0,0639	0,0610	-4,6
0,004	101,25	9,877E-03	6,025E-04	5,860E-04	0,0593	0,0610	2,8
0,01	42,25	2,367E-02	1,444E-03	1,408E-03	0,0595	0,0610	2,5
0,1	4,88	2,049E-01	1,250E-02	1,282E-02	0,0626	0,0610	-2,5
1	0,551	1,815E+00	1,107E-01	1,086E-01	0,0598	0,0610	1,9



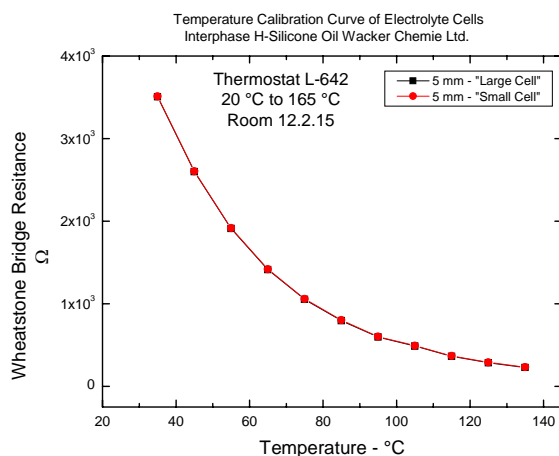
Thermostat L – 642 Room 12.2.15

20 °C to 165 °C

Baysilon M 40 Bayer AG

Thermostat Temperature Regulator Resistance Data

T / °C Programmed	R _{Pt} / Ω June 1998	R _{Pt} / Ω September 2001	R _{Pt} / Ω September 2002
Operator	Unknown	Mike Eberwein	John De Roche
20	506,91	506,70	
25	516,20	515,90	515,9
30	524,47	-	-
35	534,73	534,76	534,8
40	543,98	-	-
45	553,21	553,35	533,4
50	562,43	-	-
55	571,63	572,06	572,1
60	580,82	-	-
65	590,00	590,53	590,5
70	599,16	-	-
75	608,31	608,82	608,8
80	617,44	618,12	
85	626,56	627,21	627,2
90	635,67	-	-
95	644,76	645,82	645,8
100	653,84	-	-
105	662,91	663,91	633,9
110	671,96	-	-
115	681,00	681,99	682,2
120	690,03	-	-
125	699,04	700,15	700,2
160	708,04	-	-
135	717,02	-	717,5
140	725,99	-	-
145	734,95	-	735,0
150	743,89	-	
155	752,82	-	752,5
160	761,64	-	-
165	770,64	-	-



The graph opposite is the calibration curve of the Wheatstone bridge determined actual external resistance temperature within the experimental cell versus the programmed temperature of the high temperature thermostat. This curve was utilised to determine the actual temperature within the cell for any given resistance reading during impedance measurements. There was extremely good repeatability at high temperatures between both cell sizes as can be seen in the graph.

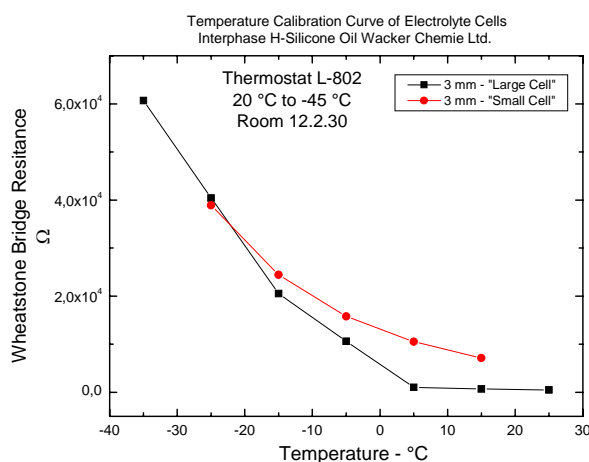
Thermostat L – 802 Room 12.2.20

25 °C to -45 °C

Baysilon M 5 Bayer AG

Thermostat Temperature Regulator Resistance Data

T / °C	R _{Pt} / Ω	R _{Pt} / Ω	R _{Pt} / Ω
Programmed	January 1995	October 2001	September 2003
Operator	Unknown	John De Roche	Hans G. Schweiger
-45	410,54	410,63	410,55
-40	-	420,29	420,59
-35	430,65	430,63	430,63
-30	-	-	-
-25	450,67	450,65	450,65
-20	-	-	-
-15	470,63	470,62	470,52
-10	-	-	-
-5	490,52	490,9	490,50
0	-	-	-
5	510,36	510,32	510,32
10	-	-	-
15	530,13	530,08	530,08
20	-	-	-
25	549,79	549,79	549,79



The graph opposite is the calibration curve of the Wheatstone bridge determined actual external resistance temperature within the experimental cell versus the programmed temperature of the low temperature thermostat. This curve was utilised to determine the actual temperature within the cell for any given resistance reading during impedance measurements. There was relatively good repeatability at low temperatures between both cell sizes as can be seen in the graph.

LiPF₆		Doping Tables			ImidC₁₆ PF₆	
MW:					MW:	
g mol⁻¹					g mol⁻¹	
151,90					455,53	
Mole Fraction Anion	Anion Moles	Weight Anion (g)	Weight Cation (g)	Cation Moles	Mole Fraction Cation	
0,5	6,71E-04	0,102	0,300	6,59E-04	0,5	
0,4	5,33E-04	0,081	0,360	7,90E-04	0,6	
0,3	3,75E-04	0,057	0,390	8,56E-04	0,7	
0,2	2,37E-04	0,036	0,420	9,22E-04	0,8	
0.1	1.18E-04	0,018	0.480	1.05E-03	0.9	

LiBF ₄		Doping Tables		ImidC ₁₆ BF ₄	
MW: g mol ⁻¹				MW: g mol ⁻¹	
93,75				397,37	
Mole Fraction Anion	Anion Moles	Weight Anion (g)	Weight Cation (g)	Cation Moles	Mole Fraction Cation
0,5	3,73E-04	0,035	5	4,53E-04	0,5
0,4	3,20E-04	0,030	0,180	4,53E-04	0,6
0,3	2,67E-04	0,025	0,280	7,05E-04	0,7
0,2	2,13E-04	0,020	0,280	7,05E-04	0,8
0.1	1.49E-04	0,014	0,380	9.56E-04	0.9

Li BC₁₂O₄F₈		Doping Tables		ImidC₁₆ BC₁₂O₄F₈	
MW:				MW:	
g mol⁻¹				g mol⁻¹	
377,84				678,44	
Mole Fraction Anion	Anion Moles	Weight Anion (g)	Weight Cation (g)	Cation Moles	Mole Fraction Cation
0,5	1,85E-04	0,070	0,150	2,21E-04	0,5
0,4	1,32E-04	0,050	0,150	2,21E-04	0,6
0,3	7,94E-05	0,030	0,150	2,21E-04	0,7
0,2	5,29E-05	0,020	0,150	2,21E-04	0,8
0.1	2.65E-05	0.010	0.150	2.21E-04	0.9

Cooling Curves

Conductivity Table of Poly(siloxane) Polymers α , β , χ , doped with Lithium Salts at (0:Li) – (32:1)

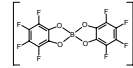
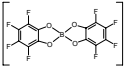
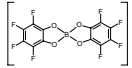
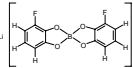
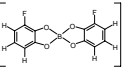
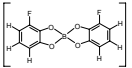
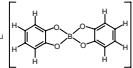
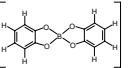
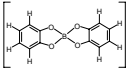
(0:Li) (32:1)		Siloxane Polymer α A6:B54-10%:90%			Siloxane Polymer β A12:B48-20%:80%			Siloxane Polymer χ A18:B42-30%:70%		
Celsius.	Kelvin	Ohms	σ	$\log \sigma$	Ohms	σ	$\log \sigma$	Ohms	σ	$\log \sigma$
$^{\circ}\text{C}$	1000/K	Ω	S cm^{-1}	$\log \text{Scm}^{-1}$	Ω	S cm^{-1}	$\log \text{Scm}^{-1}$	Ω	S cm^{-1}	$\log \text{Scm}^{-1}$
		Li [F8]			Li [F8]			Li [F8]		
										
20	3,41	6,37E+04	1,57E-05	-4,80	2,77E+05	3,61E-06	-5,44	3,83E+07	2,61E-08	-7,58
40	3,19	1,13E+04	8,87E-05	-4,05	1,36E+05	7,37E-06	-5,13	1,56E+07	6,42E-08	-7,19
60	3,00	2,19E+03	4,56E-04	-3,34	6,88E+04	1,45E-05	-4,81	1,90E+06	5,26E-07	-6,28
80	2,83	1,47E+02	6,78E-03	-2,17	9,80E+03	1,02E-04	-3,99	2,01E+05	4,98E-06	-5,30
100	2,68	3,48E+01	2,87E-02	-1,54	2,67E+02	3,75E-03	-2,42	1,40E+05	7,12E-06	-5,15
		Li [F2H6]			Li [F2H6]			Li [F2H6]		
										
20	3,41	1,56E+05	6,42E-06	-5,19	5,41E+05	1,85E-06	-5,73	3,83E+06	2,61E-07	-6,58
40	3,19	1,02E+04	9,84E-05	-4,01	1,70E+05	5,87E-06	-5,23	1,63E+06	6,12E-07	-6,21
60	3,00	1,95E+03	5,13E-04	-3,29	2,36E+04	4,23E-05	-4,37	1,83E+05	5,46E-06	-5,26
80	2,83	1,40E+02	7,16E-03	-2,15	3,47E+03	2,88E-04	-3,54	3,00E+04	3,33E-05	-4,48
100	2,68	1,04E+01	9,60E-02	-1,02	8,13E+02	1,23E-03	-2,91	5,00E+03	2,00E-04	-3,70
		Li [H8]			Li [H8]			Li [H8]		
										
20	3,41	4,76E+06	2,10E-07	-6,68	5,41E+05	1,85E-06	-5,73	2,19E+07	4,58E-08	-7,34
40	3,19	1,23E+06	8,11E-07	-6,09	1,39E+05	7,21E-06	-5,14	3,02E+06	3,31E-07	-6,48
60	3,00	1,00E+05	9,96E-06	-5,00	1,67E+04	5,98E-05	-4,22	1,18E+06	8,49E-07	-6,07
80	2,83	3,60E+04	2,78E-05	-4,56	1,66E+03	6,02E-04	-3,22	1,27E+05	7,89E-06	-5,10
100	2,68	1,19E+03	8,37E-04	-3,08	1,16E+02	8,63E-03	-2,06	9,90E+04	1,01E-05	-5,00

Table (5.1.4.)

Conductivity Table of Poly(siloxane) Polymers α , β , χ , with doped Lithium Salts at (0:Li) – (24:1)

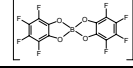
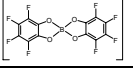
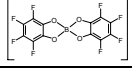
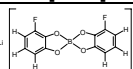
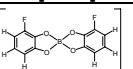
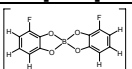
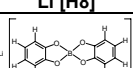
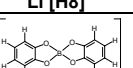
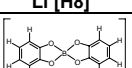
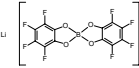
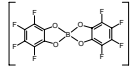
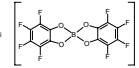
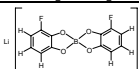
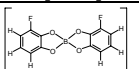
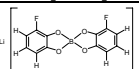
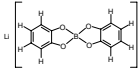
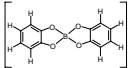
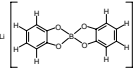
(0:Li) (24:1)		Siloxane Polymer α A6:B54-10%:90%			Siloxane Polymer β A12:B48-20%:80%			Siloxane Polymer χ A18:B42-30%:70%		
Celsius.	Kelvin	Ohms	σ	$\log \sigma$	Ohms	σ	$\log \sigma$	Ohms	σ	$\log \sigma$
$^{\circ}\text{C}$	1000/K	Ω	S cm^{-1}	$\log \text{Scm}^{-1}$	Ω	S cm^{-1}	$\log \text{Scm}^{-1}$	Ω	S cm^{-1}	$\log \text{Scm}^{-1}$
		Li [F8]			Li [F8]			Li [F8]		
										
20	3,41	1,12E+05	8,96E-06	-5,05	1,12E+06	8,89E-07	-6,051	5,29E+07	1,89E-08	-7,72
40	3,19	2,28E+04	4,38E-05	-4,36	4,22E+05	2,37E-06	-5,625	1,02E+07	9,80E-08	-7,01
60	3,00	1,20E+04	8,35E-05	-4,08	1,06E+05	9,45E-06	-5,024	9,80E+05	1,02E-06	-5,99
80	2,83	2,09E+03	4,78E-04	-3,32	5,00E+04	2,00E-05	-4,699	5,55E+05	1,80E-06	-5,74
100	2,68	2,58E+02	3,87E-03	-2,41	1,17E+04	8,55E-05	-4,068	1,40E+05	7,12E-06	-5,15
		Li [F2H6]			Li [F2H6]			Li [F2H6]		
										
20	3,41	2,53E+05	3,96E-06	-5,40	6,90E+05	1,45E-06	-5,839	3,46E+07	2,89E-08	-7,54
40	3,19	1,14E+05	8,74E-06	-5,06	2,58E+05	3,88E-06	-5,411	1,23E+07	8,15E-08	-7,09
60	3,00	2,14E+04	4,68E-05	-4,33	8,13E+04	1,23E-05	-4,910	2,25E+06	4,45E-07	-6,35
80	2,83	1,22E+04	8,19E-05	-4,09	1,27E+04	7,88E-05	-4,103	1,55E+05	6,47E-06	-5,19
100	2,68	1,60E+03	6,25E-04	-3,20	8,13E+03	1,23E-04	-3,910	1,82E+04	5,48E-05	-4,26
		Li [H8]			Li [H8]			Li [H8]		
										
20	3,41	4,26E+06	2,35E-07	-6,63	1,18E+06	8,45E-07	-6,073	1,12E+08	8,89E-09	-8,05
40	3,19	1,40E+06	7,14E-07	-6,15	4,45E+05	2,25E-06	-5,649	1,20E+07	8,30E-08	-7,08
60	3,00	3,38E+05	2,96E-06	-5,53	1,14E+05	8,79E-06	-5,056	6,71E+06	1,49E-07	-6,83
80	2,83	9,90E+04	1,01E-05	-5,00	5,88E+04	1,70E-05	-4,770	4,85E+05	2,06E-06	-5,69
100	2,68	1,19E+04	8,37E-05	-4,08	1,26E+04	7,91E-05	-4,102	9,90E+04	1,01E-05	-5,00

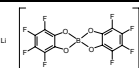
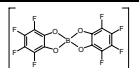
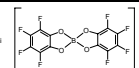
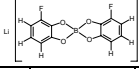
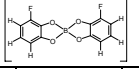
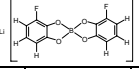
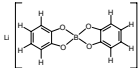
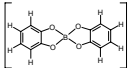
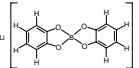
Table (5.1.5.)



Heating Curves

Conductivity Table of Poly(siloxane) Polymers α , β , χ , doped with Lithium Salts at (0:Li) – (32:1)

(0:Li) (32:1)		Siloxane Polymer α A6:B54-10%:90%			Siloxane Polymer β A12:B48-20%:80%			Siloxane Polymer χ A18:B42-30%:70%		
Celsius.	Kelvin	Ohms	σ	$\log \sigma$	Ohms	σ	$\log \sigma$	Ohms	σ	$\log \sigma$
$^{\circ}\text{C}$	1000/K	Ω	S cm^{-1}	$\log \text{Scm}^{-1}$	Ω	S cm^{-1}	$\log \text{Scm}^{-1}$	Ω	S cm^{-1}	$\log \text{Scm}^{-1}$
		Li [F8]			Li [F8]			Li [F8]		
										
20	3,41	6,37E+04	1,57E-05	-4,80	2,77E+05	3,61E-06	-5,442	3,83E+07	2,61E-08	-7,58
40	3,19	5,35E+03	1,87E-04	-3,73	1,76E+04	5,67E-05	-4,246	1,06E+06	9,42E-07	-6,03
60	3,00	6,76E+02	1,48E-03	-2,83	4,08E+03	2,45E-04	-3,610	1,18E+05	8,50E-06	-5,07
80	2,83	1,72E+02	5,80E-03	-2,24	1,06E+03	9,48E-04	-3,023	2,01E+04	4,98E-05	-4,30
100	2,68	5,35E+01	1,87E-02	-1,73	1,29E+02	7,75E-03	-2,111	4,72E+03	2,12E-04	-3,67
		Li [F2H6]			Li [F2H6]			Li [F2H6]		
										
20	3,41	1,56E+05	6,42E-06	-5,19	5,41E+05	1,85E-06	-5,733	3,83E+06	2,61E-07	-6,58
40	3,19	5,43E+03	1,84E-04	-3,74	5,35E+04	1,87E-05	-4,728	5,40E+05	1,85E-06	-5,73
60	3,00	3,67E+02	2,73E-03	-2,56	1,16E+04	8,64E-05	-4,063	1,54E+05	6,47E-06	-5,19
80	2,83	1,09E+02	9,16E-03	-2,04	5,35E+03	1,87E-04	-3,728	2,88E+04	3,47E-05	-4,46
100	2,68	6,25E+01	1,60E-02	-1,80	2,43E+03	4,12E-04	-3,385	5,00E+03	2,00E-04	-3,70
		Li [H8]			Li [H8]			Li [H8]		
										
20	3,41	-1,93E-01	-5,19	-5,73	5,41E+05	1,85E-06	-5,733	2,19E+07	4,58E-08	-7,34
40	3,19	-2,68E-01	-3,74	-4,73	3,22E+04	3,11E-05	-4,507	3,02E+06	3,31E-07	-6,48
60	3,00	-3,90E-01	-2,56	-4,06	2,51E+03	3,98E-04	-3,400	6,71E+05	1,49E-06	-5,83
80	2,83	-4,91E-01	-2,04	-3,73	4,95E+02	2,02E-03	-2,695	1,27E+05	7,89E-06	-5,10
100	2,68	-5,57E-01	-1,80	-3,38	1,16E+02	8,63E-03	-2,064	9,90E+04	1,01E-05	-5,00

Conductivity Table of Poly(siloxane) Polymers α , β , χ , with doped Lithium Salts at (0:Li) – (24:1)

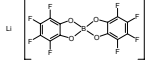
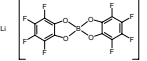
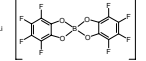
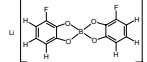
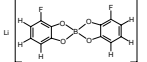
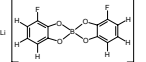
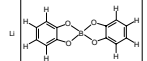
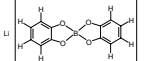
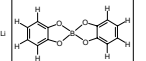
(0:Li) (24:1)		Siloxane Polymer α A6:B54-10%:90%			Siloxane Polymer β A12:B48-20%:80%			Siloxane Polymer χ A18:B42-30%:70%		
Celsius.	Kelvin	Ohms	σ	$\log \sigma$	Ohms	σ	$\log \sigma$	Ohms	σ	$\log \sigma$
$^{\circ}\text{C}$	1000/K	Ω	S cm^{-1}	$\log \text{Scm}^{-1}$	Ω	S cm^{-1}	$\log \text{Scm}^{-1}$	Ω	S cm^{-1}	$\log \text{Scm}^{-1}$
		Li [F8]			Li [F8]			Li [F8]		
										
20	3,41	5,10E+05	1,96E-06	-5,71	5,59E+06	1,79E-07	-6,747	5,65E+07	1,77E-08	-7,75
40	3,19	3,52E+04	2,84E-05	-4,55	2,29E+05	4,37E-06	-5,360	1,02E+06	9,80E-07	-6,01
60	3,00	4,26E+03	2,35E-04	-3,63	1,91E+04	5,23E-05	-4,281	9,80E+04	1,02E-05	-4,99
80	2,83	1,14E+03	8,80E-04	-3,06	5,00E+03	2,00E-04	-3,699	3,57E+04	2,80E-05	-4,55
100	2,68	5,35E+02	1,87E-03	-2,73	1,17E+03	8,55E-04	-3,068	1,40E+04	7,12E-05	-4,15
		Li [F2H6]			Li [F2H6]			Li [F2H6]		
										
20	3,41	5,38E+05	1,86E-06	-5,73	1,83E+06	5,45E-07	-6,264	2,04E+07	4,89E-08	-7,31
40	3,19	3,65E+04	2,74E-05	-4,56	1,77E+05	5,66E-06	-5,247	1,27E+06	7,88E-07	-6,10
60	3,00	5,95E+03	1,68E-04	-3,77	1,61E+04	6,23E-05	-4,206	1,44E+05	6,95E-06	-5,16
80	2,83	1,45E+03	6,88E-04	-3,16	2,80E+03	3,57E-04	-3,447	2,01E+04	4,97E-05	-4,30
100	2,68	4,45E+02	2,25E-03	-2,65	8,13E+02	1,23E-03	-2,910	6,07E+03	1,65E-04	-3,78
		Li [H8]			Li [H8]			Li [H8]		
										
20	3,41	4,26E+06	2,35E-07	-6,63	1,18E+06	8,45E-07	-6,073	1,12E+08	8,89E-09	-8,05
40	3,19	8,77E+05	1,14E-06	-5,94	3,08E+05	3,25E-06	-5,489	1,20E+07	8,30E-08	-7,08
60	3,00	2,53E+05	3,96E-06	-5,40	1,14E+05	8,79E-06	-5,056	1,38E+06	7,25E-07	-6,14
80	2,83	6,86E+04	1,46E-05	-4,84	5,15E+04	1,94E-05	-4,712	2,58E+05	3,88E-06	-5,41
100	2,68	4,22E+04	2,37E-05	-4,63	3,44E+04	2,91E-05	-4,536	9,90E+04	1,01E-05	-5,00

A <div> Ethyleneglycolmonoethylether = 120,00 mol⁻¹</div>				B <div> Diethyleneglycolmonoethylether = 166,13 mol⁻¹</div>				C Plastisizer				
Sample studied in detail		Table of preparation and synthesis of polysiloxane (H-Siloxane n = 60) with branched oligo(ethyleneglycol)										Sample of nominal interest
Test	Mole Fraction	H-Siloxane	Polymer	Polymer	A	B	C	Product	Solvent	Consistence	Comments	
No.	A : B : C	n	g	moles	%	%	%	g	2.5 ml	Observation	JDR	
1	A6:B54-10%-90%	60	0.212	0.040	90	0	0.533	0.040	90	Tolual Light gel	Desired	
2	A12:B48-20%-80%	60	0.327	0.123	80	0	0.795	0.123	80	Tolual Thick gel	Desired	
3	A18:B42-30%-70%	60	0.288	0.166	70	0	0.688	0.166	70	Tolual Soft rubber – waxy	Desired	
4	A54:B6-90%-10%	60	0.188	0.302	10	0	0.348	0.302	10	Tolual Brittle crystalline material	Interest – not further studied	
5	A48:B12-80%-20%	60	0.247	0.353	20	0	0.474	0.353	20	Tolual Brittle crystalline material	Interest – not further studied	
6	A42:B18-70%-30%	60	0.222	0.278	30	0	0.442	0.278	30	Tolual Crystalline	Interest – not further studied	
7	A60:B0-100%-0%	60	0.241	0.431	0	0	0.431	0.431	0	Tolual Powdery crystal	Interest – not further studied	
8	A0:B60-0%-100%	60	0.264	0.000	100	0	0.652	0.000	100	Tolual Turbid liquid	Interest – not further studied	
9	A6:B54-10%-90%	60	0.153	0.027	90	0	0.366	0.027	90	Tolual Light gel	Desired	
10	A12:B48-20%-80%	60	0.247	0.088	80	0	0.574	0.088	80	Tolual Thick gel	Desired	
11	A18:B42-30%-70%	60	0.226	0.121	70	0	0.512	0.121	70	Tolual Soft rubber – waxy	Desired	
Attempted removal of residual water within H-Siloxane by distillation – March 2001 [Before treatment 4.3 % Vol.] [After treatment 1.9 % Vol.] Test NMR + Carl-Fischer												
12	A12:B48-20%-80%	60	0.234	6.02E-05	20	0.083	80	0.461	0	0.544	THF Thick gel	Desired
13	A12:B48-20%-80%	60	0.298	7.66E-05	20	0.106	80	0.589	0	0.695	THF Thick gel	Desired
14	A12:B48--20%-80%	60	0.289	7.43E-05	20	0.101	80	0.558	0	0.659	Tolual Thick gel	Desired
15	A6:B54-10%-90%	60	0.182	4.67E-05	10	0.032	90	0.403	0	0.435	THF Light gel	Desired
16	A12:B48-20%-80%	60	0.265	6.81E-05	20	0.095	80	0.523	0	0.618	THF Thick gel	Desired
17	A18:B42-30%-70%	60	0.251	6.45E-05	30	0.135	70	0.433	0	0.568	THF Soft rubber – waxy	Desired
18	A24:B36–40%-60%	60	0.256	6.58E-05	40	0.183	60	0.379	0	0.562	THF Hard rubber	Not desired but studied further
19	A6:B54-10%-90%	60	0.182	4.68E-05	10	0.033	90	0.403	0	0.436	THF Thick gel	Desired
20	A12:B48-20%-80%	60	0.268	6.89E-05	20	0.096	80	0.53	0	0.626	THF Light gel	Desired
21	A18:B42-30%-70%	60	0.235	6.04E-05	30	0.126	70	0.406	0	0.532	THF Thick gel	Desired
22	A24:B36–40%-60%	60	0.244	6.27E-05	40	0.175	60	0.362	0	0.537	THF Hard rubber	Not desired but studied further
23	A17.4:B42:C0.6-29%:70%:1%	60	0.210	5.40E-05	29	0.109	70	0.363	1	0.637	THF Liquid Gel	Hindered polymerisation
24	A16.8:B42:C1.2-28%:70%:2%	60	0.205	5.27E-05	28	0.103	70	0.355	2	0.651	THF Liquid Gel	Hindered polymerisation
25	A16.2:B42:C1.8-27%:70%:3%	60	0.215	5.52E-05	27	0.104	70	0.371	3	0.779	THF Liquid Gel	Hindered polymerisation

A Ethylenglycolmonoethyl ether = 120.00 mol ⁻¹				B Diethylenglycolmonoethyl ether = 166,13 mol ⁻¹				C Plastisizer				Sample of nominal interest		
Sample studied in detail		Table of preparation and synthesis of polysiloxane (H-Siloxane n = 60) with branched oligo(ethyleneglycol)												
Test	Sample Name & Mix	H-Siloxane	Polymer	Polymer	A	A	B	B	C	C	Product	Solvent	Consistence	Comments
No.	A : B : C	n	G	moles	%	%	g	%	g	%	g	2.5 ml	Observation	JDR
26	A15.6:B42:C2.4-26%:70%:4%	60	0,230	5,91E-05	26	0,107	70	0,340	4	0,433	0,880	THF	Liquid Gel	Hindered polymerisation
27	A18:B42-30%:70%	60	0,255	6,55E-05	30	0,137	70	0,41	0	0	0,547	THF	Soft rubber – waxy	Desired
28	A18:B42-30%:70%	60	0,247	6,35E-05	30	0,133	70	0,427	0	0	0,560	THF	Soft rubber – waxy	Desired
29	A17.4:B42:C0.6-29%:70%:1%	60	0,226	5,81E-05	29	0,117	70	0,391	1	0,107	0,615	THF	Liquid	Hindered polymerisation
30	A17.7:B42:C0.3-29.5%:70%:0.5%	60	0,227	5,84E-05	29,5	0,120	70	0,393	0,5	0,054	0,567	THF	Liquid	Hindered polymerisation
31	A17.7:B42:C0.3-29.5%:70%:0.5%	60	0,222	5,71E-05	17,7	0,117	70	0,384	0,5	0,005	0,506	THF	Liquid	Hindered polymerisation
32	A17.4:B42:C0.6-29%:70%:1%	60	0,205	5,27E-05	29	0,106	70	0,354	1	0,01	0,470	THF	Liquid	Hindered polymerisation
33	A16.8:B42:C1.2-28%:70%:2%	60	0,209	5,37E-05	28	0,105	70	0,361	2	0,02	0,486	THF	Liquid	Hindered polymerisation
34	A0:B0:C2.4-0%:0%:3%	60	0,209	5,37E-05	0	0	70	0	3	0,041	0,041	THF	Liquid gel	No interest
35	A16.8:B42:C1.2-28%:70%:2%	60	0,238	6,12E-05	28	0,119	70	0,411	2	0,024	0,554	THF	Soft rubber – waxy	Desired
36	A16.2:B42:C1.8-27%:70%:3%	60	0,226	5,81E-05	27	0,109	70	0,391	3	0,034	0,534	THF	Soft rubber – waxy	Desired
37	A15.6:B42:C2.4-26%:70%:4%	60	0,16	4,11E-05	26	0,074	70	0,277	4	0,031	0,382	THF	Soft rubber – waxy	Desired
38	A16.8:B42:C1.2-28%:70%:2%	60	0,218	5,60E-05	28	0,109	70	0,377	2	0,022	0,508	THF	Soft rubber – waxy	Desired
39	A16.2:B42:C1.8-27%:70%:3%	60	0,208	5,35E-05	27	0,101	70	0,36	3	0,031	0,492	THF	Soft rubber – waxy	Desired
40	A10.8:B48:C1.2-18%:80%:2%	60	0,216	5,55E-05	18	0,07	80	0,427	2	0,021	0,518	THF	Soft rubber – waxy	Desired
41	A10.2:B48:C1.8-17%:80%:3%	60	0,218	5,60E-05	17	0,066	80	0,431	3	0,032	0,529	THF	Soft rubber – waxy	Desired
Further attempted removal of residual water within H-Siloxane through chemical treatment – March 2001 [Before treatment 2.1 % Vol.] [After treatment 1.4 % Vol.] Test NMR + Carl-Fischer														
42	A6:B54.10%:90%	60	1,12955	3,00E-04	10	0,216	90	2,69	0	0	2,906	THF	Light gel	Desired
43	A12:B48.20%:80%	60	1,14911	3,05E-04	20	0,44	80	2,74	0	0	3,180	THF	Thick gel	Desired
44	A12:B48.20%:80%	60	1,5	3,98E-04	20	0,574	80	3,17	0	0	3,744	THF	Thick gel	Desired
45	A15:B45.25%:75%	60	1,5	3,98E-04	25	0,717	75	2,98	0	0	3,697	THF	Thick gel	Desired

9
8
10
11
12
13

Conductivity Tables of Siloxane Polymers α , β , γ , doped with Lithium Salts at various Molar Ratios at 20 °C

Molar Ratio	Siloxane Polymer α A6:B54-10%:90%			Siloxane Polymer β A12:B48-20%:80%			Siloxane Polymer γ A18:B42-30%:70%		
	Ohms Ω	σ S cm ⁻¹	log σ log Scm ⁻¹	Ohms Ω	σ S cm ⁻¹	log σ log Scm ⁻¹	Ohms Ω	σ S cm ⁻¹	log σ log Scm ⁻¹
(0:Li)									
	[Li [F8]]			[Li [F8]]			[Li [F8]]		
									
1:16	3,70E+05	2,70E-06	-5,57	1,17E+06	8,58E-07	-6,06	1,17E+08	8,58E-09	-8,07
1:24	1,12E+05	8,96E-06	-5,05	1,12E+06	8,89E-07	-6,05	5,29E+07	1,89E-08	-7,72
1:32	6,37E+04	1,57E-05	-4,80	2,77E+05	3,61E-06	-5,44	3,83E+07	2,61E-08	-7,58
1:64	1,52E+05	6,58E-06	-5,18	3,91E+05	2,56E-06	-5,59	4,07E+07	2,46E-08	-7,61
	[Li [F2H6]]			[Li [F2H6]]			[Li [F2H6]]		
									
1:16	2,90E-06	2,90E-06	-5,54	3,01E+06	3,32E-07	-6,47	6,33E+07	1,58E-08	-7,80
1:24	3,96E-06	3,96E-06	-5,40	6,90E+05	1,45E-06	-5,83	3,46E+07	2,89E-08	-7,54
1:32	6,42E-06	6,42E-06	-5,19	5,41E+05	1,85E-06	-5,73	3,83E+06	2,61E-07	-6,58
1:64	7,01E-07	7,01E-07	-6,15	1,17E+06	8,56E-07	-6,06	4,07E+06	2,46E-07	-6,61
	[Li [H8]]			[Li [H8]]			[Li [H8]]		
									
1:16	8,33E+06	1,20E-07	-6,92	1,25E+06	8,00E-07	-6,09	2,00E+08	5,01E-09	-8,30
1:24	4,26E+06	2,35E-07	-6,63	1,18E+06	8,45E-07	-6,07	1,12E+08	8,89E-09	-8,05
1:32	4,76E+06	2,10E-07	-6,68	5,41E+05	1,85E-06	-5,73	2,19E+07	4,58E-08	-7,34
1:64	3,32E+06	3,01E-07	-6,52	1,17E+06	8,56E-07	-6,06	1,55E+07	6,45E-08	-7,19

Conductivity Table of Polysiloxane Polymers α , β , χ , doped with Lithium Salts at (0:Li) – (32:1)

(0:Li) (32:1)		Siloxane Polymer α A6:B54-10%:90%			Siloxane Polymer β A12:B48-20%:80%			Siloxane Polymer χ A18:B42-30%:70%		
Celsius.	Kelvin	Ohms	σ	$\log \sigma$	Ohms	σ	$\log \sigma$	Ohms	σ	$\log \sigma$
°C	1000/K	Ω	S cm ⁻¹	log Scm ⁻¹	Ω	S cm ⁻¹	log Scm ⁻¹	Ω	S cm ⁻¹	log Scm ⁻¹
		[Li [F8]]			[Li [F8]]			[Li [F8]]		
20	3,41	6,37E+04	1,57E-05	-4,80	2,77E+05	3,61E-06	-5,44	3,83E+07	2,61E-08	-7,58
40	3,19	1,13E+04	8,87E-05	-4,05	1,36E+05	7,37E-06	-5,13	1,56E+07	6,42E-08	-7,19
60	3,00	2,19E+03	4,56E-04	-3,34	6,88E+04	1,45E-05	-4,81	1,90E+06	5,26E-07	-6,28
80	2,83	1,47E+02	6,78E-03	-2,17	9,80E+03	1,02E-04	-3,99	2,01E+05	4,98E-06	-5,30
100	2,68	3,48E+01	2,87E-02	-1,54	2,67E+02	3,75E-03	-2,42	1,40E+05	7,12E-06	-5,15
		[Li [F2H6]]			[Li [F2H6]]			[Li [F2H6]]		
20	3,41	1,56E+05	6,42E-06	-5,19	5,41E+05	1,85E-06	-5,73	3,83E+06	2,61E-07	-6,58
40	3,19	1,02E+04	9,84E-05	-4,01	1,70E+05	5,87E-06	-5,23	1,63E+06	6,12E-07	-6,21
60	3,00	1,95E+03	5,13E-04	-3,29	2,36E+04	4,23E-05	-4,37	1,83E+05	5,46E-06	-5,26
80	2,83	1,40E+02	7,16E-03	-2,15	3,47E+03	2,88E-04	-3,54	3,00E+04	3,33E-05	-4,48
100	2,68	1,04E+01	9,60E-02	-1,02	8,13E+02	1,23E-03	-2,91	5,00E+03	2,00E-04	-3,70
		[Li [H8]]			[Li [H8]]			[Li [H8]]		
20	3,41	4,76E+06	2,10E-07	-6,68	5,41E+05	1,85E-06	-5,73	2,19E+07	4,58E-08	-7,34
40	3,19	1,23E+06	8,11E-07	-6,09	1,39E+05	7,21E-06	-5,14	3,02E+06	3,31E-07	-6,48
60	3,00	1,00E+05	9,96E-06	-5,00	1,67E+04	5,98E-05	-4,22	1,18E+06	8,49E-07	-6,07
80	2,83	3,60E+04	2,78E-05	-4,56	1,66E+03	6,02E-04	-3,22	1,27E+05	7,89E-06	-5,10
100	2,68	1,19E+03	8,37E-04	-3,08	1,16E+02	8,63E-03	-2,06	9,90E+04	1,01E-05	-5,00

Conductivity Table of Polysiloxane Polymers α , β , χ , with doped Lithium Salts at (0:Li) – (24:1)

(0:Li) (24:1)		Siloxane Polymer α A6:B54-10%:90%			Siloxane Polymer β A12:B48-20%:80%			Siloxane Polymer χ A18:B42-30%:70%		
Celsius.	Kelvin	Ohms	σ	$\log \sigma$	Ohms	σ	$\log \sigma$	Ohms	σ	$\log \sigma$
°C	1000/K	Ω	S cm ⁻¹	log Scm ⁻¹	Ω	S cm ⁻¹	log Scm ⁻¹	Ω	S cm ⁻¹	log Scm ⁻¹
		[Li [F8]]			[Li [F8]]			[Li [F8]]		
20	3,41	1,12E+05	8,96E-06	-5,05	1,12E+06	8,89E-07	-6,051	5,29E+07	1,89E-08	-7,72
40	3,19	2,28E+04	4,38E-05	-4,36	4,22E+05	2,37E-06	-5,625	1,02E+07	9,80E-08	-7,01
60	3,00	1,20E+04	8,35E-05	-4,08	1,06E+05	9,45E-06	-5,024	9,80E+05	1,02E-06	-5,99
80	2,83	2,09E+03	4,78E-04	-3,32	5,00E+04	2,00E-05	-4,699	5,55E+05	1,80E-06	-5,74
100	2,68	2,58E+02	3,87E-03	-2,41	1,17E+04	8,55E-05	-4,068	1,40E+05	7,12E-06	-5,15
		[Li [F2H6]]			[Li [F2H6]]			[Li [F2H6]]		
20	3,41	2,53E+05	3,96E-06	-5,40	6,90E+05	1,45E-06	-5,839	3,46E+07	2,89E-08	-7,54
40	3,19	1,14E+05	8,74E-06	-5,06	2,58E+05	3,88E-06	-5,411	1,23E+07	8,15E-08	-7,09
60	3,00	2,14E+04	4,68E-05	-4,33	8,13E+04	1,23E-05	-4,910	2,25E+06	4,45E-07	-6,35
80	2,83	1,22E+04	8,19E-05	-4,09	1,27E+04	7,88E-05	-4,103	1,55E+05	6,47E-06	-5,19
100	2,68	1,60E+03	6,25E-04	-3,20	8,13E+03	1,23E-04	-3,910	1,82E+04	5,48E-05	-4,26
		[Li [F2H6]]			[Li [F2H6]]			[Li [F2H6]]		
20	3,41	4,26E+06	2,35E-07	-6,63	1,18E+06	8,45E-07	-6,073	1,12E+08	8,89E-09	-8,05
40	3,19	1,40E+06	7,14E-07	-6,15	4,45E+05	2,25E-06	-5,649	1,20E+07	8,30E-08	-7,08
60	3,00	3,38E+05	2,96E-06	-5,53	1,14E+05	8,79E-06	-5,056	6,71E+06	1,49E-07	-6,83
80	2,83	9,90E+04	1,01E-05	-5,00	5,88E+04	1,70E-05	-4,770	4,85E+05	2,06E-06	-5,69
100	2,68	1,19E+04	8,37E-05	-4,08	1,26E+04	7,91E-05	-4,102	9,90E+04	1,01E-05	-5,00

[C₁₆-mim] [BF₄]⁻ Thermal Stability Data

Day (1)			Day (3)			Day (6)		
K	Ω	S cm ⁻¹	K	Ω	S cm ⁻¹	K	Ω	S cm ⁻¹
1000/T(K)	Resistance	log σ	1000/T(K)	Resistance	log σ	1000/T(K)	Resistance	log σ
3,73	1,00E-04	-4,00	3,73	4,71E-05	-4,33	3,73	5,30E-05	-4,28
3,60	1,25E-04	-3,90	3,60	1,26E-04	-3,90	3,60	1,26E-04	-3,90
3,47	1,66E-04	-3,78	3,47	1,52E-04	-3,82	3,46	1,52E-04	-3,82
3,35	2,11E-04	-3,68	3,35	2,16E-04	-3,67	3,37	2,09E-04	-3,68
3,25	4,52E-04	-3,35	3,25	4,39E-04	-3,36	3,25	4,39E-04	-3,36
3,14	1,11E-03	-2,95	3,14	1,25E-03	-2,90	3,14	1,25E-03	-2,90
3,05	2,00E-03	-2,70	3,05	2,00E-03	-2,70	3,04	1,67E-03	-2,78
2,96	2,63E-03	-2,58	2,97	2,63E-03	-2,58	2,97	2,63E-03	-2,58
2,87	7,10E-03	-2,15	2,87	7,05E-03	-2,15	2,87	7,05E-03	-2,15
2,79	7,96E-03	-2,10	2,81	7,96E-03	-2,10	2,81	7,96E-03	-2,10
2,72	8,91E-03	-2,05	2,72	8,77E-03	-2,06	2,72	8,89E-03	-2,05
2,64	1,13E-02	-1,95	2,65	1,13E-02	-1,95	2,65	1,06E-02	-1,98
2,58	1,05E-02	-1,98	2,57	1,22E-02	-1,92	2,57	1,22E-02	-1,92
2,51	1,23E-02	-1,91	2,51	1,34E-02	-1,87	2,51	1,23E-02	-1,91
2,45	1,19E-02	-1,92	2,45	1,06E-02	-1,97	2,46	1,08E-02	-1,97

[C₁₆-mim] [PF₆]⁻ Thermal Stability Data

Day (1)			Day (3)			Day (6)		
K	Ω	S cm ⁻¹	K	Ω	S cm ⁻¹	K	Ω	S cm ⁻¹
1000/T(K)	Resistance	log σ	1000/T(K)	Resistance	log σ	1000/T(K)	Resistance	log σ
3,73	3,50E-05	-4,46	3,729	2,19E-05	-4,66	3,73	1,95E-05	-4,71
3,60	4,04E-05	-4,39	3,604	2,52E-05	-4,60	3,59	2,24E-05	-4,65
3,47	4,66E-05	-4,33	3,471	2,94E-05	-4,53	3,47	2,56E-05	-4,59
3,35	7,98E-05	-4,10	3,35	4,98E-05	-4,30	3,34	4,43E-05	-4,35
3,25	9,44E-05	-4,03	3,244	5,90E-05	-4,23	3,24	5,25E-05	-4,28
3,14	1,26E-04	-3,90	3,148	7,91E-05	-4,10	3,14	7,03E-05	-4,15
3,05	1,94E-04	-3,71	3,044	1,21E-04	-3,92	3,05	1,08E-04	-3,97
2,96	7,43E-04	-3,13	2,957	4,65E-04	-3,33	2,95	4,13E-04	-3,38
2,87	1,04E-03	-2,98	2,871	6,52E-04	-3,19	2,88	5,78E-04	-3,24
2,79	1,36E-03	-2,87	2,792	8,47E-04	-3,07	2,79	7,48E-04	-3,13
2,72	1,86E-03	-2,73	2,714	1,12E-03	-2,95	2,71	9,95E-04	-3,00
2,64	2,77E-03	-2,56	2,644	1,73E-03	-2,76	2,64	1,56E-03	-2,81
2,58	3,05E-03	-2,52	2,577	1,89E-03	-2,72	2,58	1,68E-03	-2,77
2,51	3,26E-03	-2,49	2,504	2,01E-03	-2,70	2,51	1,85E-03	-2,73
2,45	5,01E-03	-2,30	2,439	2,15E-03	-2,67	2,45	2,00E-03	-2,70

[C₁₆-mim] [Cl]⁻ Thermal Stability Data

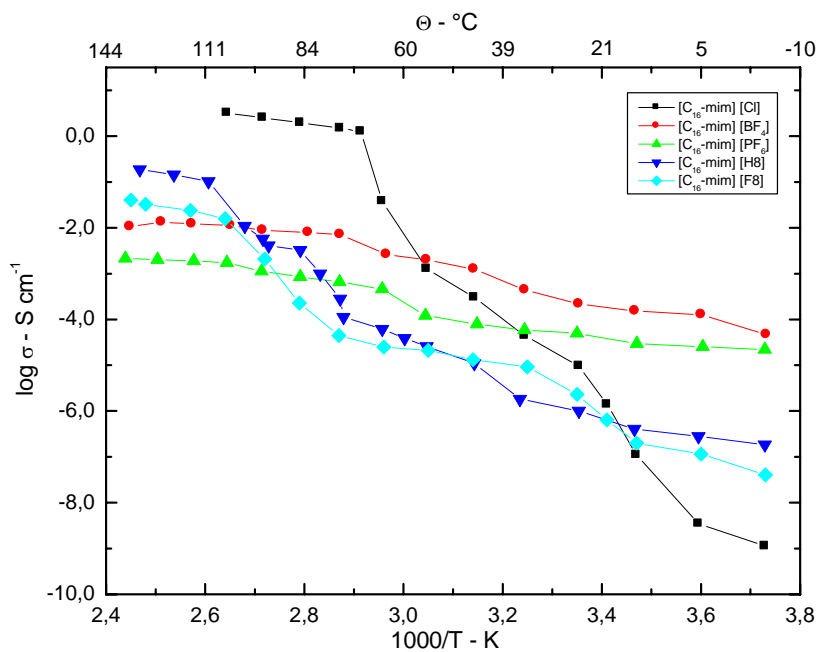
Day (1)			Day (3)			Day (6)		
K	Ω	S cm ⁻¹	K	Ω	S cm ⁻¹	K	Ω	S cm ⁻¹
1000/T(K)	Resistance	log σ	1000/T(K)	Resistance	log σ	1000/T(K)	Resistance	log σ
3,73	9,78E+08	-8,99	3,73	8,880E+08	-8,95	3,73	9,14E+08	-8,96
3,60	1,45E+08	-8,16	3,60	2,890E+08	-8,46	3,60	1,78E+08	-8,25
3,47	7,12E+06	-6,85	3,47	9,120E+06	-6,96	3,47	7,77E+06	-6,89
3,35	1,90E+06	-6,28	3,41	7,200E+05	-5,86	3,35	5,04E+04	-4,70
3,25	2,05E+05	-5,31	3,35	1,033E+05	-5,01	3,25	1,54E+04	-4,19
3,14	4,38E+04	-4,64	3,25	2,260E+04	-4,35	3,14	2,86E+03	-3,46
3,05	2,80E+03	-3,45	3,14	3,326E+03	-3,52	3,05	8,21E+02	-2,91
3,00	6,41E+02	-2,81	3,05	7,810E+02	-2,89	2,96	5,10E+00	-0,71
2,96	4,14E+01	-1,62	2,96	2,636E+01	-1,42	2,87	6,10E-01	0,21
2,87	8,67E-01	0,06	2,91	7,923E-01	0,10	2,79	4,90E-01	0,31
2,79	6,12E-01	0,21	2,87	6,749E-01	0,17	2,72	3,87E-01	0,41
2,72	4,59E-01	0,34	2,79	5,119E-01	0,29	2,64	3,55E-01	0,45
2,64	3,70E-01	0,43	2,72	3,963E-01	0,40			
			2,64	3,113E-01	0,51			

[C₁₆-mim] [H8]⁺ Thermal Stability Data

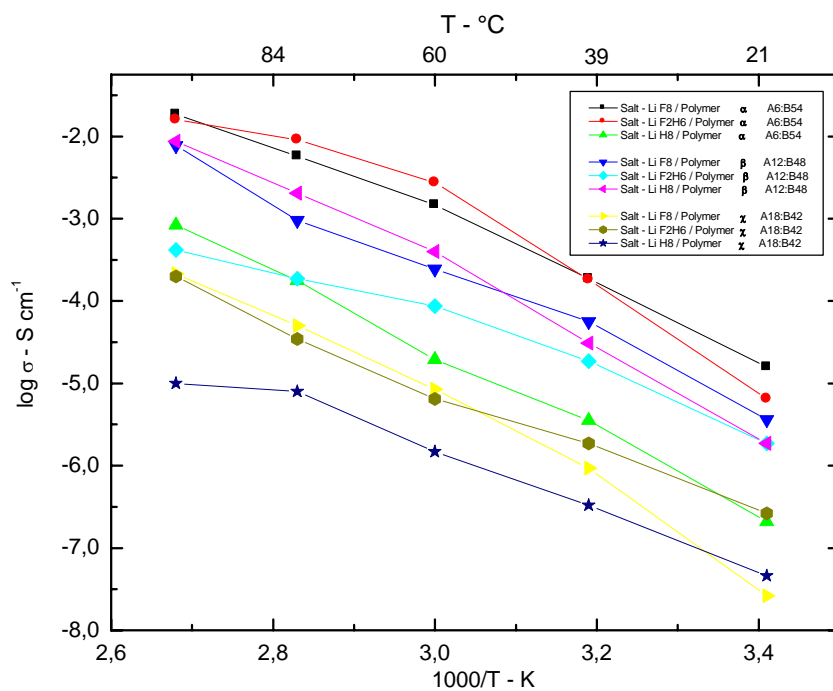
Day (1)			Day (3)			Day (6)		
K	Ω	S cm ⁻¹	K	Ω	S cm ⁻¹	K	Ω	S cm ⁻¹
1000/T(K)	Resistance	log σ	1000/T(K)	Resistance	log σ	1000/T(K)	Resistance	log σ
3,73	1,85E-07	-6,734	3,60	1,45E-07	-6,84	3,73	2,16E+07	-7,33
3,60	2,79E-07	-6,554	3,60	2,19E-07	-6,66	3,60	6,74E+06	-6,83
3,47	4,06E-07	-6,391	3,46	3,16E-07	-6,5	3,47	2,88E+06	-6,46
3,35	9,98E-07	-6,001	3,35	7,76E-07	-6,11	3,35	3,21E+05	-5,51
3,24	1,83E-06	-5,737	3,25	1,45E-06	-5,84	3,25	8,85E+04	-4,95
3,14	1,10E-05	-4,958	3,14	8,51E-06	-5,07	3,14	7,18E+04	-4,86
3,05	2,57E-05	-4,59	3,05	2,00E-05	-4,7	3,05	4,82E+04	-4,68
3,00	3,89E-05	-4,41	2,96	4,79E-05	-4,32	2,96	3,57E+04	-4,55
2,96	6,14E-05	-4,212	2,87	2,19E-04	-3,66	2,87	1,88E+04	-4,27
2,88	1,12E-04	-3,951	2,82	7,76E-04	-3,11	2,79	8,04E+03	-3,91
2,87	2,81E-04	-3,552	2,79	2,57E-03	-2,59	2,72	8,08E+02	-2,91
2,83	9,98E-04	-3,001	2,72	4,47E-03	-2,35	2,63	5,36E+01	-1,73
2,79	3,27E-03	-2,486	2,61	7,94E-02	-1,1	2,58	4,10E+01	-1,61
2,73	4,11E-03	-2,386	2,54	1,12E-01	-0,95	2,47	2,40E+01	-1,38
2,72	5,77E-03	-2,239	2,48	1,45E-01	-0,84	2,45	2,17E+01	-1,34
2,68	1,09E-02	-1,961						
2,61	1,02E-01	-0,99						
2,54	1,44E-01	-0,842						
2,47	1,86E-01	-0,731						

[C₁₆-mim] [F8]⁻ Thermal Stability Data

Day (1)			Day (3)			Day (6)		
K	Ω	$S \text{ cm}^{-1}$	K	Ω	$S \text{ cm}^{-1}$	K	Ω	$S \text{ cm}^{-1}$
1000/T(K)	Resistance	log σ	1000/T(K)	Resistance	log σ	1000/T(K)	Resistance	log σ
3,73	1,85E-07	-6,734	3,60	1,45E-07	-6,84	3,73	2,16E+07	-7,33
3,60	2,79E-07	-6,554	3,60	2,19E-07	-6,66	3,60	6,74E+06	-6,83
3,47	4,06E-07	-6,391	3,46	3,16E-07	-6,5	3,47	2,88E+06	-6,46
3,35	9,98E-07	-6,001	3,35	7,76E-07	-6,11	3,35	3,21E+05	-5,51
3,24	1,83E-06	-5,737	3,25	1,45E-06	-5,84	3,25	8,85E+04	-4,95
3,14	1,10E-05	-4,958	3,14	8,51E-06	-5,07	3,14	7,18E+04	-4,86
3,05	2,57E-05	-4,59	3,05	2,00E-05	-4,7	3,05	4,82E+04	-4,68
3,00	3,89E-05	-4,41	2,96	4,79E-05	-4,32	2,96	3,57E+04	-4,55
2,96	6,14E-05	-4,212	2,87	2,19E-04	-3,66	2,87	1,88E+04	-4,27
2,88	1,12E-04	-3,951	2,82	7,76E-04	-3,11	2,79	8,04E+03	-3,91
2,87	2,81E-04	-3,552	2,79	2,57E-03	-2,59	2,72	8,08E+02	-2,91
2,83	9,98E-04	-3,001	2,72	4,47E-03	-2,35	2,63	5,36E+01	-1,73
2,79	3,27E-03	-2,486	2,61	7,94E-02	-1,1	2,58	4,10E+01	-1,61
2,73	4,11E-03	-2,386	2,54	1,12E-01	-0,95	2,47	2,40E+01	-1,38
2,72	5,77E-03	-2,239	2,48	1,45E-01	-0,84	2,45	2,17E+01	-1,34
2,68	1,09E-02	-1,961						
2,61	1,02E-01	-0,99						
2,54	1,44E-01	-0,842						
2,47	1,86E-01	-0,731						

Combined Graph's of Salts Utilised - Day (6)

Combined graph's of poly(siloxane) polymers doped with different lithium salts
(O:Li) = (32:1)



Combined graph's of poly(siloxane) polymers doped with different lithium salts
(O:Li) = (24:1)

